Cronfa
Swansea University's Research Repository

Nonlinear Interactions in Rotordynamics

Numerical and Experimental Investigations of Internal Resonances



Prifysgol Abertawe
Swansea University

Mehmet Selim Akay

Engineering Department
Swansea University
UK

A thesis presented for the degree of
Doctor of Philosophy

29 Oct 2025

Copyright: the author, Mehmet Selim Akay, 2025
Distributed under the terms of a Creative Commons Attribution-NoDerivatives 4.0 License (CC BY-NC 4.0)

Dedication

To my loving parents...

Acknowledgements

I would like to express my sincere gratitude to my supervisors, Dr Alexander Shaw and Prof Michael Friswell, for their invaluable guidance, encouragement, and unwavering support throughout the course of my PhD study titled "Nonlinear Interactions in Rotordynamics: Numerical and Experimental Investigations of Internal Resonances" at Swansea University, UK. Their mentorship has not only equipped me with essential research skills but has also imparted important life lessons through their kindness, thoughtfulness, and empathy.

This research was made possible through the generous financial support of the Ministry of National Education of Türkiye, for which I am deeply grateful.

I also extend my appreciation to the workshop technicians for their expert guidance and assistance during the manufacturing process of the experimental rig.

Finally, I am profoundly thankful to my parents, Hasan Akay and Mevlüde Akay, and sisters, Ayşe Sümeyye Akay-Zengin and Elif Nadide Akay-Polat, for their steadfast love and support, which have been a constant source of strength and motivation.

Nonlinear interactions in rotordynamics

Numerical and Experimental Investigations of Internal Resonances

Mehmet Selim Akay

Abstract

In rotating machinery, tighter tolerances are crucial for efficiency, making rotor-stator interaction a key research area. This thesis explores the diverse nonlinear responses of rotordynamic systems, focusing on quasiperiodic internal resonances (IRs) in rotor-stator interactions through numerical and experimental analysis. Numerical continuation and time simulations were utilized on a nondimensional 2-degree-of-freedom (2-dof) gyroscopic model where a cubic stiffness was employed, as well as a hyperbolic tangent (tanh) contact model that approximates discontinuous contact. A novel quasiperiodic continuation method was introduced, demonstrating that periodic continuation methods can be extended to include nonautonomous quasiperiodic responses which included an adaptation of the Floquet theory. Nonlinear normal modes (NNMs) was also applied to study forward (FW) and backward (BW) mode coupling.

Key findings from theoretical studies indicate that IRs of frequency ratio 2:1 and 3:1 can arise even with soft nonlinearities, with damping playing a crucial role in their persistence and amplitude. Homotopy method used to switch the bifurcation diagram between different nonlinearities facilitated bifurcation analysis without prior knowledge. Experimental validation was conducted using a test rig designed to reflect the theoretical model. Experimental results confirmed the influence of damping, while additional bifurcations were attributed to real-world boundary conditions. The transition from FW and BW precession of IRs was observed in both simulations and experiments, which was termed stagnation at the point where this occurs. However, the IRs of coupling between the swinging and rotational modes were not achieved experimentally due to small basins of attraction. The use of continuation in various forms proved valuable for the analysis of the nonlinear rotating machinery.

This work advances the understanding of nonlinear rotor-stator dynamics by providing new methods for analysing and classifying IRs, while generating several future work ideas. The findings have implications for designing more robust rotating machinery, considering both numerical predictions and experimental constraints.

Keywords Rotordynamics, Bifurcation, Continuation, Internal resonance, Homotopy, Nonlinear normal modes

Declarations

This work has not previously been accepted in substance for any degree and is not being concurrently submitted in candidature for any degree.

Signed: [redacted] (candidate)

Date: 29 Oct 2025

This thesis is the result of my own investigations, except where otherwise stated. Other sources are acknowledged by footnotes giving explicit references. A bibliography is appended.

Signed: [redacted] (candidate)

Date: 29 Oct 2025

I hereby give consent for my thesis, if accepted, to be available for electronic sharing

Signed: [redacted] (candidate)

Date: 29 Oct 2025

The University's ethical procedures have been followed and, where appropriate, that ethical approval has been granted.

Signed: [redacted] (candidate)

Date: 29 Oct 2025

List of Publications

Paper M. S. Akay, A. D. Shaw, and M. I. Friswell, 'Continuation analysis of a nonlinear rotor system', Nonlinear Dynamics, vol. 105, no. 1, pp. 25–43, 2021, doi: 10.1007/s11071-021-06589-8.

Code M. S. Akay, 'Simulation and continuation codes'. doi.org/10.5281/zenodo.4586405 .2021.

Conf. M. S. Akay, 'Continuation Analysis of Overhung Rotor Bouncing Cycles with Smooth and Contact Nonlinearities', presented at the DSTA 2021, Lodz, Poland, Dec. 06, 2021. [Online]. Available: https://repozytorium.p.lodz.pl/items/78df0a76-7f87-411c-9fb4-af62e2325329

Paper M. S. Akay, A. D. Shaw, and M. I. Friswell, 'Continuation analysis of overhung rotor bouncing cycles with smooth and contact nonlinearities', International Journal of Non-Linear Mechanics, vol. 150, p. 104343, 2023, doi: https://doi.org/10.1016/j.ijnonlinmec.2022.104343.

Poster M. S. Akay, A. D. Shaw, and M. I. Friswell, 'Exploration of overhung rotor bouncing cycles with cubic and tanh-contact nonlinearities using numerical continuation', in Proceedings of ISMA 2022 International Conference on Noise and Vibration Engineering, Leuven, Belgium: KU Leuven, Sep. 2022, pp. 2644–2658. Accessed: Apr. 28, 2024. [Online]. Available: https://past.isma-isaac.be/downloads/isma2022/proceedings/Contribution_604_proceeding_3.pdf

Contents

Nomenclature **xvii**

1 Introduction **1**

1.1 Background . . . 2
1.2 Classification of different nonlinear responses . . . 3
1.3 Literature survey for the theoretical study . . . 8
1.3.1 Nonlinearity and rotor-stator interactions in rotordynamics . . . 8
1.3.2 Different rotor-stator interaction definitions . . . 9
1.3.3 Complex and simpler models . . . 11
1.3.4 Analysis methods . . . 12
1.3.5 Importance of the rotating frame perspective in the analysis of some quasiperiodic motion . . . 15
1.3.6 Wider nonlinear rotor-stator interaction literature . . . 16
1.4 NNM literature survey . . . 18
1.5 Experiment literature survey . . . 20
1.5.1 Test rigs . . . 20
1.5.2 Different experimental responses . . . 24
1.5.3 Analysis methods for the experimental studies . . . 27
1.5.4 Notes on control-based continuation . . . 28
1.6 Aim and structure of the thesis . . . 28
1.6.1 Theoretical research interest . . . 29
1.6.2 NNM research interest . . . 31
1.6.3 Experimental research interest . . . 32

2 Methods **35**

2.1 Complex DFT . . . 35
2.1.1 Signed frequencies . . . 36
2.2 Campbell diagram . . . 37
2.3 Continuation . . . 40
2.3.1 AUTO files . . . 42

3 Continuation analysis of a nonlinear overhung rotor 45
3.1 Theoretical background . . . 46
3.1.1 Definition of the system . . . 46
3.1.2 Equations of motion . . . 46
3.1.3 Nondimensionalised equations of motion . . . 49
3.1.4 Stationary frame equations in displacement coordinates . . . 50
3.1.5 Rotating frame equations of motion . . . 51
3.1.6 Natural frequency map . . . 52
3.2 Time simulation setup . . . 52
3.3 Numerical continuation setup . . . 54
3.4 Results and Discussion . . . 56
3.4.1 Numerical Continuation . . . 56
3.4.2 Time simulations . . . 61
3.5 Conclusion . . . 64

4 Continuation Analysis of Overhung Rotor Bouncing Cycles with Smooth and Contact Nonlinearities 69
4.1 Theory and Methods . . . 70
4.1.1 Equations of motion . . . 70
4.1.2 Homotopy from smooth to contact nonlinearity . . . 74
4.2 Results and Discussion . . . 76
4.2.1 The case of low damping . . . 81
4.2.2 The case of low damping and high unbalance . . . 83
4.2.3 tanh-contact . . . 85
4.3 Conclusions . . . 86

5 A Quasiperiodic Arclength Shooting-Continuation Method 89
5.1 Introduction . . . 89
5.2 A quasiperiodic arclength shooting-continuation formulation with Newton corrections . . . 90
5.2.1 Phase condition . . . 93
5.2.2 Generating an initial solution for the shooting algorithm . . . 98
5.2.3 Stability calculation with Floquet multipliers . . . 100
5.3 Results . . . 104
5.3.1 Stability calculation results . . . 105
5.3.2 DFT branches . . . 110
5.4 Conclusion . . . 111

6 Internal Resonances in the Light of NNMs in Rotordynamics 113
6.1 Introduction . . . 113
6.1.1 The method for finding FW and BW whirling NNMs . . . 114
6.1.2 Degenerate conservative IR solutions . . . 116
6.2 The effect of off-centring on rotating NNMs - proof of concept . . . 119
6.2.1 Frequency spectrum of elliptic FW and BW signal . . . 119
6.2.2 Correlation of forward and backward NNMs . . . 121
6.2.3 The effect of gravity as anisotropy on an unbalanced isotropic cubic Zilli system . . . 131
6.2.4 The effect of out of balance excitation as off-centring on cubic/tanh Zilli system . . . 135
6.3 Conclusions . . . 135

7 Experimental Investigations of Nonlinear Rotor-Stator Bouncing Interactions 139
7.1 Design of the test rig . . . 139
7.1.1 2-dof equations of motion . . . 141
7.1.2 Deciding the numerical values for the test rig . . . 147
7.1.3 Selection of bearings . . . 153
7.1.4 Data acquisition hardware and software . . . 153
7.1.5 Measuring the stator position . . . 155
7.2 A 4-dof mathematical model for the gyroscopic cubic system . . . 157
7.2.1 Definition of EOM . . . 157
7.3 Initial Campbell plots and initial simulation results . . . 159
7.3.1 Initial Campbell plots . . . 159
7.3.2 Initial simulations . . . 160
7.4 Experimental procedures and calibration . . . 163
7.4.1 Measuring the shaft bow . . . 164
7.4.2 Tapping test on the stopped rotor . . . 166
7.4.3 Tapping test on the stopped rotor daily . . . 169
7.4.4 Obtaining the force-displacement curve . . . 169
7.4.5 Tapping test on the rotor when running . . . 173
7.4.6 Tapping test on the rig . . . 173
7.5 Experiment results . . . 175
7.5.1 Bifurcation diagram measurements . . . 175
7.5.2 Campbell diagram with manufactured and assembled experimental rig data . . . 182
7.5.3 Numerical simulations and comparison with the experiment . . . 186
7.6 Conclusion . . . 195

8 Conclusion **199**
8.1 Future work 201

A AUTO files **203**
A.1 Constants file 203
A.2 Auto data file generation 204

B Required derivatives for the quasiperiodic shooting-continuation method 205
B.1 Partial derivative of the periodicity condition with respect to the period . . 205
B.2 Partial derivative of the periodicity condition with respect to the initial condition 206
B.3 Partial derivative of the periodicity condition with respect to the rotor spin speed 207
B.4 Partial derivative of the periodicity condition with respect to out-of-balance angle 208

C Experiment's Appendices **209**
C.1 Transient 2^{nd} BW mode not decaying in initial simulations 209
C.2 Selection of bearings 209
C.2.1 The stator's self-aligning ball bearing 209
C.2.2 The rods' self-aligning ball bearing 213
C.2.3 The shaft's angular contact ball bearings 213
C.2.4 The rods' alternative spherical plain bearing 213
C.3 Sensor delay study 216
C.4 Campbell plot with the modified test rig values 218
C.5 The global assembly drawing of the test rig 218

Nomenclature

$(\cdot)^{\cdot}$ Derivative with respect to arclength

$(\cdot)'$ Derivative with respect to time

$(\cdot)^T$ Transpose operator

$(\cdot)_I; {}_I(\cdot)$ Indication of initial value before any lateral displacement on 2-dof cantilever model of experimental study

$[\cdot]$ A matrix with components shown

α Ratio of x_d over x_s in 2-dof cantilever model of experimental study

α_1 Angles of the straight lines between supports of the shaft

α_2 Angles of the straight lines between supports of the stiffness rods

α_s Stator angle in experimental study

$\bar{\mathbf{F}}$ Algebraic equations for numerical continuation that are augmented with arclength condition

$\bar{\mathbf{F}}_{\mathbf{x}}$ Jacobian of $\bar{\mathbf{F}}$ with respect to $\mathbf{x}$

$\bar{W}_k$ Complex discrete Fourier transform coefficient for frequency bin index k

$\bar{w}_{t_n}$ Complex coordinates at time instance n, $\bar{w}_{t_n} = x_{t_n} + jy_{t_n}$

β Ratio of ψ_d over x_s in 2-dof cantilever model of experimental study

β_A OW Omron sensor angular shift from straight

β_B OG Omron sensor angular shift from straight

β_b Shaft bow angle at the disk

β_s Nondimensional measure of snubber-ring stiffness in 2-dof Zilli systems

β_u Unbalance angle of the disk

β_{AB} Omron sensors' assumed common angular shift from straight

β_{sh} MTI sensor angular shift from straight

$\mathbf{0}$ Filling zero matrix or vector

$\mathbf{b}$ Total force acting on the disk

$\mathbf{C}$ Damping matrix

$\mathbf{F}$ Algebraic system of equations

$\mathbf{f}$ Vector field in the rotating frame, $\mathbf{q}' = \mathbf{f}$

$\mathbf{F_u}$ Jacobian of $\mathbf{F}$ with respect to $\mathbf{u}$

$\mathbf{F_x}$ Jacobian of $\mathbf{F}$ with respect to $\mathbf{x}$

$\mathbf{F}_\lambda$ Jacobian of $\mathbf{F}$ with respect to λ

$\mathbf{G}$ Gyroscopic matrix

$\mathbf{g}$ Vector field in the stationary frame, $\mathbf{z}' = \mathbf{g}$

$\mathbf{g}^0$ Stationary frame vector field of the previous solution point on the solution family

$\mathbf{H}$ Shooting function

$\mathbf{h}$ A vector for multi-component phase condition

$\mathbf{I}$ Filling identity matrix

$\mathbf{J}$ 4×4 skew symmetric matrix

$\mathbf{J}_2$ 2×2 skew symmetric matrix

$\mathbf{K}$ Linear stiffness matrix

$\mathbf{k}$ Vector field in the rotated stationary frame, $\mathbf{v}' = \mathbf{k}$

$\mathbf{M}$ Mass matrix

$\mathbf{P}$ A repeated matrix in experimental EOM

$\mathbf{p}$ Tangent vector (direction vector) on solution family, also $\dot{\mathbf{x}}$

$\mathbf{p}^0$ Tangent vector (direction vector) at the previous point on the solution family, also $\dot{\mathbf{x}}^0$

$\mathbf{p}^1$ Tangent vector (direction vector) at the new point on the solution family, also $\dot{\mathbf{x}}^1$

$\mathbf{q}$ Rotating frame states vector of the 2-dof Zilli systems, $\mathbf{q} = \{\widetilde{\mathbf{w}}^T, \widetilde{\mathbf{w}}'^T\}^T$

$\mathbf{q}^0$ Rotating frame trajectory data of the previous solution point on solution family

$\mathbf{q}^1$ Rotating frame trajectory data of the next solution point on solution family

$\mathbf{R}$ 4×4 rotation matrix

$\mathbf{R}_2$ 2×2 rotation matrix

$\mathbf{R}_\phi$ Rotation matrix about z-axis

$\mathbf{R}_\theta$ Rotation matrix about x-axis

$\mathbf{T}$ 4×4 rotational frame transform

$\mathbf{T}^0$ Rotating frame transform matrix for the previous point on the solution branch

$\mathbf{T}^1$ Rotating frame transform matrix for the next point on solution family

$\mathbf{T}_2$ 2×2 rotational frame transform

$\mathbf{u}$ Unknown variables for the continued algebraic equations $\mathbf{F} = 0$

$\mathbf{u}^{(0)}$ Prediction of the next solution point's variables along the branch

$\mathbf{u}^{(\nu)}$ Prediction of the next solution point's variables along the branch corrected ν times in Newton iterations

$\mathbf{v}$ State vector of the rotated frame of reference, $\mathbf{v} = \mathbf{Rz}$

$\mathbf{w}$ Stationary frame coordinates, $\mathbf{w} = \{x, y\}^T$

$\mathbf{w}_{ang}$ Vector of angular coordinates of the 2-dof Zilli systems, $\mathbf{w}_{ang} = \{\theta, \psi\}^T$

$\mathbf{w}_{t_n}$ Configuration space vector housing the positions of the disk at time instance t_n, $\mathbf{w}_{t_n} = \{x_{t_n}, y_{t_n}\}^T$

$\mathbf{x}$ Extended unknowns $\mathbf{x} = \{\mathbf{u}^T, \lambda\}^T$ for the continued equations $\bar{\mathbf{F}} = \mathbf{0}$

$\mathbf{x}^0$ A known, regular solution point on the continued branch of solutions

$\mathbf{x}^1$ Next solution point to be calculated on the continued branch of solutions

$\mathbf{x}^{(0)}$ Prediction of the next solution point along the branch

$\mathbf{x}^{(\nu)}$ Prediction of the next solution point along the branch corrected ν times in Newton iterations

$\mathbf{z}$ States vector with $\mathbf{z} = \{\mathbf{w}^T, \dot{\mathbf{w}}^T\}^T$ first and velocities second

$\mathbf{z}^0$ Stationary frame trajectory data of the previous solution point on solution family

$\mathbf{z}^1$ Stationary frame trajectory data of the next solution point on solution family

$\mathbf{z}_0$ Shooting initial condition states vector in stationary frame

$\mathbf{z}_r$ r^{th} eigenvector

$\mathbf{z}_{ang}$ Angular states vector of the 2-dof Zilli systems, $\mathbf{z}_{ang} = \{\mathbf{w}_{ang}^T, \mathbf{w}_{ang}'^T\}^T$

$\mathbf{z}_{prediction}$ State vector of an initial, linear prediction of a low amplitude, regular solution point on an NNM branch

δW_{nc}^{active} Virtual work of nonconservative active forces

δ_b Shaft bow angular position

δ_u Unbalance mass angular position

$\delta_{L_1^I}$ Shaft's axial contraction due to the cantilever action of the shaft.

Δs^0 Step size, arclength between previous and predicted solution points

$\dot{\mathbf{u}}^0$ Tangent vector's components corresponding to variables

$\dot{\mathbf{x}}$ Tangent vector (direction vector) on solution family, also $\mathbf{p}$

$\dot{\mathbf{x}}^0$ Tangent vector (direction vector) at the previous point on the solution family, also $\mathbf{p}^0$

$\dot{\mathbf{x}}^1$ Tangent vector (direction vector) at the new point on the solution family, also $\mathbf{p}^1$

$\dot{\lambda}^0$ Tangent vector's component corresponding to free parameter

ϵ A small number

γ Nondimensional measure of cubic stiffness

γ_b Shaft bow angle angular position

γ_u Unbalance angle angular position

κ Homotopy paramter to switch the nonlinearity of Zilli system from cubic to tanh-contact

λ Free continuation parameter

$\lambda^{(0)}$ Prediction of the next solution point's free parameter along the branch

$\lambda^{(\nu)}$ Prediction of the next solution point's free parameter along the branch corrected ν times in Newton iterations

μ Nondimensional unbalance in experimental study

ν_1 Shaft Poisson's ratio

ν_2 Stiffness rods' Poisson's ratio

Ω Rotor spin speed

ω Generic angular frequency

Ω^0 Rotor speed parameter of the previous solution point on the solution family

Ω^1 Rotor speed parameter of the previous solution point on the solution family

$\omega^n_{k^{kinem}_{rb}}$ Natural frequency of the shaft derived from lateral stiffness acting at the stator in 2-dof cantilever model of experimental study

$\omega^n_{k_{rb}}$ Natural frequency of the 2-dof cantilever model derived from the EOM in experimental study

ω_b^{rot} Rotating frame backward whirling modal frequency

ω_b^{sta} Stationary frame backward whirling modal frequency

ω_f^{rot} Rotating frame forward whirling modal frequency

ω_f^{sta} Stationary frame forward whirling modal frequency

ω_n Natural frequency of the 2-dof systems

ω_r r^{th} natural frequency

ω_{dr} r^{th} damped natural frequency

$\Omega_{n:m}$ Campbell diagram value corresponding to IR n:m

ϕ Disk angle about z-axis (rotation angle)

ϕ_Ω Unbalance force direction at initial condition $\mathbf{z}_0$

ψ Context dependent angle about y-axis

ψ_d Disk angle about y-axis

ψ_s Stator's tangent angle in 2-dof cantilever model in experimental study

τ Normalised time in one period/quasiperiod, defined between 0 and 1

θ Context dependent angle about x-axis

θ_d Disk angle about x-axis

ε_b Shaft bow radius at the disk

ε_u Unbalance mass eccentricity

$\widetilde{\mathbf{w}}$ Rotating frame positions vector

ξ^ρ A continuation parameter linking damping and eccentricity with a given power, ρ

ζ Damping ratio

ζ_r r^{th} modal damping ratio

$\{\cdot\}$ A vector with components shown

a Disk position along the overhung shaft

a^* Disk's distance along the z-axis from the point on the z-axis that the tangent of the shaft at the disk intersects in 2-dof cantilever model in experimental study

A_1 Shaft cross-section area after lateral motion

A_2 Stiffness rods' cross-section area after lateral motion

b Stator position along the overhung shaft

b^* Stator's distance along the z-axis from the point on the z-axis that the tangent of the shaft at the stator intersects in 2-dof cantilever model in experimental study

c A notional dimension used to nondimensionalise EOMs during the design of experimental study

c Snubber ring clearance in Ch. 4

c_{rb} Radial damping coefficient at the overhung shaft distance b

d_1 Shaft diameter after lateral motion

d_1^I Shaft diameter before lateral motion

d_2 Stiffness rods' diameter after lateral motion

d_2^I Stiffness rods' diameter before lateral motion

d_d Disk diameter in experimental study

e Nondimensional eccentricity of disk or unbalance mass

E_1 Shaft's elastic modulus

F A radial force acting at the stator in 2-dof cantilever model of experimental study

f Force exerted on the stator during the force-displacement measurements

f_k Frequency of the k$^{\text{th}}$ frequency bin

f_r Radial restoring force

f_s Sampling rate

$F^a_{j_a}$ DFT's of the time simulated long trajectory mode at the $j_a{}^{\text{th}}$ solution point on branch a

$F^b_{j_b}$ DFT's of the time simulated long trajectory mode at the $j_b{}^{\text{th}}$ solution point on branch b

f^{rot}_{nl} Nondimensional nonlinear restoring force expressed in the rotating frame

f^{sta}_{nl} Nondimensional nonlinear restoring force expressed in the stationary frame

g_x Force on the disk in the x-axis due to misalignment

g_y Force on the disk in the y-axis due to misalignment

h Phase condition(s)

h_d Disk thickness in experimental study

$H_{1,2}$ Receptance FRF estimators with spectral averaging

I^I_1 Cross-section area moment of inertia of the shaft before any lateral displacement in 2-dof cantilever model of experimental study

I_p Nondimensional polar moment

I_p Nondimensional polar moment of inertia of the disk in 2-dof Zilli systems

j Imaginary unit, $j = \sqrt{-1}$

J_d Diametral moment of inertia of the disk in 2-dof Zilli systems

J^o_d Diametral moment of inertia with respect to the overhung point O of the disk in 2-dof Zilli system

J_p Polar moment of inertia of the disk in 2-dof Zilli systems

$J_{d,e}^{kinem}$ Effective diametral moment of inerta of the disk at the stator angle's intersection in 2-dof cantilever model of experimental study

K Hyperbolic tangent function's steepness parameter

k Force-displacement measurement kit stiffness

k_s Radial stator stiffness that engages after the clearance is covered by the rotor lateral motion in 2-dof Zilli systems

k_t Angular equivalent of k_{rb}, $k_t = k_{rb}b^2$

k_{3b} Cubic radial stiffness acting at overhung distance b

k_{rb} Linear radial stiffness acting at overhung distance b

L Lagrangian function, $L = T_{tot} - V_{tot}$

l_0 Shaft preload

L_1 Shaft length after lateral motion

l_1 Shaft elongation

L_1^I Shaft length before lateral motion

L_2 Stiffness rods' length after lateral motion

l_2 Stiffness rods' elongation

L_2^I Stiffness rods' length before lateral motion

m Nondimensional disk mass in 2-dof Zilli systems

m_d Disk mass in dimensional Zilli systems

m_e^{kinem} Effective mass at the stator in 2-dof cantilever model of experimental study

m_s Stator mass

m_u Unbalance mass

N Data number of discrete signal

n Degrees of freedom, or a generic index or an integer, depending on the context

$n_{b,f}^p$:$m_{b,f}^q$ n:m internal resonance expression with frequency relation $n\,\omega_{b,f}^{rot} = m\,\omega_{b,f}^{rot}$ where the left/right hand frequency belongs to p/q^{th} forward-backward natural frequency pair

n_{iter} Iteration count

N_{y1} Lateral force acting at the bearings of the shaft

N_{y2} Lateral force acting at the bearings of the stiffness rods

N_{z1} Axial force acting at the bearings of the shaft

N_{z2} Axial force acting at the bearings of the stiffness rods

Q_k k^{th} generalised, nonconservative force

q_k k^{th} generalised coordinate

Q_{x_s} Generalised force in x-direction at the stator in 2-dof cantilever model of experimental study

Q_{y_s} Generalised force in y-direction at the stator in 2-dof cantilever model of experimental study

R Half stator edge length

r Radial position of disk

r_s Stator lateral position amplitude

$R^{ab}_{j_a j_b}$ Correlation between branch a and b between solutions with indices j_a and j_b

s_r r^{th} eigenvalue

T Period/quasiperiod

t Dimensional/nondimensional time

T^0 Period/quasiperiod of the previous point on the solution branch

T^1 Period/quasiperiod of the next point on solution family

t_n Discrete time instance with index n

$T_{prediction}$ Period of an initial, linear prediction of a low amplitude, regular solution point on an NNM branch

T_{rot} Rotational kinetic energy

T_{tot} Total kinetic energy

T_{tra} Translational kinetic energy

u Rotating frame horizontal axis position

v Rotating frame vertical axis position

V_{rel} Relative speed at the contact point of rotor and stator

V_{tot} Total potential energy

$w^n_{k^{kinem}_{\phi}}$ Natural frequency of the shaft derived from the angular stiffness acting against the stator angle in 2-dof cantilever model of experimental study

x Context dependent stationary frame x-axis position

x_d x-axis position of disk

x_g x-axis position of the centre of gravity of disk

x_m Omron sensors average position measurement value

x_s Stator's x-axis position

x_u Unbalance mass position in x-axis in experimental study

x_{MTI} MTI sensors displacement reading during the force-displacement measurements

x_{OG} OG Omron sensors displacement reading during the force-displacement measurements

x_{OW} OW Omron sensors displacement reading during the force-displacement measurements

x_{sh} MTI sensor shift from centre

y Context dependent stationary frame y-axis position

y_A OW Omron sensor shift from centre

y_B OG Omron sensor shift from centre

y_d y-axis position of disk

y_d Disk lateral position in y-axis in experimental study

y_g y-axis position of the centre of gravity of disk

y_m MTI sensor position measurement value

y_s Stator lateral position in y-axis

y_u Unbalance mass position in y-axis in experimental study

z z-axis of the rotor, aligned with the axis of the shaft in its initial position which it rotates about

x_{t_n} x-axis position of disk at time instance t_n

y_{t_n} y-axis position of disk at time instance t_n

${}_I k_{\phi}^{kinem}$ The angular stiffness against the stator angle extracted from 2-dof cantilever model of experimental study

${}_I k_{rb}^{kinem}$ Linear stiffness against stator lateral motion in 2-dof cantilever model of experimental study

${}_n\mathbf{z}_0 = 0$ n^{th} element of the stationary frame initial condition $\mathbf{z}_0$

${}_{n+1}\mathbf{z}_0 = 0$ $(n+1)^{\text{th}}$ element of the stationary frame initial condition $\mathbf{z}_0$

List of Abbreviations

3D	Three dimensional
AFT	Alternating frequency-time (method)
BD	Bifurcation diagram
BW	Backward, backward whirling
CBC	Control based continuation
CPU	Central processing unit
Ch.	Chapter
DAQ	Data acquisition
DC	Direct current
DFT	Discrete Fourier transform
DL	Double-loop solution
dof	Degree of freedom
EO	Engine order
EOM	Equation(s) of motion
Eq.	Equation
FE	Finite element
FEM	Finite element method
FW	Forward, forward whirling
HBM	Harmonic balance method
IR	Internal resonance

MAC Model assurance criteria

MHBM Multi-frequency HBM

MOI Moment of inertia

MSM Multiple scales method

NNM Nonlinear normal mode

ODE Ordinary differential equation(s)

OOB Out-of-balance

PD Period doubling

SL Single-loop solution

SPO Stable periodic orbit

SS, S Synchronous solution branch

UPO Unstable periodic orbit

List of Figures

1.1 Left: A drill [1]. Right: a turbo engine [2] as examples of rotating machinery. 1

1.2 Anticlockwise (forward, FW, $\omega_f^{sta} > 0$) and clockwise (backward, BW, $\omega_b^{sta} < 0$) precessing modes of a rotor which are dependent on the drive speed Ω in gyroscopic systems. Superscript *sta* or *rot* indicates the stationary or rotating frame: $\omega^{rot} = \omega^{sta} - \Omega$. Black dot on the blue disk represents an unbalance mass which excites the system through centrifugal forces at frequency Ω. 3

1.3 The full rubbing case: *FW sliding*, if the trajectory is FW whirling. *BW sliding* if the trajectory is BW. *BW rolling* if V_{rel} (relative velocity at contact) is zero. *Dry whip* if V_{rel} is oscillating around 0 in a self-excited way. 5

1.4 The schematic representation of the rotor-stator system with nonlinear elements of cubic stiffness (brown spring) and snubber ring stiffness (blue spring), as well as linear stiffness and damping elements (black spring and damper), all isotropic around the z-axis. The stationary frame (x,y) and the rotating frame (u,v) are illustrated where the rotating frame angle is $\phi = \Omega t$ with Ω the rotor speed and t time. 30

2.1 Left: The unsigned natural frequency map in the stationary frame. Right: The signed natural frequency map in the rotating frame. 1^{st} engine order (EO) is also shown in both plots. Whirl frequencies are signed positive and negative for FW and BW whirl, respectively in the right hand plot. Note the negative frequencies indicating the BW appearance for the FW mode in the rotating frame after the 1st critical speed. 39

3.1 A schematic representation of the overhung rotor with cubic stiffness nonlinearity. 46

3.2 (a) Restoring force and (b) potential energy comparison between piecewise contact stiffness model that is used in [3] and cubic stiffness model used here. 50

3.3 The natural frequency map in stationary frame (left), and rotating frame (right). 1^{st} engine order (EO) is also shown in stationary frame frequency map. Whirl frequencies are signed positive and negative for FW and BW whirl, respectively. The 3:1 and 2:1 IR points are marked in the rotating frame. 53

3.4 One sample from each of the periodic solution families, referred to as SL (left) and DL (right) solutions corresponding to 2:1 and 3:1 IR conditions in the rotating frame. 55

3.5 (a) The bifurcation diagram generated from AUTO using the autonomous rotating frame equations of motion. Both stationary (synchronous) and periodic (asynchronous) solutions are included. The zoom views: (b) DL solutions. (c) SL solutions. (d) Synchronous resonance region. (e) The cyan coloured SL solution with ζ = 0.082. In the figure, 'SS', 'DL', and 'SL' stand for synchronous, DL and SL solution families, respectively. The legends show ζ values for the branches with corresponding colours. 57

3.6 Continuation in ζ of SL periodic solutions with Ω = 7.01 (left) and DL periodic solutions with Ω = 3.00 (right). Dashed lines indicate unstable response. Orange dots show the start of the continuation run which was continued forward and backward to complete the branch. 59

3.7 Zoom view at the bifurcation diagram where stationary and SL periodic solutions meet in the lower-ζ extreme. Teal and purple dashed lines show $\zeta = 10^{-4}$ and 10^{-5}, respectively, and "SS" stands for synchronous solutions. The stacked lines below the 0.413 amplitude level show the synchronous branches where higher amplitudes correspond to lower ζ. 60

3.8 Fold continuation in order to decrease the severity of eccentricity parameter on DL periodic solution family with $\zeta = 10^{-5}$. 60

3.9 (a) Bifurcation diagram for the angular equations of motion with initial condition $[0.0, 0.6, -1.246, 0.0]^T$. (b) and (d) show the DL response from the perspective of stationary and rotating frame of references, respectively. (c) and (e) show SL response in stationary and rotating frame, respectively. The orange dots show the stroboscopic Poincaré sampling at the drive speed after the convergence. 62

3.10 Left: Bifurcation diagrams from constant initial condition simulation results. Right: Stepped sweep tests performed by incrementing Ω on the synchronous and asynchronous responses. Blue and red circles show highest and lowest amplitude points of the trajectories, respectively, which overlap for the synchronous solutions. 63

3.11 Validation of SL orbits with ζ = 0.01 from AUTO and MATLAB. The bottom row shows the trajectory history (from left to right) during the transition from UPO to SPO at Ω = 3.47. The green squares are stroboscopic Poincaré sampling of the data at the rotor speed. Floquet multipliers are shown to indicate the stability. 65

3.12 Validation of SL orbits with ζ = 0.01 from AUTO and MATLAB. The bottom row shows the trajectory history (from left to right) during the transition from UPO to SPO at Ω = 3.47. The green squares are stroboscopic Poincaré sampling of the data at the rotor speed. Floquet multipliers are shown to indicate the stability. 66

4.1 Schematic drawing of the mechanical system used. In the figure c_r is the damping coefficient, k_r is the linear rotor stiffness, k_s is the stator stiffness that engages after a clearance c, k_3 is the cubic stiffness. All stiffness and damping components are isotropic. The rotating frame axes has an angle of $\phi = \Omega t$ with the stationary frame axes. 70

4.2 Left: Hyperbolic tangent function for various β_s and K value pairs. This paper used $\beta_s = 10, K = 150$. Right: The restoring force at the contact amplitude generated by the tanh-contact definition. The legend applies to both figures. 73

4.3 The flow of runs. (a) A direct and unlikely single parameter flow. (b) Single parameter flow with added Ω runs for more flexibility on the parameter space. (c) Fold-continuation flow: The arrows show the continuation runs in the parameter written above them and the resulting solution families, and the homotopy process in the case of κ. The red and blue boxes show the sampled orbits of cubic and contact cases, respectively. The continuation of ζ and e are optional in the exploration of the new nonlinearity for the system. The black boxes and continuation runs in (c) are only to plot the intermediate BD and does not constitute the method for reaching κ = 1. The methods in (b) and (c) are illustrated in Figure 4.4 in a representation. 75

4.4 (a) A representative cubic to contact transition with single parameter method (single arrows, see Figure 4.3a and 4.3b) and fold method (double arrows, see Figure 4.3c). (b) A representative κ homotopy is illustrated in a pair of axes perpendicular to the bifurcation diagram for the single parameter method (see Figure 4.3b). 76

4.5 At a nondimensional rotor speed of $\Omega = 5.0$; (a) a sample 3:1 (DL) internal resonance response in the rotating frame from tanh-contact, and (b) its signed frequency content, (c) a sample 2:1 (SL) internal resonance response in the rotating frame, and (d) its signed frequency content. Negative frequencies indicate a backward whirl in the present frame of reference, which is rotating with Ω. The DC components result from the unbalance excitation that is a constant force in this rotating frame. 77

4.6 Orbits at $\Omega = 5.0$ corresponding to responses of cubic (a) SL and (b) DL, tanh-contact (c) SL and (d) DL responses. Black circles in (c) and (d) show the contact level for the tanh-contact system (see Eq. 4.2). 77

4.7 The transform of the bifurcation diagram from the cubic nonlinearity (left, red) to that of the contact nonlinearity (right, blue). The zoomed view of the orange box is shown in Figure 4.9a. 79

4.8 Closer view of the homotopy of SL periodic solutions. Small orbits are from Figure 4.6. 79

4.9 Period doubling (PD) bifurcation diagrams of tanh-contact model. (a) Zoom view at the orange rectangle in Figure 4.7b. (b) Zoom view at the brown rectangle inside (a). (c) Time simulation results of SL solutions. (d) Stepped sine sweep results of DL solutions. 80

4.10 Bifurcation diagrams that correspond to a very low damping ratio value ($\zeta = 10^{-5}$) of the cubic (left, red) and contact (right, blue) nonlinearities. The zoomed views of the green and orange boxes in are shown in Figures 4.11a and 4.11b, respectively. 81

4.11 Low damping case. Zoom view of Figure 4.10 at the green and orange boxes therein. 82

4.12 Bifurcation diagrams that correspond to low damping, high forcing case for the cubic (left, red), and the contact (right, blue) nonlinearities. The orange box is given in Figure 4.13. 83

4.13 Low damping, high forcing case. Zoom view at the orange box in Figure 4.12. 84

4.14 The fictitious parts of the bifurcation diagram. Left: Smoothing at the kink of the synchronous solution branches for a stiffness ratio of $\beta_s = 6$ and $K = 30$, a value lower than the validated value of $K = 90$. Right: The fictitious periodic solution family appeared around and below the contact amplitude when $\zeta = 10^{-5}$ and $e = 0.8$. The red solution family shows the cubic case. Other parameters are given in Table 4.1. 86

5.1 Schematic representation of the quasiperiodic trajectory and the OOB angle. The red, green and blue points show the quasiperiodic repeating sections' initial states, and the arrows represent the corresponding OOB forcing directions (OOB angles) with respective colours. Left figure shows that case when the OOB angle is freed with the phase condition in Eq. 5.26. Right figure shows the case when the oob angle is assumed zero; in this case other phase conditions might be used to locally capture a unique trajectory. 94

5.2 Bifurcation diagram of the 2:1 (SL) solution of Eq. (3.19) as position amplitude vs. rotor speed obtained with the quasiperiodic continuation method explained in this chapter (see the SL branch obtained in the rotating frame in AUTO in Figure 3.5). Blue stars show the stable solutions and red stars show the unstable solutions. Thin red star shows a nonconvergent iteration, which got re-attempted with a smaller step size with success. . . 105

5.3 Magnitude of the eigenvalues of $\boldsymbol{\alpha}(t)$, which correspond to the Floquet multipliers at $t = T$ on the rotating-frame periodic solutions. The vertical line is at $t = T$, and its top is at level 1. The solution point data is given above the configuration space on the left. Floquet multipliers are given above the multiplier evolution plots on the right. 'St' stands for stability, n_{iter} is the iteration count, ν. 107

5.4 Magnitude of the eigenvalues of $\boldsymbol{\alpha}(t)$, which correspond to the Floquet multipliers at $t = T$ on the rotating-frame periodic solutions. The vertical line is at $t = T$, and its top is at level 1. The solution point data is given above the configuration space on the left. Floquet multipliers are given above the multiplier evolution plots on the right. 'St' stands for stability, n_{iter} is the iteration count, ν. Note the slight difference in the rotor speed. 108

5.5 Magnitude of the eigenvalues of $\boldsymbol{\alpha}(t)$, which correspond to the Floquet multipliers at $t = T$ on the rotating-frame periodic solutions. The vertical line is at $t = T$, and its top is at level 1. The solution point data is given above the configuration space on the left. Floquet multipliers are given above the multiplier evolution plots on the right. 'St' stands for stability, n_{iter} is the iteration count, ν. 109

5.6 DFT results. Left: DFT amplitudes. Right: DFT phases with respect to the drive speed component's phase. Green dots mark the start of the solution branches at their stable side. Stability is not indicated but solution is stable until the the fold. 110

5.7 The rotating frame Campbell diagram with overlaid DFT branches of 2:1 IR from Eq (4.2) with cubic stiffness. The thin solid black lines indicate the linear evolution of the main frequencies of the 2:1 IR with the rotor speed. 111

5.8 The rotating frame Campbell diagram with overlaid DFT branches of 2:1 IR from the Zilli system with quintic stiffness that replaces the cubic term in Eq. (4.2). The thin solid black lines indicate the linear evolution of the main frequencies of the 2:1 IR with the rotor speed. 112

6.1 Left: Fold continuation in ξ-Ω from $\xi = 1 \rightarrow 0$. Right: The corresponding look in the bifurcation diagram. Fold continuation branches end where the numerical stability is lost when $\xi \approx 0$. Purple fold continuation branch, however, made a fold and could not approach the conservative state. 117

6.2 The degenerate conservative 2:1 solutions scattered in the bifurcation diagram. 118

6.3 Locating the conservative and nonconservative 2:1 response with respect to the FW and BW NNMs. 120

6.4 Superposition of FW (green) and BW (red) orbits form the blue orbit whose DFT is given. Distortion of the FW and BW modes cause mirrored frequency component. 121

6.5 Correlation of the stationary frame FW (solid blue) and BW (solid red) NNMs without off-centring effect from gravity. x-axis of (a) is $\omega = 2\pi/T$ with period of the mode T. 123

6.6 Correlation of the rotating frame FW (solid blue) and BW (solid red) NNMs without off-centring effect from OOB. x-axis of (a) is $\omega = 2\pi/T$ with period of the mode T. 124

6.7 In the case of gravity, correlation of the stationary frame BW (solid red) and $\mathrm{FW}^{\mathrm{folded}}$ (solid blue) branches. Dashed lines in (a) show $\omega^{sta} - \Omega$ and $2\,\omega^{sta} - \Omega$ from left to right for both FW branches. x-axis of (a) is $\omega = 2\pi/T$ with period of the mode T. Note the non-zero minimum amplitude of the branches due to the gravity sag. 126

6.8 In the case of gravity, correlation of the stationary frame BW (solid red) and $\mathrm{FW}^{\mathrm{main}}$ (solid green) branches. Dashed lines in (a) show $\omega^{sta} - \Omega$ and $2\,\omega^{sta} - \Omega$ from left to right for both FW branches. x-axis of (a) is $\omega = 2\pi/T$ with period of the mode T. Note the non-zero minimum amplitude of the branches due to the gravity sag. 127

6.9 Correlation of the rotating frame BW (solid red) and rotating frame FW (solid blue) NNM branches when there is OOB forcing. x-axis of (a) is $\omega = 2\pi/T$ with period T. Note the non-zero minimum amplitude of the branches due to the stationary OOB force in the rotating frame. 130

6.10 Nondimensional amplitude vs nondimensional rotor speed of Eq. (6.9). Amplitude peaks and minimums are indicated with the same colours for each response. Black lines are related to the discussions on the correlation in Figures 6.8 and 6.9 regarding where the solution can be expected. 132

6.11 Combination resonance and IR samples from Figure 6.10. Brown dots show the stroboscopic Poincaré section. The numbers in the titles indicate the drive speed. 132

6.12 Superharmonic response samples (double-frequency vibration, secondary critical speed) from Figure 6.10. Brown dots show the stroboscopic Poincaré section. The numbers in the titles indicate the drive speed. 133

6.13 Subharmonic samples from Figure 6.10. Brown dots show the stroboscopic Poincaré section. The numbers in the titles indicate the drive speed. 134

6.14 Synchronous response samples along the BD in Figure 6.10. Brown dots show the stroboscopic Poincaré section. The numbers in the titles indicate the drive speed. 134

6.15 Rotating frame versus stroboscopic Poincaré section for $2\,\omega_f^{sta} - \omega_b^{sta} = \Omega$. Blue and green plot the stationary and rotating frame trajectory, red circles show the stroboscopic Poincaré section. Only for high amplitudes the effect of gravity fades with respect to the OOB forcing. 136

6.16 Bifurcation diagrams from time simulation, comparing the richness of the two systems: cubic nonlinearity (left) and contact nonlinearity (right). Red and black dots show the maximum and minimum of the trajectory that are connected by gray lines. 137

7.1 3D global assembly drawing of the test rig. Main parts, coordinate frame and x- and y-faces are indicated. Protective polycarbonate sheets, one pillar of the frame and sensor attachments kits are rendered transparent for clearer view. Shims that are used to centre each level with respect to the frame are not shown. 142

7.2 Schematic of the 2-dof system 143

7.3 Schematic of the equilibrium when the stator is displaced. 147

7.4 Solution of Eq. (7.12-7.14) for N_y. (a) Force displacement curve and the cubic polynomial fit showed against the linear stiffness expected. (b) Zoom view of (a). 150

7.5 Forces appearing on the bearings along a 0-7 mm stator lateral travel according to the 2dof system. 152

7.6 Stator axial displacement with stator lateral displacement 152

7.7 3D drawing of the stator. 155

7.8 Three laser sensors are used to track the stator's motion in plane (lateral displacements and the rotation angle). The stator (black), has x_s and y_s translations (red), and a rotation by angle α_s (blue). Each laser beam hits the stator (black) at an angle and an offset as indicated. 156
7.9 Experimental design Campbell plot from the eigensolution of Eq. (7.43). Left: Classical Campbell diagram. Right: Rotating frame, signed Campbell diagram [4]. Solid, dashed, and dash-dotted lines are one, two, and three times the natural frequencies of the same colour. 160
7.10 BD of the initial simulations of Eq. (7.43) with the design values, shown in stator positions. Stroboscopic Poincaré sections of at least 300 points are plotted as dots. Maximum amplitudes of the orbits are indicated with circles. 161
7.11 Simulation with experimental design values. Selected orbits that are expected in the experiment: synchronous (top), 2^1:1^1 (middle), and 2^1:1^2 (bottom). 162
7.12 Force-displacement curve at the stator with the design values, without preload (blue) and with 40 μm preload (green). 163
7.13 Photograph of the experimental test rig and data acquisition system. . . . 165
7.14 Shaft bend measurement – low (inner circle) and high speed (outer circle) runs' stator position samplings. Circles are compared. 166
7.15 Receptance FRF estimators H_1 and H_2, the coherence and the circle-fit modal analysis for the rotor's 1^{st} vibrational mode when not rotating. . . . 167
7.16 Receptance FRF estimators H_1 and H_2, the coherence and the circle-fit modal analysis for the rotor's 2^{nd} vibrational mode when not rotating. . . . 168
7.17 Daily tapping receptance FRF estimators H_1 and H_2 and the coherence for the rotor: 16:31 30.09.2024 (Run-4) 169
7.18 Daily tapping receptance FRF estimators H_1 and H_2 and the coherence for the rotor: 15:36 01.10.2024 (the day of formal runs that results in the BD (Run-5) presented in the next section.) 170
7.19 The force-displacement curve measurement kit installed on the rig. 171
7.20 Schematic drawing explaining the tightening of the stiffness rods. '135' refers to the catalogue names of these self-aligning ball bearings. 172
7.21 Force-displacement data from different measurements. Legend applies to both figures. 172
7.22 Experimental Campbell plot. Circles from the experimental tapping and lines from the design Campbell plot in Figure 7.9. 173
7.23 Impact hammer test on the rig. Five sets of five sec impact response acceleration data were averaged in auto- and cross-spectrums to get the receptance H_1 and H_2 FRF estimators and the coherence. 174

7.24 Experimental BD showing the amplitudes of stator lateral motion with drive speed. Maximum and minimum amplitudes of each family is given the same colour. 175
7.25 Zoom at the main resonance of the BD. 176
7.26 IR of type $2\,\omega_{f1}^{rot} = \omega_{b1}^{rot}$ at Ω = 113.3 rad/s from the experimental BD in Figure 7.24. 176
7.27 A sample 2^1:1^1 orbit at Ω = 97.0 rad/s that shows the preferred orientation. 177
7.28 A sample 2^1:1^1 orbit at Ω = 65.5 rad/s that shows that the trajectory is not precessing, but rather *parked*, and the orbit is periodic in both stationary and rotating frames of reference. 178
7.29 IR of type $3\,\omega_{f1}^{rot} = \omega_{b1}^{rot}$ (3^1:1^1) at Ω = 41.0 rad/s which appears periodic in both the rotating and the stationary frame. 178
7.30 Two samples of quasiperiodic -1:1 BW resonance which also appears periodic in the rotating frame at Ω = 24.7 rad/s and at Ω = 49.6 rad/s from top to bottom (see the BD at 7.24). 180
7.31 Selected orbits at Ω = 15.8, 29.0, 32.1 and 203.5 rad/s from top to bottom, from the BD given in Figure 7.24 and 7.25. 181
7.32 Comparison between the region of the BD around the main resonance with different unbalance masses. The red coloured data belong to the run with an unbalance mass of 19.46 g (Note that this is different than Figure 7.25). The green coloured data belong to the run with an unbalance mass of 28.87 g. 182
7.33 The new disk system that interprets the rotating parts as a single rigid system: the disk, stator sleeve, bearing moving parts and the connecting elements (collet and lock-bush), as well as "the shaft length around the disk" (80 mm before and 177 mm after the disk, total 277 mm shaft length). 183
7.34 Classical (left), rotating-frame (right) signed Campbell diagram with the updated experimental values. 186
7.35 Experimental and simulations BDs. 189
7.36 The stagnant (period-3) orbit on the quasiperiodic 2^1:1^1 branch. In the middle column: The pink orbit shows one quasiperiod (i.e. one repeating, precessing pattern). Blue pentagrams show the stroboscopic Poincaré section. Gray line is the trajectory of the stator that covers the time of 200 pink orbits. 192
7.37 The stagnant (period-2) orbit on the quasiperiodic 3^1:1^1 branch. In the middle column: The pink orbit shows the first quasiperiod (i.e. one repeating, precessing pattern). Blue pentagrams show the stroboscopic Poincaré section. Gray line is the trajectory of the stator that covers the time of 200 pink orbits. 193

7.38 The parked orbit on 2^1:1^1 of the experiments (see Figure 7.24). The first and second 1500 data points are marked pink and blue, respectively. 194

C.1 Simulation with experimental design values. Selected orbits with 2^{nd} BW mode not decayed even after 1000 second of simulation: synchronous (top), $2^1 : 1^1$ (middle), and $2^1 : 1^2$ (bottom). Selected orbits . The eigenvalue data for Ω = 259 rad/s is given in Eq. (C.1). 210

C.2 Sensor delay study schematic drawing. Laser beams (red lines) are projected onto the vibrating cantilever beam. 216

C.3 60 kHz sampling request from Labview gives away the stepped nature of the Omron signal. 218

C.4 The results of the sensor delay study: each measurement separately given. 219

C.5 The results of the sensor delay study: overall results. 220

C.6 Campbell diagram with the modified values: E_1 = 270 GPa, $k_{3b} := 0.7\, k_{3b}$ = 109942700 N/m^2, and with the addition of the 7900 bearing's movement compensation as the extra shaft length D = 65 mm. The internal resonance speed are: 48.8 rad/s for $2^1 : 1^1$, 32.5 rad/s for $3^1 : 1^1$, 81.3 rad/s for $3^1 : 2^1$, 188.3 rad/s for $2^1 : 1^2$. (See the accompanying bifurcation diagram in 7.35b) 221

C.7 Global assembly of the test rig. 222

List of Tables

1.1 Different responses in the literature of rotor-stator interaction studies and their classification by their respective authors. 4

3.1 Flow of continuation runs in Python CLUI file of AUTO setup. 55

4.1 The reference values of the constants that appear in Eq. 4.2 unless otherwise indicated in the text. 74

5.1 Methods for the evolution matrix eigenvalue calculation used to explain the monodromy matrix $\mathbf{m}$ better. 106

7.1 Nondimensionalisation by use of c of the stationary frame 2-dof system with c = 0.7 mm arbitrarily selected. Values with "preceding study" reference are obtained from Ch. 3.Dimensionalisation is done according to Eq. (7.11). The "designed" values come from Eqs. (7.15) and (7.16). 151

7.2 Bearings used in the experimental test rig. 153

7.3 Offset values of the laser sensor setup. 157

7.4 "Equivalent disk mass" if considered with *the stator sleeve for collet* and *the accompanying collet-nut*): $m_d = 1593.89 \cdot 10^{-3}$ kg. The entries within parentheses are not summed. 184

7.5 "Equivalent stator mass": $m_s = 750.43 \cdot 10^{-3}$ kg. The entries within parentheses are not summed. 184

7.6 "Equivalent disk diametral MOI at "the new mass centre": $J_d = 1639365.98 \cdot 10^{-9}$ kg m^2. "The new mass centre" is of the system: *the disk* + "*the stator sleeve for collet* and *the accompanying collet-nut*" + "*2301 bearing's* inner race and balls" + "the shaft length around *the disk*" and it is 3.91 mm down the disk mass centre. The entries within parentheses are not summed. 185

7.7 "Equivalent disk polar moment of inertia": $J_p = 2236895.28 \cdot 10^{-9}$ kg m^2. The entries within parentheses are not summed. 185

7.8 Expected resonances from the Campbell diagram in Figure 7.34. 186

A.1 AUTO initial conditions for rotating frame EOM 204

C.1 The eigenvalues, damping ratios and natural angular frequencies of Eq. (7.44) when Ω = 259. 211
C.2 Selection of the stator's self aligning ball bearing from NSK catalogue. . . . 212
C.3 Self-aligning ball bearing selection for the stiffness rods from NSK catalogue. 214
C.4 Angular-contact ball bearing selection for the bearings holding the shaft from NSK catalogue. 215
C.5 Selection of spherical plain bearing GE10-UK for rods. 217

Chapter 1

Introduction

Linear vibratory systems have been extensively investigated, and their behaviour has been documented in many textbooks (e.g., [5]). Although the analysis of linear response is useful in many cases, it is an exception to the general behaviour, which is nonlinear. Nonlinear aspects need to be considered in rotating machinery, as designs are becoming increasingly sensitive. Turbomachinery applications (Figure 1.1), for example, require small rotor-stator gaps in order to improve efficiency [6]. Retainer or snubber rings are used to suppress high amplitudes of lateral motion during passage through the main resonance, thereby preventing damage to the blades. However, the same snubber rings, being involved in contact failures, can excite high-amplitude nonlinear resonances that may pose a threat to structural integrity. Nonlinear rotor-stator interactions are also seen in drilling equipment (Figure 1.1), inducing mechanical wear and damage. Hence, researchers and engineers in the field are driven towards considering nonlinear interactions of rotor-stator systems, which are highly nonlinear phenomena.

Although contact is important, nonlinear rotor-stator interaction can result from other means such as geometric nonlinearities, high amplitudes, nonlinear stiffness and damp-

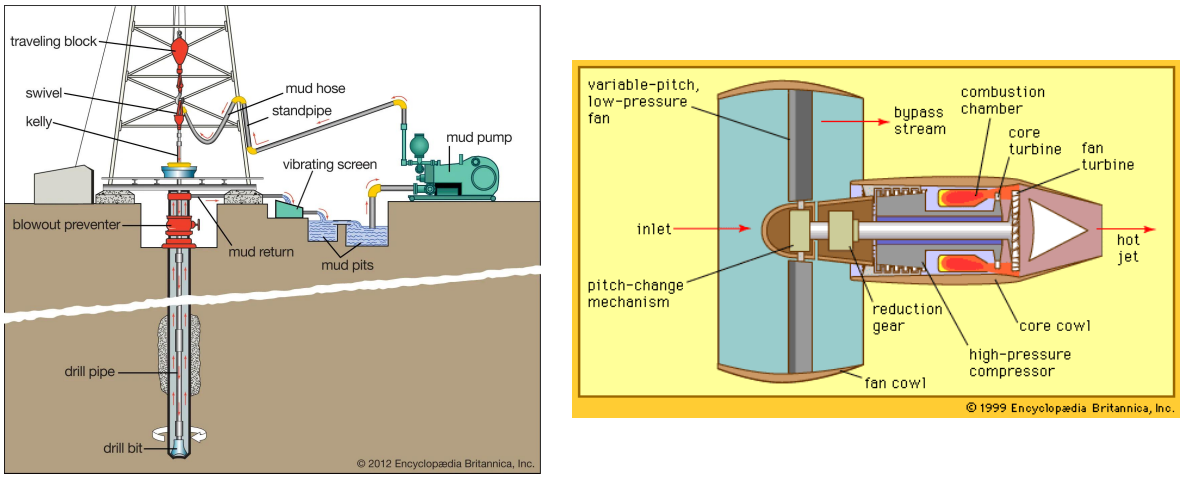


Figure 1.1: Left: A drill [1]. Right: a turbo engine [2] as examples of rotating machinery.

ing, and so on. Excitation of such nonlinear resonances might result from blade loss, manoeuvre loads, unavoidable eccentricity of the rotor, or other forms of external excitation. Thus, because this is a complex failure type due to the variety of paths leading to it and the responses caused by it, this thesis will focus on nonlinear rotor-stator interactions, with special attention to the underlying nonlinear phenomena – namely, internal resonances, which are dangerous because they generate high-amplitude motion. This introductory section will present the background, response classification, literature survey, and the aim of the thesis in Sections 1.1 through 1.6.

1.1 Background

While the linear behaviour of rotors is presented in detail in textbooks (e.g., [7, 8, 9]), the need for research on understanding the responses of interacting nonlinear rotor-stator systems is increasing due to the stricter efficiency goals, which call for smaller gaps between rotor and stator in turbomachinery [10]. The contact failure can stem from instability of the rotor such as due to asymmetric shafts, external excitation such as aircraft manoeuvres or earthquake loads, or inevitable *unbalance*, which is an offset mass that rotates with the rotor (Figure 1.2), for example, in a blade-loss scenario. When contact occurs, various responses can take place (see Section 1.2).

The motion of the rotor axis around its equilibrium in the two lateral directions is called whirling motion (also called precession or orbiting) [8, 11], as opposed to the rotation of the rotor around its axis, which is called spin. When the whirl direction matches the shaft direction, it is called *forward whirl*. However, because this thesis only considers rotors that spin anticlockwise, it is more straightforward to call anticlockwise and clockwise whirl directions *forward* (FW) and *backward* (BW) (Figure 1.2), respectively. FW and BW whirls are characteristics of linear rotating systems, whereas further forms are seen in nonlinear systems. The FW direction can be found by a right-hand rule: while pointing in the positive rotor axis direction with the right hand's thumb, FW whirl is in the direction of the fingers wrapping around the shaft axis. *Gyroscopic coupling*, which couples the motion in the two transverse directions, happens when the rotor changes its angles while spinning, thereby making the linear modes complex due to the phase difference between the two lateral motions in a whirling motion. As a result, the natural frequencies are dependent on the rotor spin speed, which also affects the rotor speed range of nonlinear resonances.

The frequency of the unbalance excitation is locked to the rotor speed Ω and plays a key role in sustaining nonlinear responses. Therefore, the coordinate frame rotating with the rotor speed Ω about the axial direction of the stationary frame, referred to as the *rotating frame*, is essential for response classification and is used extensively in this thesis. Rotor supports are *isotropic* when the support stiffness and damping are the same

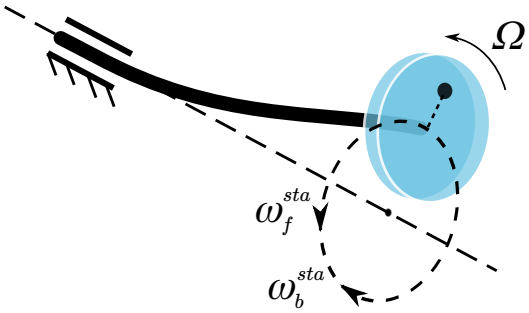


Figure 1.2: Anticlockwise (forward, FW, $\omega_f^{sta} > 0$) and clockwise (backward, BW, $\omega_b^{sta} < 0$) precessing modes of a rotor which are dependent on the drive speed Ω in gyroscopic systems. Superscript *sta* or *rot* indicates the stationary or rotating frame: $\omega^{rot} = \omega^{sta} - \Omega$. Black dot on the blue disk represents an unbalance mass which excites the system through centrifugal forces at frequency Ω.

in both transverse directions.

Nonlinear systems require special treatment in their analysis since they can change their behaviour drastically depending on the parameters of the system (such as damping ratio, unbalance, and rotor speed). Higher amplitudes can shift the resonant frequencies either to higher (stiffening) or lower values (softening). Nonlinearity can generate modes that are not bifurcations from the linear modes; instead, they only appear in the nonlinear system. Therefore, the low-amplitude oscillations of the mode cannot be linked to a certain linear mode, although they can be represented by the expansion in linear modes, which span the complete basis for the dynamic system. Thus, even in the same parameter space, multiple steady-state solutions can be obtained. The jump phenomenon can be observed where the solution can move from one solution family to the other. Thus, being able to systematically locate these so-called bifurcations is vital in nonlinear mechanical systems, requiring the use of nonlinear solution-finding techniques. While linear methods are inadequate for nonlinear systems, linear concepts often form part of the framework used to predict nonlinear responses. In fact, it is often possible to go further and view the linear response as a special case of the nonlinear response in the low-amplitude limit. However, this does not apply to all of the nonlinear responses discussed in this thesis. Nonlinear rotordynamic systems exhibit rich phenomena including period doubling, aperiodicity, and even chaos in the system's response [12, 13, 14]. In the next section, this diversity is portrayed.

1.2 Classification of different nonlinear responses

Contact - general A plethora of different modes of vibration of rotor-stator systems have been documented in the literature. The response of an isotropic rotor system is typically in the form of a constant radius circular motion known as whirling – in linear and weakly nonlinear cases this is generally synchronous, meaning it occurs at the speed of

Table 1.1: Different responses in the literature of rotor-stator interaction studies and their classification by their respective authors.

Ref.	Analy. type	Physical system properties (all isotropic if not indicated otherwise)	Fr.	Response property	Response class
[15]	S (New-mark)	-2-disk rotor with simply supported ends -Gyro, shear, rotary, torsional, friction effects considered -AISO: different lateral stiffnesses, gravity	sta.	-Partial-contact synchronous orbits	Sync
[16]	T (HBM)	-Jeffcott rotor and stator each with two dofs. -Friction between rotor and stator considered.	sta.	-Backward rolling with sliding ratio	FAR
[17]	X	-Jeffcott rotor, comparable rotor and stator masses	sta.	1) Backward roll, 2) Backward slipping	FAR
[18]	T	-An overhung rotor with longer shaft than disk position. Stator contact happens at the tip. -Friction between rotor and stator and gyroscopics considered	sta.	-BW rolling	FAR (BW-roll)
[19]	S (RK)	-Jeffcott rotor with added clearance on both bearings whose lateral motion assumed equal -Manually added gyroscopic term AISO: eccentric bearing mounting	sta.	1) 2F-B=Ω , CR, SE 2) 2/5 Ω, Super -subharmonic 3) F,Ω	1) QP-sta 2) P-sta 3) SE
[20]	T (HBM)	-Continuous vertical shaft with constraint length (bend-stretch coupling). OOB along shaft. -Gyroscopic, shear, rotary, axial effects considered	sta.	Fl + Fm - Bn = Ω (l =n or m = n), CR	QP-sta
[21]	X	-3-disk rotor driven by flexible coupling, and a flywheel OOB on disk 3	sta.	1) Somewhat continuous frequency spectrum, quasiperiodic 2) Ω and 2Ω, period-1	1) QP-sta 2) Sync
[22]	S	-Jeffcott rotor -AISO: Stator stiffness asymmetry	sta.	Period-1,2,3 Chaos	P-sta Ch
[23]	S (Finite Central diff.)	-2-disk rotor with a contacting disk in the middle. One of the disks carry an ice-block that melts down to create OOB. -Friction, aerodynamic friction, change of rotating speed as a result of contact considered	sta.	-Somewhat continuous spectrum, Main resonance ω = Ω, 2ω, heavy rub	Sync
[4]	S	-2-disk rotor. Gyro, OOB on one disk, stator between the disks. -Timoshenko beam considered	rot.	-3:2, IR	P-rot, QP-sta
[24]	S	-A Jeffcott rotor with with stator, both having two dofs. -Friction between rotor and stator considered.	sta.	-No contact -Intermittent contact -Permanent contact	Period-n Ch
[25]	S	-Overhung rotor with two disks, each unbalanced. -Gravity, gyroscopics	rot.	2_b^1:1_b^1 and 2_f^2:1_b^2 3_f^2:1_b^2 -Chaos	P-rot QP-sta Ch
[26]	X	-A cantilever beam with a motor with eccentric mass mounted to the free end, at which there is a clearance. -AISO: Gravity, loose pedestal	sta.	-1/3 SbH, 2 FW contact per 3 rotations	P-sta, SbH
	S	-A horizontal rotor with a contacting disk. One end pinned and the other supported by anisotropic stiffness -Friction, tangential viscous damping, nonelastic impacts considered -AISO: gravity (constant force term), eccentric bearing mountings	sta.	-Scattered Poincaré dots, chaos	Ch

S: Simulation
T: Theoretical
X: Experimental
Fr.: frame of reference
sta: stationary frame
rot: rotating frame
FW: Forward
BW: Backward
P-sta: Periodic response in sta
P-rot: Periodic response in rot
QP-sta: Quasiperiodic response in sta
Ch: Chaotic response
Sync: Synchronous response
FAR: Full annular rub
CR: combination resonance
IR: Internal resonance
SE: self-excited
SbH: Subharmonic
AISO: anisotropy in the model/rig.
OOB: Mention of out-of-balance excitation on the rotor
F: a forward whirl mode frequency
B: a backward whirl frequency
Ω: rotor speed

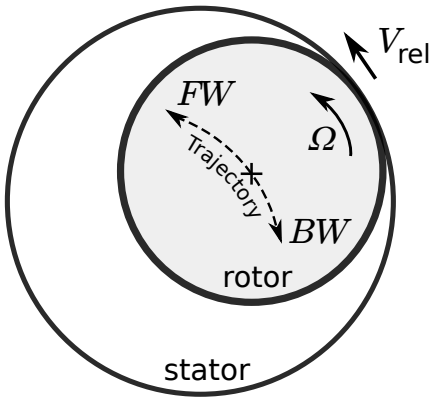


Figure 1.3: The full rubbing case: *FW sliding*, if the trajectory is FW whirling. *BW sliding* if the trajectory is BW. *BW rolling* if V_{rel} (relative velocity at contact) is zero. *Dry whip* if V_{rel} is oscillating around 0 in a self-excited way.

the shaft rotation, excited by unbalanced mass (Figure 1.2). The steady state responses of a rotor interacting with the stator can be full annular rubs [17, 27, 28, 29]. In the response of a rotor, a jump from eccentricity-driven synchronous, low amplitude, no-contact vibrations to the full annular rubbing can happen [29]. The presence of friction can lead to a dangerous case known as dry backward whirl [7]. The control of friction is critical to the control of the full rubbing-type motions. It was found that the increased friction between rubbing surfaces worsen the rubbing phenomenon, turning it to dry whips [17] which are dangerous due to rapid high amplitude response that does not disengage until the rotor slows down to very low speed. Quasiperiodicity and even chaos are observed, as well as these other types of responses in theoretical studies [30, 31, 13, 4] and also in experimental studies [32, 15, 19, 21, 20].

Contact - intermittent Especially intriguing are responses where the amplitude of shaft displacement from its rotation centre continually oscillates, also known as bouncing motions or intermittent contact cycles [4], which generate rich response patterns with or without friction. The modelling of intermittent contact response can be challenging due to the discontinuous stiffness nature of the intermittent contact problem compared to full rubbing. The intermittent contact oscillations can be periodic in the stationary frame or in the rotating frame, while being synchronous or sub-synchronous in frequency content. Synchronous partial contact responses have been observed in [33] with magnetic bearings. However, the more challenging case is that of asynchronous responses, where the response frequencies are not commensurate with the shaft speed which govern the excitation frequency [34, 3], but might still be entrained to fulfil a combination resonance relation, unlike a dry whip motion whose frequencies stay constant once initiated [35]. Besides, as Ch. 6 outlines, the bouncing, asynchronous responses are not bifurcating off a simple response. The change in physical conditions can cause the full rubbing and bouncing motions to replace each other: In a detailed basin of attraction study by Paiva

et al. [24] intermittent contacting response was found to occupy the region of full rubbing when the friction coefficient is increased.

It has been shown that the intermittent contact can be asynchronous yet it can be estimated by an *internal resonance* (IR) condition [4]: IR responses in this thesis are those which involve different modes of vibration whose frequencies are commensurate in a frame of reference, the stationary or the rotating frame, and expressed by the frequency relation such as 2:1. More information on the IR responses are given in the literature survey in the following section. It is crucial to note that different underlying modes may take part in IRs at different drive speeds. Also, the rotor speed affects the detuning of the underlying modes for a single IR (Ch. 5). Intermittent contact was a research focus recently through an industrial perspective [3], which requires more research to be fully understood.

Classification

In general, the following classification of responses of rub-impact rotor-stator systems has been identified:

1. **Full rubbing motion** (Figure 1.3):

    a. **Forward sliding**: The rotor can be under full rubbing with the stator in the FW direction as excited by the unbalance mass; hence, this motion is *synchronous* with the drive speed. This happens when the frictional forces are not strong enough to transition the whirl to the BW direction [10].
    b. **Backward sliding (dry whirl)**: As the frictional forces increase, the outer surface of the rotor is pushed into BW due to a FW rotating rotor [6].
    c. **Backward rolling**: If the frictional forces are strong enough, the rotor starts to roll without sliding inside the stator in the BW whirl direction. Depending on the clearance between the rotor and the stator, this whirl motion can be multiple times faster than the rotation of the rotor, and can cause high amplitude response [29].
    d. **Backward whip**: When the frictional forces oscillate back and forth according to the relative sliding velocity, it can make the rotor couple in a vibration mode with the stator, and the resulting motion's frequency is not a function of the rotor speed after it is generated [35] (Figure 1.3).

2. **Bouncing motion or intermittent contact**: The response is often oscillatory in amplitude, and the contact can engage and disengage in the sustained motion.

    a. **Synchronous bouncing:** This is similar to forward sliding but the rotor impacts the stator instead of continuously rubbing.
    b. **Asynchronous bouncing**: A large number of different solutions can arise in other cases: quasiperiodic and chaotic motions can be sustained (e.g. Table 1.1). The

classification of these responses is not unified in the literature. More on these responses can be found later in this chapter.

However, this classification mostly concerns the contact nonlinearity, while it ignores nonlinear interaction between the rotor and stator by other means such as oil bearings, bend-stretch coupling or heat effects [7], etc. For example, a synchronous, constant amplitude whirl in the case of geometric nonlinearity will be in neither of the above categories.

Table 1.1 shows different responses and their classification by their authors. Even though capturing each of the papers in full detail is impossible in a small table, it is evident that the responses could be classified by including the following information,

1. Label of the response according to a general, recognised classification (e.g. BW dry whip),
2. Variation of the oscillation amplitude (e.g. bouncing or constant amplitude, pure circle),
3. Nonlinearity source (e.g. contact or geometric nonlinearity),
4. Frame of reference (e.g. stationary or rotating frame),
5. Periodicity (e.g. periodic, aperiodic, chaotic),
6. Signed spectral content appearance (e.g. 2:1, 3:2, $\omega_f^{sta} - \omega_b^{sta} = \Omega$),
7. Frequency relations to the driving frequency or natural frequencies (e.g. synchronous, subharmonic, superharmonic, 2X, 1/2X, 5/3X engine order, ω_f^{sta} unrelated to Ω),
8. Poincaré section appearance (e.g. two dots to indicate period-2, closed circle to indicate quasiperiodic, scattered to indicate chaos),
9. Number of contacts per number of periods (e.g. 2 contacts per periodic bouncing cycle),
10. Intensity of rub-impact (e.g. severe vs low impacting bouncing cycles).

The extreme diversity arising from every new study with different systems analysed might make it difficult to construct a directive for response identification and classification; however, finding some agreed guidelines could attract more researchers to nonlinear rotordynamics studies. For instance, in Table 1.1, the $2\omega_f^{sta} - \omega_b^{sta} = \Omega$ motion of Ref. [19] was considered as a combination resonance. Alternatively, it could also be seen as an IR mode in the rotating frame with the frequency relation $2\omega_f^{rot} = \omega_b^{rot}$, indeed becoming the 2:1 IR investigated in the present thesis. The list above indicating the classification criteria could be a checklist for each of the observed responses in a study; omission of some of them in the studies makes the identification and classification less organised to both the researchers in the field and wider scientific audience. This highlights the need for improved frameworks for nonlinear rotordynamics that can handle much of the above variety.

The present knowledge in the nonlinear rotor-stator interactions are summarised below. The chapter has four more sections to cover, which starts with the theoretical studies. This is followed by the nonlinear normal modes (NNM) literature review in the rotor-dynamics context. After that, the experimental state-of-the-art is presented before concluding with the aim and structure of the thesis.

1.3 Literature survey for the theoretical study

1.3.1 Nonlinearity and rotor-stator interactions in rotordynamics

Nonlinearity - contact Nonlinearity in rotordynamics can originate from sources such as faults such as cracks, nonlinear bearing forces, geometric nonlinearity when shafts are flexible, and rotor–stator interactions [7, 11, 9]. The rub-impact phenomenon in rotordynamics has similarities to an impact oscillator yet with more complexity arising from the gyroscopic effects and the interaction of different FW and BW modes. The phenomenon has been studied in fields such as turbomachinery and drilling equipment [36]. Long drilling shafts with low stiffness have been documented to demonstrate nonlinearity due to rotor-stator contact [37, 36, 38]. Understanding the sustained intermittent rotor-to-stator contact response in rotating machinery is important as it might be dangerous in operating conditions [6].

Efficiency goals With the ever-stricter efficiency goals on turbine engines [10], the amplitude of the lateral oscillation has to be confined more effectively. This compels engineers to design tighter clearances for the retainer rings, which in turn increases the possibility of a rotor-stator rub failure. The rotor–stator contacting phenomenon in turbomachinery can result from a loss of blade, supports being misaligned, fatigue cracks in shafts [6, 10], and depending on the bearing type can lead to destructive oil whips [39].

Earliest contact literature Since 1960's, the rotor-stator contact phenomenon has been documented and researched [40, 41, 42, 43]. Despite this, new insights are gained every year and new aspects are considered. Among the earliest studies where the rub-impact phenomenon in rotating machinery was observed, Johnson [40] reported that for the same rotor speed, various responses could be achievable. Ehrich and O'Connor [42] noted the "hula hoop" motion of the rotor-stator couple. Black [43] used a polar receptance law with dry friction. Ehrich [44] described the following phenomena occurring in the nonlinear response of rotating systems: asynchronous response, changing amplitude for constant rotor speed, discontinuous amplitude response as rotor speed changes.

1.3.2 Different rotor-stator interaction definitions

Contact definitions - rigid impact Many approaches have been used to analyse rotor-stator contact phenomenon. Some research considered fully rigid models for the stator contact. Cole and Keogh [34] analysed the asynchronous intermittent contact phenomenon. The fundamental frequency of the Harmonic Balance Method (HBM) they used was set to the contacting frequency which was found from the contact energy conservation. They concluded that in the high frequency range the number of possible contact modes decreased with increasing damping. The study gave upper and lower limits of unbalance to achieve the periodic contacting motions. Mora et al. [45] employed a rigid impact model for the contacting interactions, and explained the transition into bouncing motions by analysing grazing bifurcation.

Contact definitions - compliant stiffness Further studies use smooth or piecewise-linear functions to represent the nonlinearity due to contact. Karpenko et al. [46] analytically solved the two-degree-of-freedom (2-dof) Jeffcott system and found that depending on the accuracy of the Taylor expansion during contact, time simulations were approximated very closely. Gyroscopic effects, friction, and snubber mass were not considered. A preloaded snubber ring in [47] shifted the bifurcation plots, added new bifurcations, and decreased the response amplitudes of the retainer ring. The position of the massless snubber ring was found from the energy spent on the ring during contact, with the help of a Lagrange multiplier. The experimental validation of this mathematical model was published by Karpenko et al. [48]. Saeed et al. [49] defined a 2-dof rotor-stator model with asymmetry whose lateral vibrations are controlled by electromagnetic poles and solved the equations using the multiple scales method (MSM).

Zilli system, internal resonance Zilli et al. [3] investigated a snubbed overhung rotor with 2-dof and gyroscopic effects (the *Zilli system*), and time-simulated a loss scenario by introducing an unbalance. The analytical model had a piecewise-linear stiffness to define contact. A synchronisation condition was derived using phasors of system frequencies. The frequencies where the intermittent contacts occurred in the bifurcation diagrams were closely approximated with this synchronisation condition. In a rapid deceleration test, higher transient energy were found more likely to yield sustained bouncing motion. Shaw et al. [4] expanded the IR idea to higher-degree-of-freedom systems by setting the condition to involve any two whirl modes. In the study, soft contact with no damping and stiff contact with damping were investigated on a finite element (FE) model that is further reduced using a subset of the linear eigenmodes. As observed in [3], the authors reported the stiffening effect that causes the predicted rotor speeds to be lower than the numerically observed ones.

Some recent studies focused on IR phenomena in rotor dynamics. In 2025 Yoshimory

et al. [50] studied the effect of the thickness of the stator on the vibrations of the rotor. Internal resonances of order 2:1 and 3:1 were observed. Kartheek and Vijayan [51] defined a stochastic FE model to conduct uncertainty quantification and drew IR diagrams to study the modal interactions in the rotor-stator contact problem. The uncertainty of contact friction and eccentric mass location were studied. Wang et al. [25] investigated the alterations in IR resonance response as a result of contact stiffness changes. They observed richer IR responses such as 7:1 and 5:1 IRs in addition to others, only with high contact stiffness.

Gravity Chipato et al. introduced friction [31] and gravity [13] to the overhung rotor system in [3]; they noted that the synchronisation condition holds in both cases. With gravity, multi-periodic and even chaotic responses appeared. However, increased rotor stiffness nullified the effect of gravity. Varney and Green [14] presented a rotor speed threshold after which the gravity can be ignored. They also investigated the effects of support asymmetry, gravity and cross-coupling stiffness on a 2-dof rotor with a compliant contact stiffness. Gravity effects were included by Taher et al. [52] where the severity of contact was detectable by the strength of 2x and 3x harmonic responses in the frequency spectrum. In a rotor with oil bearing supports studied by Briend et al. [53], both the effect of gravity and misalignment were included. Saeed et al. [49] defined a new coordinate frame to eliminate the gravity term from the EOM which resulted in quadratic terms of lateral positions.

Contact - stiffness ratio (β) The reason why a vast range of contact stiffness has been researched is that the ratio of the stator stiffness to the rotor linear stiffness greatly affects the response. For example, [54] observed that higher damping and lower stiffness eliminated multi-periodic and chaotic solutions on a similar model of a Jeffcott rotor. Shaw et al. [4] investigated soft and rigid stators where the stator stiffness values of 0.1 MN/m and 10 MN/m were used. Zilli et al. [3] used 1.32 for the stiffness ratio, while Karpenko et al. [48] chose a value of 30 for the stator stiffness to rotor stiffness ratio. As mentioned above, some authors modelled the contact directly with an impact law [45, 34]. The results from the literature with a wide range of stiffness ratios suggests that intrinsically smooth nonlinearities could generate similar responses to discontinuous stiffness models of the rotor-stator interaction. Effect of contact stiffness to the response was studied in [25].

Geometric nonlinearity, analytical HBM On the geometric nonlinearity in the context of rotordynamics, Nagasaka et al. [55] formed a mathematical model of a continuous slender shaft with asymmetrical cross-section was constrained longitudinally through bearings at each end (unlike [56] which did not constraint the ends). The gyroscopic effects

were small due to the lack of a disk. Thus, the 1:-1 IR in the stationary frame was investigated for both major and secondary critical speeds. The cause of the nonlinear response such as Hopf bifurcations and quasiperiodic motions was linked to the IR. Findings were experimentally confirmed. Previous works accompanied that study such as [57, 20, 58]. In the textbook by Ishida and Yamamoto [11], further discussions of geometric nonlinearity and their solutions were given. The textbook [11], represented the weak stiffness nonlinearity as one for which the potential energy can be expressed as a power series, whose derivatives with respect to the dimensions of the system give restoring forces. The textbook tabulates the possibility of various combination and internal resonances in geometrically nonlinear rotor-dynamics gyroscopic systems. The harmonic and subharmonic responses, as well as combination resonances, were investigated in the stationary coordinate frame. It is evident that, internal resonances such as $2\omega_f^{sta} - \omega_b^{sta} = \Omega$ or $2\omega_f^{rot} = \omega_b^{rot}$ in the rotating frame, are observed both in cubic stiffness and contact stiffness [11, 3].

Cubic and contact nonlinearities were considered in a study by Fu et al. [59] where the contact happens between an inner and an outer rotor. Yang et al. [60] investigated the sustained response branches of an aeroengine model under airplane base motions: roll, pitch and hovering. Geometric nonlinearities in both stiffness and internal damping due to large displacements of a Jeffcott rotor were studied in a numerical continuation study by Alcorta et al. [61] where inspiration came from the engineering need for the use of rotary engines in supercritical region safely. Further studies included cubic stiffness [49, 62, 61]. Some better general understanding of the smooth nonlinearity would be a stepping stone to handling the nonsmooth nonlinearity of contact. The smooth nonlinearity is softer compared to contact and can provide a less crowded bifurcation diagram so that these IR are more closely investigated.

1.3.3 Complex and simpler models

Complex Rich responses of nonlinear rotors have been investigated with finite element modelling (FEM). Chipato et al. simulated an MDOF rotor with disk and shaft contact, observing asynchronous quasiperiodic responses and stronger dry friction effects for softer stators [63]. Lahriri et al. modelled a 5-dof drive system, successfully using a pinned inner ring to prevent sustained rubbing [64]. Pennacchi et al. used FEM to study partial seal contact on a full-scale rig, detecting contact through acoustic signals and a Wheatstone bridge [15]. Their model, incorporating beam elements with 5 dofs, was reliable for soft rub analysis. Torkhani et al. investigated real-scale test rig rundowns with experimental and numerical agreement, without reporting subharmonic responses [23]. Wang et al. examined sudden unbalance on an overhung rotor, finding higher transient amplitudes at supercritical speeds and backward whirl mode excitation due to gyroscopic effects [65]. Prabith and Krishna studied multi-disk rubbing in a fan blade-off scenario, employing a

reduced FE model with Timoshenko beams [66]. Their time variational method, validated by simulations, was simpler than multiharmonic-HBM and faster than numerical integration [67]. Briend et al. [53] investigated the nonlinear dynamics of a two-disk rotor with oil bearing supports and a loose fitted ball bearing where 22 Timoshenko beam elements were used. Nikiforov et al. [68] investigated an overhung rotor whose total overhung shaft length was longer than its disk's position on the shaft. Although only 4 elements were used, this is still a relatively detailed model compared to lumped parameter models.

Simple Despite these complex models, understanding of the complex phenomena resulting from the rotor-stator rub-impact requires, by contrast, simpler models to be investigated in a more closely controlled way. The study by Ishida et al. [19] is a suitable example which shows the complexity of the rotor-stator interaction phenomena arising from even a relatively simple model. The study investigated the response patterns of a 4-dof extended Jeffcott rotor (i.e. non-centred disk position along the shaft) with clearance on one bearing only. Eccentricity of the bearing assembly was added to represent effects such as mounting errors. Numerical and experimental methods produced results with a close match, although the numerical model introduced a small change to the system. Rich response patterns were observed that included 2:1 IR in the rotating frame, though this was quasiperiodic and expressed in the stationary frame as a combination resonance expression. The paper explained the *entrainment* phenomenon theoretically using the stability of the periodic motion, which is the inclusion of a subharmonic region inside a broader region of self-excited quasiperiodic motion. As hinted under the headings above, the characteristics of the IRs of interacting rotor-stator couple are best investigated in a simple system which will give a more directed research focus.

Is has been shown that even the Zilli system [3] that is a 2-dof, gyroscopic overhung rotor is able to capture a wide range of nonlinear responses involved in rotordynamics, particularly the IRs. This system was studied, for example, by Chipato et al. [13, 31] and Shaw et al. [4, 30] for both investigating the rotor response and the analysis methods. A more developed rigid overhung model can be found in [25]

1.3.4 Analysis methods

Analytical Analytical and semi-analytical methods to solve the nonlinear equation of motions include the use of normal forms, HBM and alternating frequency/time domain methods (AFT). Karpenko et al. [46] found approximate analytical solutions for Jeffcott rotors under contact with a stator, using a Taylor expansion of the nonlinear force during contact. The multiple scales method (MSM) was applied by Hosseini and Khadem [69] to analyse nonlinear free decay of a long shaft where the nonlinearity is due to the large deformations of the shaft. Qaderi et al. [70] used MSM for analysing the combination

resonance of a long balanced shaft when there is a periodic axial load. MSM was also utilised by Saeed et al. [49] in a complicated rotor case with gravity and active magnetic bearing control. Analytical HBM was applied for slender shafts in [55] and impacting disks in [19]. The textbook [11] gives an introduction to analytical HBM application for geometric nonlinearities. Hosseini and Khadem [56] used a similar analytical HBM method to investigate the combination resonance $2\omega_f^{sta} - \omega_b^{sta} = \Omega$ of the same long shaft of [69], (where the resonance can be viewed as IR of $2\omega_f^{rot} = \omega_b^{rot}$ frequency relation).

Continuation The numerical continuation method [71] has been used extensively in the rotordynamics literature in recent decades. Sundararajan and Noah [72] used continuation in conjunction with the shooting method. Al-Solihat and Behdinan [73] used HBM and continuation methods (Harmonic balance-continuation or HBC) for analysing the response from a rotor system that is supported by bearings with cubic stiffness and damping.

HBC In the study by Von Groll and Ewins [74], after the equations of motion were converted to algebraic equations by HBM, arclength continuation was performed to efficiently find solutions, with the help of AFT to update contact forces. The method was demonstrated on a Jeffcott rotor in penalty-contact interaction with a stator of non-zero mass. Subharmonics were allowed in HBM formulations which was stated to be required by the intermittent contact motion.

A study by Peletan et al. [75] assessed the limitations of HBM in the rotor-stator contact modelling and concluded that the quasiperiodic HBC is needed for dry whip and partial rub motions. In a following study, for the continuation of the quasiperiodic solution branches, a two-frequency HBM was used and arclength continuation methods were adapted [76] where they automated the selection of harmonics from the prominent frequency content of the nonlinear force. The solution was assumed to be periodic for each of the time dimensions, and unsigned frequencies were considered. A previous study [77] showed that for the stability analysis, the time domain methods were more accurate than the frequency domain methods that are based on the modified Hill's method. A multi-frequency harmonic balance method (MHBM) was used by Fu et al. [59] on a dual rotor with rub-impact where uncertainty propagation methods were compared, namely, an arc-length ratio method and polar angle interpolation.

Salles et al. [78] used HBC to obtain the bifurcation diagram of an entire aeroengine with three shaft and four snubber elements. Component mode synthesis was used to reduce the FE model, which was further reduced to the nonlinear degrees of freedom. A special treatment of the method allowed them to find isolated solutions in the bifurcation diagram. However, the analysis of the asynchronous response was not their objective.

Another study that employed HBC was conducted by Briend et al. [53]. The vibration characteristics of a space turbopump-inspired test rig with oil bearings and loosely

fitted ball bearings during the passage through the critical speed was investigated numerically and experimentally. Both time simulations and the HBC method were used on a high-dof FE model with Timoshenko beams and 23 nodes. The authors noted that a higher number of harmonics were necessary to accurately capture the nonlinear dynamics due to the strong nonlinearity of bearing-housing contact. Experimental validation was successful. The detailed model also calculated the crushing of the ball bearing's balls and the penetration of the outer race into the bearing housing.

More recently, HBC method was used to analyse the sustained motions of a manoeuvring aircraft by Yang et al. [60] which was validated with simulations. Saddle-node and Hopf bifurcations are observed during constant-speed base manoeuvres. Interestingly, certain operational conditions manoeuvres decreased the response amplitude.

Normal forms, rotating frame Because the intermittent contact response can be seen as the synchronisation of resonant frequencies of the EOM in the rotating frame, the use of the normal forms technique was found useful to solve the nonlinear equations [30]. Shaw et al. [30] employed the normal forms method on a reduced order model together with an AFT method to update the nonlinear forces. The proposed method was demonstrated on a 2-dof overhung snubbed rotor system and a multi-disk system involving rotor-stator contact. In the study [30], the fundamental frequency of harmonic expansion in the resonant EOM was not required beforehand but calculated in the solution process.

MAC, Piece-wise smooth dynamics, NNM The modal assurance criteria (MAC) was used by [63] to identify the modal content of the nonlinear response of an interacting rotor-stator system, where the modal amplitudes of the FFT of the response were compared to the linear eigenvalue solutions of the same system. Backward whirl modes constituted many of the modal components. Piecewise-smooth dynamics was used by Mora et al. [45] to define contact for a Zilli system where the grazing bifurcations of the rub-impact phenomenon were investigated to analyse the onset of the rub-impact fault. They found that there is not a pre-bifurcating orbit to the 2:1 and 3:2 IRs and these bouncing orbits exist as a blue-sky catastrophe off the zero damping case. A similar method of piecewise-smooth model was used by [46]. Nonlinear normal modes (NNMs), originally developed by [79], were used to define complex nonlinear modes by Laxalde and Thouverez [80], which were then utilised in the analysis of turbomachinery blades with friction interfaces. More on NNMs is given later.

Simulation critique, EOM continuation Aside from experimental investigations, the primary tools for understanding rotordynamics have thus far been time simulation [13, 31, 81, 82, 4, 14, 3] and analytical and semi-analytical approaches based on the harmonic balance method [76, 75, 78, 30, 74, 11]. The time simulation approach is slow;

solutions must be continued for some arbitrary amount of time to converge to a steady state which make it excessively time-consuming for low damping cases [71], although parallelisation or sine sweep in rotor speed might mitigate that. If the chatter is involved in the contact simulations, than the cost increases rapidly unless a chatter mapping is used; e.g. see the method by [83] applied on a rigid impacting rotor by Mora et al. [45]. Also, many simulations must be run with different initial conditions if multiple solutions are to be found [4]. Even when this has been done, there is no guarantee that all responses have been found, making time simulation inefficient to investigate these systems. Analytical and semi-analytical approaches require sometimes complex formulations to transform the equations of motion to algebraic form, and still leave doubt that all solutions have been found, depending on the numerical solver's start point. However, the use of arc-length continuation does offer significant benefits in exploring the space around a given solution in the sense that it allows a complete solution family to be found without the interruption of jumps between different solution families, a common phenomenon for time simulations. It can pass the turning points, the so-called folds, possibly progressing to the unstable region [75], which make the method feasible for high resolution bifurcation diagrams [71]. However, an initial time spent to setup the continuation parameters such as those that define accuracy is required in continuation [84], e.g. for a balance between computational burden and accuracy, or for not jumping to different solution families, or for simply being able to continue finding regular points along the branch. Given the rich complexity of solutions in rotor systems, it is perhaps surprising that the method of numerical continuation, where continuation is applied directly to the equations of motion, has not previously been applied more extensively. This approach discretises the ODE in time and resulting mesh points become the unknowns of the algebraic system of equations whose zeros are found along a branch.

1.3.5 Importance of the rotating frame perspective in the analysis of some quasiperiodic motion

An early reference to the importance of the rotating frame was given by Van der Heijden [85]. Cole and Keogh [34] stressed the importance of the rotating frame to determine a periodic response for the bouncing cycles. They studied quasiperiodic responses that look periodic in the rotating frame, due to rotor-stator contact friction in an impact-law contact definition. Interestingly, a similar response was also observed in the case of very soft snubber ring stiffness [32]. Shaw et al. [4] defined the IR phenomenon in the rotating frame, and generalised the idea to multi-dof models. Shaw et al. [30] used the rotating frame, signed Campbell diagram to locate IR motion along the rotor speed range and stressed the rotating coordinate for obtaining periodic solutions.

More recently, the importance of the use of rotating coordinates was emphasised to

obtain a periodic response for the bouncing cycles by others such as Wang et al. [25] and Yoshimori et al. [50]. This shows that IR motions exhibited by the interacting nonlinear rotor-stator system often involve periodicity with respect to the rotating frame of reference. This can be explained as follows: In the rotating frame, the OOB forcing appears as a static force, appearing at the DC component of the frequency spectrum. The remaining two underlying frequencies of the IR mode become commensurate, and become locked together. In the next section (Section 1.4) the concept of mode locking is given to explain that phenomenon. Throughout the thesis, signed frequencies are used for the expressions of frequency content in either stationary or rotating frames; rotating frame frequency content is simply the left-shifted version of the stationary frame frequencies by the rotor speed Ω due to the relation $\omega_k^{rot} = \omega_k^{sta} - \Omega$ where ω_k is the k^{th} frequency bin.

1.3.6 Wider nonlinear rotor-stator interaction literature

Wider literature In the wider scope of rotor-stator contact, Cao and Yao and colleagues [86, 87] investigated grounded nonlinear energy sinks to suppress the motion of a vibrating 4-dof rotor. The nonlinear stiffness used in the study was cubic, but practically obtained using a squirrel cage: some of the rods constituting the squirrel cage had clearance of varying sizes at one end; as the amplitude of oscillation increases these clearances close one by one, creating a piecewise-linear stiffness that approximates a cubic stiffness profile. Cubic pedestal stiffness with looseness was studied in an HBM formulation, time integration and experiment by Zhang et al. [88], where quasiperiodic motion was seen in addition to subharmonic and multi-period motions.

Zhang et al. [89] investigated the rub-impact fault of a multi-disk rod fastening rotor system with rub-impact, where oil-film supports, snubber stiffness, clearances and unbalance parameters are studied. They observed period-1, -2, and -3 motion as well as quasiperiodic motion. Interestingly, the model incorporated the effects of the rod-fastened system as a cubic restoring force in both lateral directions. Other studies by Liu et al. [90, 91] dealt with modelling and simulations of rotors with disks that are joined together with bolts using detailed FE models. The studies which investigated rub and pedestal looseness when rotors with bolt-joined disks are present found that rubbing caused softened bending stiffness at the bolted joint.

Heat-related effects during rotor-stator contact was studied by Zhang et al. [92] whose model used Hertz contact theory and accounted for frictional heat generation, heat distribution and conduction, and predicted the experimental observations accurately. Jacobs et al. [93] modelled rotor-stator contact with a high speed turbine and a detailed FE model for the stator where they showed that the high contact forces can result in melting due to wear while also overcoming the aerodynamic torque on the turbine.

Rotor blades rubbing against the stator were studied by Kou et al. [94] on a disk with

wide chord blades. Pan et al. [95] studied the effect of manoeuvres of a plane on the blade rub phenomenon using a 2-disk aero-engine model, one of which was contacting with the stator. Although initially subharmonic resonance of order 1/2 was observed, increased contact stiffness caused quasiperiodic motion to appear. The sustained vibration of interacting rotor-stator of an aeroengine under rolling, pitch and hovering base motions was the subject of the study by Yang et al. [60]. Legrand et al. [96] designed an FE model to study the modal interaction between rubbing blade and casing where explicit time integration and analytical solutions are compared. The number and curvature of the blades affected the blade-casing modal interaction. Delhez et al. [97] comparatively studied reduced order models for the industrial NASA rotor 37 blade; geometric nonlinearities were included in scenarios of blade tip rubbing against a rigid casing and harmonic excitation that represents aerodynamic loading. Unlike [97], Nyssen et al. [98] studied mistuning of bladed disks with blade-casing contact failure where the casing had an abradable coating. They concluded that geometric nonlinearities are important to accurately model the contact event severity. Song et al. [99] focused on the vibrations of the rotor drum in an aero-engine under stator vane rubbing using FEM and observed stiffness hardening due to the contact. They concluded that an aero-engine can manifest superharmonic resonances as a consequence of rubbing failure since the vibration mode of the cylindrical shell corresponds to multiples of rotating frequency. Thiery and Chandran [100] used a simplified model to investigate the effect of the number of blades on the blade rub phenomenon where increasing the blade count resulted in less hazardous vibrational behaviour. Zhou et al. [101] included the geometric nonlinearity and gyroscopic effects employing time simulations and experiments. They stated that rubbing excites the natural frequencies of blades which affected the rotor vibrations. Qv et al. [102] experimentally and theoretically studied a dual rotor casing system with rotor-casing rub using FEM. They found that the rubbing influences the frequency spectrum of the case structure in a distinct way, and that the initial clearance and contact stiffness are determining factors of the rubbing violence.

Backup bearing impact for magnetically supported shafts were studied by Fonseca et al. [103, 104]. The rub-impact effects due to base excitation through landing was studied by Jarroux et al. [105] on a rotor with active magnetic bearings. The experimental response was closely reproduced in the FEM simulations, though magnetic saturation nonlinearity was not encountered. Kou et al. [106] studied the multilocation rub-impact faults of a bladed rotor with magnetic levitation bearings and magnetic saturation nonlinearity. Active magnetic dampers were used by Zaccardo and Buckner [107] which reduced the first critical speed response by 79%.

Tchomeni and Alugongo [108] investigated fluid effects on a submerged Cardan shaft with unbalanced disks. They observed aperiodic motion with the effect of rubbing and that the Cardan joint dampened the high vibration motion. Later, an experimental vali-

dation was given by Sozinando et al. [109] where the wavelet synchrosqueezing transform was used to decompose the vibratory signal that contains frequency modulation due to unbalance and rub faults. They concluded that the rub impact frequencies are attenuated when within the fluid compared to without fluid medium, and that the diagnostics with the wavelet synchrosqueezing transform are effective. The inspiration for these studies came from machines such as centrifugal pumps, mixers, and hydraulic turbines.

An interesting manipulation of the differential equations of a rub-impact rotor-stator system was given by Liu et al. [110], where they used fuzzy differential equations to visualise different expected response patterns. Even though the fuzzy state initially started around one attractor, namely, the synchronous full annular rub response to unbalance excitation, the fuzzy state separated and made the dry friction backward whirl appear as well. Fractional order dynamics of a rub-impact rotordyanamic model was studied by Cao et al. [111]

Coating effects were studied by Yang et al. [112]. Intermittently contacting quasiperiodic motion only appeared with larger coating hardness while softer coating gave full rubbing synchronous solutions. The nonlinear response of a rotor-bearing system with rotor-stator rubbing, bearing raceway waviness, local raceway defects and rotating shaft breathing crack was investigated by Cheng et al. [113]. They pointed out the importance of correctly selecting bearing radial clearance for improving fatigue life.

1.4 NNM literature survey

Mode locking As introduced earlier in this section, linear modes extend into nonlinear modes if the response is dependent on the amplitude. Nevertheless, some nonlinear modes only appear if the nonlinearities are considered. One of the reasons of the occurrence of these new modes is a concept called mode locking (or frequency-locking or phase locking) [114, 115] This happens when response frequencies appear in a linear sum relation with integer coefficients. A nonlinear mode's frequency can coincide with a rational multiple of another mode's frequency, which results in an internal resonance (IR), e.g. $a\,\omega_1 = b\,\omega_2$ where a and b are integers. The involvement of other frequencies (maybe including the forcing frequency) results in combination resonances, e.g., $a\,\omega_1 - b\,\omega_2 = c\,\omega_3$ where a, b and c are integers. This frequency relation is entrained by the driving frequency Ω [115] or established back, due to being locked, after slight perturbations of the constituent frequencies.

Mode locking was discussed in the field of rotordynamics by [85]. The study analysed combination resonances giving quasiperiodic trajectories on 2-tori with n-loop appearance in the rotating frame, which was called partial mode locking. Including gravity broke symmetry and the parallel motion on 2-tori, while adding additional frequency-locking relations so that the main frequencies are fully mode-locked, and the trajectory is periodic

in the stationary frame (such as in subharmonic resonance).

Rosenberg's NNM definition Despite being new in the rotordynamics field, the concept of modes in nonlinear systems is not new, originally attributed to Rosenberg [79]. For a review of nonlinear normal modes (NNMs) one can refer to [116, 117, 118, 119]. Two main definitions of NNMs are common, one is due to Rosenberg [79], later generalised to other periodic solutions and used in a shooting-continuation scheme by Peeters et al. [118], and the other is due to Shaw and Pierre [120], later developed further by Pesheck [121]. Rosenberg [79] defines NNM as periodic motion with "vibration in unison" (peaks and zeros happen simultaneously). The vibration in unison requirement is relaxed in most studies and periodic IRs were included in the NNM definition by Peeters et al. and Kerschen et al. [118, 117]. They also said that although neither theirs nor Rosenberg's definition include nonconservative systems, this is practically not a problem as damped systems often closely follow the undamped behaviours observed by the NNMs. According to that definition, NNMs are the nonlinear conservative systems' periodic modes that form backbones when the energy of the mode changes. This definition is intuitive and reminiscent of the way undamped linear normal modes underpin the forced and damped behaviours of linear structures.

NNM definition as a Manifold Shaw and Pierre (e.g. [120]) extended the Rosenberg definition to damped systems through the definition of an invariant manifold. This invariant manifold was defined in a phase diagram formed by a position state and its velocity counterpart (dubbed the master states), augmented by a third dimension being another state of the system. All states other than the master states are expressed as polynomial expansions of the master states [120] (or by harmonic functions in Pesheck [122] after a transform), defining invariance equations. The solution to the invariance equations defines this manifold which is tangent to the vector field. Thus, a motion starting on the manifold remains on it always, making the manifold "invariant". Pesheck [122] noted that the invariant manifold approach was generalising the analysis to linear-nonlinear damping, asymmetric nonlinearities, not necessarily periodic response, and multi-mode responses such as IR. Pesheck et al. [121] developed a Galerkin-based approach involving a numerical solution in the calculation of the invariant manifold and used it in the modal reduction of a rotating beam in [123]. The Galerkin-based method of the manifold approach [122] decreases the need for analytical calculations and makes the problem more suitable for numerical solving. This definition of an NNM is more complex, while the first one has already been used in periodic solution continuation scheme by [118, 117].

Complex nonlinear modes, NNMs for rotating systems NNMs has gained popularity in the analysis of rotating systems. Complex nonlinear modes were defined by

Laxalde and Thouverez [80] in order to investigate the modes shapes that have a phase difference between its degrees of freedom, such as in gyroscopic systems. However, the method specifically makes use of the complex eigenvalue expression to investigate the damped nonlinear modes that cannot be analysed with the conservative modes. Related to the traditional HBM as a generalisation, the time domain solution is expressed in a generalised Fourier series where the harmonics had a decay term as for an eigenvalue: $\lambda = -\beta + j\omega$. The AFT process was formulated with only the periodic (not decaying) Fourier terms. They demonstrated the method in the analysis of turbomachinery blades' vibration with frictional interfaces with success. The forced response was generated with one NNM harmonic with good agreement. Liu and Hong [124] utilised the concept in the analysis of dry whip motion on a compressor-turbine unit. Complex nonlinear modes are also used in [35, 125] for analysing the dry whip motion. The stability of the BW mode was assessed by its modal damping, which was indicative of the dry whip onset.

Recently, Wang and Ding used NNMs as defined by Peeters et al. [118] for balancing a 2-disk rotor [126]; they used the prominent frequency content of modes for modal representation. In [51], Shaw-Pierre's manifold description was used to draw probability density functions of the modes in a stochastic finite element study.

1.5 Experiment literature survey

Introduction Theoretical observations of the nonlinear phenomenon rotor-to-stator contact in the field of rotordynamics have been available in numerous publications in the last decades [10, 127, 6], which is extensively presented in the above sections. Even though the real-life cases of rotor-stator contact have led to these research, such as in the start-up of a steam turbojet, the experimental observations are relatively less commonly published due to the fact that such experiments could be dangerous and difficult [23]. Furthermore, the experimental results obtained by authors of different studies reflect closely the characteristics of only the particular test rig subject to their investigation. This is because the response is greatly affected by the physical parameters of the rig such as boundary conditions, size of the experiment, stiffness of the rotor and stators, nonlinearity source, clearance, friction at contact, damping, gyroscopic effects and others. Even on the same test rig, different responses can be observed depending on initial conditions [6].

1.5.1 Test rigs

Rig size Depending on the aims of the researcher, the test rig can be varied: if the aim is to have a high fidelity representation of real-scale turboengines, for example, then the size of the test rig is generally large; otherwise, if the aim is the isolation of various nonlinear phenomena, then smaller and versatile, bench-top scale test rigs are preferred. Test rigs

of Refs. [15, 23, 65] were large real-scale test benches (1485, 3150 and 2000 mm of shaft lengths, respectively), while [128, 28, 17, 21, 129, 27, 130, 20, 19, 64, 55, 65, 131, 52, 132], used bench-top test rigs, generally less than a metre in shaft length. For instance, a close investigation of the IR responses can be managed with a dedicated smaller scale model in a more controlled way.

Rig versatility The studies on the same test rigs can enable the researchers to decipher some of the response patterns, linking them to the parameters of the specific rig present. Therefore, the high versatility of the test rig can ensure more links established between these different responses through controlled changes in the rig.

Chu and Lu [21] used a versatile test rig to investigate the rotor-stator contact problem. The rotor speed range was 0-10,000 rpm; the shaft length range was up to 500 mm; any point on the shaft could be used as the snubber ring location. The stator clearance was adjustable by an easy-to-install stator design: 0.4, 0.6, 0.8 mm clearance was used in experiments. The stator was made from aluminium to prevent damage to the rotor. Rigid, semi-flexible and flexible coupling were used to isolate parts of the rotor from the rest. Up to three rotors were installed on the shaft.

Modularity of the test rig in the TUD (Technical University of Darmstadt) rotor test rig was emphasised by Ehehalt et al. [133]. Various types of bearings and many disks can be mounted on the shaft anywhere. The rig allows for external damping device or actuator attachment on the shaft or the device. Clamping of components on the shaft was achieved by special cone-shaped clamping sleeves. It was stated that this high contact force prevented micro-slip, eliminating the dynamic instability due to internal damping. However, collets that are available in various standard sizes could be an alternative and can still provide even clamping with high contact force on the shaft. The test rig by El-Mongy et al. [22] also featured an orthogonal damper attachment, which is not very common in the experimental studies.

A test rig by Bently Nevada [134] was used in numerous studies, e.g., [131, 129] and a similar one in [28, 87]. The rig allows for multiple disks along a shaft where sensor attachment is possible; the rig is protected with a protective sheet. The rig additionally features an oil whirl/whip kit. The test rig in Ref. [65] was suitable to different snubber ring stiffnesses of 1.2, 0.27 and 0.45 MN/m, where only the stiffer enabled bouncing cycles. Chipato et al. [32] changed the snubber ring stiffness by adjusting the length of the rods that held the snubber ring. Torkhani et al. [23] used different rotor-stator interaction surfaces to alter the friction. Kartheek et al. [51] changed the emery paper lining the rotor-stator contact surface to modify the friction. Karpenko et al. [48] changed the clearance level between 0.50 mm to 0.75 mm by swapping the stator; whereas, Briend et al. [53] used 66 μm, 116 μm and 300 μm by changing the bearing housing. The experiment of Piccoli and Weber [135] utilised conical bearing whose races are separated

axially to create variable clearance at the end of a vertical overhung rotor. Adjustment of the clearance through axial motion was applyed also by Taher et al. [52] where the outer stator had a tapered inner surface. Axial tightness was adjusted by moving the bearing at one end of a longitudinally constraint slender shaft in [20]. The dual rotors' speed ratio was variable in Ref. [132].

Mostly, the source of the nonlinearity involves the stator design; hence, it is the subject of versatility in nonlinear rotordynamics.

Rotor types Slender shafts with bend-stretch coupling were investigated in the experiments of [55, 20]. Experiments of [19] investigated the response of a 4 dof extended Jeffcott rotor with contact. An overhung rotor with contact was investigated by [128, 64, 25]. A multi-disk rotor has appeared in rotor-stator interaction experimental research [21]. Dual-rotors appeared in [59, 132, 102].

If the motor torque does not provide an ideal drive, then flywheels can be used to isolate the rotor as in [55, 17]. Despite the use of soft plastic pipes for the rotor-motor isolation in [55], this is not reported to cause unstable internal damping. A flexible coupling, flywheel and a belt driver was used in [17] to keep measured vibration from the rotor clean of the frequencies from the drive. However, the rotor itself can provide enough rotational inertia to smooth a slightly non-ideal motor drive.

Rig measurements, damping, coefficient of friction Damping is difficult to measure in an experiment unless it is explicitly added as a damper element to the rig. All connections contribute to damping, and the effect of dry friction makes damping quantification more challenging.

Dedicated external dampers were used by El-Mongy et al. [22] and Karpenko et al. [48] in a rotor rig developed at the University of Aberdeen. The test rig by Wang et al. [65] achieved damping in a controlled way through stiffness rubbers, and the damping ratio was 0.13 for all of the different stiffness cases. Cong et al. [129] utilised an impact hammer test to calculate the damping ratio of the rotor, and the first critical frequency.

In other more difficult cases, Lahriri et al. [64] analysed the free decay signal in the experiments to obtain the damping ratio from the conical swinging motion of the rotor when it is not rotating, which was found to be 0.027. The contact torque is found from the Coulomb law when sliding and from the rotor torque when stuck. Choi plotted the required friction coefficient and correlated it to the experimental data to find the experimental friction coefficient [17]. Therefore, experimental and simulation data can be analysed together to estimate some of the test rig features.

DAQ To measure the vibrations, eddy current sensors [135, 129, 48, 65] or laser displacement sensors [128] are used; whereas [32] used a consumer grade camera to trace the

rotor trajectory by post processing. Briend et al. [53] used laser sensors to measure the shaft bow.

In [129], the expected frequency range of eddy current sensor data was up to five times the rotor frequency, following the suggestion by [136]. Taher et al. [52] used a 4 kHz sampling rate. However, for a quasiperiodic trajectory that is reasonably well sampled, a minimum of 100 data points per rotation can be targetted, which makes, e.g., 5kHz sampling for rotor speed of 3000 rpm (50 Hz). Bing et al. [132] used 5.120 kHz sample rate for a dual rotor.

A clever sensor arrangement was used in [130] to measure the torsional and lateral vibration amplitudes by means of the two sensors positioned opposite to each other in the horizontal plane: the time interval between the teeth on the rotor is decomposed into components from torsional vibration, lateral vibration and the advance in the rotor angle ωt.

Nonlinearity source In [55, 20, 137] the nonlinearity was due to the bend-stretch coupling as a result of the axial constraint on the elongation of the elastic shaft. Other studies have a snubber ring (e.g. [32, 23, 65, 19]) in their models and experiments, forming the nonlinearity through the discontinuous stiffness. A partial arc was used as the contact interface in [15]. A nonlinear energy sink was used in Refs. [86, 87] that features a cubic stiffness achieved in a piece-wise manner by a squirrel cage with rods engaging one by one as the lateral amplitude of motion increases. Dai et al. [27] had a stator that is interacting with the rotor from inside.

An unconventional design was implemented in [64] to send the rub-impact motions to synchronous response without contact: four adjustable pins were located at the quadrants of the stator, sending the impacting rotor back to its low amplitude state. Ref. [129] designed a 'rub screw' which realised a short impact event between rotor and stator. Wear is thought to be responsible for some chaotic behaviours in experiments with a partial rub device by [26].

Physical effects Misalignment was present in the rig of [21], evident in the imperfect harmonic oscillation of the rotor when no contact occurs. On a vertical rotor with contact [19] the misalignment effect on the experiments was clarified in the analytical HBM analysis on 1/2 subharmonic resonance. In a horizontal rotor, gravity increased the natural frequency in the vertical direction (gravity force direction) [26]. The gravity effect on a slender shaft was included in [55]. Nagasaka et al. [55] also investigated the shaft asymmetry on a slender shaft.

Torsional vibrations were analysed by Diangui [130]. They reported that the rubbing torsional natural frequency increases with the rotor speed only to reach a maximum level despite the further increase of the rotor speed.

Karpenko et al. [48] used a preloaded stiffness in their experimental rig of a Jeffcott rotor with a mass of 9.7 kg, whose analytical model was derived elsewhere [47]. The stiffness was achieved by the stationary bars that are connected to the rotor via a hub which was interacting with the stator. The stator was much stiffer than the rotor's stiffness and assumed massless in the analytical model.

Both unbalance and earthquake-like excitation was used by [27].

Transient motion (either during run-up or run-down) under unbalance excitation was studied in [28, 23], and upon sudden unbalance it was studied by Wang et al. [65].

Abdul Azeez and Vakakis [128] investigated an overhung rotor which allowed for the gyroscopic effects to be observed. The need for external hammer impacts were noted to excite nonlinear responses in [128].The extended Jeffcott rotor (a disk that is not centred on the shaft) gave gyroscopic effects in [19]. Similar to some of the theoretical models [31, 3], they also observe the combination resonance $\omega_f^{sta} - \omega_b^{sta} = \Omega$ which is rarely published in experimental studies.

Shaft bow was included in the experimental study reported in [53] which was measured by laser displacement sensors. A bent shaft with bow equal to 75 μm was measured in [23] which compared to the disk eccentricity of 105 μm.

Briend et al. investigated a loose ball bearing where the contact can happen between the outer race and the bearing hub, and between the inner bearing race and the outer race through the balls [53].

1.5.2 Different experimental responses

Response introduction The experimental literature shows that the nonlinear rotor-stator interaction phenomenon is closely linked to the diversity of the response and to chaos in rotordynamics. Since the early studies, synchronous and asynchronous, periodic, quasiperiodic and chaotic response have been observed both theoretically and experimentally, such as [128, 13, 138, 139, 20, 52, 48, 135, 137, 25] to name a few. Refs. [28, 17, 27, 29] investigated the full annular rub, while [15, 21, 19, 140], dealt with the intermittent bouncing response.

Full rubbing Bently et al. [28] investigated dry-whip and the transition from forward precessional rub to reverse precessional rub, as well as dry and fully and partially lubricated cases. During rundown, the dry-whip motion disengaged close to the stopping speed. Choi [17] looked into backward rolling and sliding, and forward sliding motions and simulated them. Forward sliding was synchronous with rotor speed, while the backward sliding frequency was constant regardless of the rotor speed. Full and partial rubbing was studied by Dai et al. [27] on a 4-dof rotor with an inner stop under external excitation mimicking an earthquake as well as the unbalance excitation. Fumagalli [141] studied the

retainer bearing dynamics, in particular the definition of the contact and the finite duration thereof which affects the onset of the vibrations. Subsequently, dry backward whirl was studied by Bartha [29] in terms of the excitation, development and sustaining of such modes of vibration both in theory and application, inspired by small turbo compressors. High modal damping reduced the coefficient of restitution. The effect of friction on the different modes of full rubbing motions have been investigated theoretically [142, 143]. Experimental literature documents full rubbing phenomena relatively well.

Subharmonic Subharmonic response was a common occurrence in the unbalance response involving rub-impact which was encountered in [20, 19, 21, 26, 52], although Torkhani et al. [23] did not see subharmonic responses in a real scale test rig. Super-sub harmonic resonance of order 2/5 was seen in the experiments of Ishida et al. [19], while both 2/5 and 2/7 were seen in simulations. In the loose pedestal experiments by Muszynska and Goldman [26], the harmonic component (1x) in the vertical direction had lower amplitude than in the horizontal direction, while the 1/2x subharmonic component was higher in the vertical direction. This indicated that the subharmonic components are the result of contact nonlinearity, and they transfer energy between the two directions. As a practical point, the steady-state motion, where the unbalance angle was superimposed along the orbit, was presented alongside with key-phasor marks, which together made the response visually more comprehensible. A butterfly orbit (half forward and half backward whirl orbit of 1/2x sub-synchronous response) was linked to a bifurcation due to anisotropy in the same study [26].

Internal resonance and quasiperiodic response Internal resonance (IR) response is a bouncing type response, which can affect the structural integrity of rotating systems if it is not designed for such nonlinear, violent vibrations. This type of response can produce very high amplitudes, although they lock at a low amplitude. The resulting repeated impacts within a rotating system, therefore, can be quite destructive. Unlike direct resonances, which typically occur at just a narrow range of operating speeds, IR responses can occur at a broad range of operating speeds, thereby making their investigation critical in the design of real structures. These responses can be challenging to reproduce cleanly in experiments because damping eliminates many nonlinear responses. The experimental observation of IRs can fail due to high damping present, which does not mean that they cannot be realised if certain initial conditions are excited. The basin of attraction of a particular response might shrink due to damping, or it might be out of the amplitude or rotor speed range supplied by the structural and operational limits of the test rig. Therefore, it is generally not straight-forward to generate IR responses in an experiment, if it is not specifically designed for investigating them (see Ch. 7 for a dedicated test rig).

IR modes of -1:1 were seen on a horizontal slender shaft [55] where first and secondary

critical speeds were investigated using analytical HBM. Signed frequencies were used to show the frequency content of the experimental responses which were compared to the analytical ones. Quasiperiodicity (almost periodic motion) were predicted in the HBM. Quasiperiodic response was seen in the experiments of [21, 128], although signed frequencies would have supplied more insights. One response observed in [32] might be linked to the $\omega_f^{sta} - \omega_b^{sta} = \Omega$ combination resonance by inferring from the unsigned frequency content. Ishida et al. [19] saw the $2\,\omega_f^{sta} - \omega_b^{sta} = \Omega$ resonance (or the $2\,\omega_f^{rot} = \omega_b^{rot}$ in the rotating frame, a.k.a. 2:1 IR); the same response classification was seen in [20] on a slender shaft.

The teardrop shaped orbits in the soft snubber ring of Chapter et al. [32] were similar to those of the theoretical study by Cole and Keogh [34]. This is a backward precessing mode with a FW frequency component at the drive speed and a BW component (see Ch. 7) which happens when the friction is present and might be termed -1:1 BW; the FW component is higher, so the rubs are FW, but the general precession of the quasiperiodic orbit is BW. Interestingly, an overhung rotor [128] gave a Poincaré section with two isolated closed circles, which was called *period-2 quasiperiodic motion*. Ref. [19] reported 'self excited' motion where only the first forward mode is present along with the drive frequency which are incommensurate and the motion is quasiperiodic. In a stochastic FEM study by Kartheek et al. [51] IR response was studied and experimental validation was conducted.

As the literature shows, combination resonance, internal resonance and quasiperiodic motion can appear in a wide range of different manifestations.

Chaos Chaos was observed in numerous experimental studies, e.g. [137, 128, 48, 21]. The period doubling route to chaos was identified in [48] while in [128] it happened through chaotic explosions (sudden transition) which was said to be typical of many-mode systems. Delay coordinate embedding was used to analyse and detect chaos in [135] and [144]. Difficulty due to noise in the experiments was noted [135]. Chaos was linked to anisotropy and continual wear in partial rub and loose pedestal experiments by Muszynska and Goldman [26], while higher damping decreased the chaotic behaviour occurrences. Taher et al. [52] observed coexisting chaos with period-2 motion.

Contact detection and signal character Most of the rotor-stator interaction involves the rub-impact and contact phenomenon. Due to the rapid time varying features involved in rub-impact, such as transient stiffness and the instantaneous frequency content of the vibration signals, Yang et al. [131] used the nonlinear squeezing time-frequency transform (NSTFT) method to diagnose rotor-stator contact. The method gave an instantaneous frequency around the fundamental harmonic. This instantaneous frequency's oscillation frequency was $1/\mathrm{k}^{\mathrm{th}}$ of the unbalance frequency for a period-k motion (i.e. a motion with

k isolated dots in a stroboscopic Poincaré section for the stationary frame periodic orbits). Experimental validation was established on the Bently RK4 rotor test kit [134].

A novel method called adaptive chirp mode decomposition was developed in [145] based on the variational nonlinear chirp mode decomposition method [146] to detect contact faults. The new method was demonstrated to be effective in a cracking machine real-case signal, as well as for a simulated signal. Chu and Lu [81] proposed the transient stiffness method to spot rub-impact motion in both simulated and experimental data. They found that the harshness of rubbing can be estimated by the change of the transient stiffness.

Peng et al. [147] used wavelet scalograms and wavelet phase spectrums to extract features of slight and severe rub using time series from the measurements of a rub-impact test rig. They found in the slight rub case, lower frequencies are sustained while higher frequencies are intermittent; the severe rub case had more sustained frequency content, yet the higher intermittent frequencies were still present. Regardless of the severity of the impacts, the wavelet phase spectrum exhibited an irregular split of frequencies above the 3x unbalance frequency.

Wang and Chu [148] proposed a wavelet transform cross correlation method applied on acoustic emission data to locate the rubbing. Pennacchi et al. [15] set up a Wheatstone bridge with slip rings on the shaft to detect the contact, which was possible due to the electrical isolation of the shaft from the rig frame thanks to the oil bearings.

Cong et al. [129] used a parameter derived from the impact energy to assess the rotor-stator rubbing intensity or probability.

1.5.3 Analysis methods for the experimental studies

Different theoretical analysis methods accompanied the experiments. Larger rigs were mostly analysed with detailed finite element (FE) modelling, e.g. [15]. Various time integration schemes were utilised. Ref. [23] used an explicit finite central difference predictor-corrector time marching method. Ref. [65] used a Newmark method for direct integration of second order ODE. A 4th order Runge-Kutta method was used in [81]. Runge-Kutta time integration and HBM was used in [19] for an extended Jeffcott rotor rub-impact analysis. Karpenko et al. [48] used time simulations which was suitable for their chaotic system which featured a preloaded snubber ring. The governing equations were integrated by a Runge-Kutta-Fehlberg embedded 4(5) method (RKF4(5)) in [128]. Analytical HBM was used for a nonlinear slender shaft in [20, 55]. Waterfall diagrams [32, 26] were used to visualise the frequency content for a range of rotor speed. A parameter linked to impact energy was used in [129] to assess the rotor-stator rubbing intensity or probability. A stochastic FE model was developed in [51] on a two-disk rotor and used a generalised polynomial chaos expansion to quantify uncertainties.

The extensive use of time simulations in the experimental nonlinear rotordynamics literature proves its effectiveness in generating a theoretical comparison to the experimental results.

1.5.4 Notes on control-based continuation

Control-based continuation (CBC), due to Sieber and Krauskopf [149], is a non-invasive control strategy based on the classical continuation theory (e.g. [71]), that is used to follow the response of the nonlinear experiments past a fold in parameter space. Therefore, the solution is found irrespective of the stability of the response. Barton et al. ([150] used the method to investigate the response of nonlinear harvesters. In other studies [151, 152], instead of the classical continuation, a different prediction-correction algorithm was employed, avoiding the calculation of differences, such as for the Jacobian calculation, which would be degraded by noise from the experiments. Experimental NNM backbone identification was proposed by Renson et al. [153] using CBC of the NNM. CBC was used in the complex multi degree of freedom (mdof) response involving internal resonances on a nonlinear beam in [154]. This notion of experimental bifurcation analysis by employing control has not been seen in the field of rotor dynamics, but might be a useful tool for both academic and practical understanding on the nonlinear rotordynamics phenomena. For example, the actuators can be attached to the shaft of a rotor via a ring that is connected to the shaft with a self-aligning ball bearing, as done by [133] for connecting dampers to the shaft.

1.6 Aim and structure of the thesis

The literature is not comprehensive about the asynchronous internal resonance (IR) response of nonlinear rotating machinery, which are not desirable in operating conditions. It has been seen that these responses can happen in very soft nonlinearities (such as through bearings [155] or thin shafts) or hard contact nonlinearities, can exhibit at very low or high amplitude oscillations, and can persist for a long range of motion. Hence, the understanding of this phenomenon is vital for reliable design and operation of rotating machinery that features nonlinear rotor-stator interaction, by developing firmer theoretical basis for condition monitoring of rotating machines. As such, this thesis will seek answers to the following questions:

1. What is the relation between smooth and contact nonlinearities in terms of IRs?
2. How does damping and OOB excitation affect stable and unstable IR responses?
3. Are there bifurcations connecting the different families of responses or are they fundamentally isolated from each other?
4. How are the IRs linked to the underlying nonlinear normal modes (NNMs)?

5. How can they be experimentally reproduced reliably?

In order to answer these questions, the aims and objectives of the thesis are elaborated below.

1.6.1 Theoretical research interest

Main methods The literature about the nonlinear rotor-stator interactions (mostly involving contact or geometric stiffness definitions) is presented above. Although analytical methods can provide the researcher with deeper insights into the IR modes in tightly controlled cases, numerical methods are accurate and more readily applicable to engineers. Particularly, the numerical continuation methods produce detailed bifurcation diagrams for the bouncing cycles of rotors interacting with stators although no extensive use has been found in the literature for investigation in rotordynamics. AUTO [84] is a powerful software for this task, which has not been used in the analysis of these system extensively before. Its adaptive mesh formulation, Python-like user interface, use of efficient Fortran subroutines, and graphic output tools facilitates the computation and analysis. The other methods to be used are the rotating frame Campbell diagrams, and the complex discrete Fourier transform (DFT) which fits the intrinsically two-dimensional trajectories of gyroscopic systems. The methods utilised in this thesis are summarised in Ch. 2 which are,

1. Campbell diagram,
2. Complex discrete Fourier Transform,
3. Periodic continuation method using AUTO,
4. Time simulations.

For time simulations, MATLAB's [156] `ode45` is utilised which is based on the fourth order embedded RK4(5)7M Runge-Kutta time integration scheme with Dormand-Prince coefficients [157]. The relevant topic is left to the textbooks such as [158], and omitted in Ch. 2.

Aim, Part-1 Zilli et al. [3] drew attention to the bouncing IR cycles and presented the observed IR phenomena and explained it in terms of phasor diagrams. However, more comprehensive analysis has to be done for a more complete picture of this response pattern. The aim is to use numerical continuation with AUTO [84] to investigate the IR responses of an overhung rotor with cubic, gyroscopic, 2-dof EOM (cubic Zilli system), in different scenarios in order to comprehend such IR behaviour in rotordynamics in a more complete way (see the schematic representation of this system in Figure 1.4). In order to handle this physical phenomenon (the IR responses), a simple model is selected, while avoiding dealing with complicated and case-by-case scenarios that might arise from complex models. The

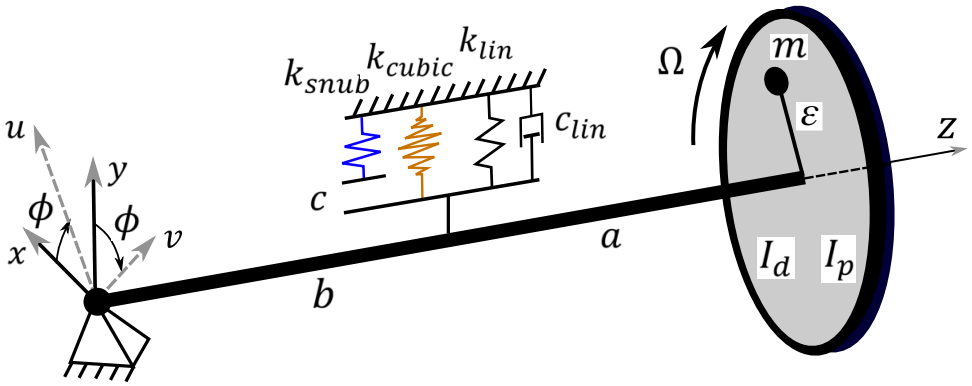


Figure 1.4: The schematic representation of the rotor-stator system with nonlinear elements of cubic stiffness (brown spring) and snubber ring stiffness (blue spring), as well as linear stiffness and damping elements (black spring and damper), all isotropic around the z-axis. The stationary frame (x,y) and the rotating frame (u,v) are illustrated where the rotating frame angle is $\phi = \Omega t$ with Ω the rotor speed and t time.

selection of cubic geometric nonlinearity is based on the fact that many nonlinear rotor-stator interacting systems with contact definitions ranging from rigid to soft compliant stiffness show these IR modes. Therefore, cubic stiffness forms a representation of the softer rotor-stator interaction. The ability of the numerical continuation method to find the unstable solutions is useful to interpret the transient response in these systems that have been presented in previous brute force time simulation studies. Ch. 3 targets this aim through the following objectives,

1. Derive a nondimensional, cubic, gyroscopic 2-dof EOM in both stationary and rotating frames that is comparable to that of the hard-contact Zilli system, [3]
2. Obtain a sample of periodic solutions of IR responses using time simulations,
3. Get the full solution branch including the unstable response,
4. Assess the Campbell diagram values for the IR modes,
5. Investigate the effects of damping and OOB-excitation severity,
6. Discuss the use of time simulations, and continuation in nonlinear rotor-stator interaction problems.

Aim, Part-2 After a more complete understanding of IR responses are drawn using a softer nonlinearity, their relation to contact nonlinearity needs to be investigated. The cubic stiffness is at the softer extreme of nonlinear rotor-stator interaction, and could be used as a basis to transition its bifurcation diagrams into that of the contact nonlinearity. Homotopy continuation will be used to explore the contact phenomenon by transitioning the EOM from the cubic nonlinearity to a smooth representation of contact, which is not encountered in the literature in the way it is performed in this thesis. This allows one to investigate more complex nonlinearities starting from the simpler ones, as well as avoiding the alternating time-frequency step. However, the advantages and disadvantages and the

considerations of both the smooth contact approximation and the homotopy method is to be investigated. Ch. 4 targets this aim via the following objectives,

1. Define a smooth contact representation that will allow for easy transition from cubic system to contact,
2. Derive the EOM that are suitable for homotopy of the nonlinear stiffness terms,
3. Investigate the damping and unbalance severity theoretically in the new bifurcation diagram (BD),
4. Discuss the smooth contact representation in terms of the required considerations for accuracy and effectiveness.

1.6.2 NNM research interest

Although the number of modes of a linear system is defined by its degrees of freedom, in a nonlinear system their number increases thanks to the bifurcations with respect to parameter changes that give rise to other modes of vibration such as IR [117]. The responses given in Table 1.1 are all sustained modes of their nonlinear rotor-stator contact systems, except for the chaotic one. The investigated IR motions are referred to as "modes" of vibration of the system. Therefore, the modal approach to the nonlinear phenomenon in rotordynamics could be a candidate for the unification of different phenomena under one umbrella, which has not been initiated before. As a first step, the generalisation of the use of available methods for the calculation of periodic nonlinear modes (such as [118]) to quasiperiodic modes is to be investigated, which is handled in Ch. 5 by following the objectives below,

1. Discuss the selection of the method (shooting-continuation method) for the quasiperiodic continuation,
2. Define the conditions for the quasiperiodic responses that can be continued with the proposed method,
3. Investigate alternatives of the phase condition that ensure uniqueness of the trajectory, at least locally,
4. Discuss initial condition generation for the method as well as the handling of the *quasiperiod*,
5. Validate the method on the 2:1 IR response on the cubic Zilli system that will have been investigated through the earlier objectives.

From the literature survey above about the nonlinear rotor-stator interactions, although the observation of the presence of IR modes is sound, the mechanisms underlying their formation is not emphasized in the research. The IR modes are an interesting case as they do not show a direct link to the underlying NNMs of the Zilli system. Therefore, in order to call the damped and forced nonlinear system's nonlinear IR responses

as NNMs, some questions have to be addressed such as how the underlying NNMs of the system interact to generate the IR responses, which is done in Ch. 6. The objectives are as follows:

1. Show that the IR responses do not form a backbone, i.e, are degenerate, in the unforced, undamped cubic Zilli system,
2. Calculate the NNMs of the cubic system in both rotating and stationary frames using shooting-continuation derived by Peeters et al. [118],
3. Discuss the frequency content of the NNMs whose harmonics might make the FW and BW modes related or unrelated,
4. Discuss the idea of off-centring that is necessary for mode-locked behaviour between FW and BW modes.
5. Calculate the NNMs when the off-centring effects are present, namely, either gravity or OOB excitation.

1.6.3 Experimental research interest

The experimental literature shows that the full rubbing phenomena such as annular FW or BW rubbing, BW sliding, and dry whip, have been investigated in experiments. However, relatively less emphasis is present in the current experimental rotordynamics literature on the bouncing cycles of IRs, e.g., 2:1 ($2\omega_f^{sta} - \omega_b^{sta} = \Omega$) on rotors with disks, although they are dangerous defects that can occur even without rub-impact failure. This type of internal resonance has been readily seen when the gyroscopic effects are prominent in theoretical studies. Therefore, a test rig that would give gyroscopic effects via an overhung disk would be suitable to investigate this response. A snubber ring contact device can be chosen as the source of the nonlinearity. However, in line with the theoretical research interest presented above, a geometric nonlinearity is a more interesting case because for geometric nonlinearities the nonlinear responses can happen at very low amplitude levels as will be pointed out in the theoretical study. This way, the aim of the experiment will be more focused on the internal resonance modes of the system, instead of the contact-related parameters such as friction. Because the aim of the establishment of this test rig is to isolate a certain type of behaviour, a bench-top test rig is designed instead of a real scale test rig. The experimental part of this thesis is given in Ch. 7 by the following objectives,

1. Derive a 2-dof mathematical model in order to dimensionalise the nondimensional 2-dof EOM that will have been derived according to the above objectives, which will make the test dimensional rig design comparable to the theoretical studies,
2. Design a bench-top size test rig with an overhung disk, a cubic stiffness device, coupled with accurate DAQ system measuring the lateral position of the stator,

3. Target the versatility of the rig for further research,
4. Derive a 4-dof mathematical model in order to obtain time simulation bifurcation diagrams and simulate the expected response from the rig,
5. Manufacture and assemble the test rig,
6. Run tapping tests on the rig frame and the rotor to obtain the rig's linear dynamic characteristics,
7. Assess the shaft bow,
8. Obtain the experimental bifurcation diagram,
9. Address the assembled rig's new characteristics in the updated mathematical model,
10. Validate the experimental behaviour with the theoretical predictions.

Conclusions are drawn at the end of each chapter.

Chapter 2

Methods

2.1 Complex DFT

The thesis makes frequent use of the complex discrete Fourier transform for which the signed frequencies are important. Because the lateral vibration of a rotor is often coupled in the two lateral directions in a general rotor-dynamics response, taking a discrete Fourier transform (DFT) of either or both of the lateral vibration data separately is less informative. Instead, the $\mathbf{w}_{t_n} = \{x_{t_n}, y_{t_n}\}^T$ lateral real coordinate signal instance at discrete time t_n can be written in a single *complex coordinate* by the transform

$$\begin{aligned} \bar{w}_{t_n} &= \{1, j\} \cdot \mathbf{w}_{t_n} \\ &= x_{t_n} + j y_{t_n} \end{aligned} \tag{2.1}$$

where the dot indicates the scalar product and $\bar{w}_{t_n}$ is the complex coordinate at discrete time t_n. The discrete Fourier transform is then:

$$\bar{W}_{f_k} = \frac{1}{N} \sum_{n=1}^{N} \bar{w}_{t_n} \ \exp\left(-j2\pi f_k t_n\right) \tag{2.2}$$

or with the vector scalar multiplication,

$$\bar{W}_k = \frac{1}{N} \{\bar{w}_{t_n}\}^* \cdot \exp\left(-j2\pi f_k \{t_n\}\right) \tag{2.3}$$

where $\bar{W}_k$ is the k^{th} Fourier coefficient corresponding to the frequency range defined by f_k. Here, $\{t_n\}$ and $\{\bar{w}_{t_n}\}$ are the vectors of N uniformly sampled time instants t_n and complex coordinates, respectively, and asterisk * denote the complex conjugate in order to counteract the conjugation imposed by the dot product. Critically, the frequencies f_k are defined as,

$$f_k = \left(-\left(N - \left\lfloor \frac{N}{2} \right\rfloor + 1\right) + k\right) \frac{f_s}{N}, \quad k = 1, 2, \ldots, N \tag{2.4}$$

where f_s is the sampling rate in (time unit)$^{-1}$.

A DFT calculated in this way allows the Nyquist frequency to not fold the spectrum as a mirror, but instead the frequencies above the Nyquist frequency display the negatively signed frequencies indicating the backward whirling components. Therefore, frequencies are not written as $f_k = (k-1)f_s/N$ with $k = 1, 2, \ldots, N$, and rather the signed f_k expression is used in Eq. (2.4).

The benefit of presenting a DFT plot this way becomes obvious when interpreting the rotational sense of the trajectory of the rotor, which is explained in Section 2.1.1.

Deciding an adequate fundamental frequency for the DFT is important for interpreting the frequency content of the periodic or quasiperiodic solutions accurately. A resolution that is less than optimal can mislead the analyst, by, e.g., masking distinct but close frequency peaks as a single peak. In this thesis, the frequency resolution is decided by a trial-and-error approach. When the frequency resolution no longer generated new spectral features, the DFT resolution was deemed adequate. While doing this, common sense was employed when interpreting whether the resolution is adequate: a 2:1 motion would generate main frequencies of 2:1 ratio.

2.1.1 Signed frequencies

The sign of a mode of vibration is determined with the following analysis: If the x-y pair of position components of an eigenvector $\mathbf{z}_r$ appear in the form $\{a, -jb\}^T$ where $a, b > 0$ with a corresponding eigenvalue that has a positive imaginary part ($+\omega_r$), then according to the counter-clockwise rotation expressed as

$$\begin{Bmatrix} \cos\omega_r t \\ \sin\omega_r t \end{Bmatrix} = \mathrm{Re}\left(\begin{Bmatrix} 1 \\ -j \end{Bmatrix} e^{j\omega_r t} \right), \tag{2.5}$$

the mode is said to be forward whirl (FW) and the frequency is assigned a positive sign. Contrarily, if the position component pair looks the same but the corresponding eigenvalue has a negative imaginary part ($-\omega_r$), then according to the clockwise rotation expressed as

$$\begin{Bmatrix} \cos\omega_r t \\ -\sin\omega_r t \end{Bmatrix} = \mathrm{Re}\left(\begin{Bmatrix} 1 \\ -j \end{Bmatrix} e^{-j\omega_r t} \right), \tag{2.6}$$

the mode is said to be backward whirling (BW) and the frequency is assigned a negative sign. Note that because of the presence of the conjugate pairs, the same analysis can be done with conjugates in mind.

One advantage of the signed frequencies is the straightforward rotating frame frequency transform for both FW and BW components, $\omega_{f,b}^{rot} = \omega_{f,b}^{sta} - \Omega$. Additionally, the use of absolute values of the sum and difference frequencies that arise in asymmetric rotors can be avoided with signed frequencies [11]. Studied such as [25, 50, 30] uses signed

frequencies, making the frequency content appear in a more informative way.

If the time vector $\{t_n\}$ is negative (such as for handling BW modes), then, if the sampling rate is calculated with $f_s = N/t_N$, the frequency axis is flipped and the complex DFT shows correct signed frequency content.

2.2 Campbell diagram

Campbell diagrams show the evolution of natural frequencies of linear rotors with the rotor speed, and the natural frequencies are the eigenvalues of the equations of motion (EOM) [7]. Equations of motion (EOM) are the differential equations that govern the dynamic motion of the system. Gyroscopic effects and support characteristics often mean that the natural frequencies change with the spin speed [7]. The natural frequencies of the general rotor EOM is calculated as follows. The linear, unforced EOM is first expressed as,

$$\mathbf{M}\ddot{\mathbf{w}} + \mathbf{C}\dot{\mathbf{w}} + \Omega\mathbf{G}\dot{\mathbf{w}} + \mathbf{K}\mathbf{w} = \mathbf{0} \tag{2.7}$$

where derivative with a dot $(\cdot)^{\cdot}$ is with respect to the time. which can be augmented by $\mathbf{M}(\mathbf{w})^{\cdot} - \mathbf{M}\dot{\mathbf{w}} = \mathbf{0}$ to give,

$$\begin{bmatrix} \mathbf{M} & \mathbf{0} \\ \mathbf{0} & \mathbf{M} \end{bmatrix} \begin{Bmatrix} \mathbf{w} \\ \dot{\mathbf{w}} \end{Bmatrix}^{\cdot} + \begin{bmatrix} \mathbf{0} & -\mathbf{M} \\ \mathbf{K} & (\mathbf{C} + \Omega\mathbf{G}) \end{bmatrix} \begin{Bmatrix} \mathbf{w} \\ \dot{\mathbf{w}} \end{Bmatrix} = \mathbf{0}. \tag{2.8}$$

With the solution ansatz $\mathbf{z} = \{\mathbf{w}^T, \dot{\mathbf{w}}^T\}^T = \mathbf{z}_r e^{s_r t}$, the eigenvalue problem becomes,

$$\begin{bmatrix} \mathbf{0} & -\mathbf{I} \\ \mathbf{M}^{-1}\mathbf{K} & \mathbf{M}^{-1}(\mathbf{C} + \Omega\mathbf{G}) \end{bmatrix} \mathbf{z}_r = s\,\mathbf{z}_r \tag{2.9}$$

with the eigenvalues s_r of the form:

$$s_r = -\zeta_r\omega_r \pm j\omega_r\sqrt{1-\zeta^2} \tag{2.10}$$

where $|s_r| = \omega_r$ is the natural frequency ($\omega_r > 0$), ζ_r is the modal damping ratio, $\omega_{dr} = \omega_r\sqrt{1-\zeta^2}$ is the damped natural frequency and $j = \sqrt{-1}$ is the imaginary unit. Note that for an undamped system the eigenvalues would look like $s_r = \pm j\omega_r$.

A Campbell diagram example

One of the EOMs that will be frequently used is the one named after Zilli et al. [3], which is expressed in the stationary frame as

$$\mathbf{w}'' - \Omega I_p \mathbf{J}_2 \mathbf{w}' + 2\zeta\mathbf{w}' + \mathbf{w} + \mathbf{f}_{nl}^{sta} = me\Omega^2 \begin{Bmatrix} \cos\phi \\ \sin\phi \end{Bmatrix} \tag{2.11}$$

where $\mathbf{w} = \{x, y\}^T$ is the stationary frame positions. The rotating frame EOM is found by the rotating frame transform $\mathbf{w} = \mathbf{T}\widetilde{\mathbf{w}}$ where $\widetilde{\mathbf{w}} = \{u, v\}^T$ is the rotating frame positions,

$$\widetilde{\mathbf{w}}'' + \big(-\Omega\mathbf{J}_2(I_p - 2) + 2\zeta\big)\widetilde{\mathbf{w}}' + \big(\Omega^2(I_p - 1) + 1 + 2\zeta\Omega\mathbf{J}\big)\widetilde{\mathbf{w}}' + \mathbf{f}_{nl}^{rot} = me\Omega^2 \begin{Bmatrix} 1 \\ 0 \end{Bmatrix} \quad (2.12)$$

where $\mathbf{f}_{nl}^{sta}$ and $\mathbf{f}_{nl}^{rot}$ are the nonlinear force expressed in the stationary and rotating frames of reference, I_p is the nondimensional polar moment of inertia (MOI), ζ is the damping ratio, Ω is the nondimensional rotor drive speed, m is the nondimensional disk mass, e is the nondimensional lateral disk eccentricity, $\phi = \Omega t$ is the nondimensional torsional rotor angle with t being the nondimensional time. Derivatives $(\cdot)'$ are with respect to the nondimensional time t. The transform matrix $\mathbf{T}$ and skew symmetric matrix $\mathbf{J}$ are defined as

$$\mathbf{T} = \begin{bmatrix} \mathbf{T}_2 & \mathbf{0}_2 \\ \Omega\mathbf{J}_2\mathbf{T}_2 & \mathbf{T}_2 \end{bmatrix}, \qquad \mathbf{J} = \begin{bmatrix} \mathbf{J}_2 & \mathbf{0}_2 \\ \mathbf{0}_2 & \mathbf{J}_2 \end{bmatrix} \quad (2.13a)$$

$$\mathbf{T}_2 = \begin{bmatrix} \cos\phi & -\sin\phi \\ \sin\phi & \cos\phi \end{bmatrix}, \qquad \mathbf{J}_2 = \begin{bmatrix} 0 & -1 \\ 1 & 0 \end{bmatrix}, \qquad \mathbf{0}_2 = \begin{bmatrix} 0 & 0 \\ 0 & 0 \end{bmatrix} \quad (2.13b)$$

For both equations, the following parameter values are used:

$$\gamma = 0.25 \qquad m = 0.9 \qquad \zeta = 0.01 \quad (2.14a)$$

$$e = 0.353 \qquad I_p = 0.143 \quad (2.14b)$$

A detailed derivation of these equations are presented in Chs. 3 and 4.

Figure 2.1 shows the Campbell plot which is derived from Eqs. (2.11) and (2.12) by their eigensolutions after removing the forcing and the nonlinear terms. The left of Figure 2.1 shows the classical representation of the Campbell diagram with unsigned modal frequencies calculated from the stationary frame EOM (Eq. (2.11)): The blue line plots the FW frequencies $|\omega_f^{sta}(\Omega)|$ and the red line plots the BW frequencies $|\omega_b^{sta}(\Omega)|$. The right of Figure 2.1 illustrates the method by Shaw et al. [30] which plots the Campbell diagram in the rotating frame with signed frequencies which are calculated from the rotating frame EOM (Eq. 2.12): The blue line plots the FW frequencies $\omega_f^{rot}(\Omega)$ and the red line plots the BW frequencies $\omega_f^{rot}(\Omega)$. Note the separation of the absolute values of FW and BW modal frequencies, $|\omega_f^{sta}(\Omega)|$ and $|\omega_b^{sta}(\Omega)|$ which overlap for $\Omega = 0$. Effectively, the rotating frame frequencies can be read directly from the stationary frame ones following the relation: $\omega^{rot}(\Omega) = \omega^{sta}(\Omega) - \Omega$. However, due to that relation in the frequencies, the intuition gained by the stationary-frame, unsigned Campbell diagram (the left of Figure 2.1) that the FW/BW frequency increases/decreases with drive speed

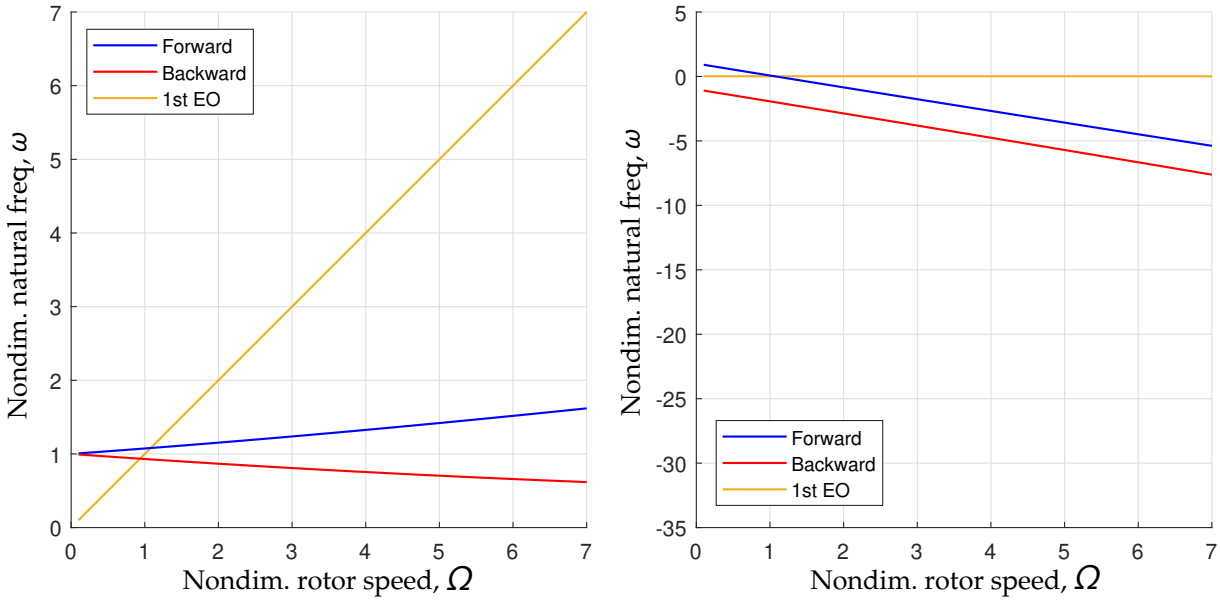


Figure 2.1: Left: The unsigned natural frequency map in the stationary frame. Right: The signed natural frequency map in the rotating frame. 1st engine order (EO) is also shown in both plots. Whirl frequencies are signed positive and negative for FW and BW whirl, respectively in the right hand plot. Note the negative frequencies indicating the BW appearance for the FW mode in the rotating frame after the 1st critical speed.

is lost when reading the modal frequency dependence on drive speed from the rotating-frame's Campbell diagram. Therefore, assuming that the Ω term outweighs any change due to gyroscopics, the rotating frequency will fall with drive speed. A counter example happened in Ch. 7 in Figure 7.9 where gyroscopic effects for the second FW-BW mode pair is so high that the FW natural frequency does not decrease but stays relatively flat with rotor speed.

Despite being a tool in the conservative space, Campbell plots are useful in the analysis of nonlinear systems. Shaw et al. [30] showed that when the natural frequency lines are plotted with integer multiple of frequencies, e.g., plotting $n\,\omega_f^{rot}(\Omega)$ instead of $\omega_f^{rot}(\Omega)$, they cross each other at points which show the onset drive speed of internal resonances (IRs) per the frequency relation $n\,\omega_f^{rot}(\Omega_{n:m}) = m\,\omega_b^{rot}(\Omega_{n:m})$, pointing to the n:m IR. This fact has been exploited throughout the thesis. Such linear predictions seem to always show a lower bound for the drive speed where IR responses begin for a stiffening nonlinearity, despite a formal proof not having been provided for this. Ch. 5 also uses a novel representation of DFT branches for IRs, and overlays them on a Campbell diagram to make the Campbell diagrams even more useful to understand expected nonlinear behaviours.

Small changes of the parameters such as the polar MOI, might affect the Campbell plot greatly, which will be evident in the following chapters of this thesis. Especially, when the natural frequency lines on a rotating frame Campbell diagram with signed frequencies are plotted with multiples of their frequency data in Chs. 3, 4, and 7, their intersection

with each other will be interpreted as a potential IR onset drive speed. However, this discussion is beyond the scope of this chapter.

2.3 Continuation

Numerical continuation allows a known solution to be used as the basis to trace a *branch of solutions*, also known as a *solution family*. In the case of *arc-length numerical continuation* [71], which was implemented in the present work, the so-called *folds* or *turning points* (Figure 4.1) of a solution can be traced without any numerical issues, regardless of the stability of solution. This contrasts well to an initial value problem that uses time simulation where a random initial condition is simulated in time using e.g., a Runge-Kutta scheme, to converge only onto stable solutions. Furthermore, numerical test functions can be employed (such as those outlined by Detroux et al. [159]) to spot bifurcations off the main branch such as fold, branch points and Neimark-Sacker bifurcations. These bifurcations which could more easily be unnoticed in an initial value problem, unless a computationally expensive basin of attraction study is conducted.

The method states that in the vicinity of a regular point, $\mathbf{u}^0$, satisfying a system of algebraic equations of the form $\mathbf{F}(\mathbf{u},\lambda) = \mathbf{0}, \mathbf{F} : R^n \times R \rightarrow R^n$, there is a continuous family of solutions given that $\mathbf{F}(\mathbf{u},\lambda)$ is continuously differentiable at this point and the Jacobian $\mathbf{F}_\mathbf{u}\left(\mathbf{u}^0,\lambda^0\right)$ is non-singular (*the Implicit Function Theorem*). Here, λ is the free parameter of the system which is to be changed to investigate the response. Therefore, as a first step, differentiating $\mathbf{F}(\mathbf{u},\lambda)$ with respect to λ gives,

$$\mathbf{F}_\mathbf{u}\frac{\mathrm{d}\mathbf{u}}{\mathrm{d}\lambda} + \mathbf{F}_\lambda = 0 \rightarrow \frac{\mathrm{d}\mathbf{u}}{\mathrm{d}\lambda} = -\mathbf{F}_\mathbf{u}^{-1}\mathbf{F}_\lambda \tag{2.15}$$

where $\mathbf{F}_\lambda$ is the derivative of the system with respect to the free parameter, λ. This implementation of continuation is called parameter continuation [160] because the parametrisation of the branch is based on λ. If the Jacobian $\mathbf{F}_\mathbf{u}$ is singular, i.e. at *fold* points, this equation becomes problematic. However, if λ is appended to the states of the system as a further unknown, $\mathbf{x} = (\mathbf{u},\lambda)$, and the parametrisation of the branch is established by the position on the branch instead of λ, the folds can be passed: An *arclength* condition expressed as $\dot{\mathbf{x}}^T \cdot \dot{\mathbf{x}} = \|\dot{\mathbf{x}}\|^2 = 1$ is used to augment the system. The derivative is with respect to the arclength s, and the vector $\dot{\mathbf{x}} = \mathrm{d}\mathbf{x}/\mathrm{d}s = \mathbf{p}$ is the direction vector along the branch. A numerically more relaxed form via finite difference would read $((\mathbf{x}^1 - \mathbf{x}^0)/\Delta s^0)^T \cdot \dot{\mathbf{x}}^0 = 1$ where $\mathbf{x}^0$ is the known *solution point* on the branch, $\mathbf{x}^1$ is the next solution point to be found. Here $\Delta s^0 = s^{(\nu=0)} - s^0$ is the step size, the arclength between the previous and predicted solution points on the branch, which calculates numerically the prediction $\mathbf{x}^{(\nu=0)} = \mathbf{x}^0 + \mathbf{p}^0\Delta s^0$. This ensures that the extended Jacobian,

$\mathbf{F}_x = [\mathbf{F}_\mathbf{u}, \mathbf{F}_\lambda]$ is full rank even at folds. Thus,

$$\bar{\mathbf{F}}(\mathbf{x}^1, s) = \begin{cases} \mathbf{F}(\mathbf{x}^1) = 0 \\ \left(\mathbf{x}^1 - \mathbf{x}^0\right)^T \cdot \dot{\mathbf{x}}^0 - \Delta s = 0, \ \left\|\dot{\mathbf{x}}^0\right\| = 1 \end{cases} \tag{2.16}$$

This next point $\mathbf{x}^1$ is initially predicted with a step such as $\left(\mathbf{u}^{(0)T}, \lambda^{(0)}\right)^T = \left(\mathbf{u}^{0T}, \lambda^0\right)^T + \left(\Delta\mathbf{u}^{0T}, \Delta\lambda^0\right)^T$. A Newton correction step, for example, can be implemented on the predicted solution: $\bar{\mathbf{F}}_\mathbf{x}\left(\mathbf{x}^{(\nu)}\right) \cdot \Delta\mathbf{x}^{(\nu)} = -\bar{\mathbf{F}}^{(\nu)}\left(\mathbf{x}^{(\nu)}\right)$ with the definition of distance as $\Delta\mathbf{x}^{(\nu)} = \mathbf{x}^{(\nu+1)} - \mathbf{x}^{(\nu)}$ where ν designates the ν^{th} correction iteration of the next point, $\mathbf{x}^1$. This yields the following Newton iteration equation:

$$\begin{bmatrix} \mathbf{F}_\mathbf{u}(\mathbf{u}^{(\nu)}, \lambda^{(\nu)}) & \mathbf{F}_\lambda(\mathbf{u}^{(\nu)}, \lambda^{(\nu)}) \\ \dot{\mathbf{u}}^{0T} & \dot{\lambda}^0 \end{bmatrix} \begin{Bmatrix} \Delta\mathbf{u}^{(\nu)} \\ \Delta\lambda^{(\nu)} \end{Bmatrix} = -\begin{Bmatrix} \mathbf{F}(\mathbf{u}^{(\nu)}, \lambda^{(\nu)}) \\ (\mathbf{u}^{(\nu)} - \mathbf{u}^0)^T \cdot \dot{\mathbf{u}}^0 + (\lambda^{(\nu)} - \lambda^0)\dot{\lambda}^0 - \Delta s^0 \end{Bmatrix} \tag{2.17}$$

After the convergence (when the solution is no longer changing with respect to a convergence criteria such as $\frac{\max\Delta\mathbf{u}^{(\bar{\nu})}}{1+\max\mathbf{u}^{(\bar{\nu})}}, \frac{\Delta\lambda^{(\bar{\nu})}}{1+\lambda^{(\bar{\nu})}} < \epsilon_\mathbf{u}, \epsilon_\lambda$ in AUTO [84]), the solution is accepted, $\mathbf{x^1} := \mathbf{x}^{(\bar{\nu})}$. Then, the next direction vector $\dot{\mathbf{x}}^1 = \{\dot{\mathbf{u}}^T, \dot{\lambda}^1\}^T = \mathbf{p}^1$ is determined from the derivation of the system at the new point: $\bar{\mathbf{F}}_\mathbf{x}(\mathbf{x}^1) \cdot \dot{\mathbf{x}}^1 = \{\mathbf{0}^T, 1\}^T$. The new direction vector is normalised to make up the new arclength equation: $\left\|\dot{\mathbf{x}}^1\right\| = 1$, which is used in the definition of the new system (see Eq. 2.16) for the calculation of the next point (see Eq. 2.17).

The above explains general continuation implementation when the branch of stationary solutions are sought, i.e., the equilibrium points of an ODE such as $\mathbf{q}' = \mathbf{f}(\mathbf{q}, \lambda)$. In the continuation of periodic orbits, there are two additional conditions, namely, periodicity $\mathbf{q}(\tau = 0) = \mathbf{q}(\tau = 1)$ and a phase locking condition such as $P_{phase}(\mathbf{q}(\tau = 0), \lambda) = q_{n+k}(\tau = 0) = 0$, where k selects one velocity arbitrarily. Also, for a periodic solution to the governing, period-normalised ODE, $\mathbf{q}' = T\mathbf{f}(\mathbf{q}, \lambda)$, the period T and the free parameter λ are constant, namely, $T' = 0$ and $\lambda' = 0$, respectively, where derivative with prime $(\cdot)'$ is taken with respect to the period-normalised time $\tau \in [0, 1)$. Lastly, adding parametrisation $P_{param}(\mathbf{q}(0), \lambda)$ (such as arclength as shown above) and gathering the equations together, one can write,

$$\begin{Bmatrix} \mathbf{q}' \\ T' \\ \lambda' \end{Bmatrix} = \begin{Bmatrix} T\mathbf{f}(\mathbf{q}, \lambda) \\ 0 \\ 0 \end{Bmatrix}, \quad \mathbf{r} = \begin{Bmatrix} \mathbf{q}(0) - \mathbf{q}(1) \\ P_{phase}(\mathbf{q}(0), \lambda) \\ P_{param}(\mathbf{q}(0), \lambda) \end{Bmatrix} = \mathbf{0} \tag{2.18}$$

The vector $\mathbf{u}$ of Eq. 2.17 will be obtained from the temporal discretisation of the periodic

solution to the 1st order ODE $\mathbf{q}' = T\mathbf{f}(\mathbf{q}, \lambda)$ of the EOM, denoting the mesh point values of $\mathbf{q}$. The discretisation of this ODE will ultimately result in a system of the form $\bar{\mathbf{F}}(\mathbf{x}) = \mathbf{0}$ for which the above discussion of arclength continuation is relevant. Discretisation in time is where the way the algebraic equations are obtained differs from the HBM methods which uses the frequency domain expansion of the periodic orbit for discretisation. The discretisation, as well as the issues of stability and step size, are left to textbooks, such as [71].

The numerical continuation method was implemented using the open source software AUTO [84], where the stability is calculated based on the work of Fairgrieve and Jepson [161]. For other continuation methods, one can refer to [116]. AUTO is controlled by the AUTO files which are explained below.

2.3.1 AUTO files

The AUTO-07p open source numerical continuation software [84] was used to apply pseudo-arclength continuation. This software is operated through a Unix Command Language User Interface (CLUI), and can be written in a Python CLUI which supports Python 3 syntax. Setting up continuation runs in AUTO entails filling three dedicated files: equations file, constants file, Python CLUI file.

Equations file

The equations file requires information on the EOM, as well as the starting conditions of parameters and a regular solution on a branch of solutions that is to be continued.

Amplitude was defined to be a solution measure in the PVLS subroutine of the equations file. The amplitudes of stationary and periodic solutions were calculated as,

$$\begin{aligned} \text{Amplitude for stationary solutions (IPS = 1)} &= \sqrt{u^2 + v^2} \\ \text{Amplitude for periodic solutions (IPS = 2)} &= \max\left(\sqrt{u^2(\tau) + v^2(\tau)}\right) \end{aligned} \tag{2.19}$$

where the normalised time τ is defined between $0 \leq \tau \leq 1$ and u and v are the two lateral positions. Here, IPS is the problem selection constant of AUTO: IPS = 1 selects the algebraic solver that finds the branches for stationary solutions (equilibrium points) and IPS = 2 selects the periodic continuation solver which calls the boundary value solver module.

Constants file

The *constants file* is where the user mainly specifies the continuation software's solution control parameters. The primary adjustments of these constants concern those that define the accuracy. More detail can be found in Appendix A.1 linking to Ch. 3. However, it is

important to note here that the very low-damping cases for the IRs studied in the thesis resulted in ill-conditioning of the Jacobian matrix $\mathbf{F_x}$ since the conservative system did not generate a defined branch. As a compensation to get the continuation running, a higher Newton correction iteration number (denoted `NWTN` by AUTO) was used, alongside increasing the total Newton-Chord iteration count (`ITNW`) before AUTO declares non-convergence. Additionally, solution acceptance tolerances were relaxed by using higher values for `EPSL` and `EPSU`, and decreasing the step size by lowering the `DSMAX` constant. AUTO documentation [84] elaborates more on the AUTO constants and the software package includes many examples where 'some experimentation' is used to fine-tune AUTO constants for accurate but computationally cheap solution.

Python CLUI file

The *Python CLUI file* contains the definition of runs in their chronological order, and other tasks such as bifurcation diagram object manipulation, file outputs and so on. The complete content of this file can be written in the AUTO CLUI shell. However, the usage of Python CLUI eases the use of the software by gathering the definitions of all AUTO runs in a source code file.

Chapter 3

Continuation analysis of a nonlinear overhung rotor

Considering the literature given in Section 1.3, the present work seeks the analysis of a 2-dof mathematical model of an overhung rotor with an isotropic cubic stiffness nonlinearity. The main focus is asynchronous orbits that are caused by internal resonance (IR) in the case of geometric nonlinearity, and similarities to the behaviours with contacting nonlinearity are seen. The results are compared to studies with discontinuous stiffness contact definitions.

These asynchronous orbits are quasiperiodic in the stationary frame due to incommensurate frequency relation between the rotor speed (forcing frequency) and the FW and BW components in the frequency spectrum. However, it has been shown that in the rotating frame that is rotating with the rotor spin speed, the forcing becomes a stationary force, making the equations of motion (EOM) autonomous [4]. At the same time, the orbits analysed in this chapter appear periodic in the rotating frame, also shown in [4], thereby becoming suitable for the periodic solution continuation methods. The continuation method (see Section 2.3) used here is applied directly to the systems of ODE using orthogonal collocation method to discretise the periodic solution [84], in contrast to Refs. [76, 78, 74] where the discretisation is achieved by harmonic balance method (HBM).

Because the quasiperiodic solutions in the stationary frame correspond to periodic solutions in the rotating frame, they are called "periodic" in this chapter. Additionally, the periodic synchronous solutions where the response frequency is synchronous with the out-of-balance (OOB) forcing frequency, appear as equilibrium points of the EOM expressed in the rotating frame. Therefore, they are referred to as "stationary" solutions.

In the rest of this chapter, Section 3.1 presents the theoretical background: the EOM are derived using Lagrange's method, nondimensionalised and transformed to the rotating frame. Section 3.1 ends with a plot of the natural frequency map featuring signed natural frequencies [30]. Time simulation setup and the continuation setup are given in Sections 3.2 and 3.3, respectively. Then the results of the continuation runs and time simulations

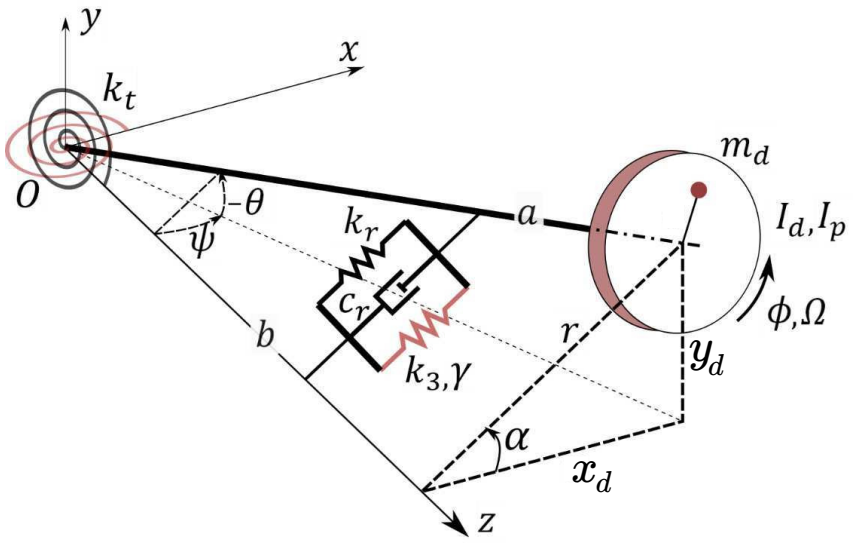


Figure 3.1: A schematic representation of the overhung rotor with cubic stiffness nonlinearity.

are presented in Section 3.4 with an extra validation of the continuation results using time simulations. Conclusions from the results, along with the future work ideas, are given in Section 3.5.

3.1 Theoretical background

3.1.1 Definition of the system

The system subject to analysis here is a two-degrees of freedom (2-dof) overhung rotor system, as shown in Figure 3.1. Here, a and b are distances from point O, up to the disk and the stiffness element, respectively; k_{rb} is the isotropic linear stiffness; k_{3b} is the isotropic cubic stiffness; c_{rb} is the linear damping coefficient; θ, ψ, ϕ are the angles of rotation about x, y, z axes, respectively; Ω is the rotor speed ($\phi = \Omega t$); J_p and J_d are polar and diametral MOIs, respectively. This system is in some ways similar to the contacting system in [3], although the piecewise linear contact is replaced by a smooth cubic stiffness k_{3b}. As an isotropic stiffening effect this cubic stiffness can represent effects such as a bend–stretch coupling due to fixed positions of the bearings, for example, in a pinned-pinned shaft [11]. Note that the derivation of the equations of motion in the next section assumes constant rotational speed, $\Omega' = 0$, and small transverse angles θ and ψ.

3.1.2 Equations of motion

In this section, the derivation of equations of motion is given which takes the transverse angles θ and ψ as the generalised coordinates. The derivation uses Lagrange's energy

method [7].

Kinetic Energy

Kinetic energy resulting from the translational motion of the disk is,

$$T_{tra} = \frac{1}{2} m_d (x_g'^2 + y_g'^2) \tag{3.1}$$

where m_d is the disk mass, $x_g = x_d + \varepsilon \cos\phi$ and $y_g = y_d + \varepsilon \sin\phi$ are the transverse translations of the disk centre of gravity,

$$x_g' = x_d' - \varepsilon\Omega \sin\phi, \quad y_g' = y_d' + \varepsilon\Omega \cos\phi \tag{3.2}$$

and x_d and y_d point to the disk centre of rotation. Derivation with a prime is with respect to dimensional time, t. For small motions, the angles θ, ψ can be defined in terms of x_d, y_d and linearised to give,

$$x_d = a\psi, \quad y_d = -a\theta \tag{3.3}$$

It is convenient to express the rotational kinetic energy with respect to the body-fixed frame of reference, i.e. a coordinate system that is fixed onto the disk. The method requires that the Euler angles be obtained from position with zero angles of rotation by applying rotations. Let the order of rotations be:

1. ψ about y-axis of xyz-coordinate frame, resulting in $x_1y_1z_1$-coordinate frame,
2. θ about x_1-axis of $x_1y_1z_1$-coordinate frame, resulting in $x_2y_2z_2$-coordinate frame,
3. ϕ about z_2-axis of $x_2y_2z_2$-coordinate frame, resulting in $\bar{x}\bar{y}\bar{z}$-coordinate frame which is fixed at the geometric centre of the disk.

for which the corresponding rotation speeds are $\dot{\psi}$, $\dot{\theta}$ and $\dot{\phi} = \Omega$. The transformation matrices needed for these transformations are:

$$\mathbf{R}_\theta = \begin{bmatrix} 1 & 0 & 0 \\ 0 & \cos\theta & \sin\theta \\ 0 & -\sin\theta & \cos\theta \end{bmatrix}, \quad \mathbf{R}_\phi = \begin{bmatrix} \cos\phi & \sin\phi & 0 \\ -\sin\phi & \cos\phi & 0 \\ 0 & 0 & 1 \end{bmatrix} \tag{3.4}$$

These matrices are used to find the angular speeds in the body-fixed frame of reference as,

$$\begin{aligned} \begin{pmatrix} \omega_{\bar{x}} \\ \omega_{\bar{y}} \\ \omega_{\bar{z}} \end{pmatrix} &= \begin{pmatrix} 0 \\ 0 \\ \Omega \end{pmatrix} + R_\phi \begin{pmatrix} \theta' \\ 0 \\ 0 \end{pmatrix} + R_\phi R_\theta \begin{pmatrix} 0 \\ \psi' \\ 0 \end{pmatrix} \\ &= \begin{pmatrix} \theta' \cos\phi + \psi' \sin\phi \cos\theta \\ -\theta' \sin\phi + \psi' \cos\phi \cos\theta \\ \Omega - \psi' \sin\theta \end{pmatrix} \end{aligned} \tag{3.5}$$

where $\omega_{\bar{x}}, \omega_{\bar{y}}, \omega_{\bar{z}}$ are the angular speed with respect to the body-fixed frame. As a result, the rotational kinetic energy can be expressed as,

$$\begin{aligned} T_{rot} =& \frac{1}{2} J_d(\omega_{\bar{x}}^2 + \omega_{\bar{y}}^2) + \frac{1}{2} J_p \omega_{\bar{z}}^2 \\ =& \frac{1}{2} J_d(\theta'^2 + \psi'^2 \cos^2\theta) + \frac{1}{2} J_p(\Omega^2 - 2\Omega\psi' \sin\theta + \psi'^2 \sin^2\theta) \end{aligned} \tag{3.6}$$

Therefore, the total kinetic energy of the disk becomes $T = T_{tra} + T_{rot}$, with small angles θ and ψ:

$$\begin{aligned} T_{tot} =& \frac{1}{2} J_d^o \left(\theta'^2 + \psi'^2\right) + \frac{1}{2} m_d \varepsilon^2 \Omega^2 - m_d a \varepsilon \Omega \left(\psi' \sin\phi + \theta' \cos\phi\right) \\ &+ \frac{1}{2} J_p \Omega^2 - J_p \Omega \psi' \theta \end{aligned} \tag{3.7}$$

where $J_d^o = J_d + m_d a^2$ is the diametral MOI of the disk with respect to point O in Figure 3.1.

Potential energy

All potential energy is due to the linear and nonlinear springs, acting in the radial direction. The conservative force can be expressed as the superposition of the linear and cubic stiffness contributions in the radial direction,

$$f_r = -k_{rb} r - k_{3b} r^3 \tag{3.8}$$

where $r = b\sqrt{\theta^2 + \psi^2}$. Therefore, the potential energy is given by:

$$V_{tot} = -\int_0^r f_r \mathrm{d}r = \frac{1}{2} k_{rb} r^2 + \frac{1}{4} k_{3b} r^4 \tag{3.9}$$

Lagrangian equations of motion

The Lagrangian function $L = T_{tot} - V_{tot}$ is found from Eq. (3.7) and (3.9) as,

$$\begin{aligned} L =& \frac{1}{2} J_d^o \left(\theta'^2 + \psi'^2\right) + \frac{1}{2} m_d \varepsilon^2 \Omega^2 - m_d a \varepsilon \Omega \left(\psi' \sin\phi + \theta' \cos\phi\right) \\ &+ \frac{1}{2} J_p \Omega^2 - J_p \Omega \psi' \theta - \frac{1}{2} k_{rb} r^2 - \frac{1}{4} k_{3b} r^4 \end{aligned} \tag{3.10}$$

The following nonconservative forces are introduced to include the effects of linear damping in the restoring force:

$$\begin{aligned} Q_1 &= -c_{rb} b^2 \theta' \\ Q_2 &= -c_{rb} b^2 \psi' \end{aligned} \tag{3.11}$$

The 2nd type Lagrange equations,

$$\frac{\mathrm{d}}{\mathrm{d}t}\left(\frac{\partial L}{\partial q'_k}\right) - \frac{\partial L}{\partial q_k} = Q_k, \qquad k = 1, 2 \tag{3.12}$$

yield the following equations of motion in the angular coordinates, $\mathbf{w}_{ang} = \{\theta, \psi\}^T$,

$$\begin{aligned} J_d^o\theta'' + J_p\Omega\psi' + c_{rb}b^2\theta' + k_{rb}^2\theta + k_{3b}^4\left(\theta^2+\psi^2\right)\theta &= -m_d\varepsilon a\Omega^2\sin\phi \\ J_d^o\psi'' - J_p\Omega\theta' + c_{rb}b^2\psi' + k_{rb}^2\psi + k_{3b}^4\left(\theta^2+\psi^2\right)\psi &= m_d\varepsilon a\Omega^2\cos\phi \end{aligned} \tag{3.13}$$

3.1.3 Nondimensionalised equations of motion

Nondimensionalisation of EOMs extract the main dynamic features of the system that affects the dynamic response. A nondimensionalisation of Eq. (3.13) is performed by dividing by $k_t = k_{rb}b^2$, which represents the angular equivalent of the radial stiffness k_{rb}, and it is related to the natural frequency of the underlying nonrotating linear system through $\omega_n^2 = k_t/J_d^o$. The nondimensionalisation achieved this way was found intuitive for this system, though it could have been done in different ways (such as through dividing by $k_{rb}a^2$ and keeping the nondimensional time definition as $t := t\omega_n$) with the same resulting nondimensional EOM - this would affect only the dimensional values if the nondimensional values used here are to be dimensionalised back. A new term γ is introduced to express the ratio of linear and cubic restoring forces:

$$\gamma = \frac{k_{3b}b^2}{k_{rb}} \tag{3.14}$$

If one keeps b constant, the ratio γ is a direct measure of cubic stiffness, which is the geometric nonlinearity used here. Thus the nondimensional equations of motion are,

$$\begin{aligned} \theta'' + I_p\Omega\psi' + 2\zeta\theta' + \theta + \gamma\left(\theta^2+\psi^2\right)\theta &= -me\Omega^2\sin\phi \\ \psi'' - I_p\Omega\theta' + 2\zeta\psi' + \psi + \gamma\left(\theta^2+\psi^2\right)\psi &= me\Omega^2\cos\phi \end{aligned} \tag{3.15}$$

where the following identities are used,

$$\begin{aligned} &I_p = \frac{J_p}{J_d^o}, \quad m = \frac{m_d a^2}{J_d^o}, \quad e = \frac{\varepsilon}{a}, \quad \zeta = \frac{c_{rb}b^2}{2I_c^o\omega_n} \\ &t := t\omega_n, \quad (\cdot)' := \frac{(\cdot)'}{\omega_n}, \quad \Omega := \frac{\Omega}{\omega_n} \end{aligned} \tag{3.16}$$

Here $(\cdot)'$ is the derivative with respect to the nondimensionalised time, which is expressed with t again to reduce symbol clutter.

The parameters were chosen to provide a system that can be reasonably compared to the system presented in [3]. Clearly, there is no direct equivalence between the coefficients describing the smooth nonlinearity in this work with the piecewise nonlinear stiffness in [3], but the values chosen give oscillating limit cycles at similar amplitudes found by Zilli. A comparison of the nonlinear functions used in this work and [3] is shown in Figure 3.2.

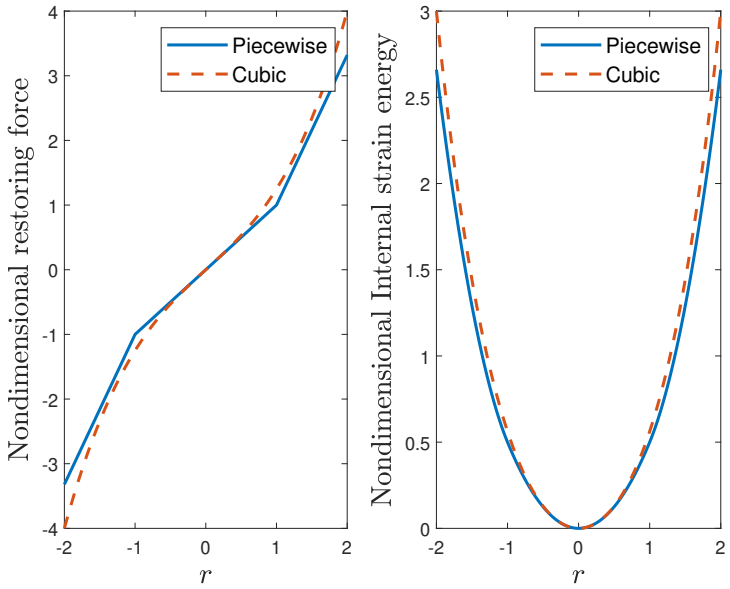


Figure 3.2: (a) Restoring force and (b) potential energy comparison between piecewise contact stiffness model that is used in [3] and cubic stiffness model used here.

The values of the unbalance and nonlinearity parameters in Eq. (3.15) were chosen to get interesting dynamics that is in similar scales to those seen in [3]. The system in [3] makes a trade-off between out-of-balance forcing and clearance, while that is between out-of-balance and cubic stiffness here. The following nondimensional values are selected: $m = 0.9,\ e = 0.353,\ I_p = 0.143,\ \zeta = 0.01$, if not otherwise varied in a continuation run.

3.1.4 Stationary frame equations in displacement coordinates

The displacement of the disk in the stationary frame can be derived from the equation of motion in Eq. (3.15) by simply applying the transformation,

$$\theta = -\frac{x_d}{a}, \quad \psi = \frac{y_d}{a} \tag{3.17}$$

The nondimensionalised stationary frame displacement equations of motion are then obtained as:

$$\begin{aligned} x'' + I_p\Omega y' + 2\zeta x' + x + \gamma\left(x^2 + y^2\right)x &= me\Omega^2\cos\phi \\ y'' - I_p\Omega x' + 2\zeta y' + y + \gamma\left(x^2 + y^2\right)y &= me\Omega^2\sin\phi \end{aligned} \tag{3.18}$$

where $x = x_d/a,\ y = y_d/a$ from Eqs. (3.3) and (3.16). In matrix form with $\mathbf{w} = \{x, y\}^T$, this becomes,

$$\mathbf{w}'' - \Omega I_p \mathbf{J_2} \mathbf{w}' + 2\zeta \mathbf{w}' + \mathbf{w} + \gamma r^2 \mathbf{w} = me\Omega^2 \begin{Bmatrix} \cos\phi \\ \sin\phi \end{Bmatrix} \tag{3.19}$$

where $r = \sqrt{x^2 + y^2} = r/a$ is the nondimensional distance of the centre of the disk from the equilibrium position in the nondimensional form, and $\mathbf{J}_2$ is the skew symmetric matrix,

$$\mathbf{J}_2 = \begin{bmatrix} 0 & -1 \\ 1 & 0 \end{bmatrix}. \tag{3.20}$$

3.1.5 Rotating frame equations of motion

A transformation in ϕ, the rotor angular position, has to be applied in the following form,

$$\mathbf{w} = \mathbf{T}_2 \widetilde{\mathbf{w}} \tag{3.21}$$

where $\widetilde{\mathbf{w}} = \{u, v\}^T$ is the rotating coordinate vector, and the transformation $\mathbf{T}_2$ is,

$$\mathbf{T}_2 = \begin{bmatrix} \cos\phi & -\sin\phi \\ \sin\phi & \cos\phi \end{bmatrix}, \quad \mathbf{T}_2^{-1} = \mathbf{T}_2^T \tag{3.22}$$

During the transformations, the first and second normalised derivatives of $\mathbf{w}$ are needed,

$$\begin{aligned} \mathbf{w}' &= \mathbf{T}_2' \widetilde{\mathbf{w}} + \mathbf{T}_2 \widetilde{\mathbf{w}}', \\ \mathbf{w}'' &= \mathbf{T}_2'' \widetilde{\mathbf{w}} + 2\mathbf{T}_2' \widetilde{\mathbf{w}}' + \mathbf{T}_2 \widetilde{\mathbf{w}}'' \end{aligned} \tag{3.23}$$

where the first and second normalised derivative of $\mathbf{T}$ are,

$$\mathbf{T}_2' = \Omega \mathbf{T}_2 \mathbf{J}_2, \quad \mathbf{T}_2'' = -\Omega^2 \mathbf{T}_2 \tag{3.24}$$

After substituting Eq.(3.23) and Eq.(3.24) to Eq.(3.19), and multiplying on the left by $\mathbf{T}_2^T$, the rotating frame equations of motion are obtained as,

$$\begin{aligned} &\widetilde{\mathbf{w}}'' + \big(-\Omega \mathbf{J}_2 (I_p - 2) + 2\zeta \big) \widetilde{\mathbf{w}}' \\ &\quad + \big(\Omega^2 (I_p - 1) + 1 + 2\zeta \Omega \mathbf{J}_2 \big) \widetilde{\mathbf{w}} + \gamma r^2 \widetilde{\mathbf{w}} = me\Omega^2 \begin{Bmatrix} 1 \\ 0 \end{Bmatrix} \end{aligned} \tag{3.25}$$

The state-space representation is:

$$
\begin{aligned}
q_1' &= q_3 \\
q_2' &= q_4 \\
q_3' &= -\Omega(I_p - 2)q_4 - 2\zeta q_3 + \left(\Omega^2(1 - I_p) - 1\right)q_1 \\
&\quad + 2\zeta\Omega q_2 + me\Omega^2 - \gamma r^2 q_1 \\
q_4' &= \Omega(I_p - 2)q_3 - 2\zeta q_4 + \left(\Omega^2(1 - I_p) - 1\right)q_2 \\
&\quad - 2\zeta\Omega q_1 - \gamma r^2 q_2
\end{aligned} \tag{3.26}
$$

where the components q_{1-4} are defined according to $\mathbf{q} = \{\widetilde{\mathbf{w}}^T, \widetilde{\mathbf{w}}'^T\}^T = \{u, v, u', v'\}^T$.

3.1.6 Natural frequency map

The natural frequency of the underlying linear system changes with rotor speed due to the gyroscopic couplings, or additionally through the dependence of the system parameters such as stiffness and damping on the rotor speed [7]. A natural frequency map, plotting the natural frequency with respect to the rotor speed, can help identify the nonlinear critical speeds [30], where harmonic, subharmonic, or IR occur [11]. The natural frequencies are shown in Figure 3.3, from an eigenvalue analysis of the linear conservative parts of the equations of motion. Figure 3.3a shows a traditional representation of the Campbell diagram, where unsigned stationary frame frequencies are plotted. Figure 3.3b shows the form suggested in [30] where a signed frequency in the rotating frame is presented. Anticlockwise whirling is indicated by a positive value, whereas clockwise whirling is indicated by a negative value. This form is invaluable for highlighting drive speeds where nonlinear resonances can occur due to modal interaction.

Figure 3.3b highlights the 3:1 and 2:1 IR points: An IR in this plot expressed as $m : n$ indicates a commensurate frequency relation of $m\,\omega_f^{rot} = n\,\omega_b^{rot}$. Here ω_f^{rot} and ω_b^{rot} are the main FW and BW frequencies appearing in the rotating frame response, respectively, and link to the stationary frame response frequencies through $\omega_f^{rot} = \omega_f^{sta} - \Omega$ and $\omega_b = \omega_b^{sta} - \Omega$. For example, the 3:1 IR response involves two main frequencies in its frequency spectrum: ω_f^{rot} and $\omega_b^{rot} := 3\,\omega_f^{rot}$, the frequency relation is $3\,\omega_f^{rot} = \omega_b^{rot}$ in the rotating frame or $3\,\omega_f^{sta} - \omega_b^{sta} = 2\,\Omega$ in the stationary frame.

3.2 Time simulation setup

The explicit time marching was performed in MATLAB [156] using the built in `ode45` function. In this study, three cases of simulations were designed: constant initial condition simulations, sweep tests, and starting data generation for AUTO.

For constant initial condition simulations, a randomly generated stationary frame

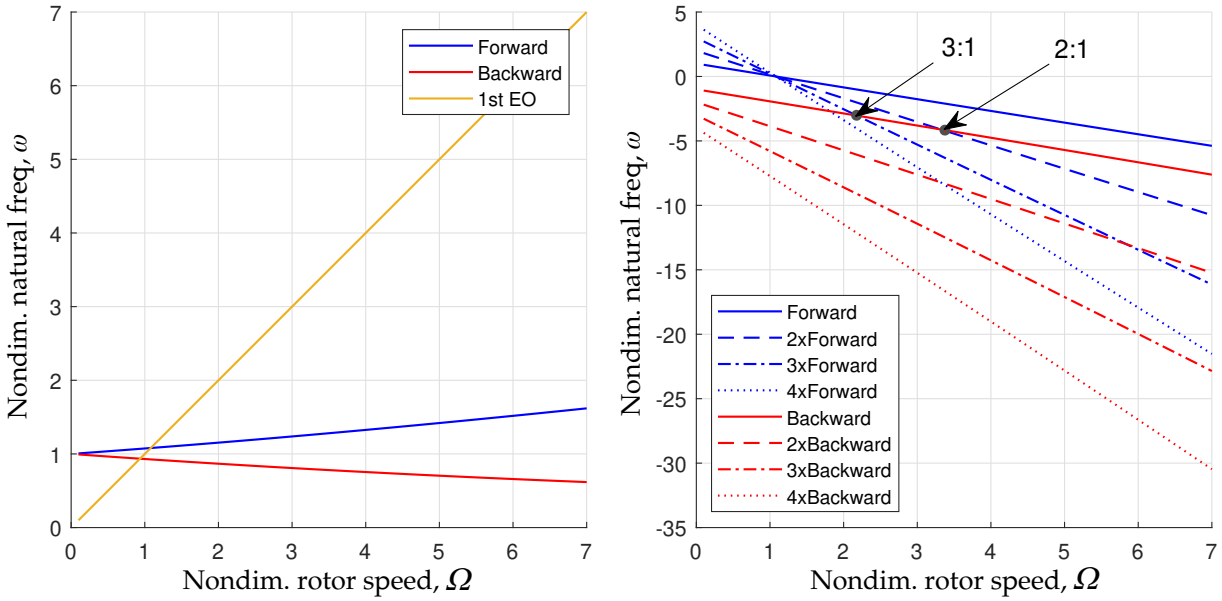


Figure 3.3: The natural frequency map in stationary frame (left), and rotating frame (right). 1st engine order (EO) is also shown in stationary frame frequency map. Whirl frequencies are signed positive and negative for FW and BW whirl, respectively. The 3:1 and 2:1 IR points are marked in the rotating frame.

initial condition in angular coordinates, $\mathbf{z}_{ang}$, was used in the entire drive speed range to initiate the simulation. The initial conditions of the rotating frame simulations, $\mathbf{q}$, were derived from this initial condition using the transformations at $t = 0$ (nondimensionalised time) given by Eq. (3.27),

$$\mathbf{T}_{\theta\psi\to xy} = \begin{bmatrix} 0 & -1 & 0 & 0 \\ 1 & 0 & 0 & 0 \\ 0 & 0 & 0 & -1 \\ 0 & 0 & 1 & 0 \end{bmatrix}, \quad \mathbf{z}_{ang} = \mathbf{T}_{\theta\psi\to xy}\mathbf{z} \tag{3.27a}$$

$$\mathbf{T}_{xy\to uv} = \begin{bmatrix} 1 & 0 & 0 & 0 \\ 0 & 1 & 0 & 0 \\ 0 & -\Omega & 1 & 0 \\ \Omega & 0 & 0 & 1 \end{bmatrix}, \quad \mathbf{z} = \mathbf{T}_{xy\to uv}\mathbf{q} \tag{3.27b}$$

$$\mathbf{q} = \mathbf{T}_{xy\to uv}^{-1}\mathbf{T}_{\theta\psi\to xy}^{-1}\mathbf{z}_{ang} \tag{3.27c}$$

$$\mathbf{z}_{ang} = \{\mathbf{w}_{ang}^T, \mathbf{w}_{ang}'^T\}^T = \{\theta, \psi, \theta', \psi'\}^T \tag{3.27d}$$

$$\mathbf{z} = \{\mathbf{w}^T, \mathbf{w}'^T\}^T = \{x, y, x', y'\}^T \tag{3.27e}$$

$$\mathbf{q} = \{\widetilde{\mathbf{w}}^T, \widetilde{\mathbf{w}}'^T\}^T = \{u, v, u', v'\}^T \tag{3.27f}$$

where the subscripts $\theta\psi$, xy, and uv represent nondimensional coordinates in their respective frames of reference. Simulations were run with damping ratio $\zeta = 0.01$, duration of nondimensional time $t_{end} = 3000$, and the relative tolerance $\epsilon = 10^{-7}$. This relative

tolerance value was adequate as lower tolerances did not show qualitative changes to the converged solution while increasing the computational time. Then, initial conditions were varied randomly to capture the responses of the system with different response types. The *parfor* looping provided by MATLAB was used to utilise 12 CPU threads in parallel.

For sweep tests, the drive speed, Ω, was swept in the range of 0.01-7.01 in the FW and BW directions. Each time a simulation of a particular drive speed finished, the last datum of the trajectory was selected as initial condition for the next Ω. To do this in the rotating coordinates, the last datum was transformed to the stationary frame using Eqs. (3.27b) and (3.27a), and then back to the rotating frame at the next drive speed using Eq. (3.27c). Because of the need of one simulation to finish for the next to start, parallel computing was not available for the sweep tests. Different initial conditions were used until the full synchronous solution families were obtained without jumps to periodic orbits. Also, the asynchronous responses found using the constant initial condition simulations were swept in the same manner. For sweep tests, the same damping ratio ζ, simulation duration t_{end}, and relative tolerance values were used as mentioned above for the constant initial condition simulations. Lastly, the synchronous and asynchronous sweep test results were plotted to form a single bifurcation diagram.

Starting data for AUTO was created in the rotating frame for different ζ; the duration of simulation was increased as the damping ratio ζ, was decreased, to ensure that the transient decayed within at most half the simulation duration. The time and state variable data that belong to one single period of the converged periodic orbits were stored in a .dat file to be used as starting periodic orbits in AUTO runs. For stationary solutions in the rotating frame, the last data points in the time series generated by the time simulations were used as initial solution input in AUTO. More details of .dat file generation can be found in the Appendix A.2.

3.3 Numerical continuation setup

The background of the numerical continuation method is given in Section 2.3, including how the *AUTO files* are used.

Continuation solution process

The flow of runs is shown in Table 3.1. The references to the single- and double-loop (SL and DL, respectively) families in Table 3.1 indicate the shape of the orbits corresponding to the 3:1 and 2:1 IRs, respectively, as seen in Figure 3.4.

Damping ratio, ζ, was selected as the main continuation parameter because the level of damping might explain the rotor speed range where the asynchronous solutions could be expected, e.g. earlier in the range and more likely to appear particularly with low damping

Table 3.1: Flow of continuation runs in Python CLUI file of AUTO setup.

Solution type	**Parameter**	**Limits**	**Methods**
Stationary, synchronous (SS)	m, mH	0.0-0.9	n/a
	γ, gamma	0.0-0.25	n/a
	Ω, Omeg	0.0-7.01	n/a
	Ω, Omeg	0.0-7.0	A1 and B1
Periodic, single-loop (SL)	Ω, Omeg	0.0-7.0	A2, B2 and C2
Periodic, double-loop (DL)	Ω, Omeg	0.0-7.0	A3

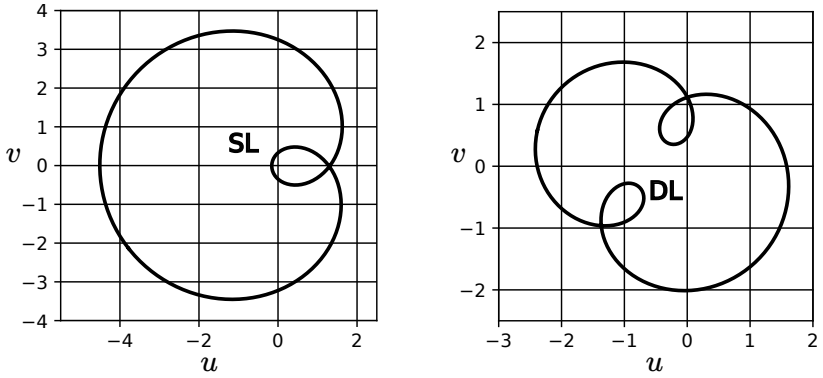


Figure 3.4: One sample from each of the periodic solution families, referred to as SL (left) and DL (right) solutions corresponding to 2:1 and 3:1 IR conditions in the rotating frame.

(see in Section 3.4). In Table 3.1, A, B and C are different ways the continuation was carried out:

A: Continuation of stationary solutions is initialised from the equilibrium at zero ($\mathbf{q} = [0\ 0\ 0\ 0]^T$). Continuation is performed through single parameter continuation of m, γ and Ω from zero to their design values, respectively. Simulation results are used to initialise the periodic solutions continuation in Ω. All of these continuation runs are done with $\zeta = 0.01$. Then, continuation in ζ is performed from a selected point of the solution family. After, from the data sampled at various ζ during this ζ-continuation, new solution branches are found with continuation in Ω.

B: Only time-simulation starting data (in the form of a .dat file) is used in Ω-continuation for different ζ values.

C: Folds in Ω are continued in ζ to trace the effect of the change of ζ.

and the cases 1, 2 and 3 are,

1: Continuation for synchronous solutions,

2: Continuation for SL solutions,

3: Continuation for DL solutions.

3.4 Results and Discussion

Results of the numerical continuation are presented first in Section 3.4.1; then in Section 3.4.2 the time simulation data used to validate these results and provide starting solutions is discussed.

3.4.1 Numerical Continuation

Figure 3.5 shows the bifurcation diagram in nondimensionalised amplitude versus rotor speed, for all of the solutions from the different ζ values investigated. Labels SS, DL and SL in the figure refer to the solution families of synchronous, DL asynchronous, and SL asynchronous solutions, respectively. Synchronous and asynchronous solutions are also referred to as stationary and periodic as they appear in the rotating frame since only the rotating frame equations of motion were used in AUTO.

For the lower ζ, the SS branch exceeds the limit of the plot. A close-up view of the SS branch is shown in Figure 3.5d. For the increased damping values, the synchronous peaks merge and form a stiffened nonlinear response peak. As the damping is further increased, the unstable solutions, which are shown with dashed lines, are lost. At higher drive speeds the amplitude of SS branch decreases very slightly with increased damping.

Figure 3.5 also shows that there is a region of nondimensionalised rotor speed between $\Omega = 1.5-2.3$ where jumps would only happen between the synchronous solutions. Chipato et al. [31] and Zilli et al. [3] also documented this phenomenon in their overhung models with frictionless contact definitions.

As damping increases, the fold at the lower end of both the DL and SL solution branches moves higher in terms of both amplitude and drive speed, with the SL branch moving beyond the range of drive speeds considered at higher damping values. The various ζ value sampling of periodic solution families was done through the continuation of the $\zeta = 0.01$ orbits in AUTO, for Methods A2 and A3 (see Table 3.1): Time simulation orbits for SL at $\Omega = 7.01$ and DL at $\Omega = 3.00$ both with $\zeta = 0.01$ were continued in ζ and the orbits sampled at different ζ were continued in Ω to obtain the bifurcation diagram in Figure 3.5. The ζ-continuation results are given in Figure 3.6. The higher damping ratio limit to the existence of SL within the given BD range and global existence for DL are $\zeta = 0.0828$ and $\zeta = 0.0117$, respectively. This shows that the increase of damping in the system would first eliminate DL solutions. This information is useful when a case produces 3:1 IR response: potentially, 2:1 response is also present in or out of the operational range.SL solution families show that the increased ζ shrinks and eliminates this type of periodic solution family out of the investigated drive speed region (see Figure 3.5e). This can be observed in Figure 3.5e where the brown, teal and cyan coloured branches correspond to ζ of 0.050, 0.075, and 0.082, respectively. Note that in this figure the dark blue dashed line shows the fold continuation (Method C2) of the SL

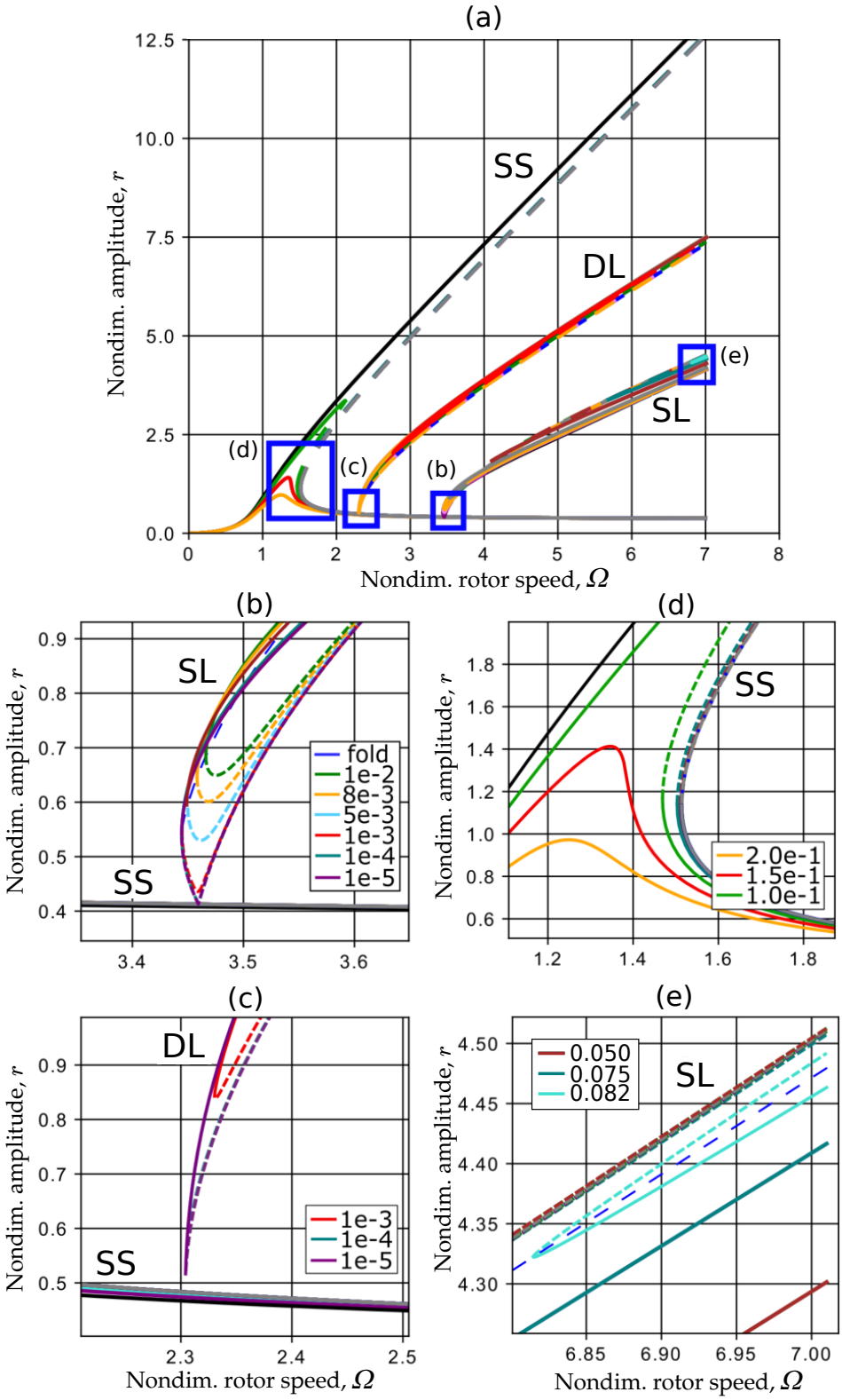


Figure 3.5: (a) The bifurcation diagram generated from AUTO using the autonomous rotating frame equations of motion. Both stationary (synchronous) and periodic (asynchronous) solutions are included. The zoom views: (b) DL solutions. (c) SL solutions. (d) Synchronous resonance region. (e) The cyan coloured SL solution with $\zeta = 0.082$. In the figure, 'SS', 'DL', and 'SL' stand for synchronous, DL and SL solution families, respectively. The legends show ζ values for the branches with corresponding colours.

solutions. Increased ζ for DL branches, however, kept these solution families as isolated amplitude circles within the drive speed region of interest until the damping ratio is above the 0.0117 limit.

Figure 3.5b and 3.5c shows that the decrease of damping extends the left-hand side of the periodic solution families downward, closing into the synchronous solutions at $\Omega = 2.31$ and $\Omega = 3.46$ for DL and SL solution families, respectively. Figure 3.5b also shows the locus of folds as ζ is freed in addition to rotor speed. At the place where the periodic and stationary solutions approach each other in amplitude, the periodic solution branches become quite sharp, making it difficult to perform continuation. As a result, the SL solution family for $\zeta = 10^{-5}$ converged only with increased number of Newton-Chord correction iterations. The results are seen in Figure 3.7.

The Campbell diagram of the linear, undamped system (Figure 3.3) shows possible locations of the IRs at $\Omega = 1.81$ for 4:1, $\Omega = 2.18$ for 3:1, $\Omega = 3.33$ for 2:1, $\Omega = 5.84$ for 3:2. Therefore, DL solution families must be related to 3:1 IRs, and SL periodic solutions must arise from 2:1 IRs. This fact is expressed as the 'entrainment' of the linear n:m motion by [85]. To investigate the relationship of the 3:1 IR to DL families, the fold with $\zeta = 10^{-5}$ was continued in a fold-continuation scheme in eccentricity as an extra continuation parameter to the drive speed, Ω. The results are presented in Figure 3.8. A decrease of nondimensional eccentricity, e, from 0.353 to 0.092 made DL solution family's left tip frequency to go down to 2.19, much closer to the 3:1 frequency of 2.18 from the Campbell diagram (Figure 3.3) although damping needs to be decreased to achieve further closeness. This is explained as follows. As the forcing is decreased, the amplitude reduces, thereby reducing the stiffening. Therefore, the IR's underlying frequencies move closer to their linear values. As a result, the solution moves closer to the critical drive speed predicted using the Campbell plot (Figure 3.3). However, decrease in the damping has to accompany decrease in the forcing so that the IR interaction is not damped out. In the vicinity of these points, any synchronous response would take very little disturbance to move onto and beyond the unstable part of the periodic solutions, possibly converging onto the stable limit cycle. It is important to note, however, that the numerical continuation cannot find conservative solutions starting from the nonconservative IR response as the conservative system generate degenerate IR solutions without a defined branch (see Section 6).

These results compare to those of contact nonlinearity studies. For example, in Ref. [30] on a similar 2-dof model with piecewise-linear stiffness contact model, the periodic solutions were observed to start in a similar range after $\Omega = 3.5$, with similar amplitudes for a 2:1 IR. Zilli et al. [3] also observed the intermittent contact motions after $\Omega = 3.4$.

No asynchronous response under contacting level amplitude can be seen in the models with a clearance because the underlying system is linear. However, the cubic stiffness model here removes this limit and bridges the gap between the synchronous and asynchronous responses. This possibly reveals the transition from synchronous to asyn-

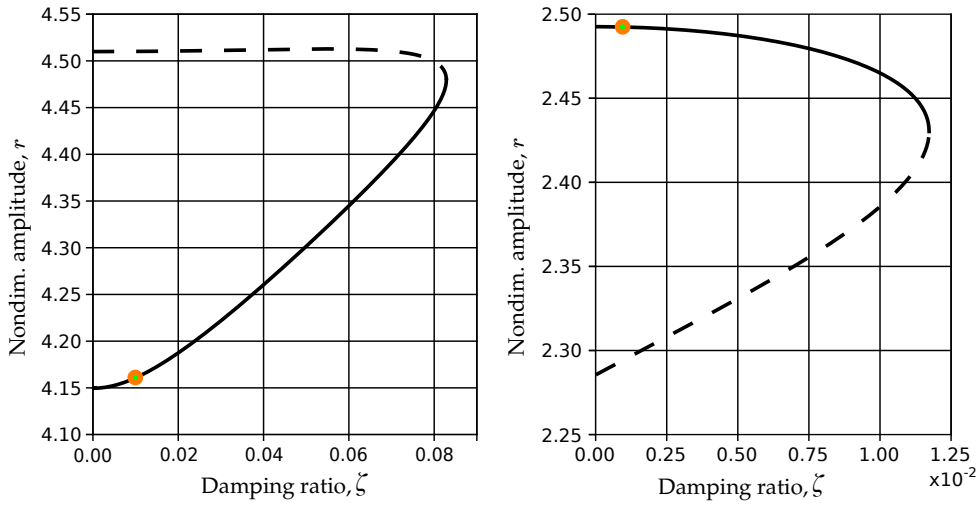


Figure 3.6: Continuation in ζ of SL periodic solutions with $\Omega = 7.01$ (left) and DL periodic solutions with $\Omega = 3.00$ (right). Dashed lines indicate unstable response. Orange dots show the start of the continuation run which was continued forward and backward to complete the branch.

chronous response, as discussed above. As a result, the stiffening effect that is seen in the contact-featuring studies is available at all amplitudes in the cubic stiffness continuous stiffness model.

The present isotropic cubic stiffness model did not produce period doubling in the continuation runs, which is an identified route to chaos in systems with stiffness asymmetry [14, 54]. Off-centring due to gravity also resulted in the chaos in [31]. Li and Païdoussis [142] reported the quasi periodic route to chaos in the presence of rubbing friction, which is not a part of the model in this study, although we observe quasi-periodicity. These indicate that the isotropic cubic stiffness model used here does not present a way to explain the chaotic behaviour. Thus, the numerical simulations with various initial conditions did not results in chaos. However, a homotopy parameter can be used to include the friction, gravity, contact (e.g. via hyperbolic tangent functions), making the cubic stiffness a base to explore these responses.

Contrary to the systems with impact definitions in the contact [45, 34], the smoothness of the trajectories of the cubic stiffness model is not broken. Despite that the soft nonlinearity with the cubic stiffness here generated the 2:1 and 3:1 IRs, Wang et al. [25] pointed out the richness of IR response in the higher contact stiffness cases, observing IRs of order up to 7:1. Also the effect of contact dissipation cannot be seen in the present model, on which Shaw et al. [4] noted that stiffer, dissipative contact definitions eliminated most of the sustained intermittent bouncing cycles, similar to damping here. Friction alone was linked to the more complicated dynamics in other literature [24, 61, 31].

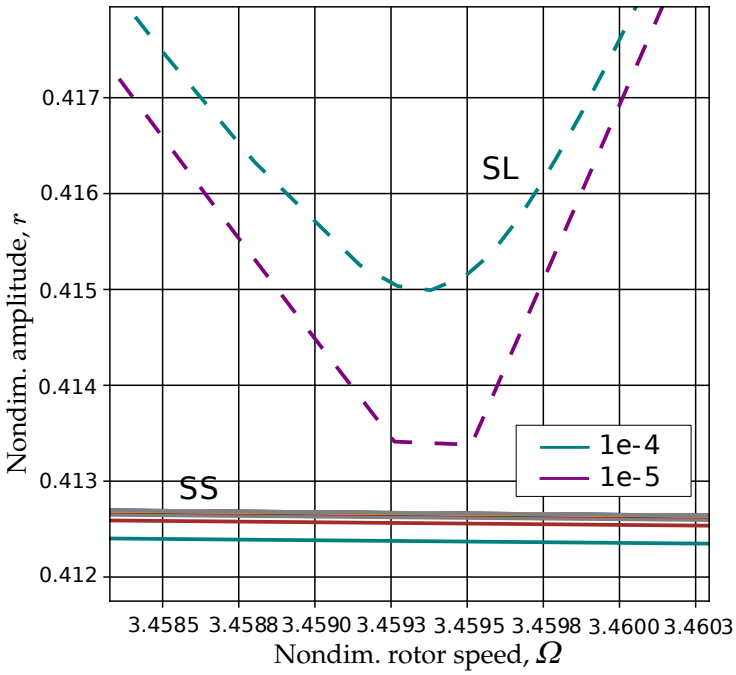


Figure 3.7: Zoom view at the bifurcation diagram where stationary and SL periodic solutions meet in the lower-ζ extreme. Teal and purple dashed lines show $\zeta = 10^{-4}$ and 10^{-5}, respectively, and "SS" stands for synchronous solutions. The stacked lines below the 0.413 amplitude level show the synchronous branches where higher amplitudes correspond to lower ζ.

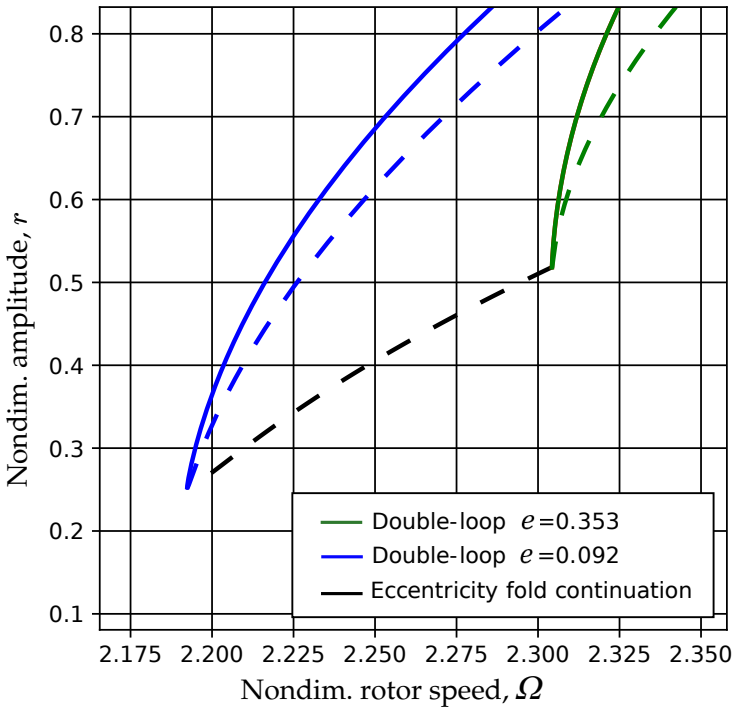


Figure 3.8: Fold continuation in order to decrease the severity of eccentricity parameter on DL periodic solution family with $\zeta = 10^{-5}$.

3.4.2 Time simulations

Constant initial condition

The simulations with constant initial conditions in the entire rotor speed range yielded different bifurcation diagrams. For convergence, the time response was checked visually to ensure that the transient response decays by half of the simulated time. The 12 thread CPU parallelisation decreased the simulation time by 5 times compared to no parallelisation. Figure 3.9 shows the response of the system to the initial conditions $[0.0, 0.6, -1.246, 0.0]^T$ in angular coordinates (physical coordinates). Asynchronous solutions appear quasiperiodic in the stationary frame and periodic in the rotating frame. It can be noted here that the quasiperiodic solutions disappear at higher drive speeds, while easily achieved in the $\Omega = 3.5 - 5.0$ region. Nonetheless, the brute force bifurcation diagrams do not show the periodic solution families at the exact place they are expected from the Campbell diagram, because the time simulations only show $\zeta = 0.01$ data, which appear with higher amplitudes, and hence with higher nonlinearity.

The DL orbits were only discovered as the initial condition was increased in amplitude (Figure 3.9). With the greater initial energy due to higher magnitude position and/or speed, the orbits settle more readily onto the asynchronous orbits, which were recorded in the transient study in Ref. [3].

Every sample on the stroboscopic Poincaré section of Figure 3.9 happens at the time when the rotor angle is zero. Also, the rotating frame trajectory is periodic. Therefore, the Poincaré dots in Figure 3.9b and 3.9c in the stationary frame overlap the rotating frame trajectory.

In order to extract the most significant features of the complete bifurcation plot, a number of random initial conditions in the order of 100 was selectively merged and illustrated in Figure 3.10a. The stable synchronous high- and low-amplitude solution families, as well as two distinct asynchronous solution families can be identified. The difficulty of finding the DL orbits was noted in the process.

Lyapunov exponents are not employed to diagnose the response as the time simulations did not produce chaotic behaviour which is not the focus of this thesis, though [13] used it for diagnosing chaos. Additionally, the synchronous and asynchronous solutions are clearly identifiable through stroboscopic Poincaré sections or by the former appearing as equilibrium points and the latter as periodic orbits in the configuration space of the rotating frame, respectively.

Sweep

Figure 3.10b shows the forward and backward sweep test results as a bifurcation diagram for both synchronous and asynchronous responses. Once the different solution families are identified with constant initial condition simulations (Figure 3.10a), it is more likely

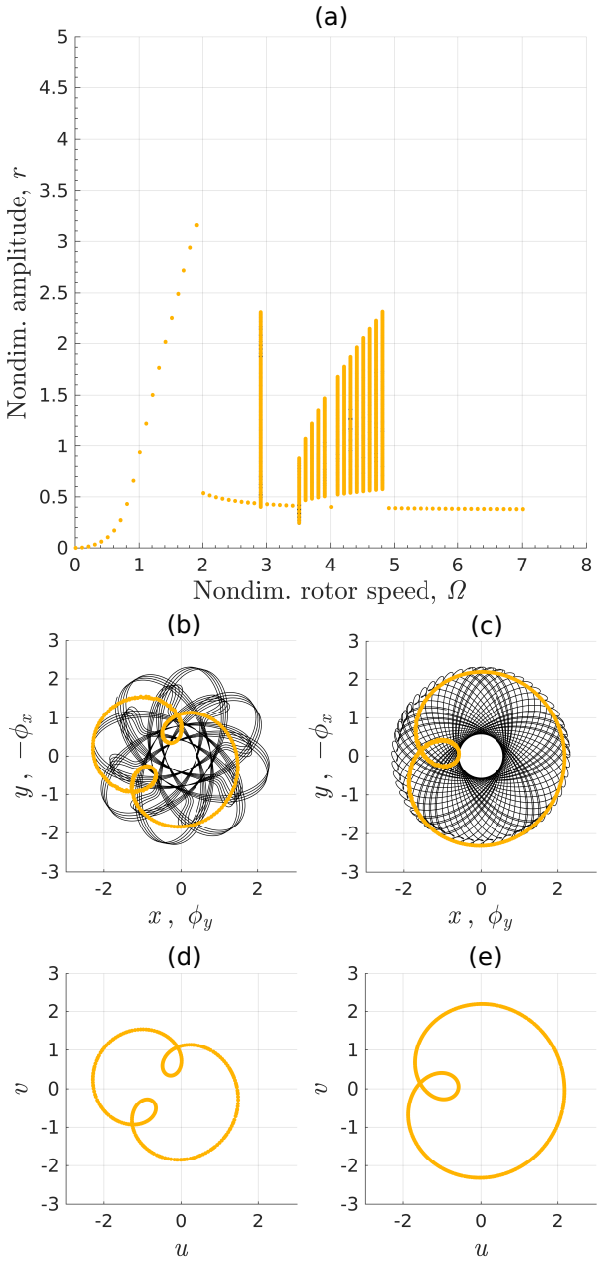


Figure 3.9: (a) Bifurcation diagram for the angular equations of motion with initial condition $[0.0, 0.6, -1.246, 0.0]^T$. (b) and (d) show the DL response from the perspective of stationary and rotating frame of references, respectively. (c) and (e) show SL response in stationary and rotating frame, respectively. The orange dots show the stroboscopic Poincaré sampling at the drive speed after the convergence.

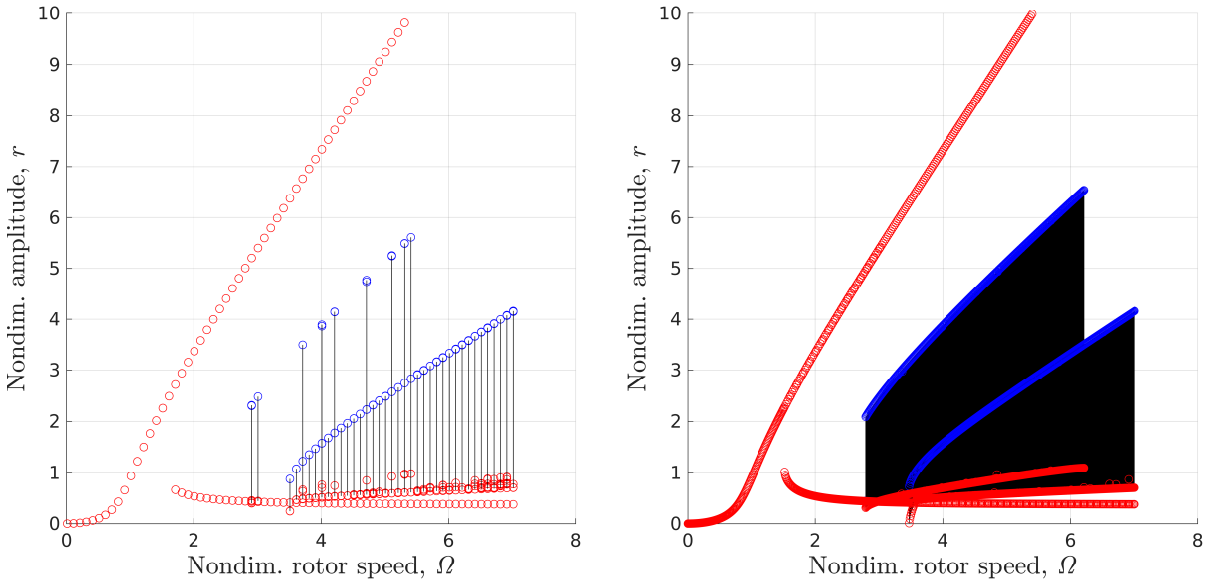


Figure 3.10: Left: Bifurcation diagrams from constant initial condition simulation results. Right: Stepped sweep tests performed by incrementing Ω on the synchronous and asynchronous responses. Blue and red circles show highest and lowest amplitude points of the trajectories, respectively, which overlap for the synchronous solutions.

for sweep tests to discover a given family of solutions (Figure 3.10b). Also note that in backwards sweep and periodic solution sweep tests, the unstable parts of the solution families are not seen, which are clearly visible in the AUTO numerical continuation results.

In the sweep tests the next increment in the same family of solutions converges with less transient motion, thereby making the extraction of system response quicker than each time simulation in the case of constant/random initial condition simulations. However, the advantage of multi-core processors cannot be utilised because in sweep test the last point of the trajectory of the previous step is required in the next step. Nonetheless, in terms of computational speed, time simulations cannot compare to numerical continuations: for example, the computation of Figure 3.5 took under 10 minutes, while time for the simulations easily reached an hour, where AUTO's multiprocessor capability cannot be ignored although it used only 4 threads.

With these constant initial condition and sweep test results, it is clear that the numerical continuation is computationally more efficient and reveals more of the system response characteristics if the periodic and stationary solution families of the rotordynamic system are of interest.

MATLAB – AUTO validation

The SL orbits were compared to those of AUTO for validation of both simulations and the continuation with each other. An unstable SL periodic orbit at $\Omega = 3.47$ with $\zeta = 0.01$, was given to MATLAB as initial condition for `ode45` simulations. Results are illustrated

in Figure 3.11. The trajectory in the `ode45` simulations stayed on the unstable periodic orbit (UPO) for the first few cycles, then diverged from this UPO to converge onto the stable periodic orbit (SPO). The diverging speed is much higher for the higher amplitude case (Figure 3.12), where also the greater rotation of the orbit is visible. A close match was obtained between the two solution methods with respect to the stable and unstable orbits. As seen in Figure 3.11 and 3.12, the absolute value of one Floquet multiplier is greater than unity for the unstable orbits.

3.5 Conclusion

This study considered the responses of an overhung rotor with an isotropic cubic stiffness. Direct application of continuation method on the equations of motion was setup by orthogonal collocations method in AUTO and validated with time simulations. The following conclusions were drawn:

1. It was shown in the present work that the previously reported bouncing cycle phenomenon for the models of hard impact and compliant snubbing rings can also be observed with a geometric nonlinearity of cubic stiffness replacing contact interaction definitions.
2. If a discontinuous stiffness was defined, then the bouncing cycles would not be present under the clearance level amplitude, due to the rotor not experiencing nonlinearity below this level. On the contrary, nonlinearity is present in all amplitude levels for the cubic nonlinearity; thus, the bouncing cycle amplitudes could get very close to the synchronous solutions.
3. Depending on the level of damping, the periodic orbit region can expand and shrink. Especially for higher ζ damping ratio values, the periodic orbits' region vanishes from the nondimensionalised rotor speed region of interest.
4. As damping tends to zero, the lower limit of drive speeds that generate these responses tends towards the critical speed predicted with linear frequencies in the natural frequency map. Decreasing the eccentricity level (or out of balance mass) makes this match closer.
5. As damping tends towards zero, the asynchronous branches approach the synchronous branch. It might be inferred that the gap closes asymptotically as ζ and oscillation amplitude approaches zero. However, synchronous solution family does not produce a branch point that links the asynchronous solutions to synchronous ones.
6. This indicates that this region requires very little disturbance to jump to the periodic orbits because of the closeness of the unstable side of periodic solutions to the stable

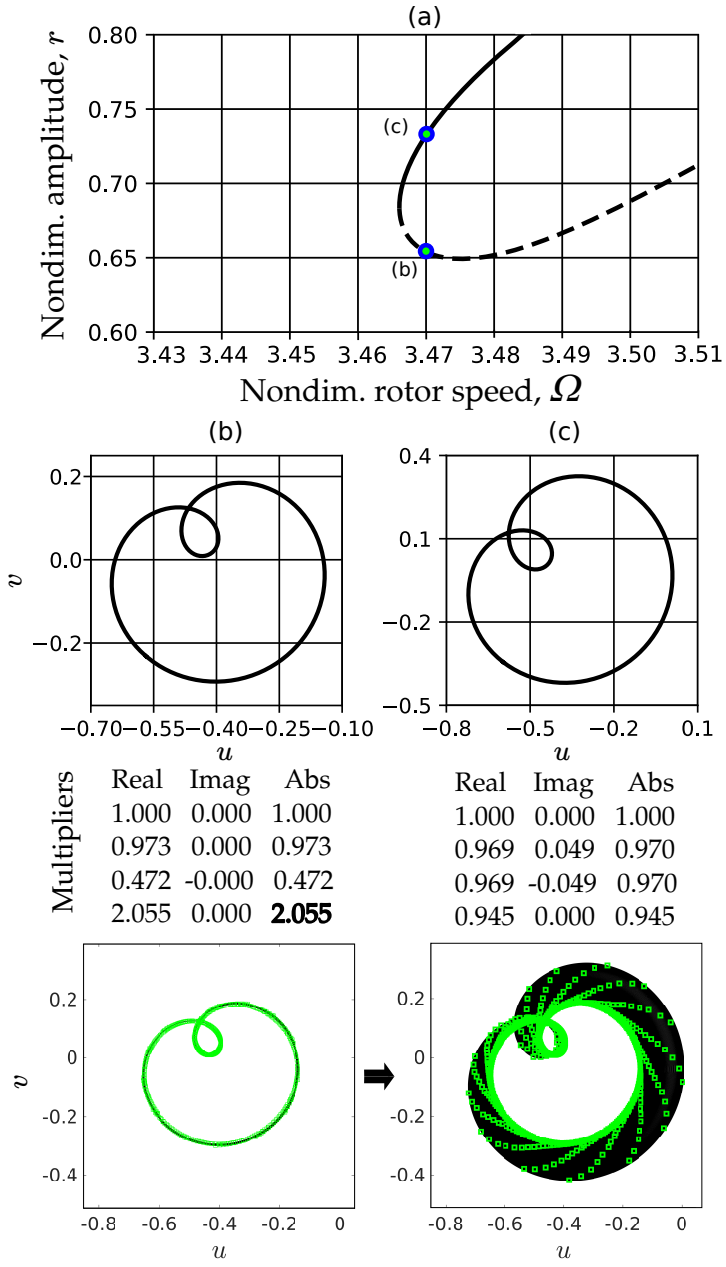


Figure 3.11: Validation of SL orbits with $\zeta = 0.01$ from AUTO and MATLAB. The bottom row shows the trajectory history (from left to right) during the transition from UPO to SPO at $\Omega = 3.47$. The green squares are stroboscopic Poincaré sampling of the data at the rotor speed. Floquet multipliers are shown to indicate the stability.

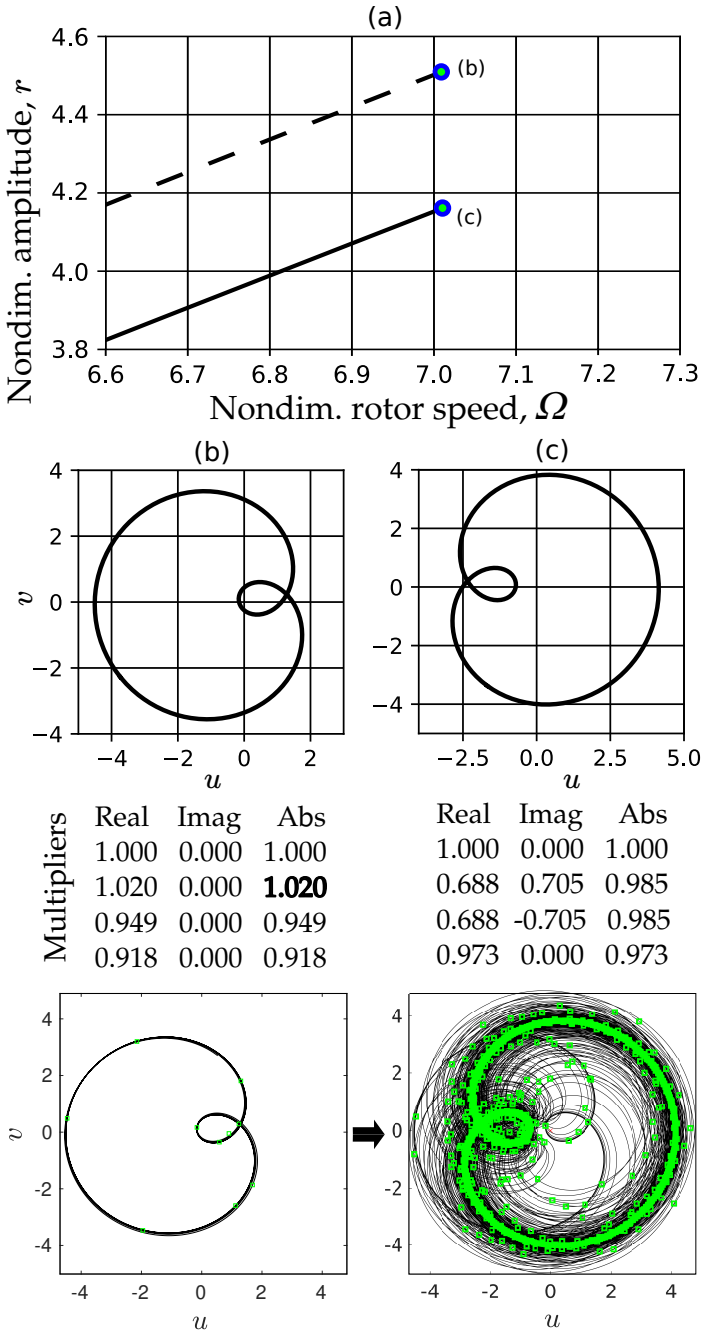


Figure 3.12: Validation of SL orbits with $\zeta = 0.01$ from AUTO and MATLAB. The bottom row shows the trajectory history (from left to right) during the transition from UPO to SPO at $\Omega = 3.47$. The green squares are stroboscopic Poincaré sampling of the data at the rotor speed. Floquet multipliers are shown to indicate the stability.

synchronous solutions.

7. As the results were compared to the previous studies featuring non-smooth contact models, the synchronous solution jump, and the nondimensional rotor speed where periodic solutions first appeared were reproduced with the cubic stiffness model adopted here.

The application of numerical continuation theory directly to the system equations proved practical and accurate in this study when compared to the brute force bifurcation diagrams. The type of low order model studied, with a simple smooth stiffening nonlinearity, is also relevant to many rotating machines with flexible shafts, that may exhibit bend stretch coupling, or overhung rotors that may show nonlinear displacements in the case of large out of balance force.

The effectiveness of this method on more complex industrial models still needs to be answered. Therefore, this method can be projected to rotor-stator contact models that define contact with functions that are more representative of contact. Particularly, a smooth nonlinearity in the definition of a complex model can be altered with the help of a homotopy parameter to a non-smooth contact definition such as hyperbolic tangent function, which is the subject of the next chapter (Ch. 4). Thus, as the current study suggests, the time simulations of the smooth nonlinearity can be used to obtain the bifurcation diagrams of the smooth-contact model, saving computational time compared to the more demanding simulations with discontinuity. Moreover, due to the close resemblance of the intermittent response patterns in this work to those in previous stiffness discontinuity studies, the effect of the time spent during contact on the response patterns is another point of interest.

Chapter 4

Continuation Analysis of Overhung Rotor Bouncing Cycles with Smooth and Contact Nonlinearities

The results from a wide range of stiffness ratios suggests that intrinsically smooth nonlinearities could generate similar responses to discontinuous stiffness models of the rotor-stator interaction. With this inspiration, in Ch. 3 the softer extreme of the contact phenomenon was investigated by replacing the snubber ring stiffness by geometric nonlinearity, namely, a comparable cubic stiffness in a 2-dof overhung rotor with gyroscopic effects (the *cubic Zilli system* [3]) .

In this chapter, in line with the research interest in Section 1.6, to explore the characteristics of the system with contact, homotopy continuation (e.g. see [71]) is applied from these cubic stiffness solutions to a hyperbolic tangent function representing a smooth approximation to the discontinuous stiffness as a contact definition.

The motivation for using homotopy is to allow a set of solution branches for a relatively inexpensive smooth nonlinearity, to form the template for the solutions of stiffer nonlinearities representing contact. This speeds up the process of obtaining a bifurcation diagram for the harsher nonlinearity, particularly in comparison to the brute force simulation methods commonly used. It also highlights the similarity of contacting systems to smoothly stiffening nonlinear systems, where the solution branches show a similar topology that is largely determined by the underlying linear gyroscopic system. The benefits would become even greater for systems with a higher number of degrees of freedom. Aside from this nonlinearity homotopy, the continuation method is also applied to traverse the parameter space.

By using a smooth approximation for hard contact, the continuation method does not need additional considerations for updating forces, as needed in many HBM-continuation schemes (see e.g. [74]). This allows for seamlessly using AUTO where its time discretisa-

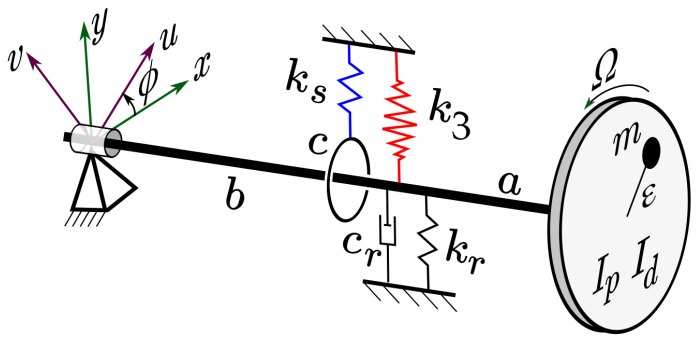


Figure 4.1: Schematic drawing of the mechanical system used. In the figure c_r is the damping coefficient, k_r is the linear rotor stiffness, k_s is the stator stiffness that engages after a clearance c, k_3 is the cubic stiffness. All stiffness and damping components are isotropic. The rotating frame axes has an angle of $\phi = \Omega t$ with the stationary frame axes.

tion mesh adapts to the harsher nature of the tanh function accurately.

In the following, Section 4.1 outlines the equations of motion and the setup for the continuation runs. Section 4.2, presents the results with relevant discussion of various cases of damping and unbalance excitations, and the effectiveness of the tanh-contact representation is discussed. In Section 4.3, conclusions are drawn both on the method and the rub-impact system analysed.

4.1 Theory and Methods

Below, first the equations of motion (EOM) is explained where the homotopy parameter is used. Then, smooth approximation of contact definition adopted is explained. A certain flow of continuation runs are proposed later for effectively using the numerical continuation method given in Section 2.3 on both the homotopy parameter and the damping and eccentricity (forcing) parameters.

4.1.1 Equations of motion

Eq. 4.1 shows the dimensional nonlinear equations of motion of the 2-dof overhung rotor in the rotating coordinate frame (Figure 4.1). The reason why the rotating frame was selected is that the investigated bouncing solutions are quasiperiodic in the stationary frame, yet periodic in the rotating frame.

$$\frac{J_d^o}{a^2}\widetilde{\mathbf{w}}'' + \left(-\omega\mathbf{J}_2\frac{J_p - 2J_d^o}{a^2} + c_r\left(\frac{b}{a}\right)^2\mathbf{I}\right)\widetilde{\mathbf{w}}' + \left(\omega^2\frac{J_p - J_d^o}{a^2}\mathbf{I} + k_r\left(\frac{b}{a}\right)^2\mathbf{I} + c_r\left(\frac{b}{a}\right)^2\omega\mathbf{J}_2\right)\widetilde{\mathbf{w}} + \mathbf{b}_{nl} = m_d\varepsilon\Omega^2\begin{Bmatrix}1\\0\end{Bmatrix} \tag{4.1a}$$

$$\mathbf{b}_{nl} = (1-\kappa)\mathbf{b}_{cubic} + \kappa\mathbf{b}_{snub} \tag{4.1b}$$

$$\mathbf{b}_{cubic} = k_3\left(\frac{b}{a}\right)^4 r_c^2\widetilde{\mathbf{w}} \tag{4.1c}$$

$$\mathbf{b}_{snub} = \frac{1}{2}\left(\tanh\left(K\left(\frac{r_c b}{a} - c\right)\frac{1}{c}\right) + 1\right)k_s\left(\frac{b}{a}\right)^2\left(1 - \frac{1}{r_c}\frac{ca}{b}\right)\widetilde{\mathbf{w}} \tag{4.1d}$$

where

- J_p is the polar MOI of the rotor,
- $J_d^o = J_d + ma^2$ is the diametral MOI with respect to the centre of the frame of reference,
- b is the position of all stiffness and damping elements on the rotor (Figure 4.1), a is the overhung distance,
- ε is the eccentricity of the disk,
- $\widetilde{\mathbf{w}}$ is the dimensional vector of positions in the rotating frame,
- $r_c = \widetilde{\mathbf{w}}^T \cdot \widetilde{\mathbf{w}}$ is the amplitude of the position of the centre of the disk,
- K is the tanh function steepness,
- k_3 is the cubic stiffness,
- k_r is the radial linear stiffness,
- ω is the rotor speed,
- $\mathbf{b}_{nl}$ is the weighted sum of the nonlinear restoring forces from snubber ring stiffness and the cubic stiffness elements,
- c is the clearance.

If Eq. 4.1 is multiplied by $\frac{1}{k_r}\frac{a}{bc}$, the following nondimensional equations of motion can be obtained, which was derived in more detail in Ch. 3 except the tanh restoring force,

$$\widetilde{\mathbf{w}}'' + (-\Omega\mathbf{J}_2(I_p - 2) + 2\zeta\mathbf{I})\widetilde{\mathbf{w}}' + (\Omega^2(I_p - 1)\mathbf{I} + \mathbf{I} + 2\zeta\Omega\mathbf{J}_2)\widetilde{\mathbf{w}} + \mathbf{f}_{nl} = me\Omega^2\begin{Bmatrix}1\\0\end{Bmatrix} \tag{4.2a}$$

$$\mathbf{f}_{nl} = (1-\kappa)\,\mathbf{f}_{cubic} + \kappa\mathbf{f}_{snub} \tag{4.2b}$$

$$\mathbf{f}_{cubic} = \gamma r^2\widetilde{\mathbf{w}} \tag{4.2c}$$

$$\mathbf{f}_{snub} = 0.5\,(\tanh\,(K\,(r-1)) + 1)\,\beta_s\,(1 - 1/r)\,\widetilde{\mathbf{w}} \tag{4.2d}$$

The following identities and redefinitions appear when transforming from Eq. 4.1 to 4.2,

$$\begin{gathered}\mathbf{J}=\begin{bmatrix}0 & -1\\ 1 & 0\end{bmatrix},\ \mathbf{I}=\begin{bmatrix}1 & 0\\ 0 & 1\end{bmatrix},\ I_p=\frac{J_p}{J_d^o},\ \gamma=\frac{k_3}{k_r}c^2,\ \beta_s=\frac{k_s}{k_r},\ \zeta=\frac{c_r b^2}{2J_d^o\omega_n},\ m=\frac{m_d a^2}{J_d^o}\\ (\cdot)'=\frac{(\cdot)'}{\omega_n},\ \Omega=\frac{\Omega}{\omega_n},\ \omega_n^2=\frac{k_r b^2}{J_d^o},\ \bar{c}=\frac{ca}{b},\ \widetilde{\mathbf{w}}:=\widetilde{\mathbf{w}}\frac{1}{\bar{c}},\ r=\frac{r_c}{\bar{c}},\ e=\frac{\varepsilon}{\bar{c}},\ t:=t\omega_n\end{gathered}\tag{4.3}$$

where

- $\widetilde{\mathbf{w}}$ is redefined to be the nondimensional position vector in the rotating frame to decrease symbol clutter,
- Ω is the nondimensional rotor speed,
- ζ is the damping ratio,
- I_p is the nondimensional polar MOI,
- m is the nondimensional mass,
- e is the nondimensional distance of the eccentric centre of mass,
- β_s is the nondimensional measure of snubber-ring stiffness,
- γ is the nondimensional measure of cubic stiffness,
- r is the nondimensional vibration amplitude in the rotating frame, $r^2=\widetilde{\mathbf{w}}^T\cdot\widetilde{\mathbf{w}}$,
- K is the tanh function steepness parameter.

The definition of the restoring force as a weighted sum of the two nonlinearities allows one to incorporate a new parameter, κ, ranging from 0 to 1 (Eq. 4.2). Table 4.1 gives the values used to obtain the results in the next section.

Contact definition

The numerical continuation method in AUTO [84] uses adaptive mesh formulation for the discretisation of the periodic solution. In order to use the adaptive mesh formulation with non-smooth systems accurately and without failures, AUTO requires smoothly approximating non-smooth functions where the solution has non-smooth derivatives [84]. Therefore, for seamlessly using AUTO, instead of the Heaviside step function to trigger the penalty stiffness of the stator, a smooth function was employed. Using AUTO with this smooth approximation eliminates extra checks such as contact engagements or a force calculation step as in many HBM-continuation schemes (see e.g. [74]). This approximation will shed light on the feasibility and considerations of using such smooth approximations for rotordynamics systems.

There are a few options for such a function replacement, namely, hyperbolic tangent (tanh), logistic or exponential. The exponential function is rather suitable for smoothly approximating a *wall*. The others are compared to the Heaviside step function in Eq. (4.4).

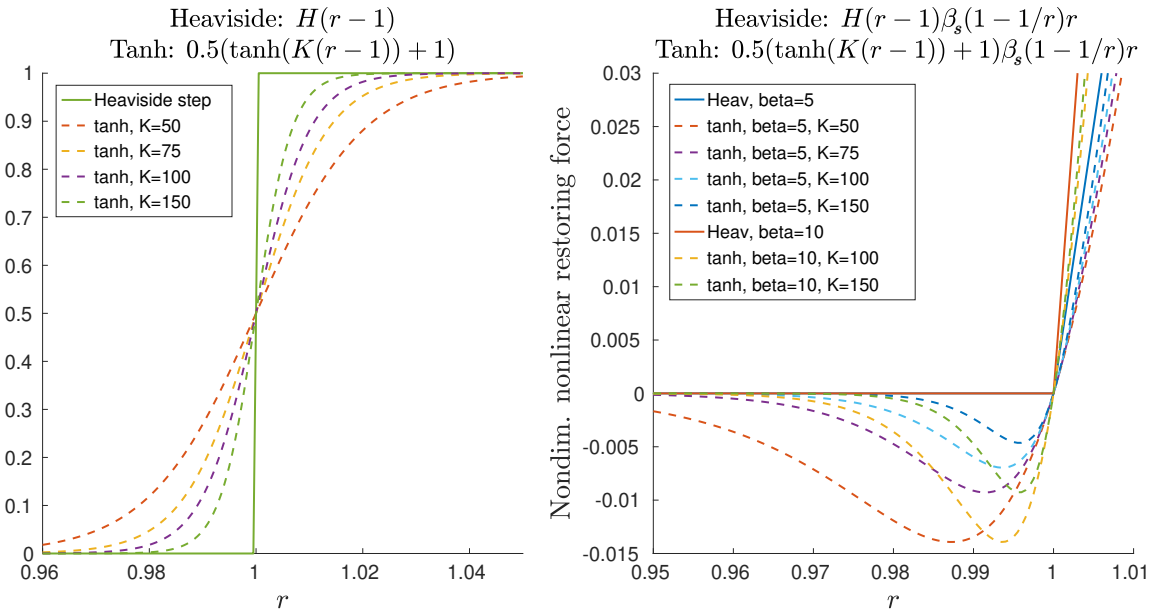


Figure 4.2: Left: Hyperbolic tangent function for various β_s and K value pairs. This paper used $\beta_s = 10, K = 150$. Right: The restoring force at the contact amplitude generated by the tanh-contact definition. The legend applies to both figures.

While both the logistic function and the tanh function are very similar to each other and suitable to represent the Heaviside step function, the tanh function was arbitrarily chosen since the logistic function is equivalent to the tanh function with two times the steepness value. The accuracy of this function is determined by the tanh-steepness parameter, K.

$$\text{Heaviside step}: \quad H(r-1) = \begin{cases} 0, r < 1 \\ 0.5, r = 1 \\ 1, r > 1 \end{cases} \tag{4.4a}$$

$$\text{Hyperbolic tangent}: \quad \frac{1}{2}\left(\tanh(K(r-1)) + 1\right) \tag{4.4b}$$

$$\text{Logistic function}: \quad \frac{1}{1+e^{-K(r-1)}} \tag{4.4c}$$

In the definition of the tanh-contact formulation, care must be taken to ensure accuracy and efficiency at the contact amplitude, where a fictitious negative restoring force is generated, see Figure 4.2b. For the same ratio between the (β_s, K) pair (e.g. (5,50) and (10,100) pairs), the fictitious force amplitude is the same, but the width of the affected zone is different. Also, observing the red lines' cascade, one can see that for a given β_s, the increase of K decreases the amplitude and the affected zone width (see Figure 4.2) together. This artificial effect of the logistic function was more pronounced than that of tanh for the same values of β_s and K, which is not presented here. Therefore, the tanh function was adopted in the present study. For a more dedicated analysis one can refer to Ref. [162] which investigated the spurious effects of different smoothing functions, namely, tanh, cosh, arctan, and quintic spline. The study stresses the importance of the

Table 4.1: The reference values of the constants that appear in Eq. 4.2 unless otherwise indicated in the text.

Parameter	**Value**
Damping ratio	$\zeta = 0.01$
Nondimensional polar moment of inertia	$J_p = 0.143$
Nondimensional disk mass	$m = 0.9$
Nondimensional distance of eccentric centre of mass	$e = 0.353$
Cubic stiffness measure	$\gamma = 0.25$
Stiffness ratio	$\beta_s = 10$
tanh-steepness parameter	$K = 150$
Nonlinearity weight	$\kappa = 0$

steepness parameter selection for accuracy.

Selection of the steepness parameter, K, is dependent on the stator stiffness ratio, β_s, because of the aforementioned effects of the tanh function. Therefore, the value of K has to be checked for accuracy of the continuation runs: Once the periodic solver of AUTO converges onto an orbit with the orthogonal collocation mesh adapted to the rapid change in the orbit due to contact, the solution should be the same to a numerical tolerance as that obtained for the EOM with the Heaviside step function, e.g. through simulations for stable solutions. The chosen value of K was determined by comparing the bifurcation diagrams from the tanh-contact model to that from a Heaviside-contact model (Figure 4.2) using the `ode45` function of MATLAB (RK4(5) scheme of Dormand and Prince [157]). This resulted in the selection of $K = 150$ for $\beta_s = 10$ (see Figure 4.2).

4.1.2 Homotopy from smooth to contact nonlinearity

The homotopy method is used to start from an 'easy' problem [163] to gradually find the solution to a more difficult problem. The parameter κ is used to switch the system response from cubic nonlinearity ($\kappa = 0$) to the contact nonlinearity ($\kappa = 1$). Despite that the method is simply the numerical continuation, the term homotopy is used to distinguish the nonlinearity change from the other parameters of the EOM. As a first approach (Figure 4.3a), a homotopy process can be applied on a starter orbit generated using the cubic nonlinearity, to change it to the response of a system with contact nonlinearity, while optionally adding other parameter changes as shown in Figure 4.3a. This might result in a failure if a different state of the parameter space is needed for κ to reach 1. For example, for a given values of ζ, e and Ω, a κ homotopy might reach a value of $\kappa = 0.8$, make a fold, and then decrease the values of κ before reaching 1. Thus, as in Figure 4.3b, additional continuation in Ω may be necessary.

To avoid this trial and error approach, Figure 4.3c shows that a more direct alternative is to trace the fold point of the cubic nonlinearity (if available) via a fold-continuation in two free parameters. In the runs, the most intuitive parameter is the rotor speed, and

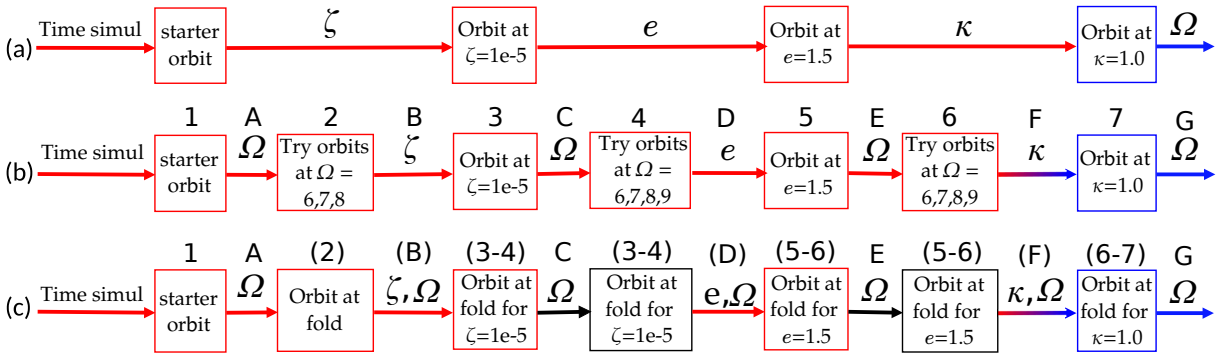


Figure 4.3: The flow of runs. (a) A direct and unlikely single parameter flow. (b) Single parameter flow with added Ω runs for more flexibility on the parameter space. (c) Fold-continuation flow: The arrows show the continuation runs in the parameter written above them and the resulting solution families, and the homotopy process in the case of κ. The red and blue boxes show the sampled orbits of cubic and contact cases, respectively. The continuation of ζ and e are optional in the exploration of the new nonlinearity for the system. The black boxes and continuation runs in (c) are only to plot the intermediate BD and does not constitute the method for reaching $\kappa = 1$. The methods in (b) and (c) are illustrated in Figure 4.4 in a representation.

the main investigation concerns the bifurcation diagrams with respect to the rotor speed. Therefore, this additional parameter was selected as Ω for both optional parameter change runs and for homotopy of the nonlinearity. The approaches in Figure 4.3b and Figure 4.3c were applied successfully, despite the greater difficulty in the numerical convergence of the fold-continuation method (Figure 4.3c) in the low ζ cases. When the damping approaches zero, the periodic solutions' isolation is not guaranteed, hence the tangent vector struggles to resolve. In order to help with the convergence, the minimum arclength step size was decreased from 0.05 to 0.0001, the number of Newton-Chord iterations was increased from 5 (default) to 7, out of which the Newton iterations were increased from 3 (default) to 5. Also, the relative convergence criterion was relaxed from 10^{-6} to $3 \cdot 10^{-6}$ for both the continuation parameters and the solution components, i.e., the states $\{\widetilde{\mathbf{w}}^T, \dot{\widetilde{\mathbf{w}}}^T\}^T$ of Eq. 4.2.

The methods in Figure 4.3b and 4.3c are illustrated in Figure 4.4. Note that the apparent locations of the branches in this illustration are arbitrary and chosen to support the methods in Figure 4.3. However, the methods outlined here can be modified in different ways. For example, both Figures 4.3 and 4.4 show that the homotopy in κ is the last step; however, other intermediate continuation runs can be done after the homotopy in κ. Nonetheless, if the cubic and the contact branches do not span a common range of Ω, and a fold does not appear, then intermediate single-parameter continuations might be resorted to, hence the preferred representation.

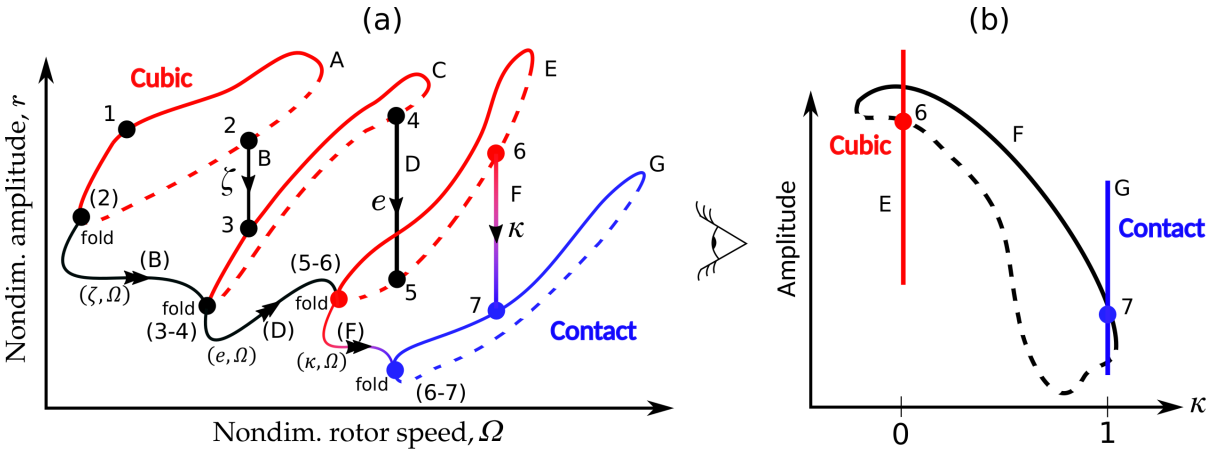


Figure 4.4: (a) A representative cubic to contact transition with single parameter method (single arrows, see Figure 4.3a and 4.3b) and fold method (double arrows, see Figure 4.3c). (b) A representative κ homotopy is illustrated in a pair of axes perpendicular to the bifurcation diagram for the single parameter method (see Figure 4.3b).

4.2 Results and Discussion

Figure 4.5 shows the investigated 3:1 and 2:1 IR responses in the rotating frame. These responses were named double loop (DL) and single loop (SL), respectively, due to their appearance. The frequency content of the SL and DL responses are shown in Figure 4.5d and 4.5b, respectively, which are the complex, signed frequency contents, $\bar{\mathbf{W}}$, obtained from the complex DFT as introduced in Section 2.1.

The DC components here indicates the response due to the unbalance forcing, which is a constant force in rotating frame. Converged IR responses of SL and DL in the rotating frame from the cubic stiffness formulation were used to start the continuation process. This corresponds to the first arrow and the first box in Figure 4.3. An orbit on this branch was used to start the continuation of the homotopy parameter, κ, switching to the contact definition, without optional parameter changes of ζ and e (Figure 4.3b).

Similarity of the responses from the cubic formulation and the contact formulation could be observed in Figure 4.6. The orientations of the loop of these orbits are different in the two systems, which might be linked to the delayed engagement of the tanh-contact nonlinearity above the amplitude level of the clearance compared to the cubic case where the nonlinearity is active at all amplitude levels. Apart from this, the orbits do not show qualitative difference.

The results for the cubic case are shown in Figure 4.7. For all the plots including those in Figure 4.7, continuous and dashed lines show stable and unstable response branches, respectively. The first thing to notice is the difference of the stiffening response between the two nonlinearities. All branches of the cubic nonlinearity bifurcation diagram (Figure 4.7a) settle onto a constant inclination as the amplitude of oscillation increases because the nonlinear force increases with the amplitude of oscillation. Therefore, the stiffening

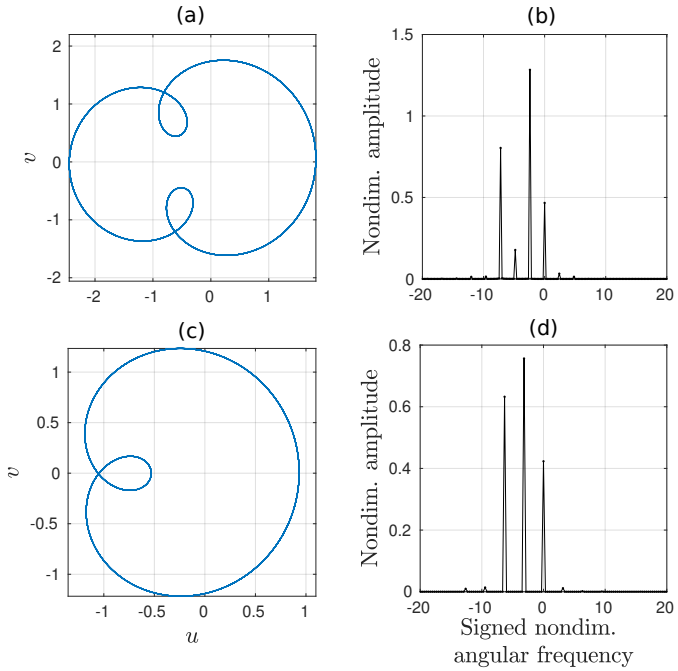


Figure 4.5: At a nondimensional rotor speed of $\Omega = 5.0$; (a) a sample 3:1 (DL) internal resonance response in the rotating frame from tanh-contact, and (b) its signed frequency content, (c) a sample 2:1 (SL) internal resonance response in the rotating frame, and (d) its signed frequency content. Negative frequencies indicate a backward whirl in the present frame of reference, which is rotating with Ω. The DC components result from the unbalance excitation that is a constant force in this rotating frame.

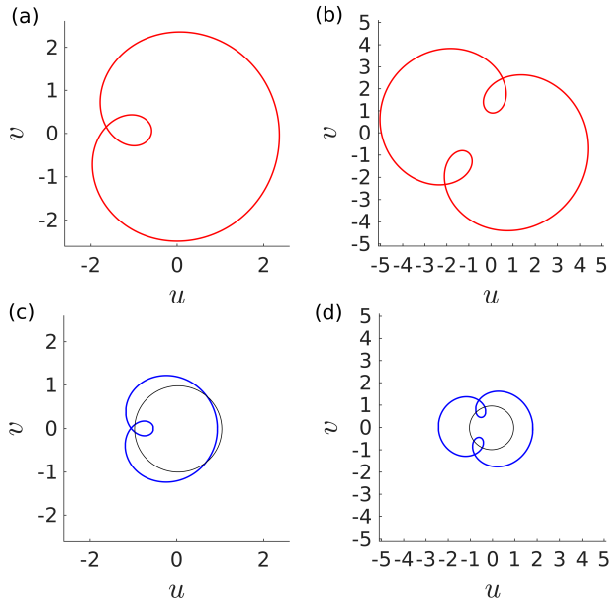


Figure 4.6: Orbits at $\Omega = 5.0$ corresponding to responses of cubic (a) SL and (b) DL, tanh-contact (c) SL and (d) DL responses. Black circles in (c) and (d) show the contact level for the tanh-contact system (see Eq. 4.2).

effect is present at all amplitude levels in the cubic nonlinearity. All branches of the tanh-contact nonlinearity have a strong stiffening effect in the lower amplitude oscillations with contact just above the amplitude level of 1, even manifested on the synchronous (S) branch with a pronounced kink. However, the relative effect of the nonlinearity decreases as the severity of contact increases. This difference can be attributed to the fact that the cubic nonlinearity is present at each amplitude level, whereas the tanh-contact nonlinearity is linear below contact and converges towards linear behaviour at high amplitudes since the effect of the stiffness change becomes less significant. Note that in Figure 4.7 (as well as in Figure 4.10 and Figure 4.12) the S and SL branches are unbounded within the shown range of rotor speed and amplitude. It should be noted that the out of balance (OOB) force rises with the square of the drive speed, and it is thought that therefore these solution branches are unbounded. For the system in Eq. (4.2) this has been validated up to $\Omega = 100$ with parameter values in Table 4.1. Previously, Ishida et al. in [20] plotted the main resonance of a bend-stretch coupling slender shaft with similar shapes but without reference to whether it is unbounded. Nagasaka et al. [55] also plotted near the main resonance of a length constraint, horizontal and slender shaft; however, the bifurcations near it make a direct comparison difficult. The main resonances for both of these studies appear unbounded in the range they are given. Although Ref. [86] used a cubic stiffness device, only stable branches were given which indicate a bounded behaviour. The analysis here corresponds to the values given in Table 4.1, which were chosen in Ch. 3 to constitute a model that is comparable to that of [3]. Unfortunately, the studies in Refs. [49] and [60] featuring cubic nonlinearity also feature contact nonlinearity or other nonlinear effects, thereby making direct comparison of the results difficult.

As shown in Figure 4.8, the lowest amplitude level for the cubic SL branch is below the contact level; after the nonlinearity switch, the lowest point moves upward above the contact level, because below the contact amplitude, there is no nonlinearity to produce these internal resonance responses.

In the contact bifurcation diagram (Figure 4.7b), the low amplitude periodic response is mostly unstable. However, a small region between the $\Omega = 4.4$–4.8 exists where the unstable periodic orbits of SL solutions might push the transitional response to the DL stable periodic orbits.

In Figure 4.7, period doubling (PD) bifurcations can be seen on the tanh-contact model, towards the lower amplitudes, which are zoomed in in Figure 4.9a. Figure 4.9b shows the SL PD region, where secondary PD bifurcation is visible. These PD responses are only stable at a very narrow rotor speed band; therefore, it might be unlikely to obtain these solutions in a real-world scenario. Nevertheless, in the brute force time simulation PD bifurcations were captured, as shown in Figure 4.9c for SL solutions where the black bars show the amplitude of the position through the trajectory. Note that, in the time simulations only the stable solutions are converged and the diagram is not as smooth as

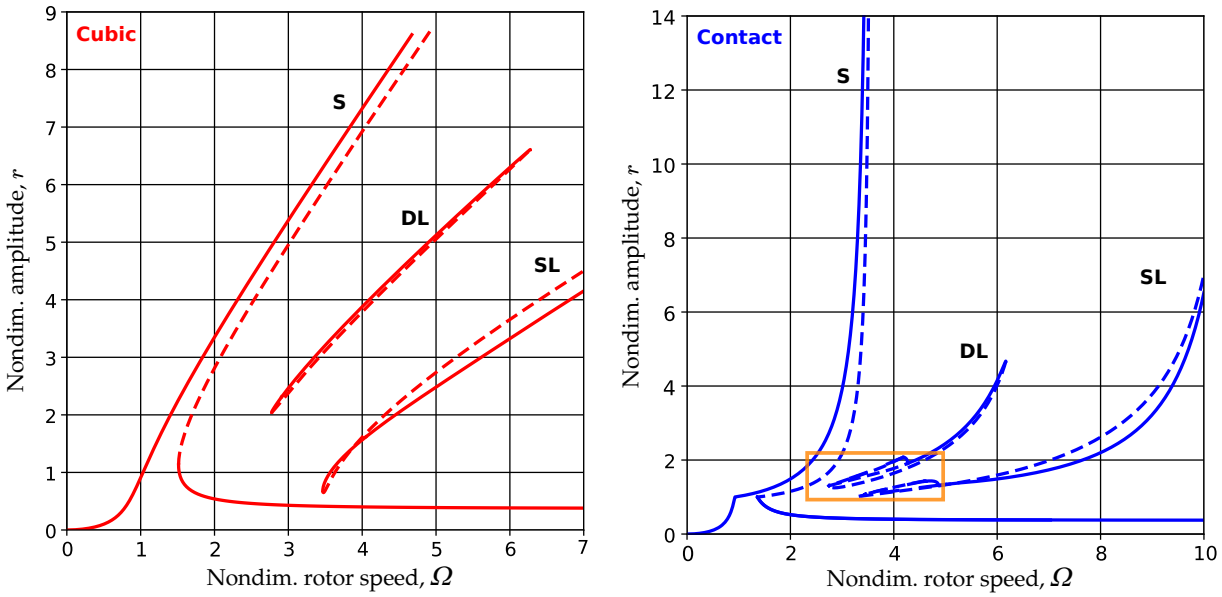


Figure 4.7: The transform of the bifurcation diagram from the cubic nonlinearity (left, red) to that of the contact nonlinearity (right, blue). The zoomed view of the orange box is shown in Figure 4.9a.

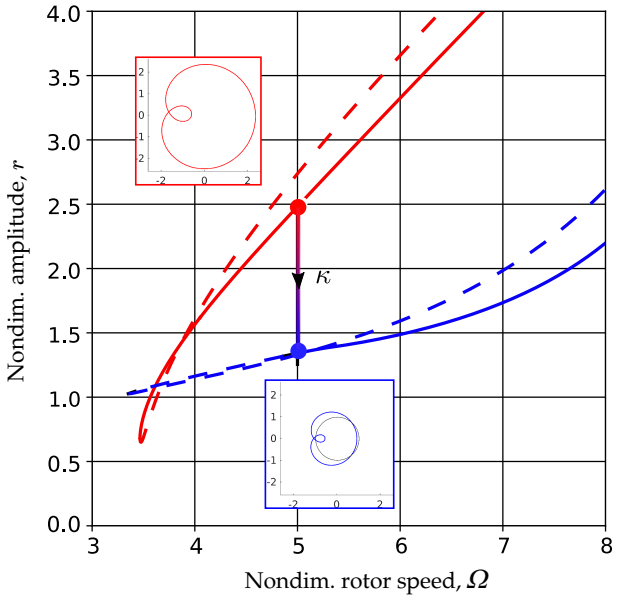


Figure 4.8: Closer view of the homotopy of SL periodic solutions. Small orbits are from Figure 4.6.

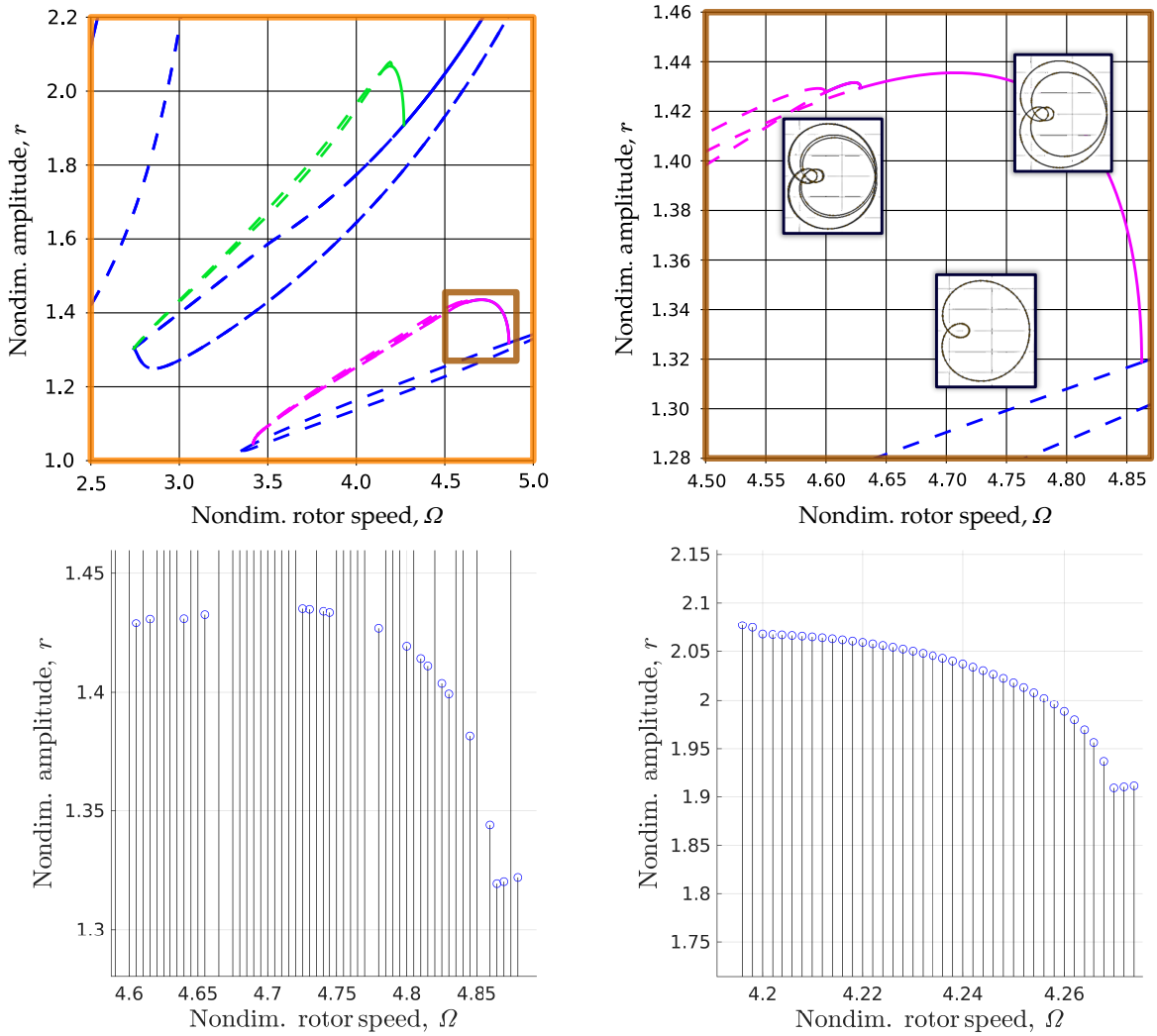


Figure 4.9: Period doubling (PD) bifurcation diagrams of tanh-contact model. (a) Zoom view at the orange rectangle in Figure 4.7b. (b) Zoom view at the brown rectangle inside (a). (c) Time simulation results of SL solutions. (d) Stepped sine sweep results of DL solutions.

that obtained from the numerical continuation process (Figure 4.9b), because some of the responses are converged onto DL or S branches, breaking the PD-branches' integrity. One can mitigate the problem when sweeping in terms of Ω in time simulations by using the end datum of a trajectory as the initial condition for the next Ω, which is shown on the DL PD solutions in Figure 4.9d. More discussion on the comparison of time simulation and numerical continuation can be found in Ch. 3. Lastly, the PD cascade could indicate a chaotic behaviour [164] despite the fact this was not experienced in the time simulations. However, if there was contact and friction, more diverse dynamics would appear as noted in [24], including chaos.The PD also appeared in the study by Van der Heijden [85].

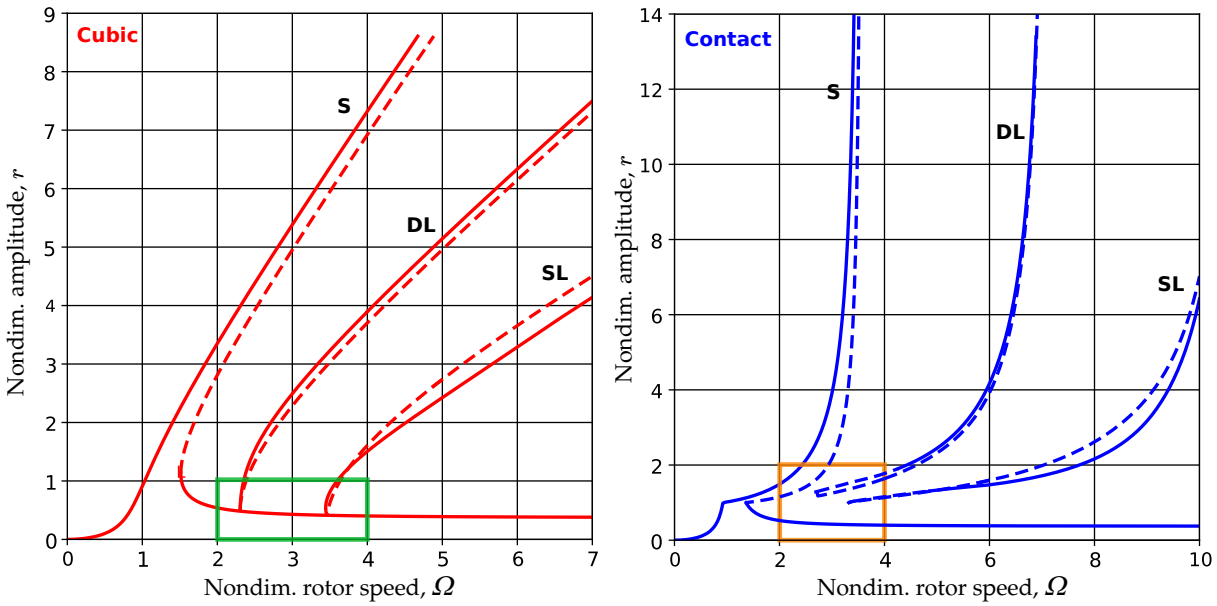


Figure 4.10: Bifurcation diagrams that correspond to a very low damping ratio value ($\zeta = 10^{-5}$) of the cubic (left, red) and contact (right, blue) nonlinearities. The zoomed views of the green and orange boxes in are shown in Figures 4.11a and 4.11b, respectively.

4.2.1 The case of low damping

To further explore the behaviour of the new nonlinearity, the original system parameters can be altered before the homotopy of the nonlinearity. One can investigate the response of the system under a different damping case, which can instantaneously change [165]. In Figure 4.10, a damping ratio of $\zeta = 10^{-5}$ was used to investigate the low damping systems of both nonlinearities comparatively. In addition to the phenomena observed in Figure 4.7, the zoom view at the lower amplitude ends of the DL and SL branches in Figure 4.11 show that low damping ensures that periodic solutions can be achieved at lower amplitude levels, closing the gap between the synchronous and asynchronous solutions. This would allow smaller perturbations of the synchronous solution to end up on the periodic solution branches for both nonlinearities more easily. However, since the contact nonlinearity is absent below the contact level, the closing of this gap is confined to right above the contact level, thereby requiring more disturbance of the synchronous solutions to settle onto periodic solutions. Besides, in the contact case, the IR response that is close to the contact amplitude is unstable. These unstable responses are likely to push the transient response either back to a low amplitude synchronous response or to a high amplitude nonlinear stable response. This still makes them very dangerous features of the BD despite that they are not achievable themselves in a theoretical or experimental simulation.

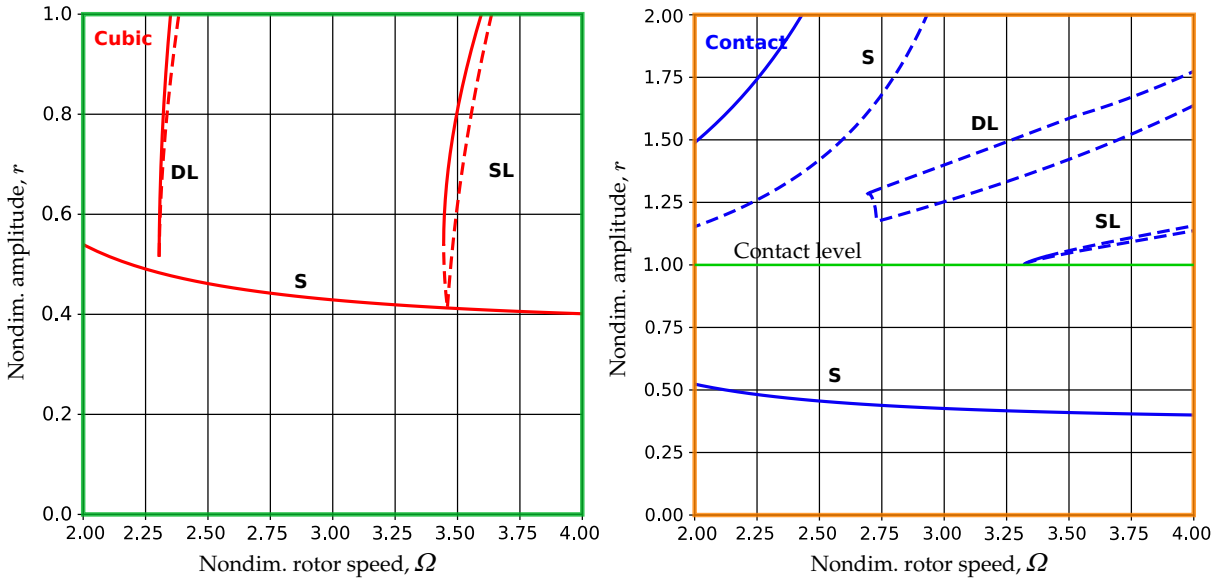


Figure 4.11: Low damping case. Zoom view of Figure 4.10 at the green and orange boxes therein.

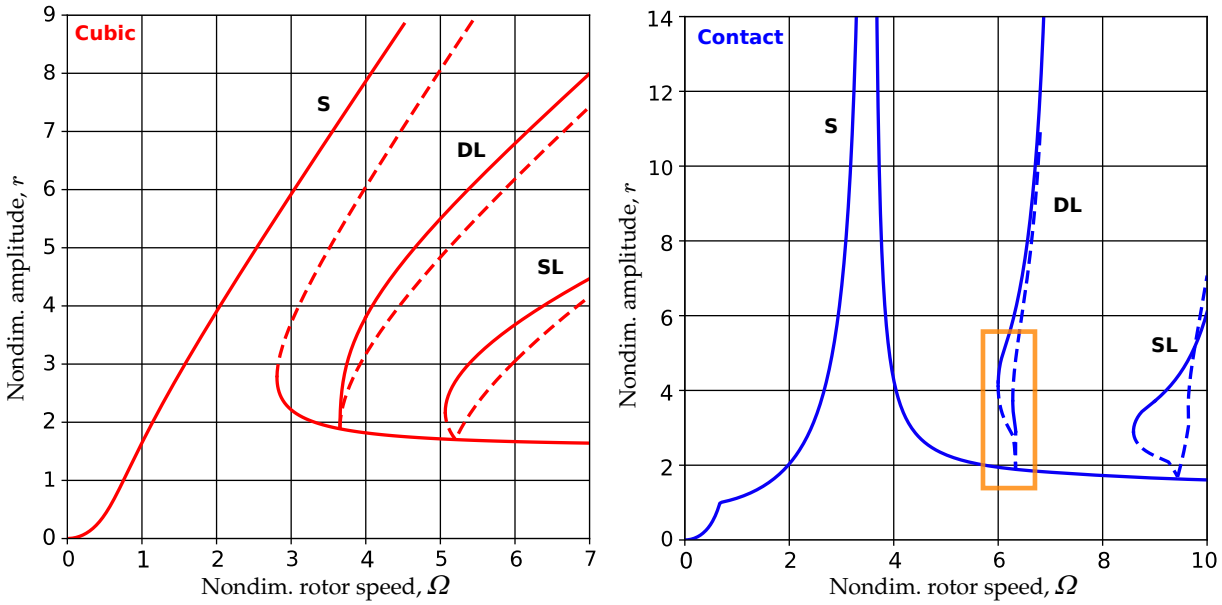


Figure 4.12: Bifurcation diagrams that correspond to low damping, high forcing case for the cubic (left, red), and the contact (right, blue) nonlinearities. The orange box is given in Figure 4.13.

4.2.2 The case of low damping and high unbalance

The unbalance excitation was increased by setting the eccentricity value greater than the contact clearance, $e = 1.5$, while the damping of the systems was retained at $\zeta = 10^{-5}$. Compared to Figure 4.10 and Figure 4.11, in Figure 4.12 the bifurcation diagram of the cubic nonlinearity looks qualitatively identical to the previous case (Figure 4.11) except that the amplitudes of oscillation are increased and the internal resonance is moved towards higher frequencies. However, the bifurcation diagram for the contact model shows a closer resemblance to the cubic case, this time: As can be seen in Figure 4.12b, the closing of the contact synchronous and asynchronous solutions is clearly visible. Similar to the cubic nonlinearity, the higher unbalance pushed the region of internal resonance to higher frequencies. However, since the nonlinearity decreases with amplitude in the tanh-contact nonlinearity, the periodic solution families straighten. This phenomenon twisted the DL branch (Figure 4.13) so much that a new stable zone formed below the main stable zone. This indicates that the same solution family can generate different amplitude solutions of the same nature within the investigated rotor speed region, breaking an intuition of having the stable solutions of the same solution family located adjacent, for example, in a stepped sine test. The fact that the same solution branch can carry different separated stable regions was mentioned earlier in [85].

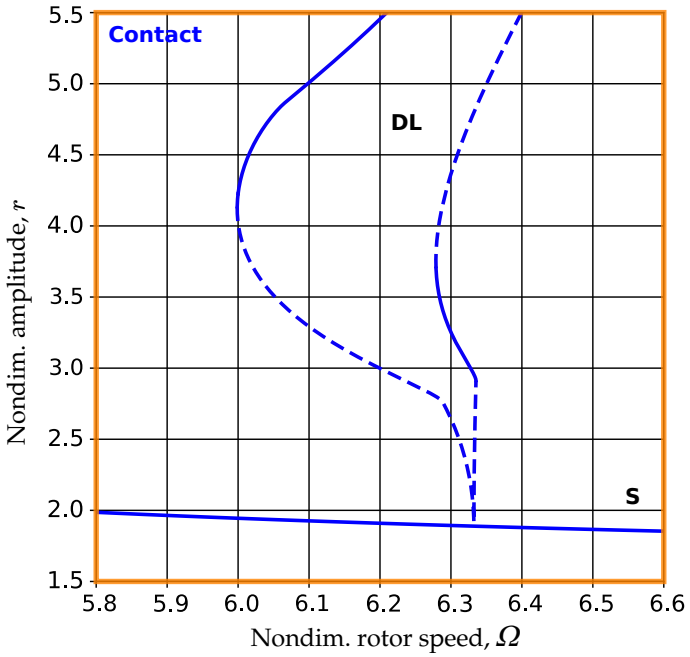


Figure 4.13: Low damping, high forcing case. Zoom view at the orange box in Figure 4.12.

4.2.3 tanh-contact

The selection of the steepness, K, of the hyperbolic tangent function was found to be important to avoid contamination of the bifurcation diagram with non-realistic effects. As pointed out in Section 4.1.1, the value of K was determined so that the bifurcation diagrams of the time simulations of the tanh-contact model overlapped with that of the Heaviside step functions. This indeed eliminated most of the fictitious response. However, for certain values of the parameters and a value of tanh-steepness smaller than the validated value, the effect of the tanh-contact being a smooth approximation of the contact was visible.

The fictitious response mainly contaminated around the grazing point at the contact amplitude, because the accuracy of the tanh function is impacted here by the steepness K the most. However, it is easy to diagnose in the contact case: if the nonlinear response features such as IRs or unstable synchronous response appear below the grazing point (contact amplitude) then this particular solution is artificial because the system is linear below the contact amplitude. Additionally, the effect is not believed to cause the same level of deviation from the response to contact defined by the Heaviside step function for responses with amplitudes far from the grazing point. Figure 4.14 shows two such cases with artificial responses. In Figure 4.14a there are soft kinks below the contact amplitude, although these would be located at the contact amplitude if it was a true discontinuous stiffness. Even an unstable region is visible between the fold points on the left-hand branch of synchronous solutions (Figure 4.14a). In Figure 4.14b, one can see the periodic solution family around and below the amplitude of contact. The numerical continuation continued right onto this new solution family for a certain combination of accuracy constants of the runs. However, the fact that this jump occurred shows that they are related to the actual periodic solutions. Nevertheless, the solution was not reliable for the tanh-steepness, K, values less then validated by the comparative brute force simulations.

The reason follows from Figure 4.2b, where the restoring force due to the contact definition is plotted. The tanh-contact restoring force below the point of contact has a false negative value in a small region of oscillation amplitude. This means that the solution is pushed upwards (towards a higher amplitude) in this region while no force should have been present from the contact. However, the increase of the tanh-steepness decreases this effect considerably, by decreasing the affected amplitude region (on the x-axis of the plot) and shrinking the fictitious restoring force amplitude (on the y-axis of the plot). For the values of $\beta_s = 10$ and $K = 150$, no such effects were observed in the practical scale, that is, compared to the step size in the continuation runs.

Recently, regularisation of piecewise smooth systems with such sigmoid functions was analysed in [166] which concluded that for both numerical continuation and numerical simulation methods the use of such approximations can represent the dynamics of the

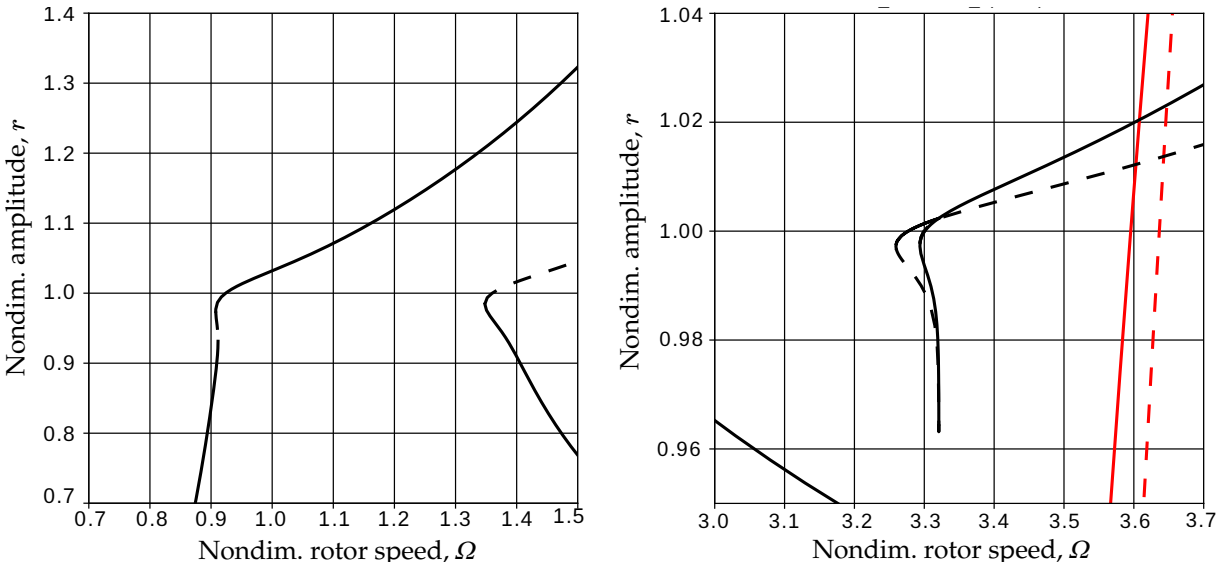


Figure 4.14: The fictitious parts of the bifurcation diagram. Left: Smoothing at the kink of the synchronous solution branches for a stiffness ratio of $\beta_s = 6$ and $K = 30$, a value lower than the validated value of $K = 90$. Right: The fictitious periodic solution family appeared around and below the contact amplitude when $\zeta = 10^{-5}$ and $e = 0.8$. The red solution family shows the cubic case. Other parameters are given in Table 4.1.

underlying non-smooth system. Additionally, they observed in their case study an increased numerical robustness and reduction in the computational burden. Kim et al. [162] compared different smoothing functions in that regard.

4.3 Conclusions

In this chapter, a new concept of performing the homotopy from one nonlinearity to the other was studied. The method was demonstrated on a smooth modification of the *Zilli system* [3] that features a tanh-contact stiffness nonlinearity. The numerical continuation method was employed in the process of changing the parameters of the original cubic stiffness model, as well as in the homotopy of the nonlinearity weight, κ, that transitions from the cubic to the tanh-contact nonlinearity. The method appears to be a potentially powerful tool for the investigation of more complex nonlinearities starting from a simpler and smoother case. The results were in agreement with the simulations, which were used to validate the contact stiffness. The following conclusions can be drawn:

On the method

The whole bifurcation diagram can be computed quickly using numerical continuation, including the unstable regions that convey useful information on the response of the system. The user, however, has to note the considerable time needed to setup the correct accuracy constants (in AUTO [84]) adjusting the discretisation and tolerances for computational

accuracy and efficiency, such as the maximum and minimum step sizes, the mesh interval count and its adaptation rate, the accepted solution accuracy and so on.

Nonlinear force homotopy made the investigation of the new nonlinearity possible without any prior knowledge on the new system.

The method is useful particularly when the known response belongs to a simple smooth nonlinearity such as a geometrical nonlinearity such as a cubic stiffness instead of a discontinuous stiffness, and shows similar responses to those from the new nonlinearity. The cubic nonlinearity was shown to be such a case in the preceding study in Ch. 3.

However, more complex nonlinearities can give more complex bifurcation diagrams, that are not easily obtainable from a solution of the simpler system. As such, only the responses that are related in both systems can be analysed in the presented method. For example, a 2:1 internal resonance response in the cubic system cannot result in a branch of 3:2 internal resonance responses in the contact system for the IR responses investigated. However, the responses of the 2:1 (SL) and 3:1 (DL) solutions are quite common in the literature. Generally, with lower damping and forcing, the IR responses approach the rotating frame Campbell diagram prediction. However, as undamped, unforced system cannot be reached from the damped and OOB-forced system, a classic backbone curve cannot be drawn.

Contrary to the approaches in the field of rotordynamics such as those with HBM and shooting method formulations, the direct approach using the system of equations with the tanh-contact definition was straightforward thanks to the ease of use of AUTO while supplying with a high bifurcation diagram resolution when compared to the time simulations. The selection of the tanh-contact smooth approximation of the discontinuous stiffness nonlinearity was useful in terms of the ease of setup of the method, not necessitating a correction scheme for the correct calculation of contact forces. Nonetheless, the tanh steepness (accuracy) has to be decided for accuracy around the contact level to avoid prediction of fictitious responses. The solution procedure has the system of equations in first order form, although they need to be discretised to fit into this continuation method. The sophisticated adaptive mesh formulation of AUTO worked well in the non-smooth approximation of the contact discontinuity.

On the dynamics of the system

Some insight of the dynamics of the system was developed. The loss of proper damping could make the synchronous unbalance response jump to the periodic (quasiperiodic in the stationary frame) solutions more readily because lower damping ratios are responsible for lower amplitudes of the asynchronous response. The asynchronous contact response at low amplitudes are mostly unstable; however, with low damping, their amplitudes are also low. This means that the excitation of the above the contact level does not settle the response on the IR solutions, but the UPO's can direct the transient response towards

synchronous response with even higher amplitudes.

The increased unbalance excitation pushed the periodic response higher in amplitude, into the more linear regions of contact nonlinearity. This made the stiffening effect less pronounced in the periodic branches, straightening them in the bifurcation diagrams. As this happened, a new stable solution zone emerged on the DL branch in addition to the regular stable zone. This means that the same pattern of solutions can be observed at different amplitudes.

The nonlinear rotordynamics show versatile response, which fragments the research in them. However, a more unifying analysis approach could require less manipulation of the governing system of equations, thereby linking many underlying phenomena. Although forced and damped, the distinct IR branches here are nonlinear modes of the system. Thus, nonlinear normal modes (NNMs) concept is a candidate for this unification. First Ch. 5 will investigate the generalisation of an available periodic solution computation method to include quasiperiodic response, such as the IRs appearing in the stationary frame, in order to demonstrate that diverse phenomena can be gathered under a more encompassing view. Secondly, although superposition does not apply to nonlinear modes, this group of IR responses investigated in this chapter is linked to the underlying, stiffened FW and BW nonlinear modes of the system, inferred from the frequency content. In Ch. 6, the underlying mechanism behind the IRs here will be investigated in terms of FW and BW NNMs of the Zilli system.

Chapter 5

A Quasiperiodic Arclength Shooting-Continuation Method

5.1 Introduction

In the previous chapters, the internal resonances (IRs) of the softer extreme of the rotor-stator interactions on a 2-dof, gyroscopic system was investigated. These IRs are quasiperiodic in the stationary frame, while periodic in the rotating frame that rotates with the rotor spin speed. Therefore, the aim here is to show and draw attention to the possibility of generalising an available tool for periodic solution calculation, namely, shooting-continuation method, as a tool for unifying the rich nonlinear responses seen in rotordynamics (see Table 1.1), in line with the research interest in Section 1.6.2. This chapter presents a new way of quasiperiodic continuation under the constraint that the trajectory has a repeating, but rotated trajectory section in the stationary frame which corresponds to a periodic motion in the rotating frame. That way, one can consider the use of the "same" tool on an EOM without the need to transform to other coordinate systems, or to manipulate the system in other ways. Practically, remaining in the stationary frame might become convenient when examining a system with both static and rotating components, such as a shaft and its support structure.

The method is based on the shooting-continuation method given in [118] for nonlinear normal modes (NNMs), while [167] applied a shooting-continuation method on rotor-dynamics. The choice of shooting is based on that it is more intuitive to be on the time domain as compared to the more complicated multidimensional harmonic balance methods (e.g. [168, 76]): The number of nonlinear algebraic equations is defined by the state count of the system, unlike in HBM method where the accuracy of the solution defines the harmonics which then defines the size of the algebraic system. The shooting method does not require an alternating frequency-time step for force updates, as it already time-simulates the trajectory. It also comes with stability as a by product thanks

to the Floquet theory. It is the most non-invasive way of uncovering the periodic solution branches, saving considerations such as discretisation by trial functions or adaptive orthogonal collocations.Additionally, this method can be extended as a multiple-shooting method (e.g. [169]) which is not the focus in this chapter.

The presented shooting-continuation method consists of numerical continuation in system parameters (e.g. rotor speed) in addition to period of the response. A "period" indicates the time interval of the repeating smallest section of the trajectory which forms the periodic solutions in the rotating frame. Due to that definition, it is also referred to as a "quasiperiod" in this chapter. In Section 5.2, after the formulation is explained, a fitting utilisation of Floquet theory for stability analysis is elaborated, and choice of phase condition is discussed. The results are given in Section 5.3 where main components of the 2:1 IR are obtained as distinct branches using complex DFT (Section 2.1), which are used to augment the Campbell diagram.

5.2 A quasiperiodic arclength shooting-continuation formulation with Newton corrections

The n-dof eom studied here is of the form,

$$\mathbf{M}\mathbf{w}'' + \mathbf{C}\mathbf{w}' + \Omega\mathbf{G}\mathbf{w}' + \mathbf{K}\mathbf{w} + \mathbf{f}_{nl}(\mathbf{w}, \mathbf{w}') + \mathbf{f}(t, \Omega) = \mathbf{0} \tag{5.1}$$

where $\mathbf{w} = \{x, y\}^T$ is the stationary frame position states, $\mathbf{f}_{nl}$ is the nonlinear force, $\mathbf{f}$ is the linear force, $\mathbf{0}$ is the zero-vector. This has the first order form:

$$\mathbf{z}' = \mathbf{g}(t, \mathbf{z}(t, \mathbf{z}_0, \Omega), \Omega) = \begin{Bmatrix} \mathbf{w}' \\ -\mathbf{M}^{-1}[\mathbf{C}(\Omega)\mathbf{w}' + \mathbf{K}\mathbf{w} + \mathbf{f}_{nl}(\mathbf{w}, \mathbf{w}') + \mathbf{f}(t, \Omega)] \end{Bmatrix} \tag{5.2}$$

where $\mathbf{z} = \{\mathbf{w}^T, \mathbf{w}'^T\}^T$ is the states vector in the stationary frame, Ω is the rotor spin speed. The shooting function can be defined as an augmented periodicity condition:

$$\mathbf{H}(\mathbf{z}_{p0}, T_p, \Omega_p) = \mathbf{R}(\theta_{se}(\Omega, T))\ \mathbf{z}_p(T_p, \mathbf{z}_{p0}, \Omega_p) - \mathbf{z}_{p0} = \mathbf{0}, \tag{5.3}$$

where $\mathbf{z}_p$ indicates a quasiperiodic solution, and $\mathbf{z}_{p0}$ indicates the initial condition for that solution, T_p is the *quasiperiod* of the signal, i.e. a smallest repeating section of trajectory. Here, θ_{se} is the amount of the rotation applied by $\mathbf{R}$ and the subscripts "se" stand for 'start-end', referring to angle coverage in the stationary frame configuration space by one quasiperiod. The rotation matrix rotates the coordinates so that the end point of the

trajectory appears the same as the initial point in the inertial frame,

$$\mathbf{R}_2 = \begin{bmatrix} \cos\theta_{se} & \sin\theta_{se} \\ -\sin\theta_{se} & \cos\theta_{se} \end{bmatrix} \tag{5.4}$$

or in the presented 2-dof (4-state) example here,

$$\mathbf{R} = \begin{bmatrix} \mathbf{R}_2 & \mathbf{0} \\ \mathbf{0} & \mathbf{R}_2 \end{bmatrix} \tag{5.5}$$

where the 2×2 rotation matrix is the transpose of the 2×2 rotating frame transform matrix, $\mathbf{R}_2 = \mathbf{T}_2^T$. As it is evident from Eq. (5.5), this rotation matrix rotates the velocity states, and it does not give the new frame a rotation speed (unlike a rotating frame transform). If, as in the specific case here, the quasiperiodic solution trajectory is indeed periodic in the rotating frame that is rotating with the rotor spin speed, then $\theta_{se} = \Omega T$ is a known value along the branch which might be greater than 2π in magnitude, where T is the quasiperiod. Additionally, the rotation matrix $\mathbf{R}$ also defines a 'rotated' frame of reference, distinct from the rotating frame with the transform,

$$\mathbf{v} = \mathbf{R}\mathbf{z}. \tag{5.6}$$

Taylor expansion around a regular solution point for a parameter λ of the system Eq. (5.2) gives, omitting the subscripts "p" for clarity,

$$\mathbf{H}(\mathbf{x}) = \left.\frac{\partial \mathbf{H}}{\partial \mathbf{z}_0}\right|_{\mathbf{x}^{(\nu)}} \Delta\mathbf{z}_0 + \left.\frac{\partial \mathbf{H}}{\partial T}\right|_{\mathbf{x}^{(\nu)}} \Delta T + \left.\frac{\partial \mathbf{H}}{\partial \lambda}\right|_{\mathbf{x}^{(\nu)}} \Delta\lambda + \dots \tag{5.7}$$

where $\mathbf{x} = \{\mathbf{z}_0^T, T, \lambda\}^T$, and $\lambda = \Omega$ for this chapter. Since the solution is quasiperiodic (although a periodic orbit can be extracted with a rotating frame perspective), any trajectory with time length T, a *quasiperiod*, will be a solution. Therefore, in order to fix the solution in space, one can capture the trajectory at a phase condition $h = 0$. After the selection of a proper phase condition (see Section 5.2.1), the last condition is the arclength condition along the branch:

$$||\dot{\mathbf{x}}||^2 = 1 \tag{5.8}$$

where, the derivative with a dot $(\cdot)^{\cdot}$ is with respect to the arclength parameter s, and double-pipe $||\cdot||$ denotes the L2-norm (Euclidean norm). Or, in a numerically more relaxed form, the arclength condition can be expressed as:

$$\begin{aligned} ||\dot{\mathbf{x}}||^2 = 1 \rightarrow \langle \dot{\mathbf{x}}, \Delta\mathbf{x} \rangle &= \Delta s \\ \rho = \langle \mathbf{p}^0, \Delta\mathbf{x} \rangle - \Delta s^0 &= 0 \end{aligned} \tag{5.9}$$

where, the bracket calculates the scalar vector product, Δs^0 is the step size, and $\mathbf{p}^0 = \dot{\mathbf{x}}^0$ is the tangent vector tangent to the solution branch parametrised by the arclength s, at the known solution point. The superscripts 0 indicate that the solution is known to be a regular point on the branch of solutions. The distance to the previously known solution is indicated with $\Delta\mathbf{x} = \mathbf{x}^{(\nu)} - \mathbf{x}^0$ which is distinct from $\Delta\mathbf{x}^{(\nu)}$. Here, $\Delta\mathbf{x}^{(\nu)}$ is the Newton correction at its ν^{th} iteration (see Eq. (5.11a)) which defines the iterated solution point following the update: $\mathbf{x}^{(\nu+1)} = \mathbf{x}^{(\nu)} + \Delta\mathbf{x}^{(\nu)}$. The corrections $\Delta\mathbf{x}^{(\nu)}$ of the prediction $\mathbf{x}^{(0)} = \mathbf{x}^0 + \mathbf{p}^0\Delta s^0$ come from the Newton iterations, which terminates when the next solution point $\mathbf{x}^1 = \mathbf{x}^{(\nu_{last})}$ is found when the relative error is small: $||\mathbf{H}^{(\nu)}||/||\mathbf{z}_0^{(\nu)}|| < \epsilon$ (see Ref. [118] for this convergence criterion).

The shooting system of algebraic equations are gathered from Eqs. (5.3), (5.26) and (5.9),

$$\mathbf{F}(\mathbf{x}) = \begin{cases} \mathbf{H} = 0 \\ h = 0 \\ \rho = 0 \end{cases} \tag{5.10}$$

Therefore, the Newton corrections are formulated by taking 1st order Taylor expansion of Eq. (5.10) to give the following equation in the form $\mathbf{F}_\mathbf{x}|_{\mathbf{x}^\nu}\Delta\mathbf{x}^{(\nu)} = -\mathbf{F}|_{\mathbf{x}^\nu}$ where $\mathbf{F}_\mathbf{x}$ is the Jacobian of the full system of algebraic equations in Eq. (5.10),

$$\begin{bmatrix} \frac{\partial\mathbf{H}}{\partial\mathbf{z}_0}\Big|_{\mathbf{x}^{(\nu)}} & \frac{\partial\mathbf{H}}{\partial T}\Big|_{\mathbf{x}^{(\nu)}} & \frac{\partial\mathbf{H}}{\partial\lambda}\Big|_{\mathbf{x}^{(\nu)}} \\ \frac{\partial h}{\partial\mathbf{z}_0}\Big|_{\mathbf{x}^{(\nu)}} & \frac{\partial h}{\partial T}\Big|_{\mathbf{x}^{(\nu)}} & \frac{\partial h}{\partial\lambda}\Big|_{\mathbf{x}^{(\nu)}} \\ & \mathbf{p}^{0^T} & \end{bmatrix} \begin{Bmatrix} \Delta\mathbf{z}_0 \\ \Delta T \\ \Delta\lambda \end{Bmatrix}^{(\nu)} = -\begin{Bmatrix} \mathbf{H}(\mathbf{x}^{(\nu)}) \\ h(\mathbf{x}^{(\nu)}) \\ \langle\mathbf{p}^0,\ \mathbf{x}^{(\nu)} - \mathbf{x}^0\rangle - \Delta s^0 \end{Bmatrix} \tag{5.11a}$$

$$\begin{bmatrix} \frac{\partial\mathbf{H}}{\partial\mathbf{z}_0}\Big|_{\mathbf{x}^{(\nu)}} & \frac{\partial\mathbf{H}}{\partial T}\Big|_{\mathbf{x}^{(\nu)}} & \frac{\partial\mathbf{H}}{\partial\lambda}\Big|_{\mathbf{x}^{(\nu)}} \\ \frac{\partial h}{\partial\mathbf{z}_0}\Big|_{\mathbf{x}^{(\nu)}} & \frac{\partial h}{\partial T}\Big|_{\mathbf{x}^{(\nu)}} & \frac{\partial h}{\partial\lambda}\Big|_{\mathbf{x}^{(\nu)}} \\ & \mathbf{p}^{0^T} & \end{bmatrix} \begin{Bmatrix} \Delta\mathbf{z}_0 \\ \Delta T \\ \Delta\lambda \end{Bmatrix}^{(\nu)} = -\begin{Bmatrix} \mathbf{H}(\mathbf{x}^{(\nu)}) \\ h(\mathbf{x}^{(\nu)}) \\ 0 \end{Bmatrix} \tag{5.11b}$$

where,

$$\mathbf{p}^0 = \dot{\mathbf{x}}^0 = (\dot{\mathbf{z}}_0, \dot{T}, \dot{\lambda})^0 \tag{5.12a}$$

$$(\mathbf{z}_0, T, \lambda)^{(\nu+1)} = (\mathbf{z}_0, T, \lambda)^{(\nu)} + (\Delta\mathbf{z}_0, \Delta T, \Delta\lambda)^{(\nu)}. \tag{5.12b}$$

and $\lambda = \Omega$ for this chapter. The last line of Eq. (5.11b) is used by [118] and it comes from the arclength condition effectively keeps the correction direction orthogonal to the previous tangent; in Eq. (5.11a) the last equation brings the corrections back to the orthogonal line at the tip of the prediction. Note that this might not appear perpendicular in a 2-dimensional bifurcation diagram visualisation (e.g. Amplitude vs. rotor speed).

First, the new tangent vector at the newly found solution point is found,

$$\begin{bmatrix} \frac{\partial \mathbf{H}}{\partial \mathbf{z}_0}\Big|_{\mathbf{x}^{(\nu)}} & \frac{\partial \mathbf{H}}{\partial T}\Big|_{\mathbf{x}^{(\nu)}} & \frac{\partial \mathbf{H}}{\partial \lambda}\Big|_{\mathbf{x}^{(\nu)}} \\ \frac{\partial h}{\partial \mathbf{z}_0}\Big|_{\mathbf{x}^{(\nu)}} & \frac{\partial h}{\partial T}\Big|_{\mathbf{x}^{(\nu)}} & \frac{\partial h}{\partial \lambda}\Big|_{\mathbf{x}^{(\nu)}} \\ & \mathbf{p}^{0^T} & \end{bmatrix} \mathbf{p}^1 = -\begin{Bmatrix} \mathbf{0} \\ 0 \\ 1 \end{Bmatrix} \tag{5.13a}$$

$$\mathbf{p}^1 = \begin{Bmatrix} \dot{\mathbf{z}}_0 \\ \dot{T} \\ \dot{\Omega} \end{Bmatrix}^1 \rightarrow ||\mathbf{p}^1||^2 = 1 \tag{5.13b}$$

where $\mathbf{p}^1$ is the tangent at the newly converged solutions, and the superscript "1" indicate this new point along the branch of solutions. Note that instead of the previous tangent $\mathbf{p}^0$, a basis-vector can be used such as $\mathbf{e}_k$ whose elements are zero except the k^{th} entry which is one. The tangent vector is normalised for consistency with the step size updates. Then the prediction of the next solution is,

$$\mathbf{x}^{(\nu=0)} = \mathbf{x}^1 + \mathbf{p}^1 \Delta s^1 \tag{5.14}$$

where the new step size Δs^1 is updated as,

$$\Delta s^1 = \left| \left(\frac{\nu^{desired}}{\nu} \right) \Delta s^0 \right| \ \text{sign}\left(\Delta s^0 \langle \mathbf{p}^0, \mathbf{p}^1 \rangle \right) \tag{5.15}$$

where $\nu^{desired}$ is the desired iteration count and ν is the total iteration count of the last correction step. The same process is repeated after setting the superscripts 1 to 0.

5.2.1 Phase condition

The OOB angle, ϕ_Ω is already available as a phase condition which might be set to zero for every point along the solution branch, and the initial condition of the trajectory will be attached to that phase condition, indicating that h is not used in the formulation. Firstly, because the rotor speed is a free parameter (i.e. it is not simply a function of quasiperiod T), this makes the system $\mathbf{F}$ underdetermined but still a solution can be found by Moore-Penrose inverse which minimises the Euclidean norm of the correction vector $\Delta \mathbf{x}^{(\nu)}$. However, since $\theta_{se} = \Omega T$ can be greater than 2π, there are other trajectory points along a certain quasiperiodic section where the OOB angle is zero, $\phi_\Omega = 0$. This results in some problem at the solution points along the branch where both the OOB angle is zero $\phi_\Omega = 0$ and the trajectory is not locally uniquely defined by $\phi_\Omega = 0$. When this happens, the trajectory might make a 'false fold' and return back on the solution branch. Therefore, a phase condition is needed which can properly link the next solution point to the previous solution point, in addition to keeping $\phi_\Omega = 0$. Poincaré orthogonality

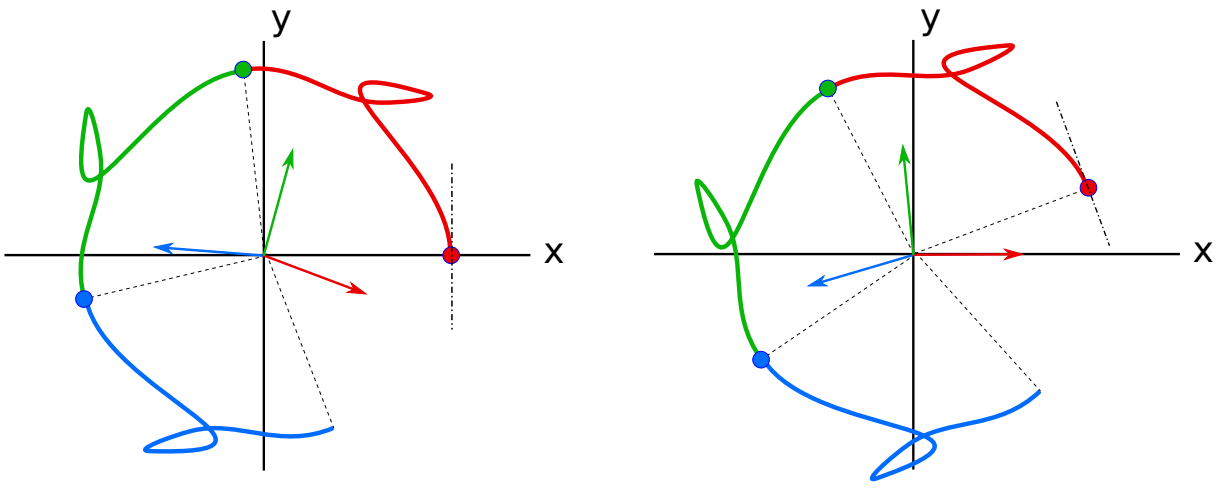


Figure 5.1: Schematic representation of the quasiperiodic trajectory and the OOB angle. The red, green and blue points show the quasiperiodic repeating sections' initial states, and the arrows represent the corresponding OOB forcing directions (OOB angles) with respective colours. Left figure shows that case when the OOB angle is freed with the phase condition in Eq. 5.26. Right figure shows the case when the oob angle is assumed zero; in this case other phase conditions might be used to locally capture a unique trajectory.

condition as the phase condition was not numerically reliable and was causing 'false folds'. Instead, an integral phase condition is used which is given by Doedel and Heidemann [170] which minimises the integral of the distance between the periodic trajectories of the previous and current solution points, effectively keeping the solution profile the same as the previous solution point. Note that $\mathbf{z}' = \mathbf{g}(\mathbf{z}, t)$ and $\mathbf{q}' = \mathbf{f}(\mathbf{q})$ are the stationary and rotating frame EOMs, respectively, with the transform $\mathbf{z} = \mathbf{T}\mathbf{q}$ given in Eq. (2.13), and the vector field transforms as $\mathbf{f} = \mathbf{T}^{-1}(\mathbf{g} - \Omega\mathbf{J}\mathbf{z})$, and $\mathbf{J}$ is the skew-symmetric matrix given in Eq. (5.55). Note that the phase condition formulation here involves the rotor speed Ω so that instead of the general parameter λ, the expressions explicitly refer to Ω as the free parameter. The phase condition, then, can be expressed as,

$$h = \int_0^1 \left(\mathbf{q}^1(\tau T^1) - \mathbf{q}^0(\tau T^0)\right)^T \cdot \dot{\mathbf{q}}^1(\tau T^1) \mathrm{d}\tau = 0 \tag{5.16}$$

or integration by parts results in,

$$h = \int_0^1 \mathbf{q}^1(\tau T^1)^T \cdot \dot{\mathbf{q}}^0(\tau T^0) \mathrm{d}\tau = 0 \tag{5.17}$$

where superscripts 1 and 0 mark the current and previous solution points, the current solution point data time scale is (τT^1) and previous solution point time scale is (τT^0), and the dot indicates matrix multiplication, and overdot indicates time derivation. The superscript $(\cdot)^T$ denotes transpose of a matrix. With the transforms, these phase conditions

become:

$$h = \int_0^1 \left(\mathbf{T}^{1^{-1}}\mathbf{z}^1 - \mathbf{T}^{0^{-1}}\mathbf{z}^0\right)^T \cdot \left(\mathbf{T}^{1^{-1}}\left(\mathbf{g}^1 - \Omega^1\mathbf{J}\mathbf{z}^1\right)\right)\mathrm{d}\tau = 0, \tag{5.18}$$

$$h = \int_0^1 \left(\mathbf{T}^{1^{-1}}\mathbf{z}^1\right)^T \cdot \left(\mathbf{T}^{0^{-1}}\left(\mathbf{g}^0 - \Omega^0\mathbf{J}\mathbf{z}^0\right)\right)\mathrm{d}\tau = 0. \tag{5.19}$$

It is important to clarify the distinction between similar notation: z_0 is the current initial condition and $\mathbf{z}^0$ is the known solution's time trajectory vector; the known solution is independent of the current initial condition. Note that the equality $\mathbf{J}\mathbf{T}^{-1} = \mathbf{T}^{-1}\mathbf{J}$ is used which is true for the transform matrix $\mathbf{T}$ and not for a general matrix. The calculation for the first form in Eq. (5.18) of the phase condition is more cumbersome compared to Eq. (5.19), though less data is needed to be circulated to the next solution point's calculation loop in the former. Therefore, both forms are given further below, successively. The partial derivative of these phase conditions with respect to the stationary frame (quasiperiodic) initial conditions is,

$$\begin{aligned}\frac{\partial h}{\partial \mathbf{z}_0} = \int_0^1 \Bigg[&\left(\mathbf{T}^{1^{-1}}\frac{\partial \mathbf{z}^1}{\partial \mathbf{z}_0}\right)^T \cdot \left(\mathbf{T}^{1^{-1}}\left(\mathbf{g}^1 - \Omega^1\mathbf{J}\mathbf{z}^1\right)\right) \\ &+ \left(\mathbf{T}^{1^{-1}}\left(\mathbf{g_z}^1 - \Omega^1\mathbf{J}\right)\frac{\partial \mathbf{z}^1}{\partial \mathbf{z}_0}\right)^T \cdot \left(\mathbf{T}^{1^{-1}}\mathbf{z}^1 - \mathbf{T}^{0^{-1}}\mathbf{z}^0\right)\Bigg]\mathrm{d}\tau.\end{aligned} \tag{5.20}$$

and,

$$\frac{\partial h}{\partial \mathbf{z}_0} = \int_0^1 \left(\mathbf{T}^{1^{-1}}\frac{\partial \mathbf{z}^1}{\partial \mathbf{z}_0}\right)^T \cdot \left(\mathbf{T}^{0^{-1}}\left(\mathbf{g}^0 - \Omega^0\mathbf{J}\mathbf{z}^0\right)\right)\mathrm{d}\tau. \tag{5.21}$$

The partial derivative of the phase condition with respect to the rotor speed $\partial h/\partial\Omega$ can be expressed as,

$$\begin{aligned}\frac{\partial h}{\partial \Omega} = \int_0^1 \Bigg[&\left(\frac{\partial \mathbf{T}^{1^{-1}}}{\partial \Omega}\mathbf{z}^1 + \mathbf{T}^{1^{-1}}\left(\frac{\partial \mathbf{z}^1}{\partial \Omega}\right)\right)^T \left(\mathbf{T}^{1^{-1}}(\mathbf{g}^1 - \Omega^1\mathbf{J}\mathbf{z}^1)\right) \\ &+ \left(\mathbf{T}^{1^{-1}}\mathbf{z}^1 - \mathbf{T}^{0^{-1}}\mathbf{z}^0\right)^T \left(\frac{\partial \mathbf{T}^{1^{-1}}}{\partial \Omega}(\mathbf{g}^1 - \Omega^1\mathbf{J}\mathbf{z}^1) + \mathbf{T}^{1^{-1}}\left(\frac{\partial \mathbf{g}^1}{\partial \Omega} - \mathbf{J}\mathbf{z}^1 - \Omega^1\mathbf{J}\frac{\partial \mathbf{z}^1}{\partial \Omega}\right)\right)\Bigg]\mathrm{d}\tau\end{aligned} \tag{5.22}$$

and,

$$\frac{\partial h}{\partial \Omega} = \int_0^1 \left(\frac{\partial \mathbf{T}^{1^{-1}}}{\partial \Omega}\mathbf{z}^1 + \mathbf{T}^{1^{-1}}\left(\frac{\partial \mathbf{z}^1}{\partial \Omega}\right)\right)^T \left(\mathbf{T}^{0^{-1}}\left(\mathbf{g}^0 - \Omega^0\mathbf{J}\mathbf{z}^0\right)\right)\mathrm{d}\tau. \tag{5.23}$$

The partial derivative of the phase condition to the period is expressed as,

$$\frac{\partial h}{\partial T} = \left[\left(\mathbf{T}^{1^{-1}} \mathbf{z}^1 - \mathbf{T}^{0^{-1}} \mathbf{z}^0 \right)^T \cdot \left(\mathbf{T}^{1^{-1}} \left(\mathbf{g}^1 - \Omega^1 \mathbf{J} \mathbf{z}^1 \right) \right) \right]_{\tau=1} \tag{5.24}$$

and,

$$\frac{\partial h}{\partial T} = \left[\left(\mathbf{T}^{1^{-1}} \mathbf{z}^1 \right)^T \cdot \left(\mathbf{T}^{0^{-1}} \left(\mathbf{g}^0 - \Omega^0 \mathbf{J} \mathbf{z}^0 \right) \right) \right]_{\tau=1} . \tag{5.25}$$

A numerical integral method such as trapezoidal can be used for integration along the normalised time τ. The first of these pair of phase conditions requires that the information on the previous solution point's stationary frame trajectory $\mathbf{z}^0$, period T^0, rotor speed Ω^0 are circulated into the correction iterations of the new solution point; whereas, the second of the pair additionally requires the vector field $\mathbf{g}^0$. Also note that the matrix $\partial \mathbf{z}^1 / \partial \mathbf{z}_0$ in Eq. (5.20) is the evolution matrix for the current solution point, which is derived in Appendix B.2 and its relation to the monodromy matrix is given in stability calculations under Section 5.2.3. In the case that the solution has not converged yet, the superscripts 1 will be replaced with (ν) indicating the ν^{th} Newton correction iteration.

Alternative phase condition:

The phase condition can be expressed in the stationary frame where the solution looks quasiperiodic, one can assume the phase condition:

$$\mathbf{h}(\mathbf{z}_0, T, \Omega, \phi_\Omega) = \begin{Bmatrix} {}_n\mathbf{z}_0 \\ {}_{n+1}\mathbf{z}_0 \end{Bmatrix} = \begin{Bmatrix} 0 \\ 0 \end{Bmatrix} \tag{5.26}$$

meaning that the n^{th} and $(n+1)^{\text{th}}$ element of the state vector $\mathbf{z}$ is set to zero, with n being the number of the degree of freedom (dof), one corresponding to a position and the other to a velocity (making $2n$ states $\mathbf{z} = \{\mathbf{w}^T, \mathbf{w}'^T\}^T$). Here ϕ_Ω is the unbalance force direction or, equivalently, OOB angle at the initial condition $\mathbf{z}_0$. ϕ_Ω which is related to but not the same as $\phi = \Omega t$ used in previous chapters for the OOB angle. That is because the $\phi = \Omega t$ is relevant provided that the OOB angle is known to be zero at $t = 0$.

This selection of the phase condition targets capturing the quasiperiodic trajectory reliably, satisfying (at least locally) the uniqueness of the trajectory. It relies on the fact that these quasiperiodic whirling solutions will satisfy either conditions of ${}_n\mathbf{z}_0 = 0$ (i.e. last coordinate's position is zero) or ${}_{n+1}\mathbf{z}_0 = 0$ (i.e. first coordinate's velocity is zero) at many different locations, but they are satisfied together only locally during the full trajectory. Such a phase condition can always be found if the rotating frame trajectory is periodic and the stationary frame trajectory is filling the space under the amplitude of the trajectory by its quasiperiodic precession. Alternative phase conditions such as this one would give the same quasiperiodic solution but with a different initial condition, noting

that any repeating section with period T is called a quasiperiod and solves the EOM.

This, however, brings about the need to consider the OOB angle (ϕ_Ω) as a free parameter since it needs to adjust to keep the phase condition met (see Figure 5.1). Only one OOB angle parameter is needed in the multi-disk case if there is one rotor because this OOB angle rather defines the rotor's angular position with respect to the inertial frame. All other OOB forcing angles of other disks will be a function of this one OOB angle. The formulation is done as follows,

$$\mathbf{M}\mathbf{w}'' + \mathbf{C}\mathbf{w}' + \Omega\mathbf{G}\mathbf{w}' + \mathbf{K}\mathbf{w} + \mathbf{f}_{nl}(\mathbf{w}, \mathbf{w}') + \mathbf{f}(t, \Omega, \phi_\Omega) = \mathbf{0} \tag{5.27}$$

$$\mathbf{z}' = \mathbf{g}(t, \mathbf{z}(t, \mathbf{z}_0, \Omega, \phi_\Omega), \Omega, \phi_\Omega) = \begin{Bmatrix} \mathbf{w}' \\ -\mathbf{M}^{-1}[\mathbf{C}(\Omega)\mathbf{w}' + \mathbf{K}\mathbf{w} + \mathbf{f}_{nl}(\mathbf{w}, \mathbf{w}') + \mathbf{f}(t, \Omega, \phi_\Omega)] \end{Bmatrix} \tag{5.28}$$

$$\mathbf{H}(\mathbf{z}_{p0}, T_p, \Omega_p, \phi_{\Omega_p}) = \mathbf{R}(\theta_{se}(\Omega, T))\ \mathbf{z}_p(T_p, \mathbf{z}_{p0}, \Omega_p, \phi_{\Omega_p}) - \mathbf{z}_{p0} = \mathbf{0}. \tag{5.29}$$

Expansion of the periodicity condition $\mathbf{H} = \mathbf{0}$ around the solution point $\mathbf{x}_p = \{\mathbf{z}_{p0}^T, \Omega_p, \phi_{\Omega_p}\}^T$ gives, omitting the subscript "p" for clarity,

$$\mathbf{H}(\mathbf{x}) = \left.\frac{\partial \mathbf{H}}{\partial \mathbf{z}_0}\right|_{\mathbf{x}^{(\nu)}} \Delta\mathbf{z}_0 + \left.\frac{\partial \mathbf{H}}{\partial T}\right|_{\mathbf{x}^{(\nu)}} \Delta T + \left.\frac{\partial \mathbf{H}}{\partial \lambda}\right|_{\mathbf{x}^{(\nu)}} \Delta\lambda + \left.\frac{\partial \mathbf{H}}{\partial \phi_\Omega}\right|_{\mathbf{x}^{(\nu)}} \Delta\phi_\Omega + \dots. \tag{5.30}$$

Then, the extended system for corrections is given as,

$$\begin{bmatrix} \left.\frac{\partial \mathbf{H}}{\partial \mathbf{z}_0}\right|_{\mathbf{x}^{(\nu)}} & \left.\frac{\partial \mathbf{H}}{\partial T}\right|_{\mathbf{x}^{(\nu)}} & \left.\frac{\partial \mathbf{H}}{\partial \lambda}\right|_{\mathbf{x}^{(\nu)}} & \left.\frac{\partial \mathbf{H}}{\partial \phi_\Omega}\right|_{\mathbf{x}^{(\nu)}} \\ \left.\frac{\partial \mathbf{h}}{\partial \mathbf{z}_0}\right|_{\mathbf{x}^{(\nu)}} & \left.\frac{\partial \mathbf{h}}{\partial T}\right|_{\mathbf{x}^{(\nu)}} & \left.\frac{\partial \mathbf{h}}{\partial \lambda}\right|_{\mathbf{x}^{(\nu)}} & \left.\frac{\partial \mathbf{h}}{\partial \phi_\Omega}\right|_{\mathbf{x}^{(\nu)}} \\ \mathbf{p}^{0^T} & & & \end{bmatrix} \begin{Bmatrix} \Delta\mathbf{z}_0 \\ \Delta T \\ \Delta\lambda \\ \Delta\phi_\Omega \end{Bmatrix}^{(\nu)} = -\begin{Bmatrix} \mathbf{H}(\mathbf{x}^{(\nu)}) \\ \mathbf{h}(\mathbf{x}^{(\nu)}) \\ \langle \mathbf{p}^0,\ \mathbf{x}^{(\nu)} - \mathbf{x}^0 \rangle - \Delta s^0 \end{Bmatrix} \tag{5.31a}$$

$$\begin{bmatrix} \left.\frac{\partial \mathbf{H}}{\partial \mathbf{z}_0}\right|_{\mathbf{x}^{(\nu)}} & \left.\frac{\partial \mathbf{H}}{\partial T}\right|_{\mathbf{x}^{(\nu)}} & \left.\frac{\partial \mathbf{H}}{\partial \lambda}\right|_{\mathbf{x}^{(\nu)}} & \left.\frac{\partial \mathbf{H}}{\partial \phi_\Omega}\right|_{\mathbf{x}^{(\nu)}} \\ \left.\frac{\partial \mathbf{h}}{\partial \mathbf{z}_0}\right|_{\mathbf{x}^{(\nu)}} & \left.\frac{\partial \mathbf{h}}{\partial T}\right|_{\mathbf{x}^{(\nu)}} & \left.\frac{\partial \mathbf{h}}{\partial \lambda}\right|_{\mathbf{x}^{(\nu)}} & \left.\frac{\partial \mathbf{h}}{\partial \phi_\Omega}\right|_{\mathbf{x}^{(\nu)}} \\ \mathbf{p}^{0^T} & & & \end{bmatrix} \begin{Bmatrix} \Delta\mathbf{z}_0 \\ \Delta T \\ \Delta\lambda \\ \Delta\phi_\Omega \end{Bmatrix}^{(\nu)} = -\begin{Bmatrix} \mathbf{H}(\mathbf{x}^{(\nu)}) \\ \mathbf{h}(\mathbf{x}^{(\nu)}) \\ 0 \end{Bmatrix} \tag{5.31b}$$

$$\mathbf{p}^0 = \dot{\mathbf{x}}^0 = (\dot{\mathbf{z}}_0, \dot{T}, \dot{\Omega}, \dot{\phi}_\Omega)^0 \tag{5.32a}$$

$$(\mathbf{z}_0, T, \lambda, \phi_\Omega)^{(\nu+1)} = (\mathbf{z}_0, T, \lambda, \phi_\Omega)^{(\nu)} + (\Delta\mathbf{z}_0, \Delta T, \Delta\lambda, \Delta\phi_\Omega)^{(\nu)}, \tag{5.32b}$$

and the new tangent vector for the arclength continuation is calculated as,

$$\begin{bmatrix} \frac{\partial \mathbf{H}}{\partial \mathbf{z}_0}\Big|_{\mathbf{x}^{(\nu)}} & \frac{\partial \mathbf{H}}{\partial T}\Big|_{\mathbf{x}^{(\nu)}} & \frac{\partial \mathbf{H}}{\partial \lambda}\Big|_{\mathbf{x}^{(\nu)}} & \frac{\partial \mathbf{H}}{\partial \phi_\Omega}\Big|_{\mathbf{x}^{(\nu)}} \\ \frac{\partial \mathbf{h}}{\partial \mathbf{z}_0}\Big|_{\mathbf{x}^{(\nu)}} & \frac{\partial \mathbf{h}}{\partial T}\Big|_{\mathbf{x}^{(\nu)}} & \frac{\partial \mathbf{h}}{\partial \lambda}\Big|_{\mathbf{x}^{(\nu)}} & \frac{\partial \mathbf{h}}{\partial \phi_\Omega}\Big|_{\mathbf{x}^{(\nu)}} \\ & & \mathbf{p}^{0T} & \end{bmatrix} \mathbf{p}^1 = -\begin{Bmatrix} \mathbf{0} \\ \mathbf{0} \\ 1 \end{Bmatrix}, \tag{5.33a}$$

$$\mathbf{p}^1 = \begin{Bmatrix} \dot{\mathbf{z}}_0 \\ \dot{T} \\ \dot{\lambda} \\ \dot{\phi}_\Omega \end{Bmatrix}^1 \rightarrow ||\mathbf{p}^1||^2 = 1. \tag{5.33b}$$

where $\lambda = \Omega$ for this chapter. The partial derivatives needed are derived in Appendix B for the shooting function $\mathbf{H}$. The partial derivative of the phase condition vector $\mathbf{h}$ is as follows: $\partial \mathbf{h}/\partial \mathbf{z}_0$ is a $2 \times n$ matrix whose elements are zero except at indices $(1, n)$ and $(2, n+1)$ which are 1, where n is the dof. Other partial derivatives are zero vectors: $\partial \mathbf{h}/\partial T = \partial \mathbf{h}/\partial \Omega = \partial \mathbf{h}/\partial \phi_\Omega = 0, 0^T$.

The nonautonomous stationary frame equations can be made autonomous, e.g., by the addition of an uncoupled nonlinear oscillator, as suggested by [84] to Eq. 5.2:

$$X' = X - \Omega Y - X(X^2 + Y^2) \tag{5.34a}$$

$$Y' = Y + \Omega X - Y(X^2 + Y^2) \tag{5.34b}$$

whose solution is $X = \cos(\Omega t)$ and $Y = \sin(\Omega t)$ which replace the forcing harmonic terms, where a prime $(\cdot)'$ indicates time derivative. This way, the information of the OOB force direction ϕ_Ω is loaded onto this oscillator's solutions. However, this is not necessary for the method here.

5.2.2 Generating an initial solution for the shooting algorithm

A time simulation can reveal some of the steady-state response expected from the system. The shooting method requires

1. the initial condition $\mathbf{z}_0$ that satisfies a phase condition $\mathbf{h}$,
2. the OOB angle ϕ_Ω at the initial condition according to the phase condition mentioned above,
3. the period T of the repeating signal (the *quasiperiod*),

at the specific rotor speed Ω. The time simulation trajectory can be parsed for the first two points above.

Finding the period One can perform a DFT analysis and get the main frequencies to work out the period. Autocorrelation can be done to find the period of synchronous periodic solutions of the rotor. For finding the period of periodic IR solutions, as well as the quasiperiodic solutions that are periodic in a rotating frame, the following can be done:

1. The trajectory is handled in the configuration space of the disk (i.e. x-y space).
2. Every kth amplitude peak is sampled.
3. The coefficient of variation of amplitude at these sampled peaks are recorded and checked against a small value:

$$\begin{aligned}
\mu_r &= \sum_{i=1}^{N^{data}} r_i \\
\mu_r^{pks} &= \frac{1}{N^{pks}} \sum_{i=1}^{N^{pks}} \left(r_i^{pks} - \mu_r \right) \\
\sigma_r^{pks} &= \sqrt{\frac{1}{N^{pks}} \sum_{i=1}^{N^{pks}} \left(r_i^{pks} - \mu_r^{pks} \right)^2} \\
c_r^{pks} &= \frac{\sigma_r^{pks}}{\mu_r^{pks}} >= \epsilon_r^{pks}
\end{aligned}$$

   where r is the amplitude of the trajectory in the configuration space (x, y), and the subscript i and superscript pks show that the data belong to the i^{th} of the sampled peaks, μ is the arithmetic average, σ is the standard deviation, c is the coefficient of variation, and ϵ is a small value.
4. The coefficient of variation of the corresponding phase differences are recorded, where phase is the angular position of the trajectory in the configuration space, and checked against a small value:

$$\begin{aligned}
\phi &= \arctan_2(y, x) \\
\Delta\phi_i^{pks} &= \phi_{i+1}^{pks} - \phi_i^{pks} \\
\mu_{\Delta\phi}^{pks} &= \frac{1}{N^{pks} - 1} \sum_{i=1}^{N^{pks}-1} \Delta\phi_i^{pks} \\
\sigma_{\Delta\phi}^{pks} &= \sqrt{\frac{1}{N^{pks} - 1} \sum_{i=1}^{N^{pks}-1} \left(\Delta\phi_i^{pks} - \mu_{\Delta\phi}^{pks} \right)^2} \\
c_\phi^{pks} &= \frac{\sigma_{\Delta\phi}^{pks}}{\mu_{\Delta\phi}^{pks}} >= \epsilon_{\Delta\phi}^{pks}
\end{aligned}$$

   where ϕ is the phase of the data point in the configuration space (x, y).

5. The coefficient of variation of the corresponding time differences are recorded and checked against a small value:

$$\begin{aligned}
\Delta t_i^{pks} &= t_{i+1}^{pks} - t_i^{pks} \\
\mu_{\Delta t}^{pks} &= \frac{1}{N^{pks}-1} \sum_{i=1}^{N^{pks}-1} \Delta t_i^{pks} \\
\sigma_{\Delta t}^{pks} &= \sqrt{\frac{1}{N^{pks}-1} \sum_{i=1}^{N^{pks}-1} \left(\Delta t_i^{pks} - \mu_{\Delta t}^{pks}\right)^2} \\
c_t^{pks} &= \frac{\sigma_{\Delta t}^{pks}}{\mu_{\Delta t}^{pks}} >= \epsilon_{\Delta t}^{pks}
\end{aligned}$$

   where t is the time.
6. If the check is not satisfied for any of the inequality checks above, then k is incremented `k:=k+1`.

This process finds the repeating section of the signal and its *quasiperiod*. It is not affected by the configuration space phase swept by the trajectory in one quasiperiod. This method only works for a trajectory which looks periodic in some rotating frame rotating with a constant speed.(as assumed here). It is not suitable for a true quasiperiodic solution for which there is not a rotating frame with periodic trajectory, since in that case these coefficients of variation are always high. The same code can be used to detect periodicity. Additionally, it can be used to find the rotating frame rotational speed which make the trajectory look periodic in the configuration space. This can be done by analysing the configuration space phase stretch needed in one period so that the trajectory reaches where it starts.

5.2.3 Stability calculation with Floquet multipliers

If, for a certain initial condition, the rotating frame solution is periodic (as assumed here), the Floquet analysis (see e.g. the text book [171]) can be done in the rotating frame. The stationary frame 1st order EOM is $\dot{\mathbf{z}}(t, \mathbf{z}_0) = \mathbf{g}(t, \mathbf{z}(t, \mathbf{z}_0))$ in the first order form (which is autonomous if Eq. 5.34 is used as states: $\dot{\mathbf{z}}(t, \mathbf{z}_0) = \mathbf{g}(\mathbf{z}(t, \mathbf{z}_0)))$ whereas the rotating frame 1st order EOM is $\dot{\mathbf{q}}(t, \mathbf{q}_0) = \mathbf{f}(\mathbf{q}(t, \mathbf{q}_0))$ where $\mathbf{f}(\mathbf{q}(t, \mathbf{q}_0))$ is periodic with period T. Note that $\mathbf{q}_0$ denotes here the initial condition of the periodic solution in the rotating frame and the trajectory is written dependent on the initial conditions. The monodromy matrix $\partial \mathbf{q}(T, \mathbf{q}_0)/\partial \mathbf{q}_0$ can be calculated from the stationary frame quasiperiodic evolution matrix as follows,

$$\frac{\partial \mathbf{q}(t, \mathbf{q}_0)}{\partial \mathbf{q}_0} = \mathbf{T}^{-1}(\Omega t) \frac{\partial \mathbf{z}(t, \mathbf{z}_0)}{\partial \mathbf{z}_0} \mathbf{T}(0). \tag{5.35}$$

where $\mathbf{T}$ is the rotating frame transform matrix given in Eq. (2.13).

Instead, the rotating frame transform matrix can be replaced by the stationary frame rotation matrix $\mathbf{R}$ (Eq. 5.5) for which the transform is performed via $\mathbf{v}(t, \mathbf{v}_0) = \mathbf{R}\mathbf{z}(t, \mathbf{z}_0)$. Then, the Floquet multipliers can be found from the eigenvalues of $\frac{\partial \mathbf{v}(T, \mathbf{v}_0)}{\partial \mathbf{v}_0}$ that is calculated using the stationary frame evolution matrix as follows,

$$\begin{aligned} \frac{\partial \mathbf{v}(t, \mathbf{v}_0)}{\partial \mathbf{v}_0} &= \mathbf{R}(\Omega t) \frac{\partial \mathbf{z}(t, \mathbf{z}_0)}{\partial \mathbf{z}_0} \mathbf{R}^{-1}(0) \\ &= \mathbf{R}(\Omega t) \frac{\partial \mathbf{z}(t, \mathbf{z}_0)}{\partial \mathbf{z}_0} \end{aligned} \tag{5.36}$$

The proof and validation are given below and the results are given in Figures 5.3-5.5.

Proof The first order variation of the solution is given by the Taylor series:

$$\mathbf{q}(T, \mathbf{q}_0 + \Delta \mathbf{q}_0) = \mathbf{q}(T, \mathbf{q}_0) + \left. \frac{\partial \mathbf{q}}{\partial \mathbf{q}_0} \right|_{t=T} \Delta \mathbf{q}_0 + \dots \tag{5.37}$$

Therefore, the first order variation of the last point of the periodic trajectory with respect to its initial condition is the matrix $\partial \mathbf{q} / \partial \mathbf{q}_0 |_{t=T}$. With a similar analysis to that of Eq. B.6 in Appendix B, the matrix $\partial \mathbf{q} / \partial \mathbf{q}_0 |_{t=T}$ can be calculated by the time simulation of the following equations,

$$\boldsymbol{\alpha}'_{rot}(t) = \mathbf{f}_{\mathbf{q}}(\mathbf{q}(t, \mathbf{q}_0)) \boldsymbol{\alpha}(t) \tag{5.38a}$$

$$\boldsymbol{\alpha}_{rot}(t) = \frac{\partial \mathbf{q}(t, \mathbf{q}_0)}{\partial \mathbf{q}_0} \tag{5.38b}$$

$$\boldsymbol{\alpha}_{rot}(t = 0) = \frac{\partial \mathbf{q}_0}{\partial \mathbf{q}_0} = I_{2n \times 2n} \tag{5.38c}$$

$$\mathbf{m} = \boldsymbol{\alpha}_{\mathbf{q}}(T) \tag{5.38d}$$

where $\boldsymbol{\alpha}_{\mathbf{q}}$ is the evolution matrix in the rotating frame, and the subscript $(\cdot)_{rot}$ is in comparison to $\boldsymbol{\alpha}$ of Eq. B.6 which is in the stationary frame; and $\mathbf{f}_{\mathbf{q}}(t, \mathbf{q}_0)$ is periodic with period T. The so-called monodromy matrix $\mathbf{m}$ is a measure of variation of solutions of the linearized system after one period for periodic solutions. If any one of the eigenvalues of $\mathbf{m}$ has magnitude greater than 1, then the periodic solution is unstable. The stationary frame counterpart of the same equation is the same as that calculated for the $\partial \mathbf{H} / \partial \mathbf{z}_0$

calculation, as shown in Eq. B.6, repeated below in 5.39.

$$\boldsymbol{\alpha}'(t) = \mathbf{g}_{\mathbf{z}}(t, \mathbf{z}(t, \mathbf{z}_0))\boldsymbol{\alpha}(t) \tag{5.39a}$$

$$\boldsymbol{\alpha}(t) = \frac{\partial \mathbf{z}(t, \mathbf{z}_0)}{\partial \mathbf{z}_0} \tag{5.39b}$$

$$\boldsymbol{\alpha}(t=0) = \frac{\partial \mathbf{z}_0}{\partial \mathbf{z}_0} = I_{2n\times 2n} \tag{5.39c}$$

$$\widetilde{\mathbf{m}} = \boldsymbol{\alpha}(T) \tag{5.39d}$$

where $\widetilde{\mathbf{m}}$ is not periodic with period T.

The rotating frame transform $\mathbf{z} = \mathbf{T}\mathbf{q}$ is as given in Eq. (2.13). Alternatively, if the stationary frame is made autonomous by augmenting the system of ODE with the nonlinear oscillator in Eq. (5.34), the transform can be expressed as follows for the 2-dof Zilli system,

$$\mathbf{z} = \mathbf{T}\mathbf{q}\ ,\ \mathbf{T} = \begin{bmatrix} \mathbf{T}_2 & \mathbf{0} & \mathbf{0} \\ \Omega\mathbf{T}_2\mathbf{J}_2 & \mathbf{T}_2 & \mathbf{0} \\ \mathbf{0} & \mathbf{0} & \mathbf{T}_2 \end{bmatrix} \tag{5.40}$$

$$\mathbf{z} = [x, y, x', y', X, Y]^T\ ,\ \mathbf{q} = [u, v, u', v', 1, 0]^T. \tag{5.41}$$

The rotating frame transform to the augmented system is not defined with a separate letter as the equations would not change. In that case, the rotating matrix would become,

$$\mathbf{R} = \begin{bmatrix} \mathbf{R}_2 & \mathbf{0} & \mathbf{0} \\ \mathbf{0} & \mathbf{R}_2 & \mathbf{0} \\ \mathbf{0} & \mathbf{0} & \mathbf{R}_2 \end{bmatrix}. \tag{5.42}$$

where $\mathbf{R}_2$ is defined in Eq. (5.4) and $\mathbf{T}_2$, $\mathbf{J}_2$ and $\mathbf{0}$ are defined in Eq. (2.13). However, for the stability calculations the last states that come from the X-Y nonlinear oscillator (Eq. (5.34)) is redundant as the rotating frame solutions are already autonomous and periodic without these last two states; this creates an additional Floquet multiplier that is 1.

In order to calculate the Floquet multipliers in the stationary frame without the need to transform the EOM, the relation between $\partial\mathbf{q}(t, \mathbf{q}_0)/\partial\mathbf{q}_0$ and $\partial\mathbf{z}(t, \mathbf{z}_0)/\partial\mathbf{z}_0$ must be known so that knowing $\partial\mathbf{z}(t, \mathbf{z}_0)/\partial\mathbf{z}_0$ would suffice without the knowledge of $\partial\mathbf{q}(t, \mathbf{q}_0)/\partial\mathbf{q}_0$. Here, $\partial\mathbf{q}(t, \mathbf{q}_0)/\partial\mathbf{q}_0$ can be expressed in terms of the stationary frame trajectory as follows,

$$\begin{aligned} \frac{\partial \mathbf{q}(t, \mathbf{q}_0)}{\partial \mathbf{q}_0} &= \frac{\partial}{\partial \mathbf{q}_0}\left(\mathbf{T}^{-1}(\Omega t)\mathbf{z}(t, \mathbf{z}_0)\right) \\ &= \mathbf{T}^{-1}(\Omega t)\frac{\partial \mathbf{z}(t, \mathbf{z}_0)}{\partial \mathbf{q}_0} \end{aligned} \tag{5.43}$$

where $\partial \mathbf{z}(t, \mathbf{q}_0)/\partial \mathbf{q}_0$ can be expanded as,

$$\begin{aligned}\frac{\partial \mathbf{z}(t, \mathbf{z}_0)}{\partial q_{0j}} &= \lim_{\varepsilon \to 0} \frac{\mathbf{z}(t, \mathbf{T}(0)(\mathbf{q}_0 + \varepsilon \mathbf{e}_j)) - \mathbf{z}(t, \mathbf{T}(0)\mathbf{q}_0)}{\varepsilon} \\ &= \lim_{\varepsilon \to 0} \frac{\mathbf{z}(t, \mathbf{z}_0 + \varepsilon \mathbf{T}(0)\mathbf{e}_j) - \mathbf{z}(t, \mathbf{z}_0)}{\varepsilon}\end{aligned} \tag{5.44}$$

which appears the same as the directional derivative,

$$\frac{\partial \mathbf{z}(t, \mathbf{z}_0)}{\partial \mathbf{z}_0} \mathbf{T}(0)\mathbf{e}_j = \lim_{\varepsilon \to 0} \frac{\mathbf{z}(t, \mathbf{z}_0 + \varepsilon \mathbf{T}(0)\mathbf{e}_j) - \mathbf{z}(t, \mathbf{z}_0)}{\varepsilon}. \tag{5.45}$$

Therefore,

$$\frac{\partial \mathbf{z}(t, \mathbf{z}_0)}{\partial q_{0j}} = \frac{\partial \mathbf{z}(t, \mathbf{z}_0)}{\partial \mathbf{z}_0} \mathbf{T}(0)\mathbf{e}_j \tag{5.46}$$

or, for all columns,

$$\frac{\partial \mathbf{z}(t, \mathbf{z}_0)}{\partial \mathbf{q}_0} = \frac{\partial \mathbf{z}(t, \mathbf{z}_0)}{\partial \mathbf{z}_0} \mathbf{T}(0) \tag{5.47}$$

and when combined with Eq. (5.43) the sought relation is found as,

$$\frac{\partial \mathbf{q}(t, \mathbf{q}_0)}{\partial \mathbf{q}_0} = \mathbf{T}^{-1}(\Omega t) \frac{\partial \mathbf{z}(t, \mathbf{z}_0)}{\partial \mathbf{z}_0} \mathbf{T}(0). \tag{5.48}$$

As a result, once $\partial \mathbf{z}(t, \mathbf{z}_0)/\partial \mathbf{z}_0$ is determined from the integral of Eq. (5.39), then using Eq. (5.48) one can calculate the monodromy matrix $\partial \mathbf{q}(T, \mathbf{q}_0)/\partial \mathbf{q}_0$. This way the Floquet analysis can be done in the stationary frame without the need to transform the EOM, although still the transform matrix is needed. However, the rotating frame transform matrix can be replaced by the stationary frame rotation matrix $\mathbf{R}$ (Eq. 5.5). The rotation follows the transform $\mathbf{v}(t, \mathbf{v}_0) = \mathbf{R}\mathbf{z}(t, \mathbf{z}_0)$. Then the transform of the evolution matrix becomes,

$$\begin{aligned}\frac{\partial \mathbf{v}(t, \mathbf{v}_0)}{\partial \mathbf{v}_0} &= \mathbf{R}(\Omega t) \frac{\partial \mathbf{z}(t, \mathbf{z}_0)}{\partial \mathbf{z}_0} \mathbf{R}^{-1}(0) \\ &= \mathbf{R}(\Omega t) \frac{\partial \mathbf{z}(t, \mathbf{z}_0)}{\partial \mathbf{z}_0}\end{aligned} \tag{5.49}$$

where $\mathbf{v}'(t, \mathbf{v}_0) = \mathbf{k}(\mathbf{v}(t, \mathbf{v}_0))$ is the equation of motion in the instantaneously rotated, stationary frame, and $\mathbf{R}(t = 0) = \mathbf{I}$.

Validation with EOM transform

The transform of the EOM from stationary frame to rotating frame can be done as follows,

$$\mathbf{z}' = \mathbf{g}(\mathbf{z}) \Leftarrow \mathbf{z} = \mathbf{T}\mathbf{q}\ , \quad \mathbf{z}' = \mathbf{T}'_{rot}\mathbf{q} + \mathbf{T}\mathbf{q}'\ , \quad \mathbf{T}'_{rot} = \Omega\mathbf{J}\mathbf{T} \tag{5.50}$$

$$\mathbf{T}\mathbf{q}' = \mathbf{g}(\mathbf{T}\mathbf{q}) - \mathbf{T}'_{rot}\mathbf{q} \tag{5.51}$$

$$\mathbf{q}' = \mathbf{T}^{-1}\mathbf{g}(\mathbf{T}\mathbf{q}) - \mathbf{T}^{-1}\mathbf{T}'_{rot}\mathbf{q}\ , \quad \mathbf{T}^{-1}\mathbf{T}'_{rot} = \Omega\mathbf{J} \tag{5.52}$$

$$\mathbf{q}' = \mathbf{f}(\mathbf{q}) = \mathbf{T}^{-1}\mathbf{g}(\mathbf{T}\mathbf{q}) - \Omega\mathbf{J}\mathbf{q} \tag{5.53}$$

$$\mathbf{f}(\mathbf{q}(t)) = \mathbf{T}^{-1}(t)\mathbf{g}(\mathbf{T}(t)\mathbf{q}(t)) - \Omega\mathbf{J}\mathbf{q}(t). \tag{5.54}$$

where

$$\mathbf{J} = \begin{Bmatrix} \mathbf{J}_2 & \mathbf{0} \\ \mathbf{0} & \mathbf{J}_2 \end{Bmatrix}\ , \quad \mathbf{J}_2 = \begin{Bmatrix} 0 & -1 \\ 1 & 0 \end{Bmatrix}. \tag{5.55}$$

Then the Jacobian,

$$\mathbf{f}_{\mathbf{q}} = \mathbf{T}^{-1}\mathbf{g}_{\mathbf{z}}\mathbf{T} - \Omega\mathbf{J}. \tag{5.56}$$

Therefore, following the time derivatives as in Appendix B,

$$\frac{\mathrm{d}}{\mathrm{d}t}\left(\frac{\partial \mathbf{q}(t,\mathbf{q}_0)}{\partial \mathbf{q}_0}\right) = \mathbf{f}_{\mathbf{q}}\left(\frac{\partial \mathbf{q}(t,\mathbf{q}_0)}{\partial \mathbf{q}_0}\right) \tag{5.57}$$

$$\frac{\mathrm{d}}{\mathrm{d}t}\left(\mathbf{T}^{-1}(\Omega t)\frac{\partial \mathbf{z}(t,\mathbf{z}_0)}{\partial \mathbf{z}_0}\mathbf{T}(0)\right) = \left(\mathbf{T}^{-1}\mathbf{g}_{\mathbf{z}}\mathbf{T} - \Omega\mathbf{J}\right)\left(\mathbf{T}^{-1}(\Omega t)\frac{\partial \mathbf{z}(t,\mathbf{z}_0)}{\partial \mathbf{z}_0}\mathbf{T}(0)\right) \tag{5.58}$$

$$(\mathbf{T}^{-1})'(\Omega t)\frac{\partial \mathbf{z}(t,\mathbf{z}_0)}{\partial \mathbf{z}_0} + \mathbf{T}^{-1}(\Omega t)\frac{\mathrm{d}}{\mathrm{d}t}\left(\frac{\partial \mathbf{z}(t,\mathbf{z}_0)}{\partial \mathbf{z}_0}\right) = \left(\mathbf{T}^{-1}\mathbf{g}_{\mathbf{z}}\mathbf{T} - \Omega\mathbf{J}\right)\left(\mathbf{T}^{-1}(\Omega t)\frac{\partial \mathbf{z}(t,\mathbf{z}_0)}{\partial \mathbf{z}_0}\right) \tag{5.59}$$

$$\frac{\mathrm{d}}{\mathrm{d}t}\left(\frac{\partial \mathbf{z}(t,\mathbf{z}_0)}{\partial \mathbf{z}_0}\right) = \mathbf{g}_{\mathbf{z}}(t,\mathbf{z}_0)\left(\frac{\partial \mathbf{z}(t,\mathbf{z}_0)}{\partial \mathbf{z}_0}\right) \tag{5.60}$$

where identity $\mathbf{T}(\mathbf{T}^{-1})' = -\Omega\mathbf{J}$ is used.

5.3 Results

The bifurcation diagram of the 2:1 quasiperiodic internal resonance is calculated following the quasiperiodic shooting-continuation formulation given in the previous section (Section 5.2) and shown in Figure 5.2. The quasiperiodic shooting-continuation method numerically required smaller step sizes to not jump onto synchronous solutions, compared to the periodic shooting-continuation which is formulated around the periodicity condition.

It is also important to note that, although the cubic Zilli system was analysed here, the method presented in this chapter do not rely on the nonlinearity, but rather depends on the response type. Therefore, other nonlinearities, such as quintic (see the mention

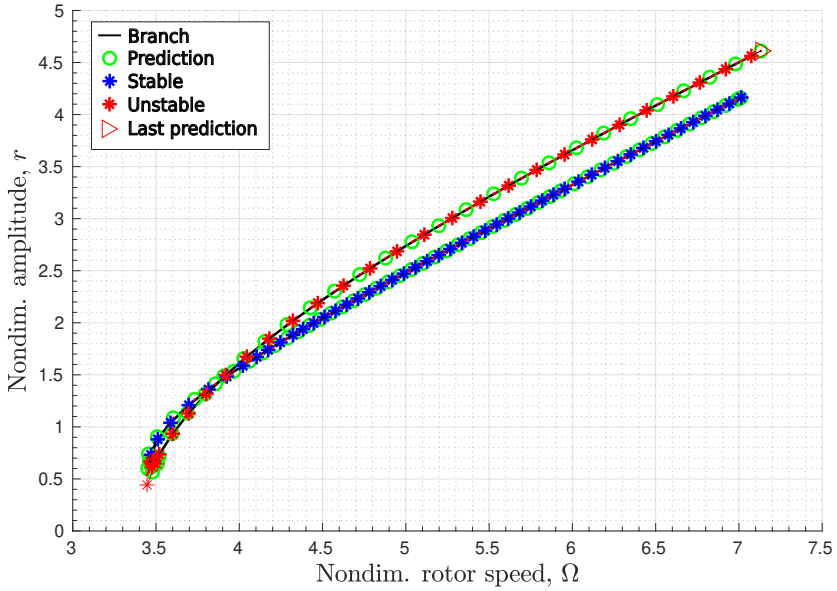


Figure 5.2: Bifurcation diagram of the 2:1 (SL) solution of Eq. (3.19) as position amplitude vs. rotor speed obtained with the quasiperiodic continuation method explained in this chapter (see the SL branch obtained in the rotating frame in AUTO in Figure 3.5). Blue stars show the stable solutions and red stars show the unstable solutions. Thin red star shows a nonconvergent iteration, which got re-attempted with a smaller step size with success.

in Figure 5.8), would work the same way in that method, provided that the solution is quasiperiodic and has a periodic look in the rotating frame of the rotor. Though, it is important to notice that in rotating machinery, this type of response is not uncommon and observed many times in theoretical studies [34, 31, 133, 85, 25].

5.3.1 Stability calculation results

In order to better understand the monodromy matrix $\mathbf{m} = \partial\mathbf{q}(T, \mathbf{q}_0)/\partial\mathbf{q}_0$, the time evolutions of the magnitudes of the eigenvalues of the evolution matrices are plotted in Figures 5.3 - 5.5 according to the methods in Table 5.1: Firstly, because the eigenvalues from methods (i) and (ii) in this list are exactly the same, Figures 5.3 - 5.5 give the result of only one in the first of the subfigures of these figures as the stationary frame result. Secondly, the stationary frame EOM was made autonomous with an uncoupled nonlinear oscillator (see Eq. (5.34) at the end of Section 5.2.1). As a result, there are extra two eigenvalues corresponding to the nonlinear oscillator states X and Y; because these states are uncoupled from the EOM and are periodic solutions, they themselves add another multiplier with magnitude 1. Thirdly, the second of the subfigures in Figures 5.3 - 5.5 (method (iii)) were calculated using a periodic implementation of the shooting-continuation method presented in this chapter on the periodic solutions of the same 2:1

Table 5.1: Methods for the evolution matrix eigenvalue calculation used to explain the monodromy matrix $\mathbf{m}$ better.

Method	**Matrix whose eigenvals. are presented**	**Eq. used**	**Presented in Figure**
(i)	The rotated frame evolution matrix $\partial\mathbf{v}(t,\mathbf{v}_0)/\partial\mathbf{v}_0$ calculated using the stationary frame evolution matrix $\partial\mathbf{z}(t,\mathbf{z}_0)/\partial\mathbf{z}_0$.	Eq. (5.49)	Subfigures (a) for Figures 5.3 - 5.5
(ii)	The rotating frame evolution matrix $\partial\mathbf{q}(t,\mathbf{q}_0)/\partial\mathbf{q}_0$ calculated using the stationary frame evolution matrix $\partial\mathbf{z}(t,\mathbf{z}_0)/\partial\mathbf{z}_0$.	Eq. (5.48)	Subfigures (a) for Figures 5.3 - 5.5
(iii)	The rotating frame evolution matrix $\partial\mathbf{q}(t,\mathbf{q}_0)/\partial\mathbf{q}_0$ calculated directly in the rotating frame.	Eq. (5.38)	Subfigures (b) for Figures 5.3 - 5.5

IRs in the rotating frame, which is formulated as follows,

$$\begin{aligned}\mathbf{H}(\mathbf{z}_0,T,\Omega) &= \mathbf{R}(2\pi)\mathbf{z}(T,\mathbf{z}_0,\Omega)-\mathbf{z}_0\\ &= \mathbf{z}(T,\mathbf{z}_0,\Omega)-\mathbf{z}_0=\mathbf{0}\end{aligned} \tag{5.61a}$$

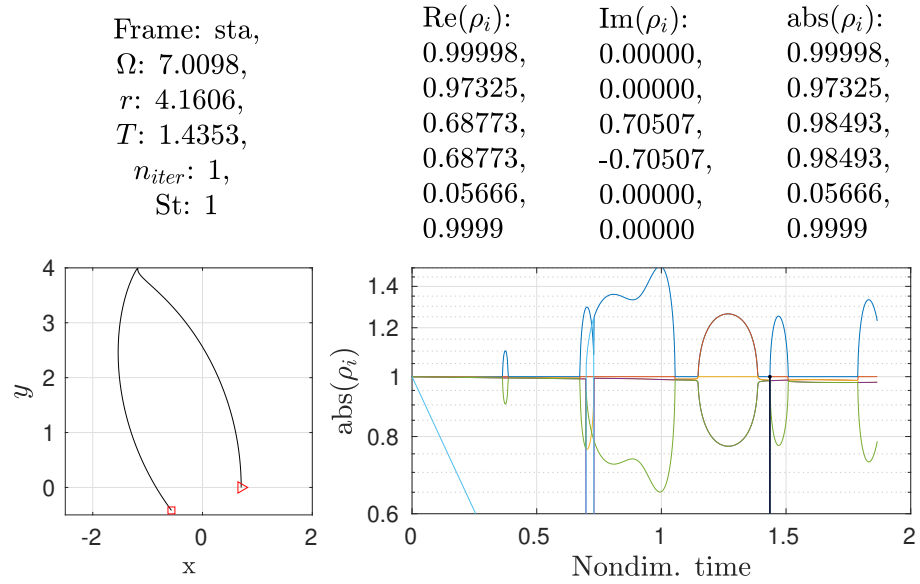
$$\begin{bmatrix} \left.\frac{\partial\mathbf{H}}{\partial\mathbf{z}_0}\right|_{\mathbf{x}^{(\nu)}} & \left.\frac{\partial\mathbf{H}}{\partial T}\right|_{\mathbf{x}^{(\nu)}} & \left.\frac{\partial\mathbf{H}}{\partial\Omega}\right|_{\mathbf{x}^{(\nu)}} \\ \left.\frac{\partial h}{\partial\mathbf{z}_0}\right|_{\mathbf{x}^{(\nu)}} & \left.\frac{\partial h}{\partial T}\right|_{\mathbf{x}^{(\nu)}} & \left.\frac{\partial h}{\partial\Omega}\right|_{\mathbf{x}^{(\nu)}} \\ & \mathbf{p}^{0^T} & \end{bmatrix} \begin{Bmatrix}\Delta\mathbf{z}_0\\ \Delta T\\ \Delta\Omega\end{Bmatrix}^{(\nu)} = -\begin{Bmatrix}\mathbf{H}(\mathbf{x}^{(\nu)})\\ h(\mathbf{x}^{(\nu)})\\ \langle\mathbf{p}^0,\ \mathbf{x}^{(\nu)}-\mathbf{x}^0\rangle-\Delta s^0\end{Bmatrix} \tag{5.61b}$$

$$h(\mathbf{z}_0,T,\Omega) = {}_{n+1}\mathbf{z}_0 = 0, \tag{5.61c}$$

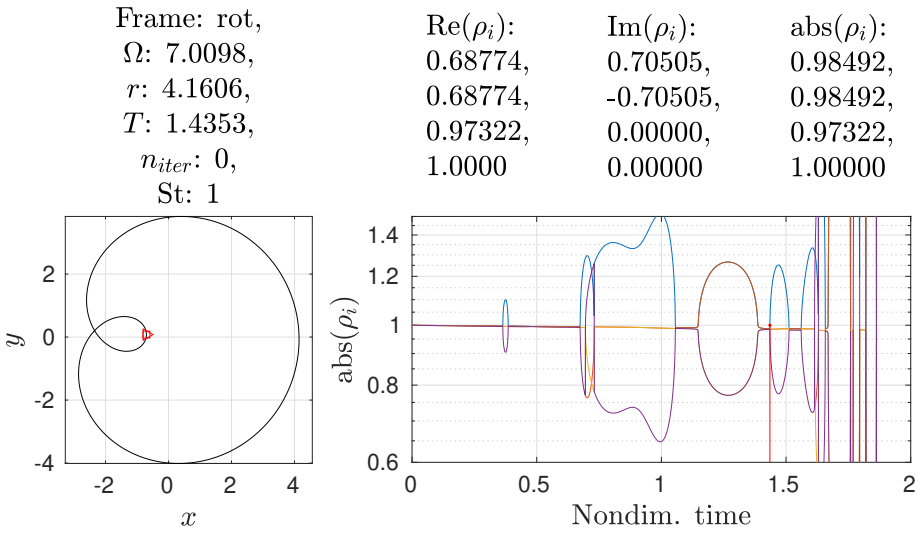
and the rest of the discussion in Section 5.2 on the calculation of branch of solutions is relevant. For the related methods one can refer to [72, 118].Eq. (5.61) gives the continuation implementation where the free parameter of the continuation is a system parameter; whereas the NNM continuation method presented by Peeters et al. [118] uses period as the free parameter.

Figures 5.3 and 5.4 show that the eigenvalues of the evolution matrices are the same for all of the three methods in Table 5.1: Both transforming the stationary frame evolution matrix to the rotating frame using Eq. (5.48) and transforming the stationary frame evolution matrix to the rotated frame using Eq. (5.49) preserves the evolution of the magnitude of the multipliers in time with respect to calculating the evolution matrix in the rotating frame directly using Eq. (5.38). Nevertheless, Figure 5.5 shows that a different quasiperiodic section of the same trajectory gives a different time evolution for the magnitude of the eigenvalues, but the Floquet multipliers are the same, and thus indicate the stability correctly.

When looking at Figures 5.3 and 5.4, the perceived jump of the eigenvalues can be noticed, which is simply the artefact of reordering the magnitudes of the eigenvalues. Excessive growth of the eigenvalue magnitudes after the vertical line that indicated the

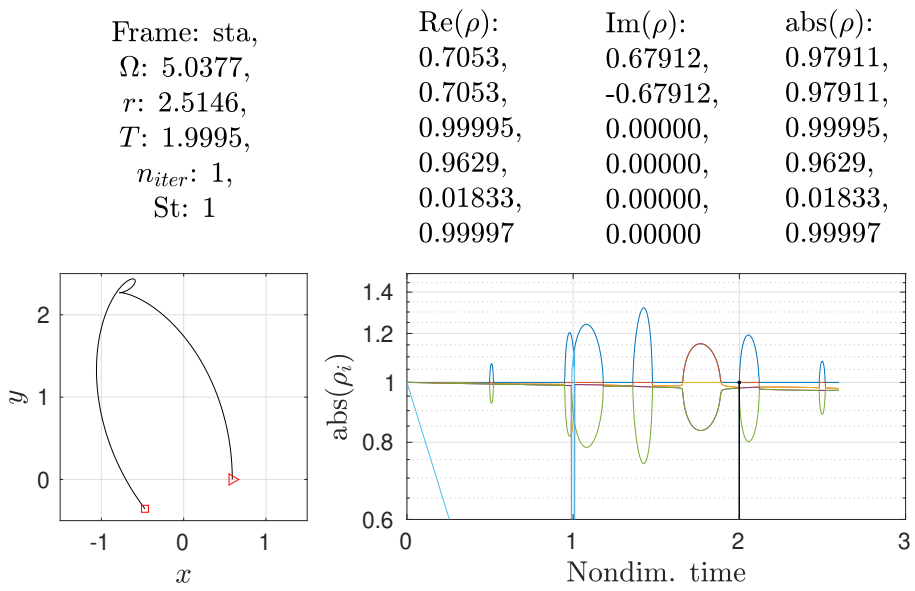


(a) Magnitude of eigenvalues calculated using methods (i) or (ii) in Table 5.1 for the stable solution at $\Omega = 7.0098$ on the quasiperiodic solution branch for the stationary frame EOM.

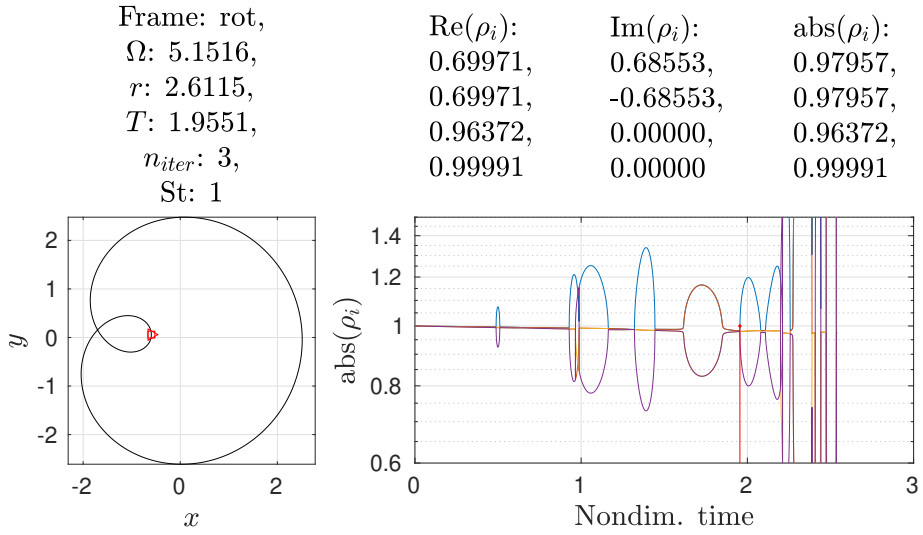


(b) Magnitude of eigenvalues calculated using method (iii) in Table 5.1 for the stable solution at $\Omega = 7.0098$ on the periodic solution branch for the rotating frame EOM.

Figure 5.3: Magnitude of the eigenvalues of $\boldsymbol{\alpha}(t)$, which correspond to the Floquet multipliers at $t = T$ on the rotating-frame periodic solutions. The vertical line is at $t = T$, and its top is at level 1. The solution point data is given above the configuration space on the left. Floquet multipliers are given above the multiplier evolution plots on the right. 'St' stands for stability, n_{iter} is the iteration count, ν.

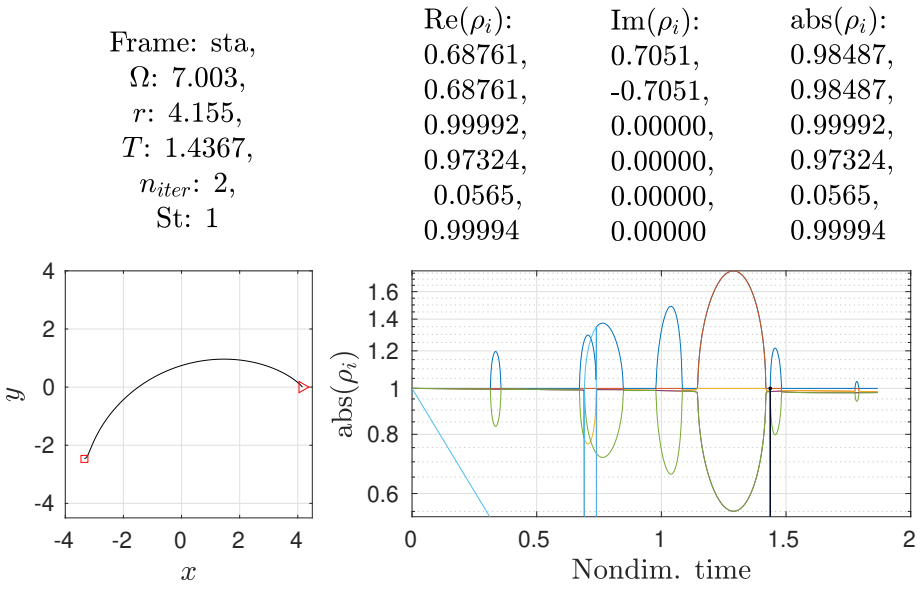


(a) Magnitude of eigenvalues calculated using methods (i) or (ii) in Table 5.1 for the stable solution at $\Omega = 5.0377$ on the quasiperiodic solution branch for the stationary frame EOM.

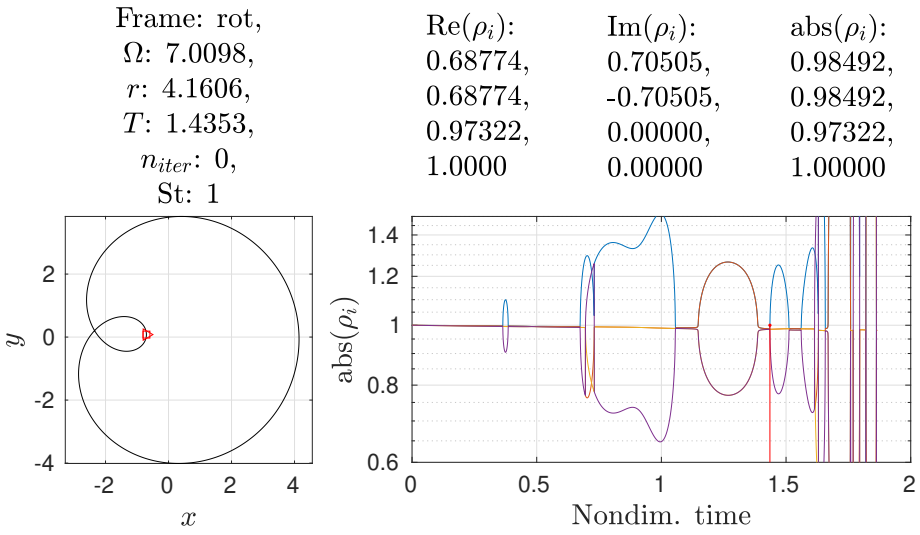


(b) Magnitude of eigenvalues calculated using method (iii) in Table 5.1 for the stable solution at $\Omega = 5.1516$ on the periodic solution branch for the rotating frame EOM.

Figure 5.4: Magnitude of the eigenvalues of $\boldsymbol{\alpha}(t)$, which correspond to the Floquet multipliers at $t = T$ on the rotating-frame periodic solutions. The vertical line is at $t = T$, and its top is at level 1. The solution point data is given above the configuration space on the left. Floquet multipliers are given above the multiplier evolution plots on the right. 'St' stands for stability, n_{iter} is the iteration count, ν. Note the slight difference in the rotor speed.



(a) Magnitude of eigenvalues calculated using methods (i) or (ii) in Table 5.1 for the stable solution at $\Omega = 7.003$ on the quasiperiodic solution branch for the stationary frame EOM.



(b) Magnitude of eigenvalues calculated using method (iii) in Table 5.1 for the stable solution at $\Omega = 7.0098$ on the periodic solution branch for the rotating frame EOM.

Figure 5.5: Magnitude of the eigenvalues of $\boldsymbol{\alpha}(t)$, which correspond to the Floquet multipliers at $t = T$ on the rotating-frame periodic solutions. The vertical line is at $t = T$, and its top is at level 1. The solution point data is given above the configuration space on the left. Floquet multipliers are given above the multiplier evolution plots on the right. 'St' stands for stability, n_{iter} is the iteration count, ν.

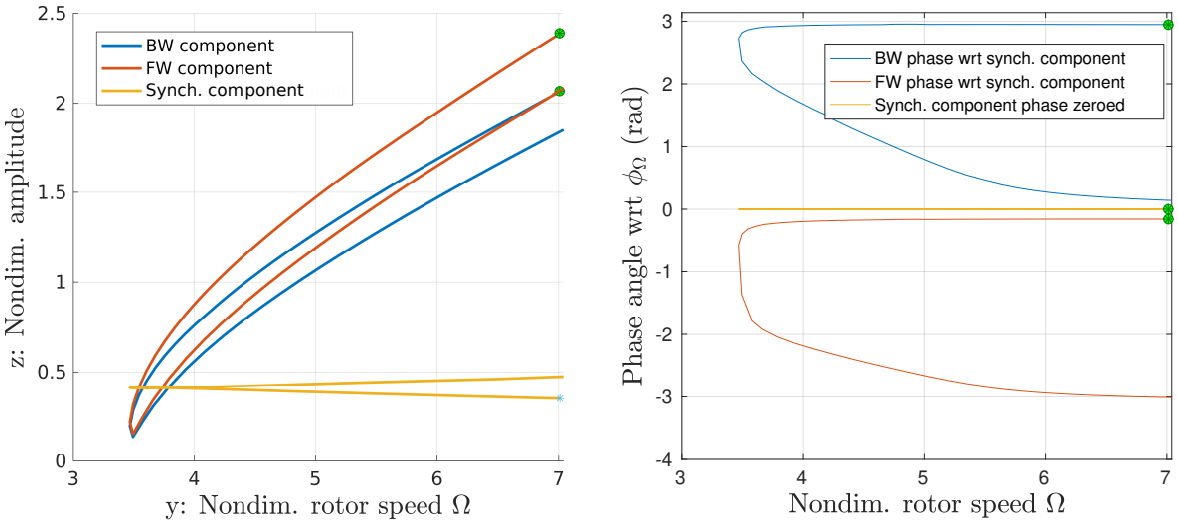


Figure 5.6: DFT results. Left: DFT amplitudes. Right: DFT phases with respect to the drive speed component's phase. Green dots mark the start of the solution branches at their stable side. Stability is not indicated but solution is stable until the the fold.

quasiperiod T is also visible. Lastly, subfigures (a) and (b) of Figures 5.3 and 5.4 show samples that are at slightly different positions along the branch due to the branches being calculated with separate methods. Next, the results of the DFT analysis are given showing well-separated, discrete frequency component branches; dense spectra do not seem to occur in this work.

5.3.2 DFT branches

The frequency content of IR modes can give the finger print of the mode, indicating the number of underlying frequencies/modes, the commensurability of the main constituent frequencies, and the relation of the frequencies in the stationary or rotating frame of reference. This analysis can be done for the whole branch, extracting the branches of the underlying modal contributions to the IR, which shows their evolution along the branch. The DFT results are shown in Figure 5.6 which shows that the amplitude dependence of the FW and BW modes are slightly different, FW component being the higher of the two contributions. Despite the increase of the OOB forcing with rotor speed ($f = me\Omega^2$) the frequency contribution in the drive speed did not change the same level because of energy transfer to FW and BW components. In the stable/unstable high-amplitude end, the FW/BW component is in-phase with the forcing, and the other component is out-of-phase with the forcing.

The Campbell diagram of the underlying linear system is given with the overlaid DFT branches of the 2:1 IR in Figure 5.7. This allows one to make use of the Campbell diagram in the light of the nonlinear response expectations, along with interpreting the frequency line intersecting point as IR predictions which was done in [30]. As can be seen in Figure

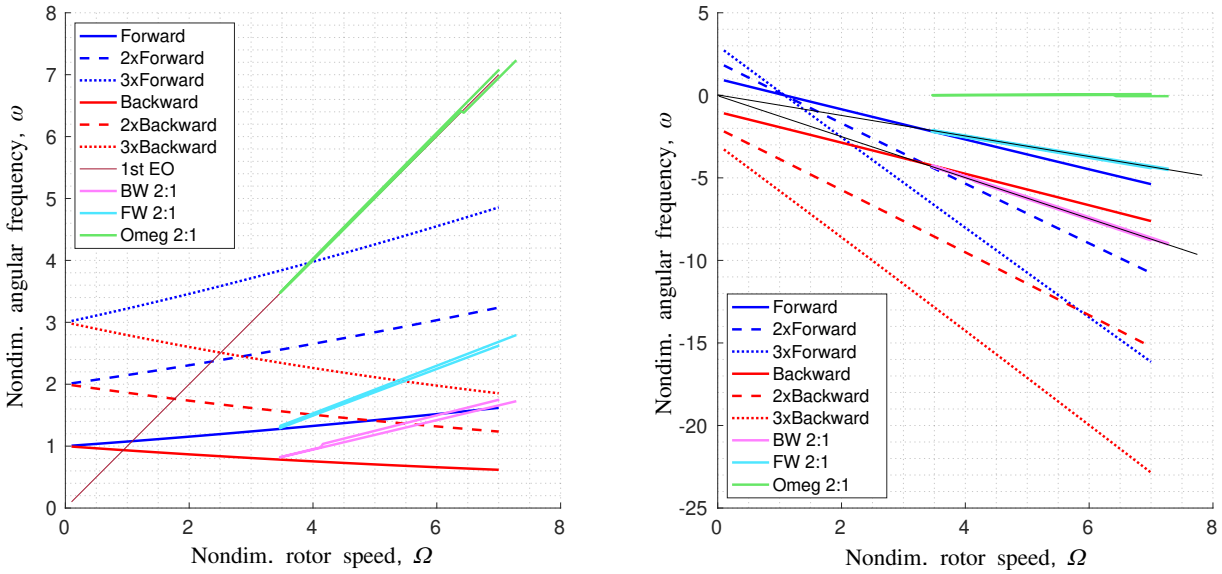


Figure 5.7: The rotating frame Campbell diagram with overlaid DFT branches of 2:1 IR from Eq (4.2) with cubic stiffness. The thin solid black lines indicate the linear evolution of the main frequencies of the 2:1 IR with the rotor speed.

5.7, the intersection of $2\,\omega^{rot}_{f,linear}$ (- -) and $1\times\omega^{rot}_{b,linear}$ (—) is the point where the BW frequency content $\omega^{rot}_{b,2:1}$ (—) emanates which is where $2\omega^{rot}_{f,2:1}$ content would appear due to the relation $2\,\omega^{rot}_{f}=\omega^{rot}_{b}$.

Figure 5.7 shows that once the onset drive speed and underlying frequency is established (or any other solution in the family), the frequencies for the rest of the family are fixed by the locked 2:1 relationship. The observation from Figure 5.7 also shows that the DFT branches $\omega^{rot}_{b,2:1}$ (—) and $\omega^{rot}_{f,2:1}$ (—) are linear in the Campbell diagram. This fact was also mentioned in [11] for $\omega^{sta}_{f}-\omega^{sta}_{b}=\Omega$ response. Interestingly, this linearity is also present with the quintic stiffness (Figure 5.8) replacing the cubic stiffness in Eq. (4.2).

5.4 Conclusion

In this chapter, a quasiperiodic continuation method is defined for continuing the quasiperiodic solutions of a nonautonomous, isotropic, gyroscopic rotor-stator system with cubic nonlinearity. The bifurcation diagram was successfully obtained for the quasiperiodic solutions. This shows that the available tools for the periodic continuation can be utilised and generalised to cover more diverse rotordynamics phenomena such as quasiperiodicity. Here, the quasiperiodic solutions are confined to those that have a periodic look in the rotating frame of the rotor; however, the periodicity information of the general case of quasiperiodic motion can potentially be extracted by a sophisticated transform, as it is distinct from the case of chaos, widening the scope of this assumption. Stability calculation with the Floquet theory was achieved without a full EOM transform to rotating frame. The DFT branches of the main frequencies of the 2:1 IR are plotted and presented

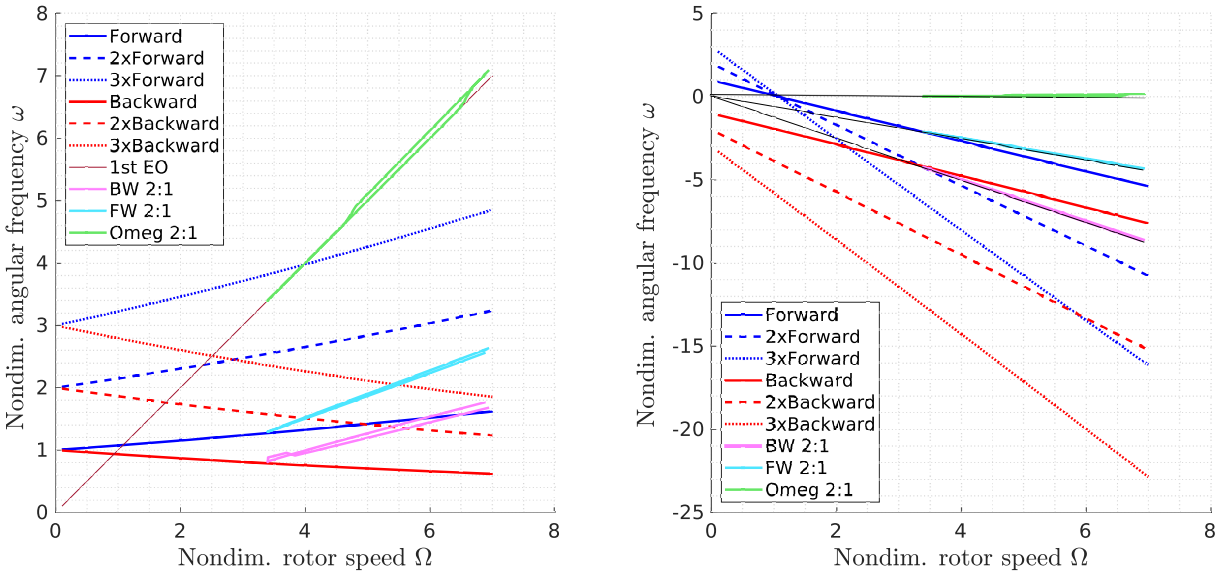


Figure 5.8: The rotating frame Campbell diagram with overlaid DFT branches of 2:1 IR from the Zilli system with quintic stiffness that replaces the cubic term in Eq. (4.2). The thin solid black lines indicate the linear evolution of the main frequencies of the 2:1 IR with the rotor speed.

in the Campbell diagram for comparison with the linear system frequencies. The ratio of the contributing frequencies ($2\,\omega_f^{rot} = \omega_b^{rot}$) to the 2:1 IR infers the interaction of the underlying FW and BW modes which is investigated in the light of NNMs in the next chapter where the idea of NNM correlation is given with and without off-centring effects.

Chapter 6

Internal Resonances in the Light of NNMs in Rotordynamics

6.1 Introduction

In the previous chapter, a quasiperiodic continuation method was defined as a demonstration of the unification of the diverse rotordynamics phenomena (Table 1.1) by generalising the available methods. To do that, a shooting-continuation implementation was performed on the quasiperiodic 2:1 internal resonance (IR) solutions of the cubic Zilli system. A frequency analysis showed the frequency content of the IR, which was used to infer the involvement of the underlying FW and BW nonlinear normal modes (NNMs).

In this chapter, in line with the research interest in Section 1.6, the first question that arises when interpreting the diverse nonlinear phenomena in rotordynamics as NNMs, is tackled: How are these underlying NNMs giving rise to the related IR response, especially when the mode is not a direct bifurcation from a conservative mode of the system? For example, some of the responses of the rotating systems such as the 2:1 IR discussed in this thesis, show no bifurcations from the conservative FW or BW NNMs, nor does it relate to any low-amplitude, close-to-linear region. Off-centring-like effects (maybe nonconservative) must play a role in the formation of such IRs. Therefore, new tools are needed for an NNM interpretation in rotordynamics.

The NNMs of conservative systems have been studied and backbone curves derived [117]. However, in the rotating frame, the OOB excitation is a constant force (given a constant rotor speed); therefore, the effect of the OOB on the undamped NNMs is of interest. The constant force appearance of the OOB in the rotating frame creates *off-centring* by adding a static displacement, causing the BW and FW modes to couple, hence the resulting IR modes. Gravity sag or misalignment of the shaft can create the similar off-centring effect in the stationary frame, but without the OOB forcing, gravity does not excite the system the way OOB does in the rotating frame.

In the following, Section 6.1.1 explains the utilised method for drawing the NNMs. This is followed in Section 6.1.2 by the explanation that for the investigated IR responses, classical approach to backbone curves does not work. In the following section (Section 6.2) the effects of off-centring on the coupling of FW and BW modes are discussed in order to explain the formation of the IRs in the light of NNMs. First, in Section 6.2.1, the need for off-centring is explained by showing that the elliptic-oval shape of a modal trajectory results in mirrored harmonics in the frequency spectrum, which indicates that the modes that are not purely circular are more likely to interact with an opposite-signed mode, if the frequencies coincide. Extending this idea, in Section 6.2.2, the frequency contents of NNMs of the cubic Zilli system are correlated to assess whether they will interact, in various cases with or without off-centring effects. In Section 6.2.3, the effect of gravity and OOB is evaluated in line with the correlation in Section 6.2.2. The results show that off-centring effects make frequency contents of different modes correlate in a special way, leading to a form of mode-locking. The amplitude levels of the $\omega_f^{sta} - \omega_b^{sta} = \Omega$ and $2\,\omega_f^{sta} - \omega_b^{sta} = \Omega$ are shown to reflect the predictions by the correlation method developed here.

6.1.1 The method for finding FW and BW whirling NNMs

There have been analytical [79, 120] and semi-analytical [80, 122] methods for the NNM calculation. However, as noted in [117], for large degree of freedom systems and accuracy in large amplitudes of motion numerical methods are required, which are more suitable for the numerical continuation method, thereby making the bifurcation analysis easier. Analytical methods find exact solutions that are capped in accuracy (such as expressing a solution suggestion "to order" ϵ or ϵ^2 accuracy in multiple scales). This is not the limitation in the numerical methods where the accuracy is linked to tighter tolerances for solution acceptance in the iterative processes and, in the HBM, the number of harmonics expanding the periodic solution.

The nonlinear dynamics of a structural system is affected greatly by its backbone structure (e.g [172]). Just like the insight gained with the unstable branches, the backbone structure is bound to provide even more understanding, such as the twist of the backbones or whether they hint at IR with other modes. In a conservative Duffing oscillator, any initial condition would generate a point on the backbone structure. However, in the conservative, gyroscopic cubic Zilli system, only very particular initial conditions result in the backbones for pure FW and BW branches, and more general initial conditions result in some arbitrary combination of FW and BW whirl.

Peeters et al. [118] presented an algorithm to trace conservative NNMs, extending the definition of Rosenberg [79]. The method is comprised of the shooting method to calculate a periodic motion of the conservative system from an initial state near the

periodic solution, and the arclength continuation that finds the branch of the calculated nonlinear mode, forming its backbone. The stability is found through Floquet multipliers. The method will be used on the cubic Zilli system's ODEs (derived in Ch. 3) in the stationary frame,

$$\mathbf{w}'' - \Omega I_p \mathbf{J}_2 \mathbf{w}' + 2\zeta \mathbf{w}' + \mathbf{w} + \gamma \mathbf{w} r^2 + \mathbf{f}_0 = me\Omega^2 \begin{Bmatrix} \cos\phi \\ \sin\phi \end{Bmatrix}, \quad \mathbf{X} = \begin{Bmatrix} x \\ y \end{Bmatrix} \tag{6.1a}$$

$$\begin{aligned} \gamma = 0.25 \quad m = 0.9 \quad \zeta = 0 \\ e = 0.353 \quad I_p = 0.143 \quad f_0 = 0.9 \end{aligned} \tag{6.1b}$$

where $\mathbf{w} = \{x, y\}^T$ is the stationary frame states vector, and $\mathbf{f}_0$ is the constant gravity force vector if it is used. Note that in order to investigate the off-centring effect of the OOB-forcing on the FW and BW modes, and their correlations, at one point, the forcing term on the right-hand side is kept.

In order to obtain the FW and BW modes' backbones, a low amplitude purely circular linear FW (or BW) motion's initial conditions in state space form ($\mathbf{z} = \{\mathbf{w}^T, \mathbf{w}'^T\}^T$) are given along with the linear modes' period (see Eq. (6.2) and the textbook [7] for derivation). For Eq. (6.1), these are expressed as follows,

$$\mathbf{z}_{prediction}(t=0) = \epsilon \left[\cos\omega t,\ \pm\sin\omega t,\ -\omega\sin\omega t,\ \pm\omega\cos\omega t\right]^T \big|_{t=0}, \quad \omega = 2\pi/T_{prediction}$$

$$T_{prediction} = 2\pi \left(\frac{\Omega I_p}{2} \pm \sqrt{\left(\frac{\Omega I_p}{2}\right)^2 + 1} \right)^{-1}$$

$$+: \text{FW whirl},\ -: \text{BW whirl}. \tag{6.2a}$$

Note that $T_{prediction}$ can appear negative for BW motions. For NNMs that produce other than pure circles due to off-centring effects, this FW or BW perturbation is applied around the static equilibrium. Additionally, for the rotating frame, the prediction for the period is through the frequency relation $\omega^{rot} = \omega^{sta} - \Omega$,

$$T_{prediction} = 2\pi \left(\frac{\Omega I_p}{2} \pm \sqrt{\left(\frac{\Omega I_p}{2}\right)^2 + 1} - \Omega \right)^{-1}. \tag{6.3}$$

Then, these initial conditions and the periods are converged to a (numerically) true periodic motion for the nonlinear system (with cubic stiffness) via the shooting algorithm, yielding a point on the branch. A tangent vector is then computed according to arclength-continuation formulated around tracing the zeros of periodicity function to predict the next 'initial condition-period' pair $(\mathbf{z}_0^T, T)$. The shooting method converges the prediction to another point on the branch.

This method is used in the next section in order to discuss the off-centring effect on

the frequency content of the NNMs and their possibility of interaction through a concept of NNM correlation.

6.1.2 Degenerate conservative IR solutions

The investigated IRs here do not pre-bifurcate from a conservative orbit; instead, they stem from degenerate conservative solutions. This was also noticed in a similar system, though with impact law definitions instead of cubic stiffness used here, by Mora et al. [45] where the emergence of the IRs was stated to appear as a blue-sky catastrophe. In the discussion below, firstly, the 3:1 IR periodic solutions using the rotating frame EOM of the cubic Zilli system (see given in Eq. (6.5))are continued towards zero damping and zero forcing. The continuation ends at different locations on the bifurcation diagram depending on the decrease rates of forcing and damping with respect to each other. Secondly, a shooting-continuation attempt using the same rotating frame EOM (Eq. (6.5)) is illustrated which gave away the degenerate family of conservative 2:1 response that can be obtained at various amplitudes in a range of rotor speed.

Continuation in a parameter that links damping and excitation

The rotating-frame EOM of the cubic Zilli system is modified to give Eq. (6.4), with the only addition of the new ξ parameter and its power ρ:

$$\widetilde{\mathbf{w}}'' + (-\Omega\mathbf{J}_2(J_p-2) + 2\xi^\rho\zeta\mathbf{I})\widetilde{\mathbf{w}}' + (\Omega^2(J_p-1)\mathbf{I} + \mathbf{I} + 2\xi^\rho\zeta\Omega\mathbf{J}_2)\widetilde{\mathbf{w}} + \gamma\widetilde{\mathbf{w}}r^2 = m\xi e\Omega^2\begin{Bmatrix}1\\0\end{Bmatrix} \tag{6.4}$$

with values of J_p, m, e and ζ from Eq. (6.1b). A fold-continuation in the ξ-Ω parameter pair was done in AUTO [84], by homotopy of ξ from 1 to 0, on the periodic 3:1 IR solutions of Eq. (6.4). This fold continuation is presented in Figure 6.1 for various ρ values which resulted in different end points in the vicinity of unforced, undamped parameter space. As ξ takes both damping and OOB-excitation towards zero, the solution process loses numerical stability as a result of the loss of the linking between underlying FW and BW modes. This shows that conservative 3:1 IR solutions cannot be reached from the nonconservative ones. In the following, conservative case's degenerate solutions are given to support this further.

Shooting-continuation of conservative 2:1 solutions

A 2:1 (SL) orbit generated by time simulations with decreasing damping and OOB forcing towards zero was continued in a shooting-continuation scheme with both OOB and

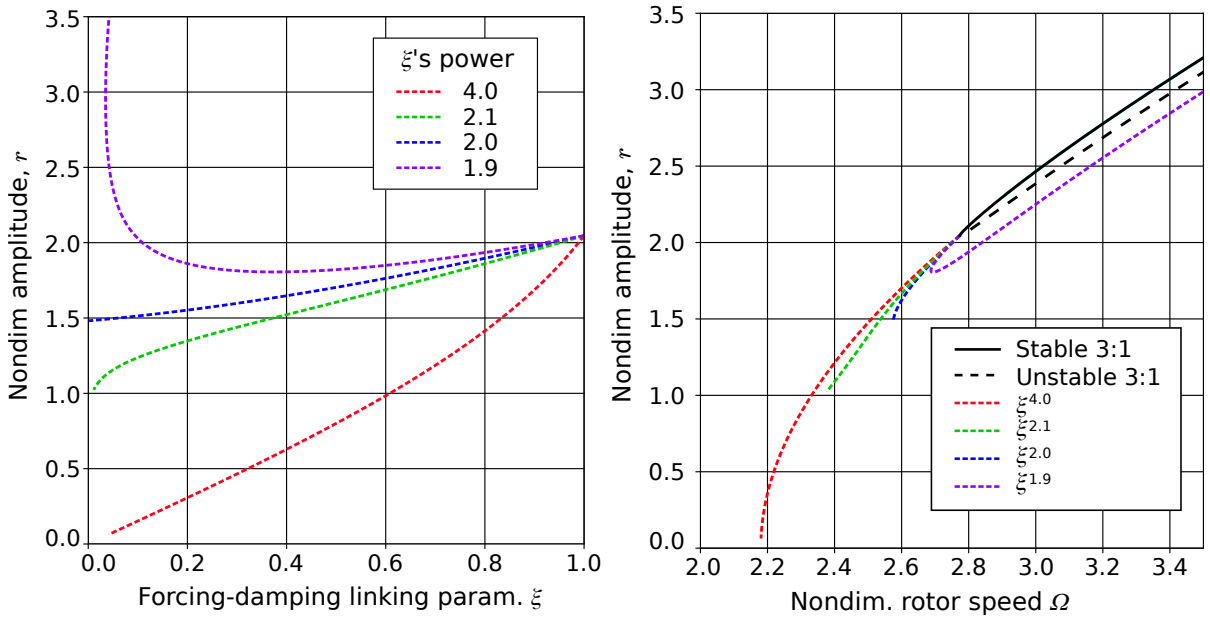


Figure 6.1: Left: Fold continuation in ξ-Ω from $\xi = 1 \rightarrow 0$. Right: The corresponding look in the bifurcation diagram. Fold continuation branches end where the numerical stability is lost when $\xi \approx 0$. Purple fold continuation branch, however, made a fold and could not approach the conservative state.

damping omitted. The following, conservative, stationary frame equation was used,

$$\widetilde{\mathbf{w}}'' - \Omega \mathbf{J}_2 (I_p - 2)\widetilde{\mathbf{w}}' + (\Omega^2 (I_p - 1)\mathbf{I} + \mathbf{I})\widetilde{\mathbf{w}} + \gamma \widetilde{\mathbf{w}} r^2 = \mathbf{0}. \tag{6.5}$$

As seen in Figure 6.2, the generation of 2:1 IR becomes arbitrary. This shows that the 2:1 IR is not distinct as a branch of solutions in the conservative case as the modes do not lock but rather coincide at a "correct" frequency ratio. These conservative, degenerate solutions demonstrate why the OOB forcing magnitudes and damping coefficients found in experiments and real machines could generate distinct IR branches: Once the OOB and non-zero damping are present in the dynamics, the degenerate solutions collapse and form defined IR branches that are located at different rotor speed ranges in a bifurcation diagram, depending on these parameters.

It is of interest to locate the degenerate solutions and the full system's 2:1 branch against the NNMs in the Ω-ω-r space for a fuller picture of the IR. This is done in Figure 6.3 where a number of NNM branches of FW and BW modes are drawn for a range of rotor speeds to form an 'NNM surface' in Figure 6.3a. These NNM branches (and the NNM surfaces) are shown in the rotating frame with frequencies ω_f^{rot} and $\omega_b^{rot}/2$ for FW and BW modes, respectively; however, they are the same branches that would be obtained if they were calculated by solving the stationary frame EOM, only their positions in the Ω-ω-r space would appear differently according to the frequency relation: $\omega^{sta} = \omega^{rot} + \Omega$.

The observations from Figure 6.3 are as follows: Any 2:1 orbit (whether conservative or not) has to be confined to where the relation $2\,\omega_f^{rot} = \omega_b^{rot}$ can be achieved. In Figure 6.3a,

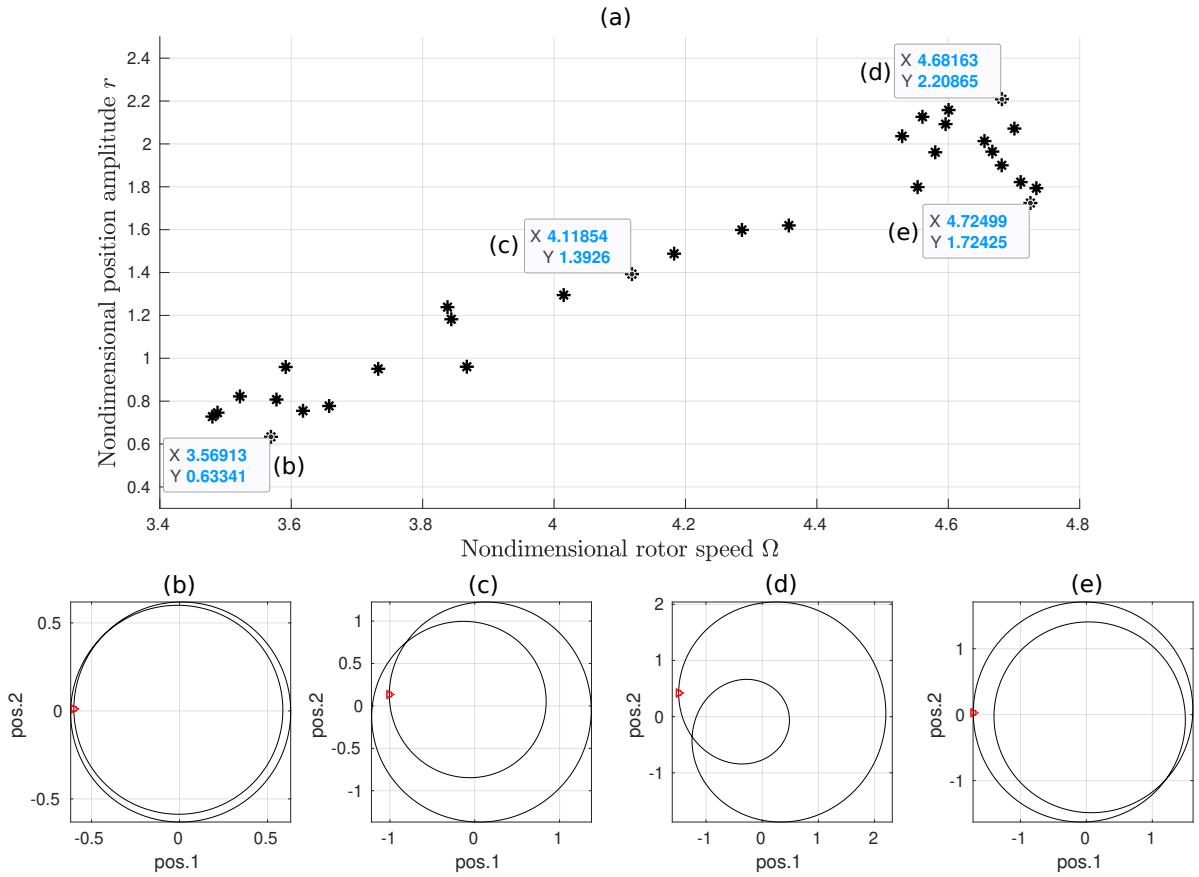


Figure 6.2: The degenerate conservative 2:1 solutions scattered in the bifurcation diagram.

this region is where these FW and BW NNM surfaces overlap. Indeed, all 2:1 solutions appear even more limited to a vertical plane which passes through the origin as shown in Figure 6.3b (see also the linear lines in Figure 5.7 which are the projections of these planes onto Ω-ω space of the Campbell diagram). This was also the case with a quintic stiffness instead of cubic stiffness (see, Figure 5.8).

It is established above that the 2:1 IR of the full system (damped and OOB-forced) is not continuously liked to the conservative, degenerate 2:1 solutions. However, the mechanism underlying the formation of the 2:1 through the lens of the underlying NNMs of the system needs to be investigated, which is done next via the concept of correlation of NNMs.

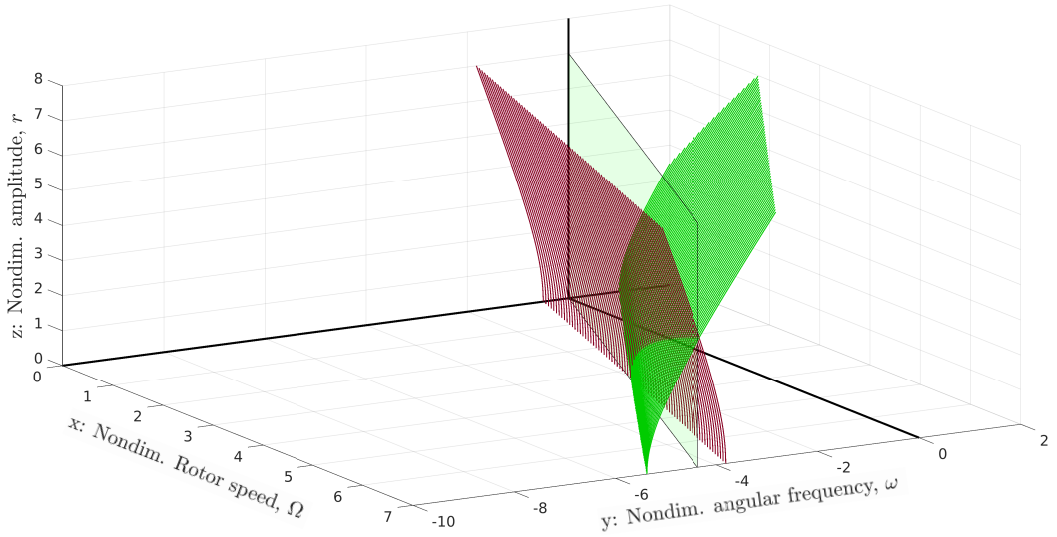
6.2 The effect of off-centring on rotating NNMs - proof of concept

The NNMs are affected by the isotropy of the system. Nagasaka et al. [55] pointed out that the effect of gravity was needed to lock 1:(-1) IR. Van der Heijden [85] also stressed that the 'full mode locking', i.e., one that resulted in periodic solution in the stationary frame, happened when the gravity/misalignment was included. In the isotropic system, the conservative forces are isotropic with respect to either frame of reference (stationary or rotating). However, constant external forces such as misalignment/gravity in the stationary frame, or OOB force in the rotating frame, can shift the static equilibrium in the respective frames of reference. Due to the nonlinear restoring force, this *off-centring* effect causes the NNMs' frequency content to include harmonics, and possibly exchange energy between modes. Therefore, one cannot think of backbone of these internally resonant modes in a regular sense since the branch of such responses vanish without the off-centring effect of the OOB forcing.

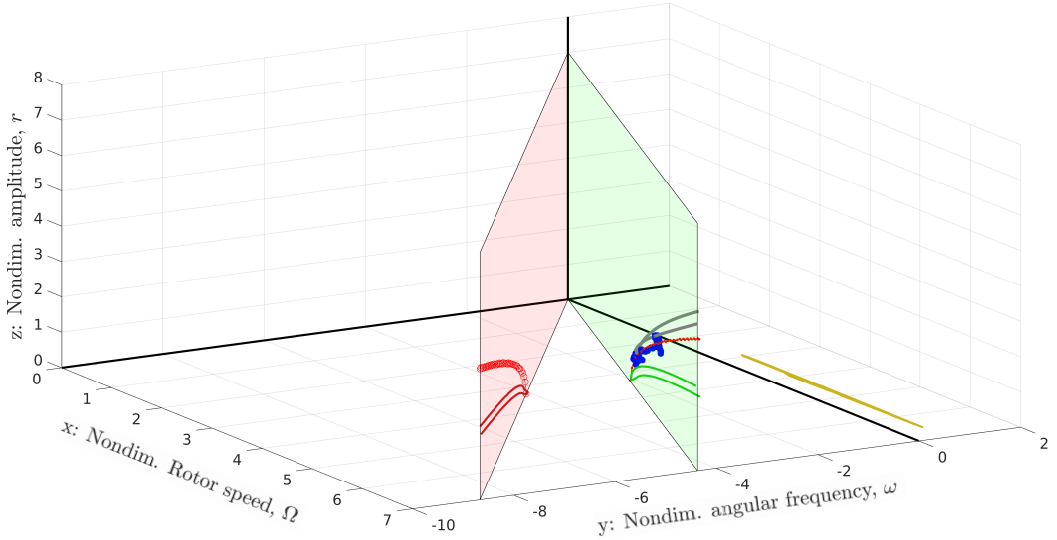
Below, firstly, the frequency content of a FW and a BW elliptic orbit is given to show mirrored frequency content. Secondly, frequency spectrum correlation is used to predict whether and at which amplitude level an IR mode can be expected. Lastly, effects of gravity/misalignment and OOB forcing on the Zilli system's bifurcation diagram obtained by time simulations is shown.

6.2.1 Frequency spectrum of elliptic FW and BW signal

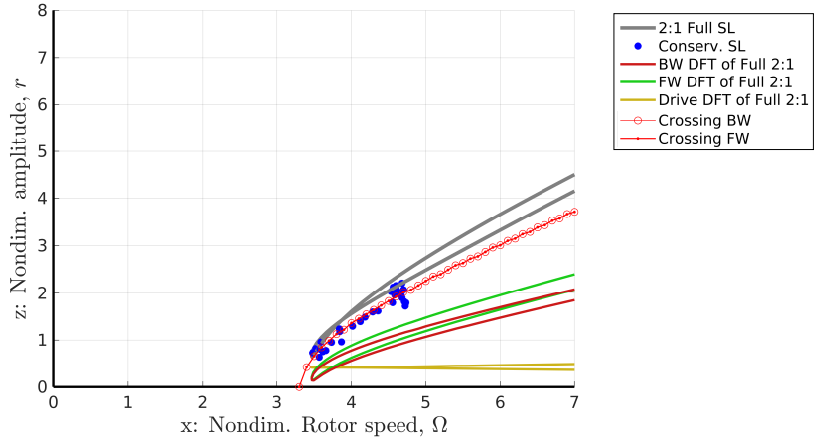
Modes of axisymmetric rotors with isotropic bearings are pure circles of FW or BW whirling, and the OOB does not cause BW modes to be excited [7]. On the contrary, deviation from pure circles, by off-centring effects, results in elliptic-oval shaped modes. In the case of elliptic orbits, the dominant FW (BW) frequency component of the FW (BW) mode becomes mirrored in the frequency spectrum around the DC component at



(a) FW (green, ω_f^{rot}) and BW (red, $\omega_b^{rot}/2$) NNMs surfaces of the cubic Zilli system in 3D-Campbell diagram. Green vertical plane passes through the crossing and the origin.

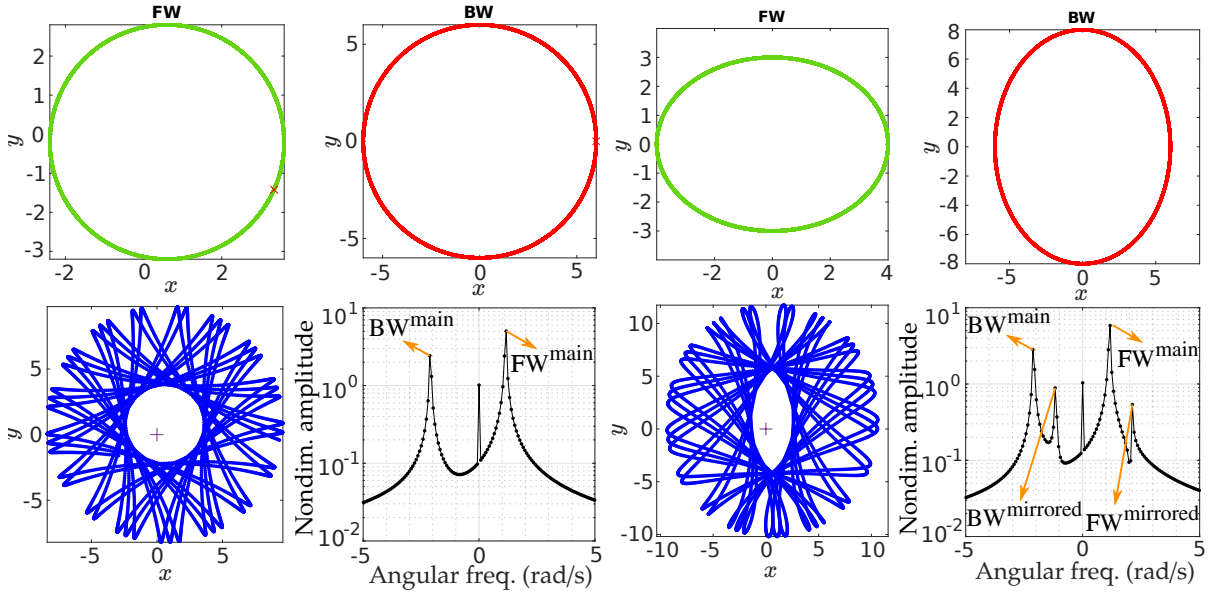


(b) SL branch in Figure 5.2 with its DFT peaks from Figure 5.6. The green plane shows the crossing of $\omega_f^{rot} = 1/2\,\omega_b^{rot}$, and red plane of $2\,\omega_f^{rot} = \omega_b^{rot}$. Legend in (c).



(c) Side view of 6.3b. Legend also applies to (b).

Figure 6.3: Locating the conservative and nonconservative 2:1 response with respect to the FW and BW NNMs.



(a) Incommensurate circular FW and BW example orbits

(b) Incommensurate elliptic FW and BW example orbits

Figure 6.4: Superposition of FW (green) and BW (red) orbits form the blue orbit whose DFT is given. Distortion of the FW and BW modes cause mirrored frequency component.

zero. This is illustrated in Figure 6.4: When the motion is formed by pure circles of $\mathrm{FW}^{\mathrm{main}}$ and $\mathrm{BW}^{\mathrm{main}}$ frequencies, the spectrum shows these in the superposed signal; and when the FW and BW motions are elliptic in shape, the frequency spectrum also shows the mirrored frequencies '$\mathrm{FW}^{\mathrm{mirrored}} = -\,\mathrm{BW}^{\mathrm{main}}$' and '$\mathrm{BW}^{\mathrm{mirrored}} = -\,\mathrm{FW}^{\mathrm{main}}$'. Thus, in the case that these motions represent modes of a rotor, the positive (FW) OOB forcing frequency can match this $\mathrm{FW}^{\mathrm{mirrored}}$ harmonic component of the BW elliptic mode and excite it. Often, the off-centring makes the orbit oval with many harmonics of the main frequency. Therefore, BW modes become susceptible to OOB-excitation and, thereby, being internally locked to FW modes. Besides, if one harmonic of the FW mode matches one $\mathrm{FW}^{\mathrm{mirrored}}$ harmonic of the elliptic BW mode, both modes can be excited. As a result, the *correlation* of the frequency content of different modes can indicate the possibility of modal interactions, which is presented next. It is important to note that this effect is visible only with complex DFT analysis (see Section 2.1) of complex signals $(x + jy)$, not on the separate signals of x and y coordinates.

6.2.2 Correlation of forward and backward NNMs

In the following, the idea of correlation of the frequency content of the FW and BW NNMs is discussed. If the FW and BW modes, or any two mode, carry overlapping frequency content, then the forcing signal of one mode can excite the motion of the other mode. Therefore, higher possibility of modal interaction is deduced. The correlation calculation takes account of the fact that the forcing signal generated during one mode will have

a similar frequency content to that of the motion signal of the same mode. Therefore, frequency domain correlation between the motion signals of the two signals is taken as indication of potential energy transfer and coupling between modes. The correlation is calculated according to the following formula,

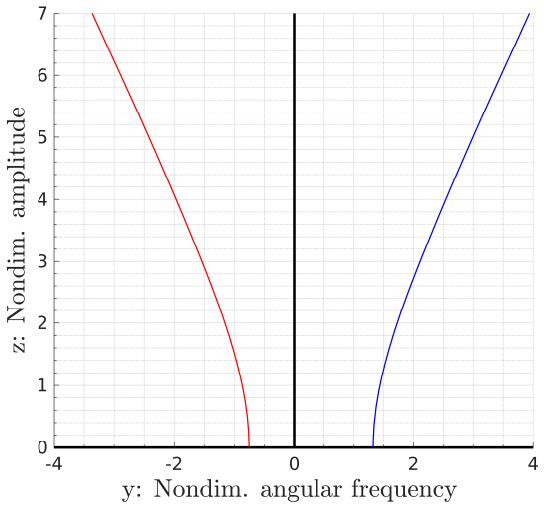
$$R^{ab}_{j_a j_b} = \frac{\langle |F^a_{j_a}|, |F^b_{j_b}| \rangle}{\text{norm}\{|F^a_{j_a}|\}\text{norm}\{|F^b_{j_b}|\}}, \tag{6.6}$$

where complex number magnitude is shown with $|\cdot|$. Here, a and b are different branches, e.g., one belongs to a FW mode and the other to a BW mode, j_a and j_b are the solution point indexes on those branches, $F^a_{j_a}$ and $F^b_{j_b}$ are the DFTs of the time simulated long trajectory mode at the j_ath and j_bth solution point on branch a and b, respectively. The magnitudes are used to check the maximum possible correlation in each frequency content, reminding that this aims to be an estimate of the excitability between different modes, rather than exact comparison of different modes including their phases with respect to each other.

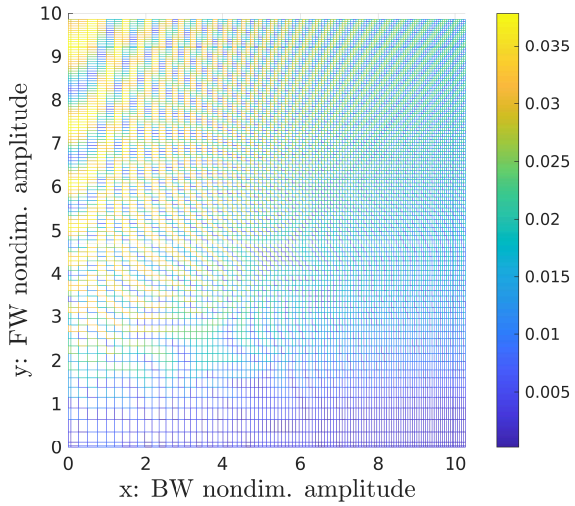
This analysis gives an expectation on where on the branches of these NNMs one expects the FW and BW mode interaction in a combination resonance or IR relation. In that sense, this is a commentary on the extension of the Campbell plot in the 3$^{\text{rd}}$ dimension which is the amplitude of oscillation. Different scenarios are explained below regarding the presence or lack of off-centring effects.

No correlation without off-centring

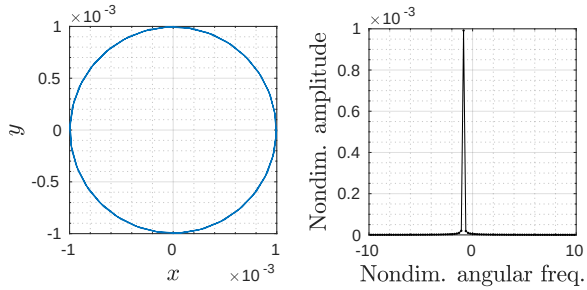
The main FW and BW NNMs are not correlating in frequency content in either stationary or rotating coordinate frames, as seen in Figures 6.5 and 6.6, respectively. Therefore, excitation of one is not expected to cause the excitation of the other, because there is not any off-centring effect.



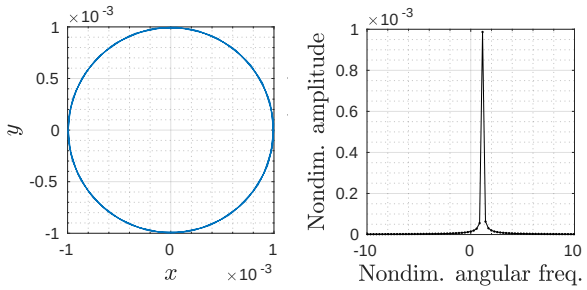
(a) Branches of BW (red) and FW (blue) NNMs at $\Omega = 4$ without misalignment or OOB. branches in (a).



(b) Correlation of the solid red and blue branches in (a).

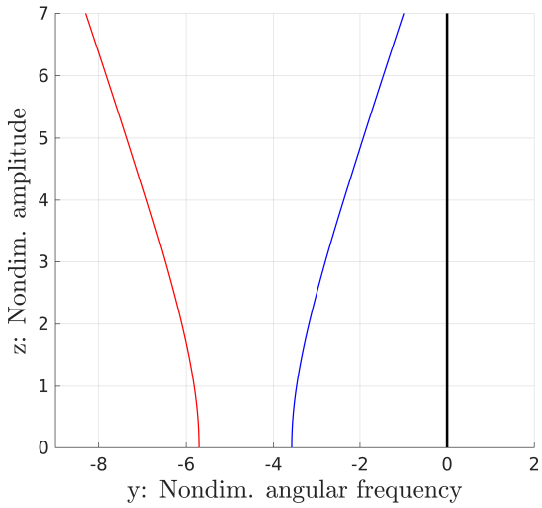


(c) Sample of DFT on a BW branch (at $\Omega = 2$).

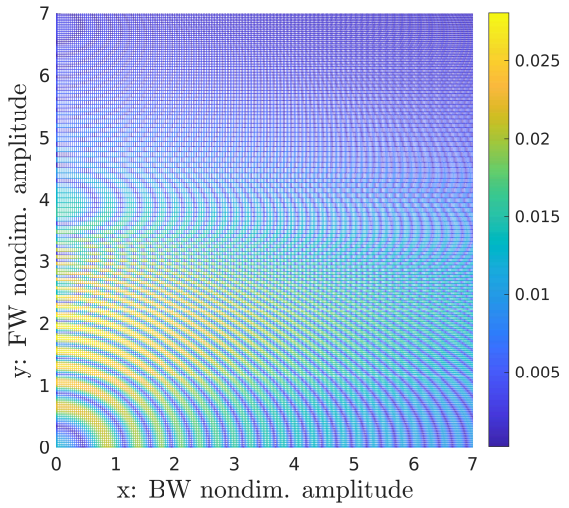


(d) Sample of DFT on a FW branch (at $\Omega = 2$).

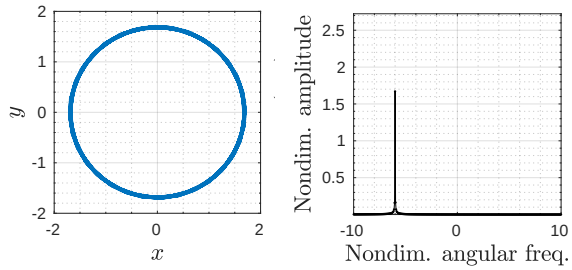
Figure 6.5: Correlation of the stationary frame FW (solid blue) and BW (solid red) NNMs without off-centring effect from gravity. x-axis of (a) is $\omega = 2\pi/T$ with period of the mode T.



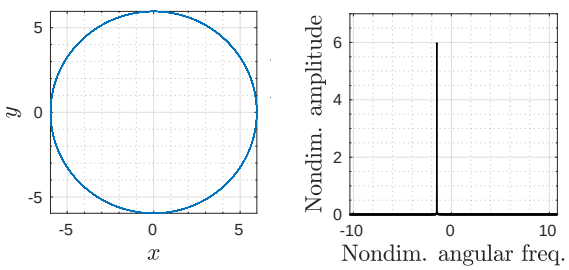
(a) Branches of BW (red) and FW (blue) NNMs at $\Omega = 5$ without gravity or OOB.



(b) Correlation of the solid red and blue branches in (a).



(c) Sample of DFT on a BW branch (at $\Omega = 5$).



(d) Sample of DFT on a FW branch (at $\Omega = 5$).

Figure 6.6: Correlation of the rotating frame FW (solid blue) and BW (solid red) NNMs without off-centring effect from OOB. x-axis of (a) is $\omega = 2\pi/T$ with period of the mode T.

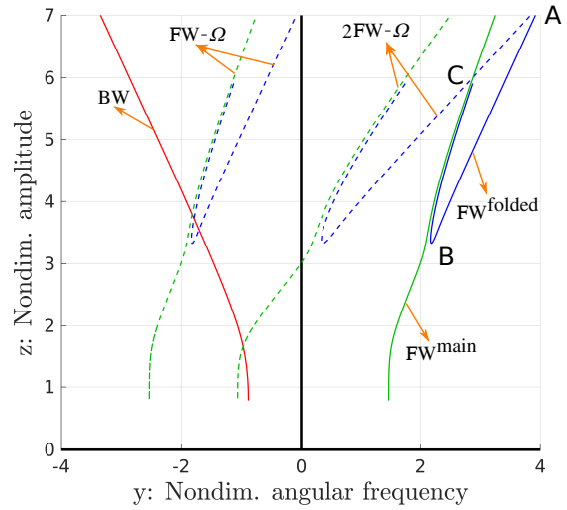
Off-centring by gravity/misalignment or OOB forcing

Gravity The FW branch bifurcates in the presence of gravity sag/misalignment as seen in Figures 6.7 and 6.8 which is the result of the conservative equation Eq. (6.7) with the same values as in Eq. (6.1b).

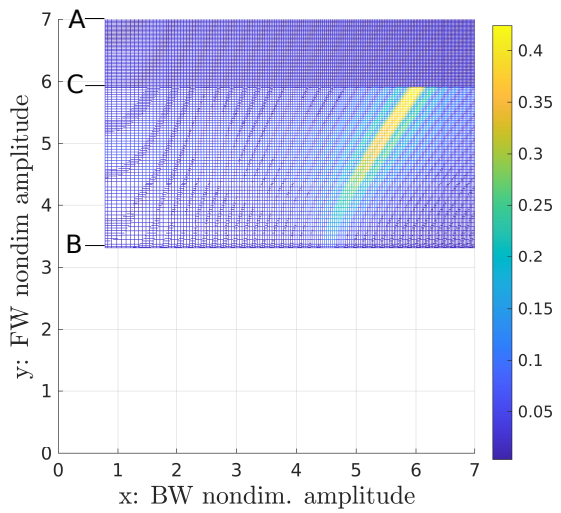
$$\mathbf{w}'' - \Omega I_p \mathbf{J}_2 \mathbf{w}' + \mathbf{w} + \gamma \mathbf{w} r^2 + f_0 = \begin{Bmatrix} 0 \\ 0 \end{Bmatrix}, \quad \mathbf{w} = \begin{Bmatrix} x \\ y \end{Bmatrix} \tag{6.7}$$

The FW and BW modes become more correlated, particularly after the amplitude level of around $r = 4$ for both modes, which is around the same level as the crossing of the $\omega_f^{sta} - \Omega$ and ω_b^{sta} branches, making $\omega_f^{sta} - \omega_b^{sta} = \Omega$ combination resonance. Observation from the time-simulation bifurcation diagram of the full system (damped, OOB-forced and misalignment) in Figure 6.10 shows that this resonance is achieved above the amplitude level of this crossing which corresponds to the higher correlation region. This method can be more systematically broken down into the following steps:

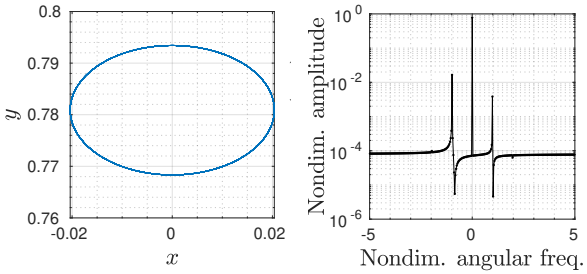
1. There is an NNM branch for each of the FW and BW mode which carry ω_f^{sta} and ω_b^{sta} modal frequencies (Figure 6.8a) for $\Omega = 4$.
2. The NNM correlation is performed (Eq. (6.6)) on these two branches which give the carpet plot in Figure 6.8b.
3. In that plot (Figure 6.8b), there is a region where the correlation starts to get higher: Amplitudes 4.5 for BW and 3.5 for FW mode in Figure 6.8b. This amplitude range is called the 'correlation amplitude level'.
4. A shifted FW branch is found that crosses the BW branch around this 'correlation amplitude level': The FW branch is shifted by $-\Omega$, and it now shows frequencies $\omega_f^{sta} - \Omega$ (see in Figure 6.8a). And now it crosses the BW branch that show ω_b^{sta} modal frequencies around the 'correlation amplitude level'.
5. A failed shifting can be seen in Figure 6.8a: The shifted FW branch that shows frequencies $2\omega_f^{sta} - \Omega$ would not cross the BW branch at the 'correlation amplitude level' which is where the correlation starts to give higher values. Therefore, this shifting is discarded.
6. For the ω-range where these branches overlap, the frequency relation $\omega_f^{sta} - \Omega = \omega_b^{sta}$ can be written. Therefore, between these branches the combination resonance of resonance $\omega_f^{sta} - \omega_b^{sta} = \Omega$ is inferred.
7. A hypothesis is developed: "The response must appear around the same amplitude level as the 'correlation amplitude level' because a trajectory that lives around that amplitude would exhibit underlying modes that can correlate in that particular frequency relation."
8. The hypothesis is tested by looking at the actual response in the bifurcation diagram of the damped, forced system in Figure 6.10: The amplitude level of $\omega_f^{sta} - \omega_b^{sta} = \Omega$



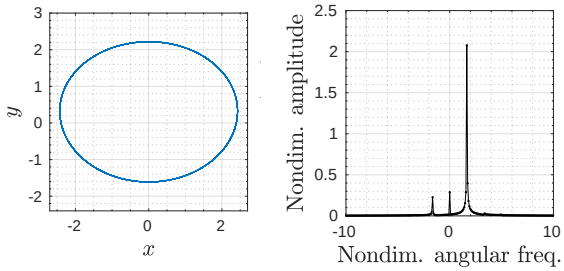
(a) Branches of BW (red), $\mathrm{FW}^{\mathrm{main}}$ (green) and $\mathrm{FW}^{\mathrm{folded}}$ (blue) NNMs at $\Omega = 4$ when there is gravity.



(b) Correlation of the red and blue solid branches in (a). Shorter arm (B-C) correlates better.



(c) Sample DFT of BW (at $\Omega = 2.15$).

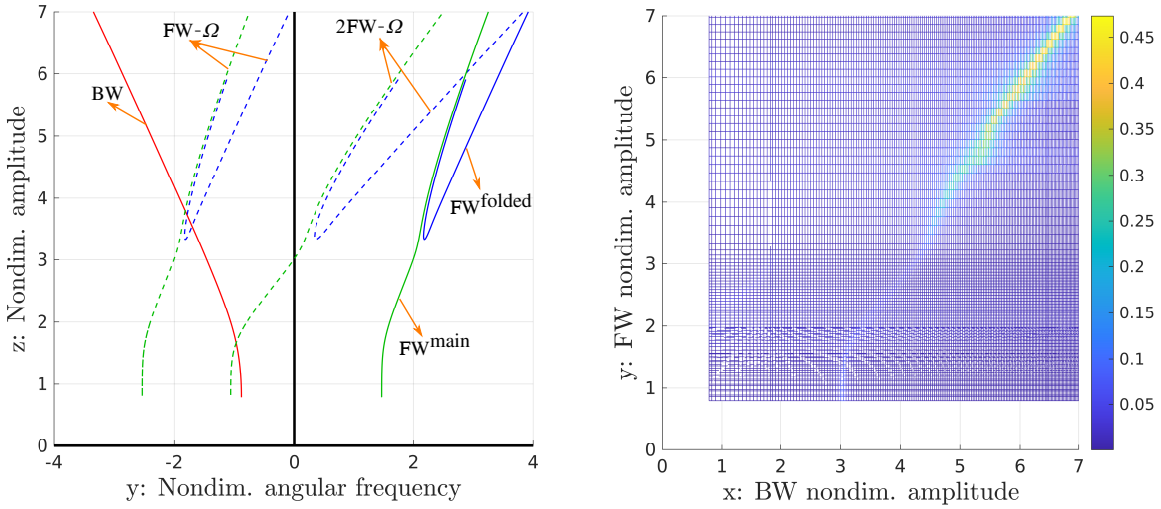


(d) Sample DFT of $\mathrm{FW}^{\mathrm{folded}}$ (at $\Omega = 2.15$).

Figure 6.7: In the case of gravity, correlation of the stationary frame BW (solid red) and $\mathrm{FW}^{\mathrm{folded}}$ (solid blue) branches. Dashed lines in (a) show $\omega^{sta} - \Omega$ and $2\,\omega^{sta} - \Omega$ from left to right for both FW branches. x-axis of (a) is $\omega = 2\pi/T$ with period of the mode T. Note the non-zero minimum amplitude of the branches due to the gravity sag.

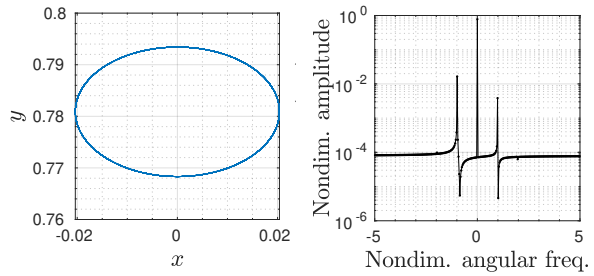
branch at the rotor speed $\Omega = 4$ appears around the 'correlation amplitude level' (see the black lines in Figure 6.10). Therefore, the hypothesis is confirmed.

This indicates that a combination resonance with frequency relation $\omega_f^{sta} - \Omega = \omega_b^{sta}$ is expected around the level of the crossing in a numerical or test rig experiment. Additionally, in Figure 6.7, the side of the $\mathrm{FW}^{\mathrm{folded}}$ branch that is aligned with the main FW branch correlates while the folded side of the FW NNM branch does not.

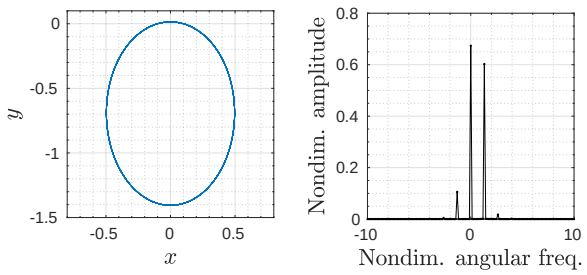


(a) Branches of BW (red), $\mathrm{FW}^{\mathrm{main}}$ (green), $\mathrm{FW}^{\mathrm{folded}}$ (blue) NNMs at $\Omega = 4$ when there is gravity.

(b) Correlation of the red and green solid branches in (a).



(c) Sample DFT of BW (at $\Omega = 2.15$).



(d) Sample DFT of $\mathrm{FW}^{\mathrm{main}}$ (at $\Omega = 2$).

Figure 6.8: In the case of gravity, correlation of the stationary frame BW (solid red) and $\mathrm{FW}^{\mathrm{main}}$ (solid green) branches. Dashed lines in (a) show $\omega^{sta} - \Omega$ and $2\,\omega^{sta} - \Omega$ from left to right for both FW branches. x-axis of (a) is $\omega = 2\pi/T$ with period of the mode T. Note the non-zero minimum amplitude of the branches due to the gravity sag.

OOB forcing The rotating frame BW and FW NNM correlation is given in Figure 6.9. Although OOB forcing is included, the system of ODE (Eq. (6.8)) is still autonomous, and the force is constant in the rotating frame, similar to the case in the stationary frame with gravity and without OOB.

$$\widetilde{\mathbf{w}}'' - \Omega\mathbf{J}_2(I_p - 2)\widetilde{\mathbf{w}}' + (\Omega^2(I_p - 1)\mathbf{I} + \mathbf{I})\widetilde{\mathbf{w}} + \gamma\widetilde{\mathbf{w}}r^2 = me\Omega^2\begin{Bmatrix}1\\0\end{Bmatrix} \tag{6.8}$$

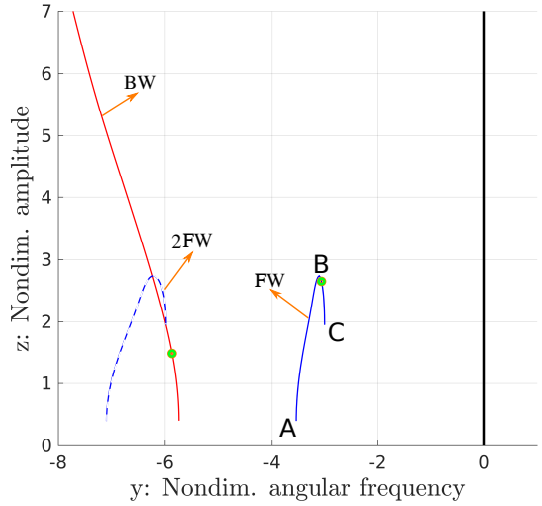
Compared to Figure 6.6 which shows rotating frame FW and BW modes without off-centring of OOB-forcing, here the branches are more correlated. Additionally, the FW NNM has a curving branch here and some parts of the branch gives 2:1 looking solutions already (as shown in Figure 6.9d). The almost purely circular BW solutions correlate with this morphing FW branch only after the maximum amplitude of the FW branch. The high-correlation regions match the crossing of BW branch with ω_b^{rot} frequencies (red line) and FW branch with $2\,\omega_f^{rot}$ frequencies (dashed blue line). Therefore, the NNM correlation method predicts the 2:1 IR in the case of OOB forcing at a certain amplitude. This method, as in the gravity case above, can be broken down into the following steps in a more systematic way:

1. There is an NNM branch for each of the FW and BW mode which carry ω_f^{rot} and ω_b^{rot} modal frequencies (Figure 6.9a) for $\Omega = 5$ – a drive speed picked.
2. The NNM correlation is performed using Eq. (6.6) on these two branches and the carpet plot in Figure 6.9b is given.
3. In that plot (Figure 6.9b), there is a region where the correlation starts to get higher: Amplitudes 3.5 for BW and 2.5 for FW mode in Figure 6.9b. This amplitude range is roughly called the 'correlation amplitude level'.
4. A shifted FW branch is found that crosses the BW branch around this 'correlation amplitude level': The FW branch is shifted by multiplying it by 2, and it now shows frequencies $2\,\omega_f^{rot}$ (see in Figure 6.9a). And now it crosses the BW branch that show ω_b^{rot} modal frequencies around the 'correlation amplitude level'.
5. For the ω-range where these branches overlap, the frequency relation $2\,\omega_f^{rot} = \omega_b^{rot}$ can be written. Therefore, between these branches the 2:1 IR with frequency relation $2\,\omega_f^{rot} = \omega_b^{rot}$ is inferred.
6. A hypothesis is developed: "The response must appear around the same amplitude level as the 'correlation amplitude level' because a trajectory that lives around that amplitude would exhibit underlying modes that can correlate in that particular frequency relation."
7. The hypothesis is tested by looking at the actual response in the bifurcation diagram of the damped, forced system in Figure 6.10: The amplitude level of the 2:1 branch at

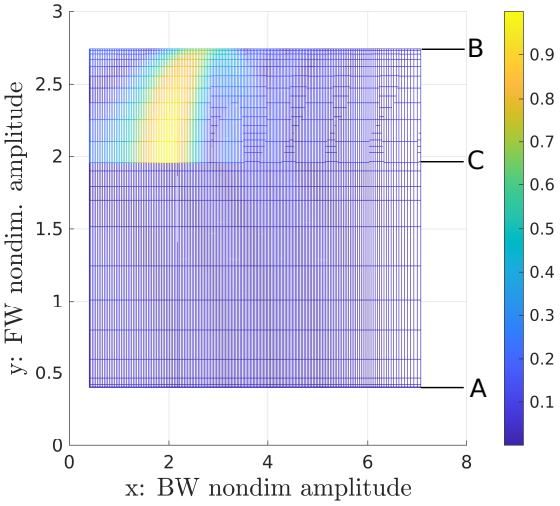
the rotor speed $\Omega = 5$ appears around the 'correlation amplitude level'. Therefore, the hypothesis is confirmed.

For testing the hypothesis, instead of Figure 6.10, Figure 4.10 which show a very low damping ratio case or Figure 4.12 which show a high OOB excitation case can be used to test the hypothesis and confirm it. Thus, it can be argued that this 'correlation amplitude level' is not affected much by the damping or forcing in the system.

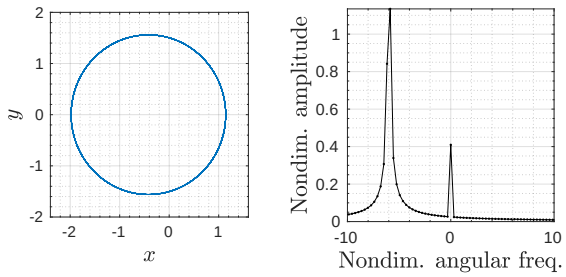
This shows that the off-centring effect of the OOB makes the NNM branches more related in their frequency content, hence, more likely to be excited together or to exchange energy, being locked in a mode. This kind of analysis, starting from the NNM branches and utilising their correlation can be useful for predicting an amplitude level for the IR branches during the design phase of an experiment. Note that this method not only predicts an amplitude, but also establishes the expected resonance by finding a multiple or shift for the branches so that their crossing corresponds to the increased NNM correlation.



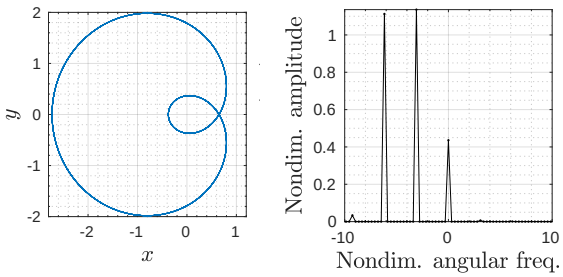
(a) Branches of BW (red), FW (blue) NNMs at $\Omega = 5$ when there is OOB forcing in rotating frame. Dashed branch for two times the FW branch frequencies, $2\,\omega_f^{rot}$.



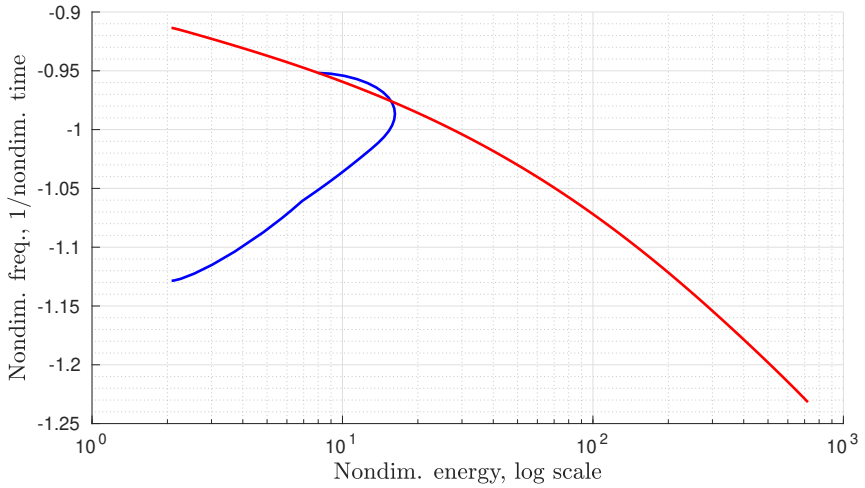
(b) Correlation of the red and blue solid branches in (a). Shorter arm (B-C) correlates better.



(c) Sample DFT of BW (at $\Omega = 5$), shown with green dot on the red branch.



(d) Sample DFT of FW (at $\Omega = 5$), shown with green dot on the red branch.



(e) Frequency-energy plot [118] of BW (ω_b^{rot}) and FW ($2\,\omega_f^{rot}$) NNMs.

Figure 6.9: Correlation of the rotating frame BW (solid red) and rotating frame FW (solid blue) NNM branches when there is OOB forcing. x-axis of (a) is $\omega = 2\pi/T$ with period T. Note the non-zero minimum amplitude of the branches due to the stationary OOB force in the rotating frame.

6.2.3 The effect of gravity as anisotropy on an unbalanced isotropic cubic Zilli system

Gravity sag or rotor-stator misalignment is a means of creating the off-centring in the system, which is needed for modal interaction, as discussed above. The results from Eq. (6.9) are presented in Figures 6.10–6.14.

$$\begin{gathered}\mathbf{w}'' - \Omega I_p \mathbf{J}_2 \mathbf{w}' + 2\zeta \mathbf{w}' + \mathbf{w} + \gamma \mathbf{w} r^2 + f_0 = me\Omega^2 \begin{Bmatrix} \cos\phi \\ \sin\phi \end{Bmatrix}, \quad \mathbf{w} = \begin{Bmatrix} x \\ y \end{Bmatrix} \\ \gamma = 0.25 \quad m = 0.9 \quad \zeta = 0.01 \\ e = 0.353 \quad I_p = 0.143 \quad f_0 = 0.9 \end{gathered} \tag{6.9}$$

When the gravity sag/misalignment is present in the EOM, along with OOB, different modes of vibration can be observed in the bifurcation diagram. In Figure 6.10, in addition to the main resonance, there are superharmonic peaks and subharmonic response, as well as $\omega_f^{sta} - \omega_b^{sta} = \Omega$ (or $\omega_f^{rot} - \omega_b^{rot} = \Omega$) and $2\,\omega_f^{sta} - \omega_b^{sta} = \Omega$ (or $2\,\omega_f^{rot} = \omega_b^{rot}$) combination resonance branches are visible. This shows that the off-centring of gravity allows for more interaction between the FW and BW modes of the system compared to only OOB-forcing. Additionally, the locations of $\omega_f^{sta} - \omega_b^{sta} = \Omega$ combination resonance in the bifurcation diagram in Figure 6.10 can be estimated from the crossing of the shifted FW branch (with frequencies $\omega_f^{sta} - \Omega$) and the BW branch (with frequencies ω_b^{sta}) (such as in Figure 6.8 which is for $\Omega = 4$) because the correlation starts after this level.

Figures 6.11 - 6.14 illustrate the sample orbits from the BD in Figure 6.10. The diversity when the off-centring effects of OOB and gravity sag are combined is remarkable: subharmonic and superharmonic resonances, as well as combination resonances can be seen in addition to the IR of order 2:1. The various families of responses can be distinguished in various ways. Firstly, they form distinct branches on the experimental bifurcation diagram. In addition, the number, position and spacing of peaks in the frequency response can be used to distinguish different resonances. For example, frequency peaks of $\Omega/2$ and Ω would indicate subharmonic resonance of order 1/2, or a frequency relation between the main frequency peaks such as $\omega_f^{sta} - \omega_b^{sta} = \Omega$ would indicate a combination resonance, a fundamentally different response. And finally, the Poincaré section which also implies the rotating frame orbit can be inspected. The overlaid stroboscopic Poincaré sections indicate periodicity: if it forms a closed circle, the response is quasiperiodic; if it forms n localised points, the response is a period-n motion, if it forms only one localised point, then it is synchronous with the drive speed.

Figure 6.15 illustrates the effect of the gravity sag/misalignment on the rotating frame trajectory, and compares it to the stroboscopic Poincaré section taken in the stationary frame. At low amplitudes, the gravity sag/misalignment is dominant, and the quasiperi-

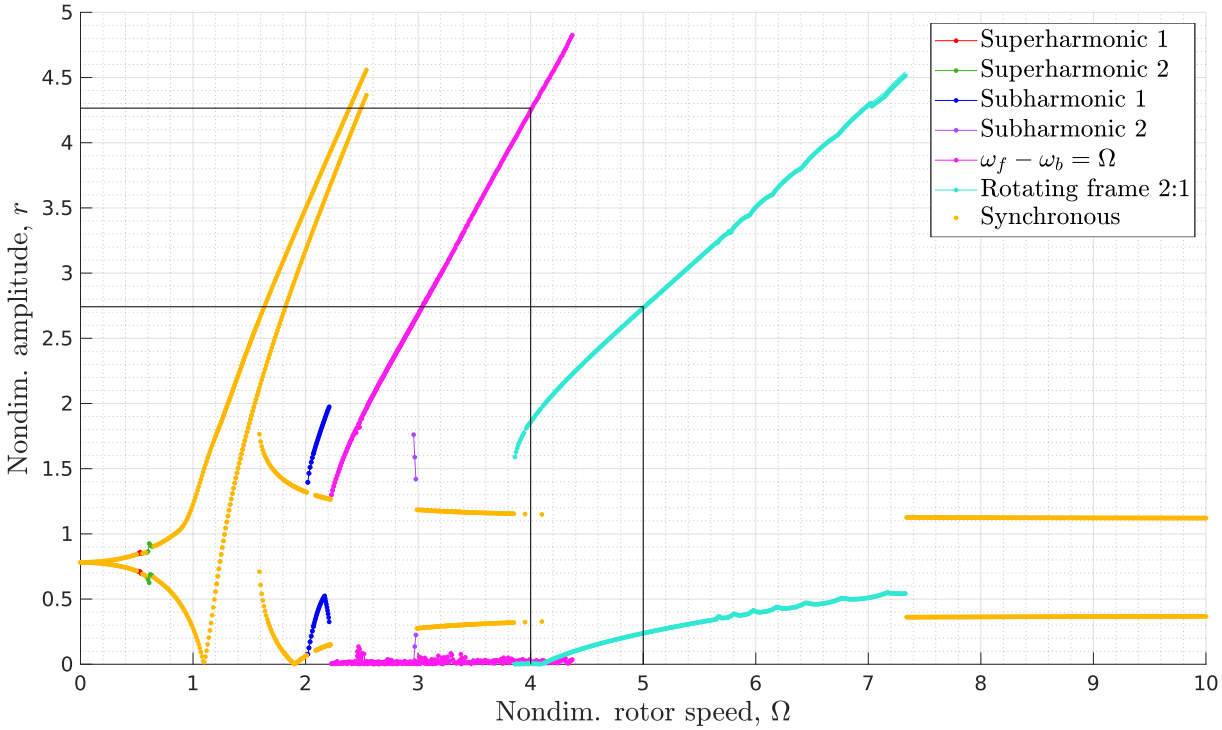
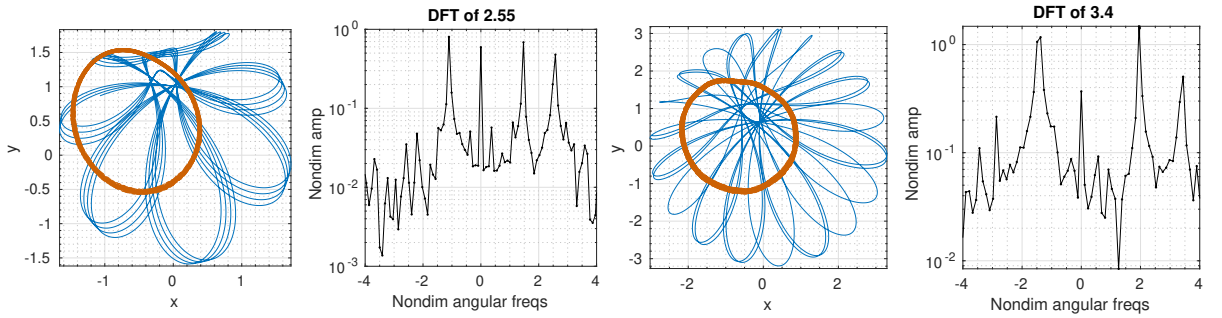
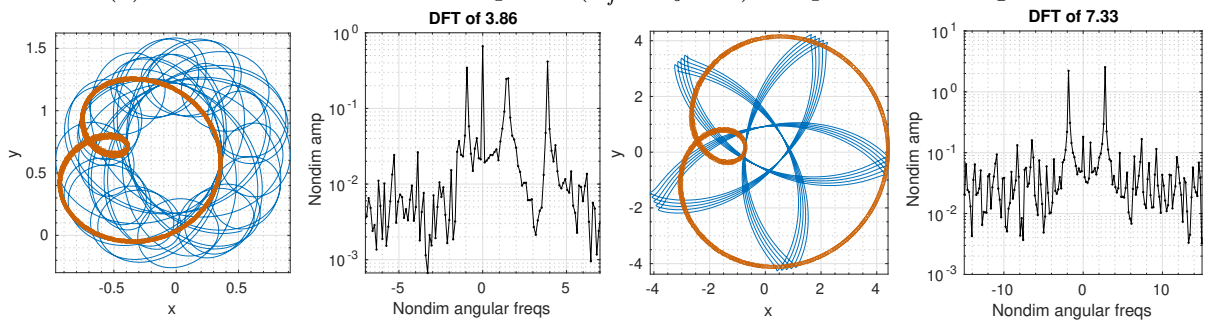


Figure 6.10: Nondimensional amplitude vs nondimensional rotor speed of Eq. (6.9). Amplitude peaks and minimums are indicated with the same colours for each response. Black lines are related to the discussions on the correlation in Figures 6.8 and 6.9 regarding where the solution can be expected.

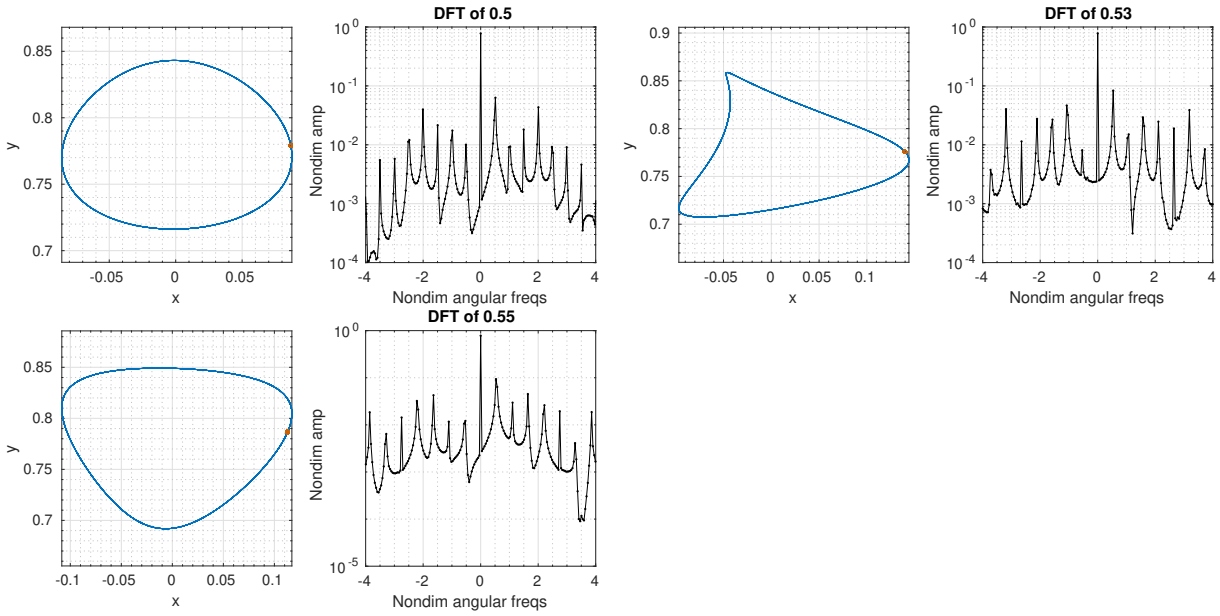


(a) Combination resonance response ($\omega_f - \omega_b = \Omega$) samples seen in Figure 6.10.

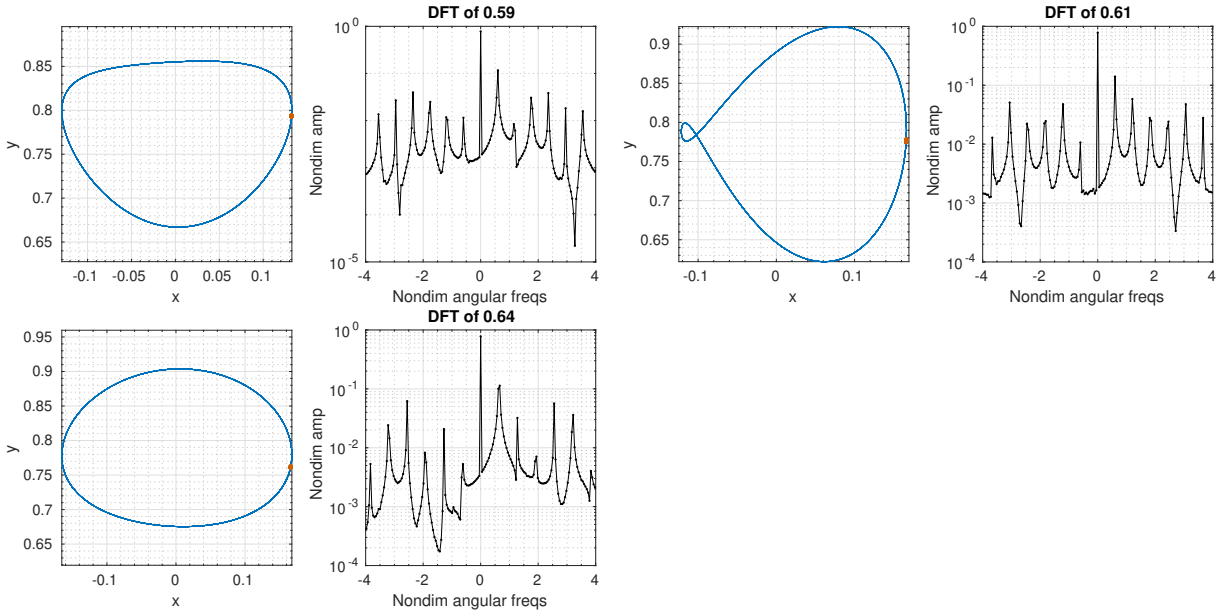


(b) 2:1 IR response ($2\,\omega_f - \omega_b = \Omega$) samples seen in Figure 6.10.

Figure 6.11: Combination resonance and IR samples from Figure 6.10. Brown dots show the stroboscopic Poincaré section. The numbers in the titles indicate the drive speed.

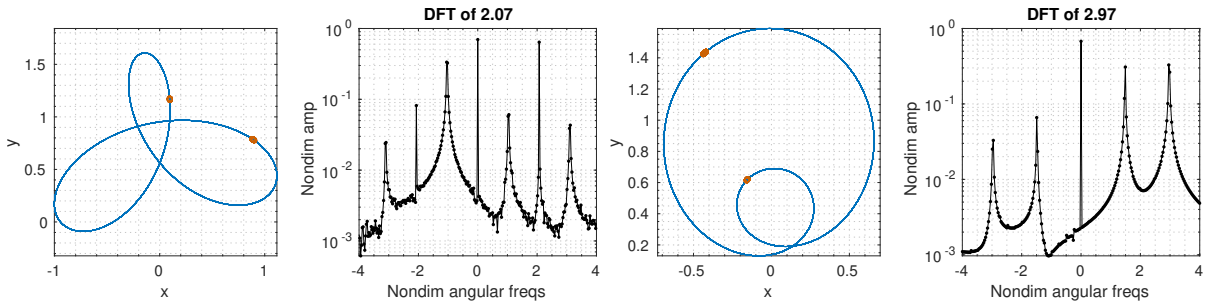


(a) Superharmonic response samples with peak frequencies of $\omega = -2\,\Omega$ and Ω from Figure 6.10.



(b) Superharmonic response samples with peak frequencies of $\omega = 2\,\Omega$ and Ω from Figure 6.10.

Figure 6.12: Superharmonic response samples (double-frequency vibration, secondary critical speed) from Figure 6.10. Brown dots show the stroboscopic Poincaré section. The numbers in the titles indicate the drive speed.



(a) Subharmonic resonance sample with frequency peaks at $\omega = -\Omega/2$ and Ω.

(b) Subharmonic resonance sample with frequency peaks at $\omega = \Omega/2$ and Ω.

Figure 6.13: Subharmonic samples from Figure 6.10. Brown dots show the stroboscopic Poincaré section. The numbers in the titles indicate the drive speed.

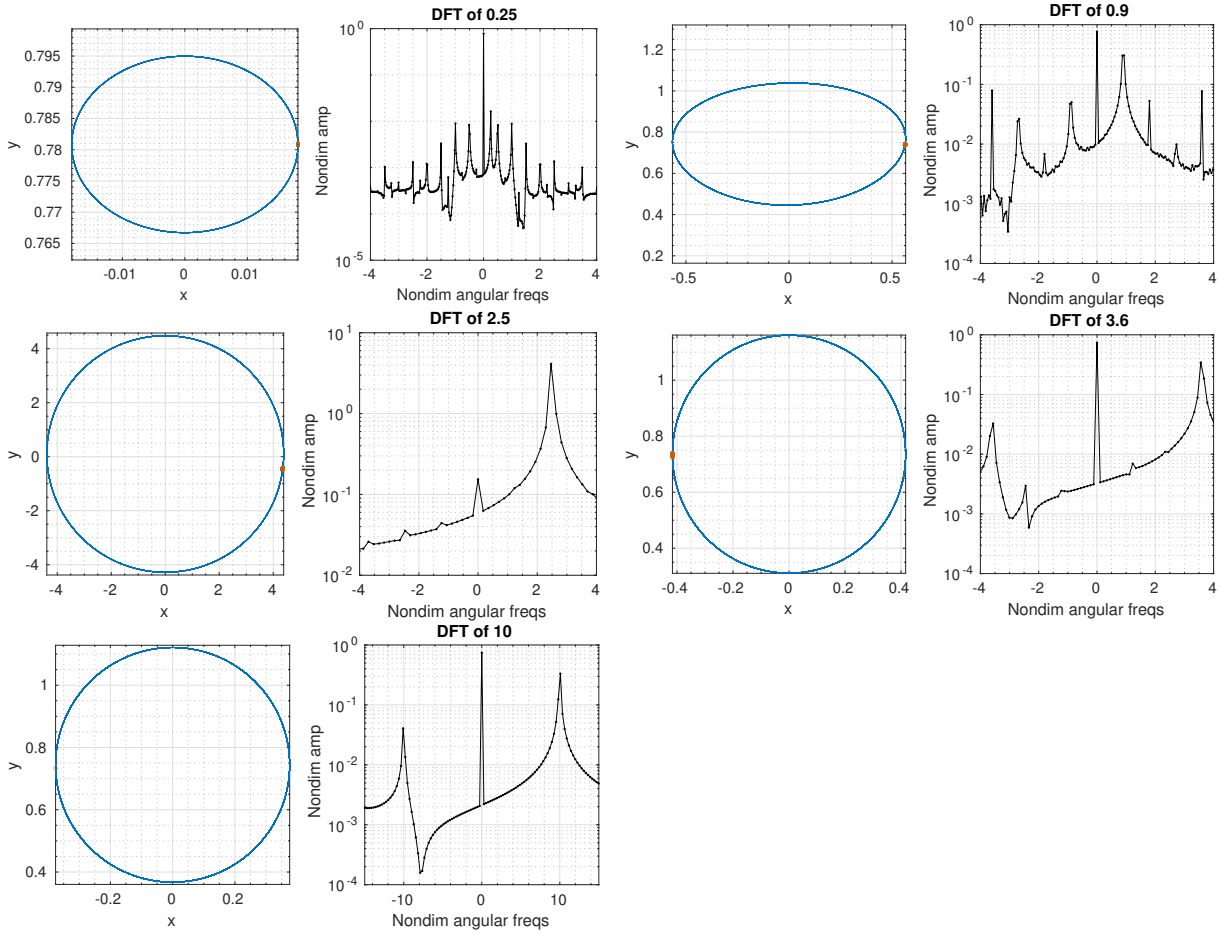


Figure 6.14: Synchronous response samples along the BD in Figure 6.10. Brown dots show the stroboscopic Poincaré section. The numbers in the titles indicate the drive speed.

odic rotating frame trajectory is far from periodic. As the stiffened amplitude of motion increases with the rotor speed, the rotating frame trajectory starts to follow the stroboscopic Poincaré section. Therefore, only at higher amplitudes one can ignore the gravity sag/misalignment where the response is governed by the OOB forcing, rather than the gravity sag/misalignment. This shows that, in general, the stroboscopic Poincaré section does not represent the rotating frame trajectory in the presence of gravity sag.

6.2.4 The effect of out of balance excitation as off-centring on cubic/tanh Zilli system

The effect of out of balance excitation on the nonlinear system Eq. (6.8) is well discussed in the previous chapters for cubic stiffness (Ch. 3 and 4), and in the contact-focusing previous literature [4, 30, 31, 13, 3]. Particularly, OOB excitation is responsible for the excitation of the main resonance as well as the sustained IR motion which were called SL (2:1, $2\,\omega_f^{rot} = \omega_b^{rot}$, single loop) and DL (3:1, $3\,\omega_f^{rot} = \omega_b^{rot}$, double loop) in those chapters. The bifurcation diagrams of the isotropic cubic Zilli system (Eq. (6.8)) and isotropic tanh-contact Zilli system (derived in Eq. (4.2)) are shown in Figure 6.16 which was obtained in brute force time simulations. This shows that the interaction between the underlying modes is more likely with the harsher nonlinearities which would make the NNMs loaded with many harmonics.

6.3 Conclusions

This chapter investigated by exploitation of the NNM concept further for more robust understanding of the quasiperiodic IR responses observed in gyroscopic rotordynamic systems by exploring the link between the underlying FW and BW NNMs. First, it is established that the 2:1 IR response is degenerate in the conservative case. Then, correlation between the underlying modes are discussed regarding the interaction of the FW and BW modes in the conservative cases, with and without off-centring effects, as well as the undamped, OOB-forced case. This showed that the correlation of NNMs can predict the occurrence of their interaction as a combination resonance or IR. Although the proposed NNM correlation idea is useful to explain the formation of the quasiperiodic rotating IRs, further research has to be conducted to understand further. NNMs of the Zilli system with contact nonlinearity can be investigated for validation of the preliminary observations here.

So far in the thesis, the theoretical investigations have explored the nonlinear responses observed in the nonlinear rotor-stator systems, particularly focusing on the quasiperiodic IRs. The effects of damping and eccentricity have been investigated, two of the most variable parameters, and the questions on IR formation have been tackled. Next, a test

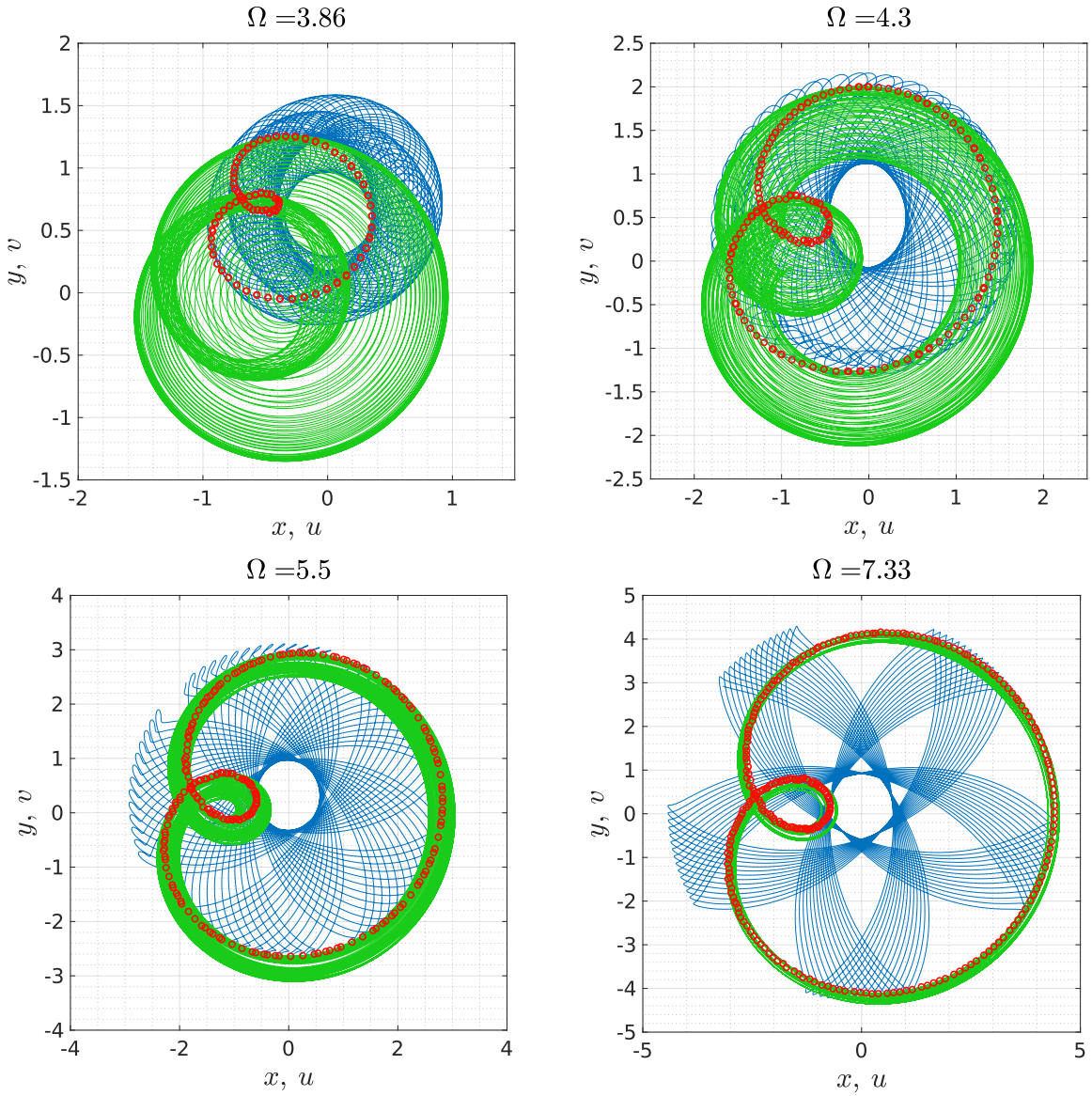


Figure 6.15: Rotating frame versus stroboscopic Poincaré section for $2\,\omega_f^{sta} - \omega_b^{sta} = \Omega$. Blue and green plot the stationary and rotating frame trajectory, red circles show the stroboscopic Poincaré section. Only for high amplitudes the effect of gravity fades with respect to the OOB forcing.

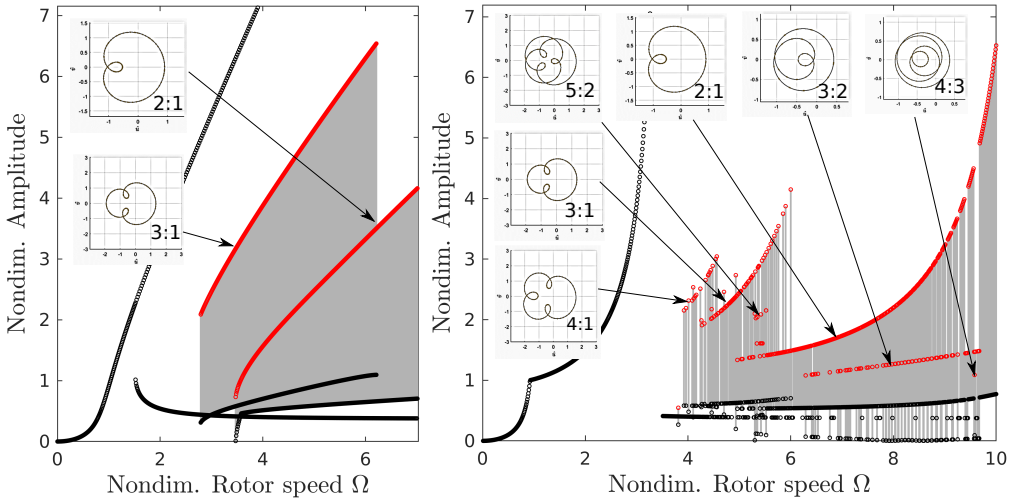


Figure 6.16: Bifurcation diagrams from time simulation, comparing the richness of the two systems: cubic nonlinearity (left) and contact nonlinearity (right). Red and black dots show the maximum and minimum of the trajectory that are connected by gray lines.

rig will be built for the validation of the understanding gained in the theoretical studies.

Chapter 7

Experimental Investigations of Nonlinear Rotor-Stator Bouncing Interactions

7.1 Design of the test rig

The preceding theoretical studies in Chs. 3 and 4 showed that the cubic nonlinearity is able to generate some of the nonlinear responses that are excited due to a compliant or rigid contact nonlinearity. These studies showed that common internal resonances (IRs) that are seen in the hard contact (either rigid or compliant stiffness) nonlinearity and can be generated by the soft, cubic nonlinearity. The bifurcation diagram (BD) of one of them can be homotopy-continued into the other's.

In line with the research interest (Section 1.6.3) the aim in this chapter is to confirm the excitation of nonlinear responses such as the interaction of the underlying linear modes as IRs, and testing their prediction as proposed previously in theoretical studies, by using a bench-top test rig. Therefore, in the experiments a cubic stiffness nonlinearity is designed using the notion of bend-stretch coupling to investigate the IR phenomenon. The experimental design and test rig decisions include:

1. A versatile rig that is adaptable to other stiffness definitions, such as in [21]. Despite being pinned to the rotor by a self-aligning ball bearing, the stator is to be designed separately so that different boundary conditions for the stator and different clearances or contact surfaces can be achieved for alternative experimental setups. Therefore, the stator is to be designed as an external device that is attached to the rotor.
2. A cantilever rotor is to be used, such as used in [128, 65]. The nonlinear forces, either by means of friction, contact or geometric nonlinearity, or axial forces, will effect the bending of the shaft, but are assumed negligible for understanding the

underlying linear system. The Campbell plots, naturally, do not take into account the complicated affects that result from the coupling of the cantilever rotor to the stator, but it ought to match the experimental Campbell diagram when the cubic stiffness is not acting.

3. The linear stiffness is to be achieved purely by the cantilever action. This cantilever boundary condition is more straightforward to implement in experiments than omnidirectional angular stiffness.
4. The nonlinear stator stiffness is to be achieved with rod mountings similar to ([17] or [48]. However, in order to create a bend stretch coupling for generating a cubic stiffness the axial position of the stator is constraint by attaching it to the end of the rotor by a self-aligning ball bearing, and to the ground by pinned-pinned rods.
5. The data acquisition (DAQ) system is to be capable of at least 5 kHz sampling. [21] used 1.6 kHz; [52] used 4 kHz; 5.120 kHz in a dual rotor by Bing et al. [132]. Ref. [129] gave a reference by setting the expected vibration frequency at $5 \times \Omega$ where Ω is the rotor spin speed). However, for high quality data higher sampling is needed: For instance, for the 2:1 IR response, the largest prominent frequency of the oscillation is the drive frequency which will be maximum 50 Hz (3000 rpm). 100 points per revolution would make a needed 5 kHz sampling. Note that complex DFT will be used so that the frequencies above Nyquist frequency will usefully indicate BW (negative) frequencies (see Section 2.1).
6. A discrete mathematical model of 4-dof is to be defined for conducting time simulations. The shaft mass is assumed to be negligible compared to the disk and stator, and the stator to disk distance is assumed to be short enough to approximate a rigid connection between them. Axial effects are neglected because the axial natural frequency is expected to be much higher than the lateral frequencies (see in Section 7.1.1). Therefore, the 4-dof model is expected to suffice to represent the experimental dynamics. The generalised coordinates are the lateral translational displacement pair and angular displacement pair of the disk.
7. Due to the high number of connecting joints, the damping is bound to be difficult to measure. Therefore, the experimental results are to be utilised for updating the damping value. However, for an initial estimate, the nondimensional damping values used in Chs. 3 and 4 can be transformed into dimensional values and used.

The test rig that meets these experimental design decisions is unique to the knowledge of the author when combining the factors of the nonlinear investigation aims, the versatility of the stator design, bench-top sizes, and being suitable for the detailed investigations of nonlinear rotor-stator interactions. The test rig to be manufactured is illustrated in Figure 7.1.

The manufactured test rig has a cantilever shaft that is connected to the disk towards the free tip where the shaft may be coupled to the stator. The use of the cantilever

boundary condition instead of a pinned boundary condition was due to the robustness and reliability of cantilever's implementation: coupling between a shaft that is pinned at the drive end would cause problems with the coupling, especially when a flexible coupling might incur internal rotor damping leading to instability, or exert complicated forces on the rotor. For the shaft material, case hardened silver steel was used.

The stator is linked to the ground by 4 stiffness rods in pinned-pinned boundary conditions, which creates bend-stretch coupling. In this version, there is not a clearance; though, the design is adaptable to other implementations of the stator nonlinear stiffness.

There are four pillars of the rig which were padded underneath with levelling washers for achieving isotropy of the frame. The motor is located at the top plate, which drives the shaft at constant speed. The bearing level is located under the motor plate, where a pack of three angular contact ball bearings in DBD configuration satisfy cantilever boundary conditions for the shaft. One more plate is located at the bottom above the ground for the stiffness rods.

The laser sensors are attached to the frame by means of extrusion segments which are not shown in Figure 7.1 for a clearer view, but are visible in the photograph of the rig in Figure 7.13. The x-face (y-face) is where Omron (MTI) laser sensors are placed which measure the stator displacement in the x-direction (y-direction).

In the rest of this chapter, Section 7.1.1 give a 2-dof equations of motion (EOM) so that in Section 7.1.2 the dimensional values aimed in the design are obtained from the nondimensional 2-dof studies in Chs. 3 and 4. Then, in Section 7.1.3 gives bearing selection which is included in Appendix C.2 in more detail. Section 7.1.4 explains the details of the DAQ system. The stator's position was measured by using three laser sensors which is elaborated in Section 7.1.5.

Then, the next section (Section 7.2) gives the 4-dof EOM followed by the time simulations in Section 7.3. The experimental rig's calibration was given in Section 7.4 which includes the measurements for the shaft-bow, the force-displacement curve, and the the rig's natural frequencies. The experimental results are given in Section 7.5 including the experimental Campbell plot, as well as the experimental BD measurements. An updated Campbell diagram for the manufactured rig is drawn in Section 7.5.2. Then, the 4-dof EOM is updated and the simulation results are compared to the experiments in Section 7.5.3. Lastly, conclusions are drawn in Section 7.6.

7.1.1 2-dof equations of motion

Figure 7.2 shows the schematic drawing of the 2-dof EOM derived below in order to estimate the natural frequencies of the system. This discussion is done here before the 4-dof model is developed because the preceding mathematical models were 2-dof (cubic and tanh-contact Zilli cubic model in the previous chapters, see Chs. 3 and 4), and would

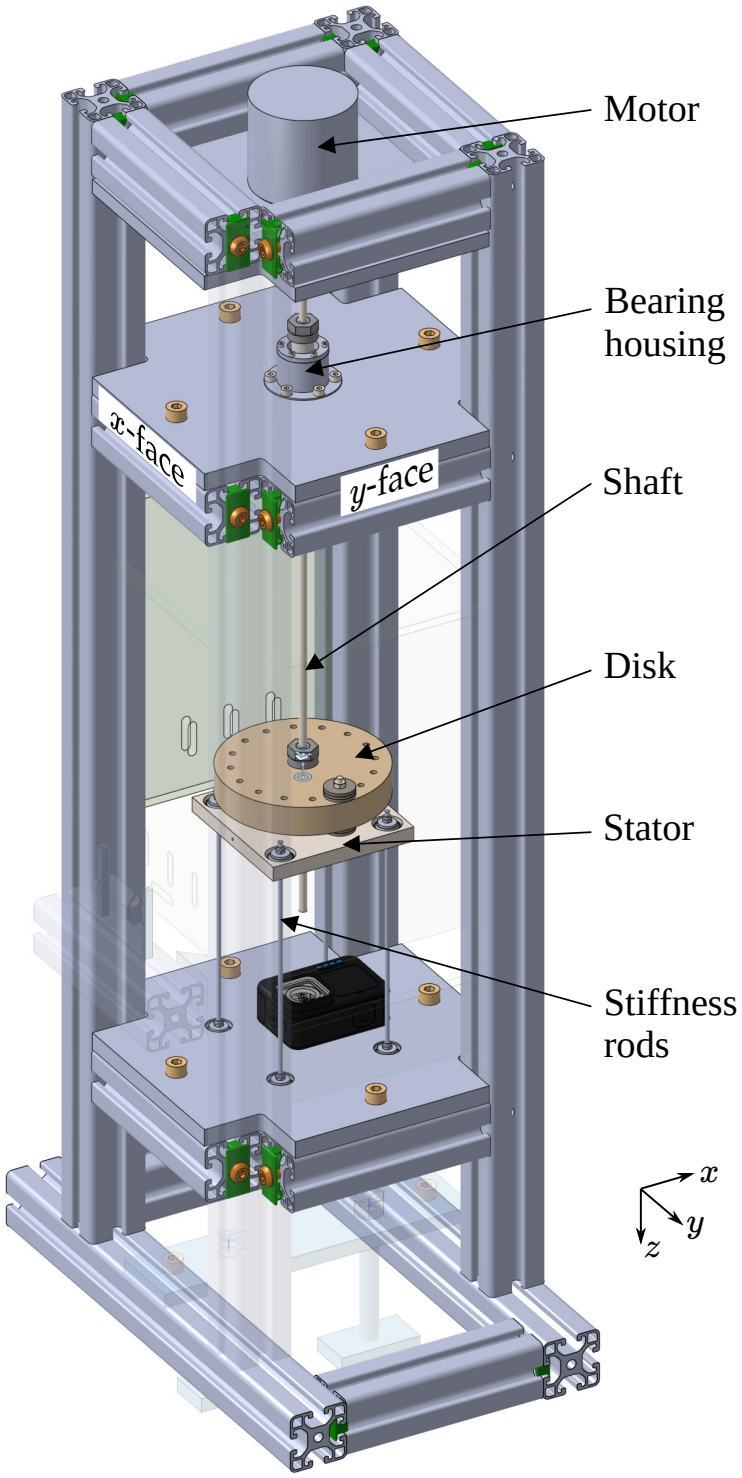


Figure 7.1: 3D global assembly drawing of the test rig. Main parts, coordinate frame and x- and y-faces are indicated. Protective polycarbonate sheets, one pillar of the frame and sensor attachments kits are rendered transparent for clearer view. Shims that are used to centre each level with respect to the frame are not shown.

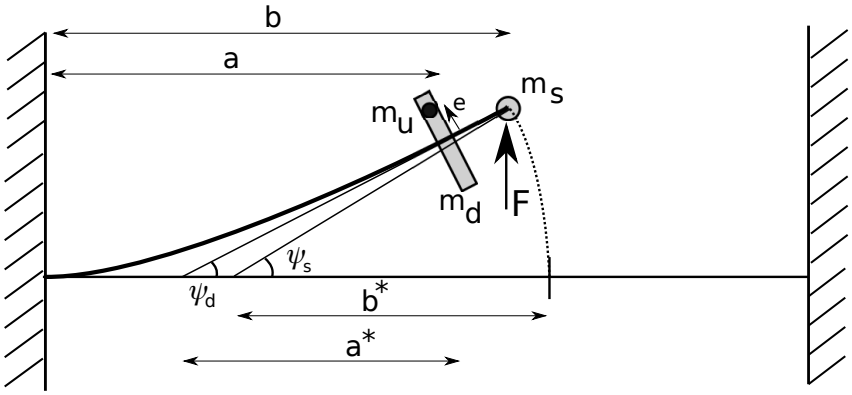


Figure 7.2: Schematic of the 2-dof system

be more easily compared to a 2-dof model. This comparison will be used to calculate the optimal dimensional values in the experimental design.

Kinematics and natural frequency estimates

The 2-dof model below includes the disk and the stator placed on a cantilever shaft. The stator is located at the tip. The force F at the tip of the cantilever shaft causes a displacement at the stator. From the strength of materials (e.g. [173]), based on the geometry shown in Figure 7.2 the kinematics of a cantilever beam with lateral tip force F in the 2-dof formulation,

$$\psi_d = Fa_I(2b_I - a_I)/(2EI) \tag{7.1a}$$
$$\psi_s = Fb_I^2/(2EI) \tag{7.1b}$$
$$x_d = Fa_I^2(3b_I - a_I)/(6EI) \tag{7.1c}$$
$$x_s = Fb_I^3/(3EI) \tag{7.1d}$$
$$x_d/\psi_d = a_I(3b_I - a_I)/(3(2b_I - a_I)) \tag{7.1e}$$
$$x_s/\psi_s = 2b_I/3 \tag{7.1f}$$
$$x_d/x_s = a_I^2(3b_I - a_I)/(2b_I^3) \tag{7.1g}$$
$$\psi_d/\psi_s = a_I(2b_I - a_I)/(b_I^2) \tag{7.1h}$$
$$a^* = x_d/\tan(\psi_d) \approx x_d/\psi_d = a_I(3b_I - a_I)/(3(2b_I - a_I)) \tag{7.1i}$$
$$b^* = x_s/\tan(\psi_s) \approx x_s/\psi_s = 2b_I/3 \tag{7.1j}$$
$$\alpha = x_d/x_s = a_I^2(3b_I - a_I)/(2b_I^3) \tag{7.1k}$$
$$\beta = (x_d/x_s)/(a^*) = \psi_d/x_s = 3a_I(2b_I - a_I)/(2b_I^3) \tag{7.1l}$$

where a and b are the disk and stator's distance from the cantilever end; a^* and b^* are the disk and stator's distance from their tangent angle intersection points; x_d, x_s, ψ_d, ψ_s are the lateral displacement of disk and stator and angle of the shaft at the disk and stator, respectively; α and β are the calculated variables as defined. All super-subindexes

I indicate that the value is the initial value before any lateral displacement.

From the kinematics in Eq. (7.1), the stiffness, inertia and natural frequency variables can be extracted in angular coordinates as

A – using angular stiffness

$$ {}_I k_{\phi}^{kinem} = F b^* / \psi_s = (4/3) E_1 I_1^I / b_I \tag{7.2a} $$

$$ J_{d,e}^{kinem} = m_s b_I^{*2} + \left(J_d + (m_d + m_u) a_I^{*2} \right) \left(\frac{\psi_d}{\psi_s} \right)^2 \tag{7.2b} $$

$$ \omega_{k_{\phi}^{kinem}}^{n} = \sqrt{ {}_I k_{\phi}^{kinem} / J_{d,e}^{kinem} } \tag{7.2c} $$

where m_u, m_d and m_s are the mass of the unbalance, disk and stator, J_d is the diametral moment of inertia of the disk. $J_{d,e}^{kinem}$ is the effective diametral moment of inertia of the disk at the stator. k_{ϕ} is the angular stiffness against the shaft angle at the stator. $w_{k_{\phi}^{kinem}}^{n}$ is the angular natural frequency of the shaft. E_1 is the shaft elastic modulus and I_1^I is the cross-section area moment of inertia of the shaft without lateral motion. The same can be written in terms of the lateral coordinates as,

B – using lateral stiffness

$$ {}_I k_{rb}^{kinem} = F / x_s = 3 E_1 I_1^I / b_I^3 \tag{7.3a} $$

$$ m_e^{kinem} = m_s + \left(J_d + (m_d + m_u) a_I^{*2} \right) / a_I^{*2} \left(\frac{x_d}{x_s} \right)^2 \tag{7.3b} $$

$$ \omega_{k_{rb}^{kinem}}^{n} = \sqrt{ {}_I k_{rb}^{kinem} / m_e^{kinem} } \tag{7.3c} $$

where m_e^{kinem} is the effective mass at the stator and ${}_I k_{rb}^{kinem}$ is the lateral stiffness due to cantilever for a lateral force acting at "b" distance, i.e, at the stator (i.e. at the connection of the shaft and the rods). $\omega_{k_{rb}^{kinem}}^{n}$ is the natural frequency of the shaft derived from lateral stiffness acting at the stator.

Derivation of the EOM and natural frequency

The 2-dof EOM is derived by the Lagrange method. Along with the linear stiffness k_{rb}, a cubic stiffness k_{3b} acts at the stator laterally. This will have an effect on the potential energy. First, the kinetic energy can be written as follows,

$$ T_{tra} = \frac{1}{2} m_d \left(x_d'^2 + y_d'^2 \right) + \frac{1}{2} m_u \left(x_u'^2 + y_u'^2 \right) + \frac{1}{2} m_s \left(x_s'^2 + y_s'^2 \right) \tag{7.4a} $$

$$ T_{rot} = \frac{1}{2} J_d \left(\theta_d'^2 + \psi_s'^2 \cos {\theta_d}^2 \right) + \frac{1}{2} J_p \left(\Omega^2 - 2\,\omega \psi_d' \sin\theta_d + \psi_d'^2 \sin^2\theta_d \right) \tag{7.4b} $$

$$ \approx \frac{1}{2} J_d \left(\theta_d'^2 + \psi_d'^2 \right) + \frac{1}{2} J_p \Omega^2 - J_p \Omega \psi_d' \theta_d \qquad \text{(with small angles)} \tag{7.4c} $$

$$ \tag{7.4d} $$

and the total potential energy,

$$V_{tot} = \frac{1}{2}k_{rb}r_s^2 + \frac{1}{4}k_{3b}r_s^4\,, \quad r_s^2 = x_s^2 + y_s^2 \tag{7.5a}$$

$$L = T_{tra} + T_{rot} - V_{tot} \tag{7.5b}$$

where Ω is the constant shaft speed; subscripts u, d and s indicate the unbalance, the disk and the stator, respectively; x and y are the lateral displacements and θ and ψ are the angular displacements; J_d and J_p are the diametral and polar moments of inertia of the disk at its centre; k_{rb} is the lateral stiffness at the stator. The prime notation $(\cdot)'$ indicates the time derivative. For the rotational kinetic energy, the reader is referred to the EOM derivation in Ch. 3. The nonconservative forces are defined to come from the damping at the stator lateral motion,

$$Q_{x_s} = -c_{rb}x_s' \tag{7.6}$$

$$Q_{y_s} = -c_{rb}y_s' \tag{7.7}$$

where, c_{rb} is the damping constant acting laterally at the stator.

The cantilever kinematics with a lateral force at the tip (see e.g. [173]) relate any two of the lateral displacements and/or angles,

$$x_d = \psi_d \frac{a}{3}\frac{3b-a}{2b-a} \qquad y_d = -\theta_d \frac{a}{3}\frac{3b-a}{2b-a} \tag{7.8a}$$

$$x_s = \psi_d \frac{2b^3}{3a(2b-a)} \qquad y_s = -\theta_d \frac{2b^3}{3a(2b-a)} \tag{7.8b}$$

$$x_u = x_d + \varepsilon\cos(\Omega t) \qquad y_u = y_d + \varepsilon\sin(\Omega t) \tag{7.8c}$$

where the following relations between the displacements can be noted,

$$\alpha = \frac{y_d}{y_s} = \frac{x_d}{x_s} = \frac{a^2(3b-a)}{2b^3} \tag{7.8e}$$

$$\beta = \frac{\psi_d}{x_s} = \frac{-\theta_d}{y_s} = \frac{3a(2b-a)}{2b^3}. \tag{7.8f}$$

By using the 2^{nd} type Lagrange equations,

$$\frac{\mathrm{d}}{\mathrm{d}t}\left(\frac{\partial L}{\partial x_s'}\right) - \frac{\partial L}{\partial x_s} = Q_{x_s} \tag{7.5}$$

$$\frac{\mathrm{d}}{\mathrm{d}t}\left(\frac{\partial L}{\partial y_s'}\right) - \frac{\partial L}{\partial y_s} = Q_{y_s}, \tag{7.6}$$

the EOM in the 2-dof model in the stationary frame angular form is:

$$\begin{aligned}\theta_d''\frac{m_e}{\beta} + J_p\beta^2\,\omega\frac{\psi_d'}{\beta} + k_{rb}\frac{\theta_d}{\beta} + c_{rb}\frac{\theta_d'}{\beta} + k_{3b}\left(\frac{r_{\theta\psi}}{\beta}\right)^2\frac{\theta_d}{\beta} &= -m_u\varepsilon\Omega^2\alpha\sin(\Omega t)\\ \psi_d''\frac{m_e}{\beta} - J_p\beta^2\,\omega\frac{\theta_d'}{\beta} + k_{rb}\frac{\psi_d}{\beta} + c_{rb}\frac{\psi_d'}{\beta} + k_{3b}\left(\frac{r_{\theta\psi}}{\beta}\right)^2\frac{\psi_d}{\beta} &= m_u\varepsilon\Omega^2\alpha\cos(\Omega t)\end{aligned} \tag{7.7}$$

where $r_{\theta\psi} = sqrt\theta_d^2 + \psi_d^2$ and ε is the eccentricity of the unbalance mass. In the stationary frame lateral displacement form, the EOM is (see Eq. (7.8)):

$$\begin{aligned}x_s''m_e + J_p\Omega\beta^2 y_s' + k_{rb}x_s + c_{rb}x_s' + k_{3b}r_s^2x_s &= m_u\varepsilon\Omega^2\alpha\cos(\Omega t)\\ y_s''m_e - J_p\Omega\beta^2 x_s' + k_{rb}y_s + c_{rb}y_s' + k_{3b}r_s^2y_s &= m_u\varepsilon\Omega^2\alpha\sin(\Omega t)\end{aligned} \tag{7.8}$$

where, $m_e = (m_d + m_u)\alpha^2 + J_d\beta^2 + m_s$ is the effective mass.

The natural frequency derived from the kinematics in Eqs. (7.2) and (7.3), is equal to the one from the formal derivation of the 2-dof EOM.

C – using the EOM

$$m_e = m_s + J_d\beta^2 + (m_d + m_u)\alpha^2 \tag{7.9a}$$

$$\omega_{k_{rb}}^n = \sqrt{k_{rb}^I/m_e} \tag{7.9b}$$

$$\omega_n = \omega_{k_{rb}}^n = \omega_{k_{rb}^{kinem}}^n = \omega_{k_\phi^{kinem}}^n \tag{7.9c}$$

where k_{rb}^I is the lateral stiffness at the stator, given by Eq. (7.3a).

The nondimensional form of the EOM can make the important features of the system stand out in terms of the resulting dynamics. The nondimensional form can be expressed as:

$$\begin{aligned}x_s'' + I_p\Omega y_s' + x_s + 2\zeta x_s' + \gamma r_s^2x_s &= \mu\Omega^2\cos(\Omega\tau)\\ y_s'' - I_p\Omega x_s' + y_s + 2\zeta y_s' + \gamma\hat{r}_s^2y_s &= \mu\Omega^2\sin(\Omega\tau)\end{aligned} \tag{7.10}$$

where, the following identities and definitions are used,

$$\begin{aligned}x_s := \frac{x_s}{c}, \qquad y_s := \frac{y_s}{c}, \qquad (\cdot)' = \frac{(\cdot)'}{\omega_n}, \qquad \Omega := \Omega/\omega_n, \qquad \tau = t\omega_n, \qquad \omega_n^2 = \frac{k_{rb}}{m_e}\\ I_p = \frac{J_p\beta^2}{m_e}, \qquad \zeta = \frac{c_{rb}}{(2m_e\omega_n)}, \qquad \gamma = \frac{k_{3b}c^2}{k_{rb}}, \qquad \mu = \frac{m_u}{m_e}\frac{\varepsilon}{c}\alpha\end{aligned} \tag{7.11}$$

where τ is the nondimensional time, $(\cdot)'$ is redefined to denote the nondimensional time derivative, I_p is the nondimensional polar moment of inertia, and c is a notional dimension. Here, justification of the use of a notional dimension c in the nondimensionalisation despite that it does not represent a physical feature, is as follows: The nondimensional cubic

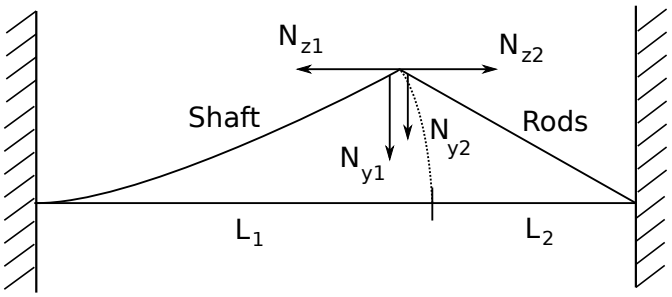


Figure 7.3: Schematic of the equilibrium when the stator is displaced.

stiffness measure γ and nondimensional unbalance μ are adjustable with it, as seen in Eq. (7.11). Therefore, the experimental cubic stiffness and unbalance will be adjustable with respect to each other, in order to meet the nondimensional values used in the previous studies in Chs. 3 and 4, so long as the lateral motion is within the capability of the rig (i.e. below 9 mm).

7.1.2 Deciding the numerical values for the test rig

Figure 7.3 shows the schematic drawing of the planned test rig. The part labelled "1" is the shaft, and the part labelled "2" is the stiffness rods. The rods' boundary conditions are pinned-pinned, and the shaft's boundary condition is cantilever at one end and 'pinned to the stator' at the other. The shaft connects to the stiffness rods through the stator. The stiffness rods create an effect of bend-stretch coupling. The decision on the test rig dimensional design values comes firstly from the decision on the shaft diameter (5 mm), as a first indication of the size of the benchtop test rig that is planned. Secondly, the nondimensional to dimensional value conversion using Eq. (7.11) guides the design (this comparison is given in Table 7.1). The maximum bearing forces are then calculated for the bearing selection.

Calculation of bearing forces through optimisation of stator position

To have an idea of the bearing forces that are expected during the dynamic operation of the rotor-stator pair which is supposed to follow the kinematic conditions as follows,

- The shaft is deflected on its own as a cantilever as a result of a lateral force at the stator (the same way as in Section 7.1.1). The shaft is denoted by subscript 1.
- The stiffness rods (four of them) are simply supported at both ends and deflect as a result of the same force. The rods are denoted by subscripts 2.

The effect of the resulting axial force on the shaft is neglected, which is a softening effect on the axial force loaded on the bearings. Therefore, the force calculation here is conservative. The force equilibrium (Figure 7.3) is calculated by solving the equilibrium

equations in Eq. (7.12) with the `fsolve` function of MATLAB [156]. The equilibrium equations are:

$$L_1\cos(\alpha_1) + L_2\cos(\alpha_2) = L_1^I + L_2^I + l_0 \tag{7.12a}$$

$$N_{z1} = N_{z2} \tag{7.12b}$$

where l_0 is the initial axial preload in metres; L_1 and L_2 are the length of the shaft and the rods, N_{z1} and N_{z2} are the axial force on the shaft and the stiffness rods, α_1 and α_2 are angles of the straight lines between supports of the shaft and the stiffness rods, respectively. One can write,

$$\begin{aligned} &\alpha_1 \approx \tan^{-1}(y_s/L_1) && N_{y1} = k_1 l_1 \sin(\alpha_1) && N_{z1} = k_1 l_1 \cos(\alpha_1) \\ &\alpha_2 \approx \tan^{-1}(y_s/L_2) && N_{y2} = k_2 l_2 \sin(\alpha_2) && N_{z2} = k_2 l_2 \cos(\alpha_2) \end{aligned} \tag{7.13}$$

where, y_s is the lateral motion of the stator (the junction of the shaft and the stiffness rods), N_{y1} and N_{y2} are the lateral force appearing on the shaft and the stiffness rods, k_1 and k_2 are the axial stiffness of the shaft and stiffness rods, l_1 and l_2 are the axial elongations of the shaft and the rods, respectively. Also,

$$\delta_{L_1^I} = \frac{3}{5}\frac{y_s^2}{L_1^I} - \left(L_1^I - \sqrt{{L_1^I}^2 - y_s^2}\right) \tag{7.14a}$$

$$\begin{aligned} &L_1 = L_1^I - \delta_{L_1^I} + l_1 && L_2 = L_2^I + l_2 && A_1 = \frac{\pi}{4}d_1^2 && A_2 = 4\frac{\pi}{4}d_2^2 \\ &d_1 = d_1^I\left(1 - \frac{l_1}{L_1^I}\nu_1\right) && d_2 = d_2^I\left(1 - \frac{l_2}{L_2^I}\nu_2\right) && k_1 = \frac{E_1 A_1}{L_1} && k_2 = \frac{E_2 A_2}{L_2} \end{aligned} \tag{7.14b}$$

where $\delta_{L_1^I}$ is the axial contraction due to the cantilever action of the shaft. The values d_1 and d_2 are the diameters, ν_1 and ν_2 are the Poisson's ratios, A_1 and A_2 are the cross-sectional areas, E_1 and E_2 are the Young's moduli of the shaft and the rods, respectively. The calculations makes use of the input values below which are found by trial-error around the initial decision of the shaft diameter (d_1^I = 5 mm):

$$L_1^I = 300 \text{ mm} \qquad L_2^I = 150 \text{ mm} \qquad l_0 = 5\ \mu\text{m} \tag{7.15a}$$

$$d_1^I = 5 \text{ mm} \qquad d_2^I = 3 \text{ mm} \qquad a_I = 270 \text{ mm} \tag{7.15b}$$

$$b_I = L_1^I \qquad d_d = 110 \text{ mm} \qquad h_d = 20 \text{ mm} \tag{7.15c}$$

$$m_d = 1433.06 \text{ g} \qquad m_s = 828.03 \text{ g} \qquad m_u = 10 \text{ g} \tag{7.15d}$$

$$\varepsilon = 45 \text{ mm} \qquad E_1 = 210 \text{ GPa} \qquad E_2 = 70 \text{ GPa} \tag{7.15e}$$

$$\nu_1 = 0.28 \qquad \nu_2 = 0.33 \qquad \rho_1 = 7800 \text{ kg/m}^3 \tag{7.15f}$$

where d_d and h_d are the disk's diameter and thickness, respectively. The following calculations are utilised for lateral motion,

$$J_d = \frac{1}{16} m_d d_d^2 + \frac{1}{12} m_d h_d^2 = 1135254.51 \cdot 10^{-9} \text{ kg m}^2$$
$$J_p = \frac{1}{8} m_d d_d^2 = 2175025.87 \cdot 10^{-9} \text{ kg m}^2 \tag{7.16a}$$
$$I_1^I = \frac{\pi}{64} d_1^{I4} = 0.306796 \cdot 10^{-12} \text{ m}^4$$
$$k_{rb}^I = \frac{3E_1 I_1}{b_I^3} = 715.834 \text{ N/m} \quad w_n^I = \sqrt{k_{rb}^I / m_e} = 19.412 \text{ rad/s}. \tag{7.16b}$$

Figure 7.4 shows the linear ($F_r = k_{rb} r$) and cubic ($F_3 = k_{3b} r^3$) lateral forces and a cubic polynomial fit to the data reveals the estimated cubic and linear stiffness values,

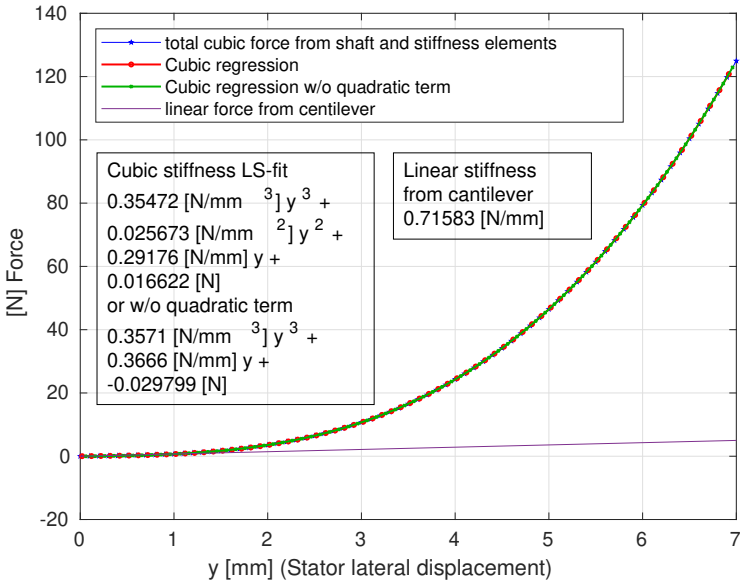
$$k_{3b} = 354719609.39 \text{ N/m}^3 \tag{7.17a}$$
$$k_{rb} = 715.83 \text{ N/m}. \tag{7.17b}$$

It is important to notice that the aim is not to obtain a high-fidelity model of the rig; the main take-away of this study here is to acquire a cubic stiffness dimensional value that is relatively comparable to the preceding nondimensional value in the dimensionalised form. Therefore, for the linear stiffness, the value of k_{rb} that comes from the cantilever motion will be used instead of the fit's linear term. Additionally, Figure 7.4 also indicates that the linearity is more dominant in the lateral stator amplitude region below the level of 1 mm.

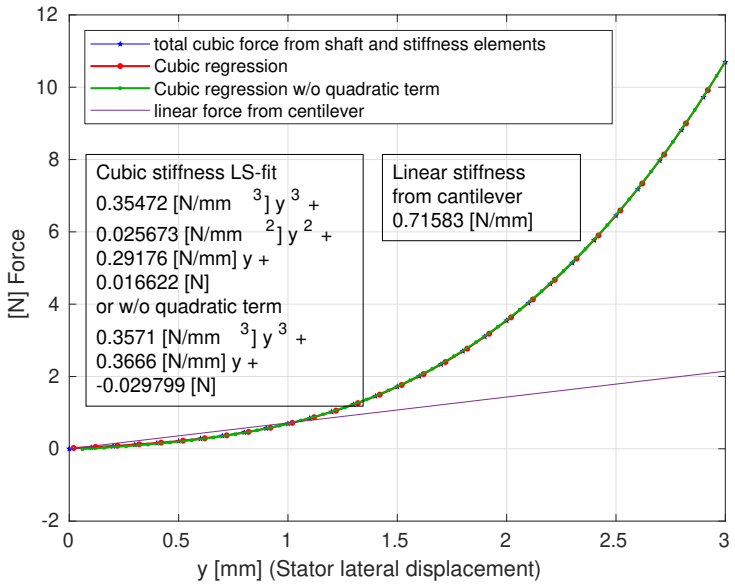
The dimensionalisation results are given with the dimensional and nondimensional value comparisons in Table 7.1. The dimensional identities that are presented in Eq. (7.11) are used. Table 7.1 shows that the dimensional stiffness values in Eq. (7.17) match the nondimensional values used in the preceding chapters in Chs. 3 and 4.

Figure 7.5 shows the axial force of the rig. As shown in Figure 7.5, the expected maximum axial force emerging from the system is around 1800 N at the maximum expected lateral stator displacement of 7 mm, which will be used for bearing selection.

Figure 7.6 shows that as the lateral displacement occurs in the stator, the stator also moves axially by about 30 μm in 7 mm of lateral movement. This is thought to have no effect on the dynamics predicted.



(a)



(b)

Figure 7.4: Solution of Eq. (7.12-7.14) for N_y. (a) Force displacement curve and the cubic polynomial fit showed against the linear stiffness expected. (b) Zoom view of (a).

Table 7.1: Nondimensionalisation by use of c of the stationary frame 2-dof system with c = 0.7 mm arbitrarily selected. Values with "preceding study" reference are obtained from Ch. 3.Dimensionalisation is done according to Eq. (7.11). The "designed" values come from Eqs. (7.15) and (7.16).

Polar moment of inertia J_p:	
I_p preceding study	0.143 Nondimensional
J_p dimensionalisation	0.011087 kg m^2
J_p design	0.002175 kg m^2
Unbalance $u = me$:	
preceding study	0.3177 Nondimensional
dimensionalisation	0.00049673 kg m
design	0.00045 kg m
Cubic stiffness γ, k_3:	
γ preceding study	0.25 Nondimensional
k_3 dimensionalisation	365233520.9252 N/m^3
k_{3b} design	354719609.3959 N/m^3
γ nondim. outcome of design	0.2428 Nondimensional
Viscous damping ζ, c_{rb}:	
ζ preceding study	0.01 Nondimensional
c_{rb} dimensionalisation	0.74 N/(m/s)
c_{rb} not-known in design	missing
Maximum rotor speed to achieve Ω_{max}:	
Ω_{max} preceding study	10 Nondimensional
Ω_{max} dimensionalisation	194.12 rad/s (=10×w_n^I)
Ω_{max}^{motor} motor capacity	314.16 rad/s (3000 rpm)
Maximum stator displacement expected r_{max}	
r_{max} preceding study	19 Nondimensional
$r_{s,max}$ dimensionalisation	0.0133 m
$r_{s,max}$ designed	0.007 m

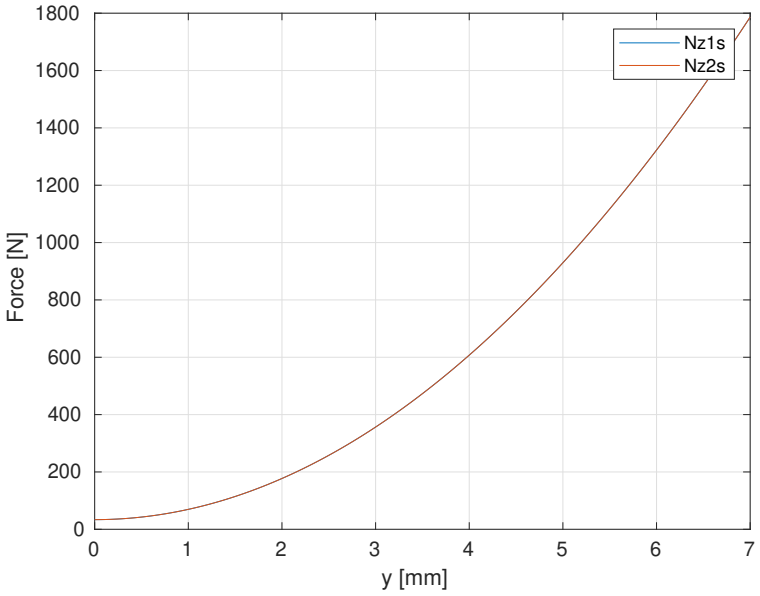


Figure 7.5: Forces appearing on the bearings along a 0-7 mm stator lateral travel according to the 2dof system.

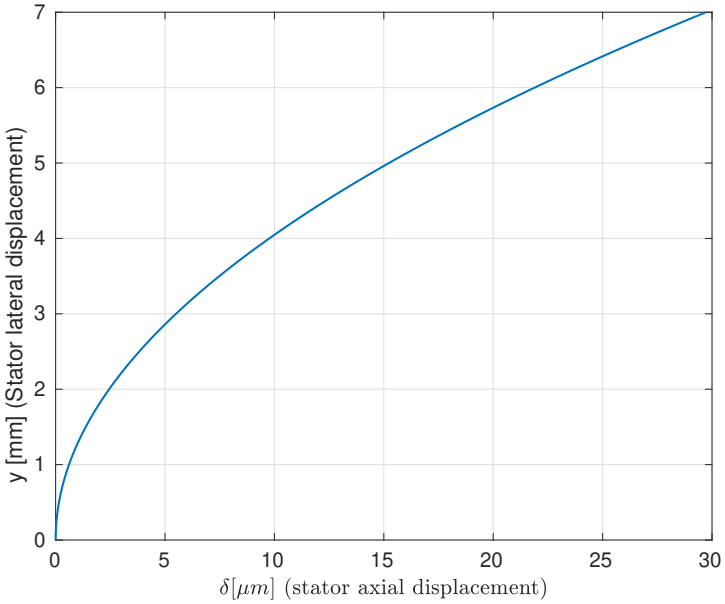


Figure 7.6: Stator axial displacement with stator lateral displacement

Table 7.2: Bearings used in the experimental test rig.

Position	**Type**	**Bearing**
Shaft cantilever end	ACBB	3 × NSK 7900 A5 TNY P4 (Triplex DBD)
Shaft stator end	SABB	1 × NSK 2301
Pinned-pinned stiffness rods' ends	SABB	7 × NSK 135, 1 × SKF 135

ACBB: Angular contact ball bearing. SABB: self aligning ball bearing.

Lastly, for axial motion the following calculations are made,

$$A_1^I = \frac{\pi}{4} {d_1^I}^2 = 19.635 \cdot 10^{-6} \text{ m}^2 \qquad A_2^I = \frac{\pi}{4} {d_2^I}^2 \times 4 = 28.274 \cdot 10^{-6} \text{ m}^2 \quad \text{(4 rods)} \tag{7.18a}$$

$$k_1^I = \frac{E_1 A_1^I}{L_1^I} = 13744467.859 \text{ N/m} \quad k_2^I = \frac{E_2 A_2^I}{L_2^I} = 13194689.145 \text{ N/m} \tag{7.18b}$$

$$\begin{aligned} \omega_{n,\,axial}^I &= \sqrt{(k_1^I + k_2^I)/((m_d + m_u)(a_I/b_I)^2 + m_s)} \\ &= 3672.93 \text{ rad/s} \\ &= 189.2\, \omega_n^I \end{aligned} \tag{7.18c}$$

Because of the high ratio of the axial natural frequency $\omega_{n,\,axial}^I$ to the lateral natural frequency ω_n^I (see Eq. (7.16)), the interaction of the axial motion with lateral motion is unlikely. Additionally,

$$m_{shaft} = \rho_1 \frac{\pi {d_1^I}^2}{4} L_1^I = 45.95 \text{ g} \tag{7.19a}$$

$$\text{shaft}-\text{to}-\text{disk mass ratio} = m_{shaft}/m_d = 0.032. \tag{7.19b}$$

Therefore, the shaft mass is neglected compared to the disk mass due to the low value of shaft-to-disk mass ratio.

7.1.3 Selection of bearings

Bearings that fit the design purpose are given in Table 7.2. Mainly, the NSK Rolling Bearing catalogue [174] is used. The reader is referred to Appendix C.2 for the details of the bearing selection process.

7.1.4 Data acquisition hardware and software

The data acquisition system included the following hardware:

- National Instruments (NI) cDAQ-9178 hub.
- NI 9223 ±10V analog input device: for tacho voltage input from the motor, the Omron sensors (OG and OW), and the MTI sensor.

- NI 9234 ±5V analog input device with integrated electronic/circuit piezoelectric (IEPE/ICP) capability: for use with the impact hammer and accelerometers in the tapping tests (ICP current of 4 mA was used).
- NI 9263 analog output: for motor speed voltage 0-5V control.
- 2 × NI 252C03 piezoelectric accelerometers (ICP current of 4 mA was used).
- PCB Piezoelectronics impact hammer (ICP current of 4 mA was used).
- Motor BLDC 58: 24 Vdc brushless motor whose integrated speed controller varies speed between 100-3000 rpm by $0-5$ Vdc input. It also outputs the tacho voltage to postprocess for speed measurement.
- 2 × Omron ZX2-LD100 0.5M: Class 2 CMOS laser displacement sensor. Range 100 ± 35 mm with ±5 Vdc output, 5 μm resolution, min. sampling interval of 33 μs. One of them is referred to as "OG" and the other as "OW" (see Appendix C.3 for differences.)
- MTI LTC-120-40-SA: Class 3R CMOS laser displacement sensor. Range 120 ± 20 mm with $0-10$ Vdc output ($1-9$ Vdc covers 40 mm range) and sampling rate of 40 kHz.

The motor "BLDC 58" is a 24 Vdc brushless motor. The speed control unit is integrated, and varies the speed in the range 100-3000 rpm with 0-5 Vdc speed control input.

The software system used is as follows:

- Labview 2017 SP1 Base, Full, Professional 32bit
- NI-DAQmx 17.0 Full 32/64bit
- CompactRio 17 Full 32bit
- Scilab 5.3.3 32-bit
- Scilab Labview Gateway 32-bit

with licences needed:

- LabView 2017 SP1 Development System
- LabView 2017 SP1 Application Builder
- LabView 2017 Database Connectivity Toolkit
- LabView 2017 Report Generation Toolkit for Microsoft Office

Postprocessing was done both with LabView [175] and Matlab [156].

Depending on the data acquisition task, different sampling rates were used. For a 3000 rpm rotor speed, or 50 rps (Hz), which is the maximum capability of the motor used, a minimum sampling rate can be set at 50Hz∗100points= 5kHz. Indeed, in most of the runs of the experiment, 10 kHz was used. Because of the use of the complex DFT (Section 2.1) whose input is the stator displacement in the complex plane ($x + jy$), the frequency

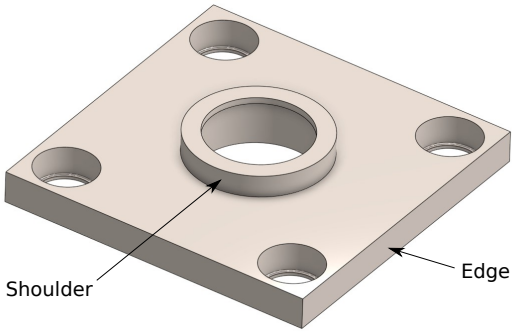


Figure 7.7: 3D drawing of the stator.

spectrum's folding does not happen and the frequencies above the Nyquist frequency show BW whirl components.

The differences in the data acquisition characteristics of the two Omron sensors and the MTI sensor are given in Appendix C.3. The sensor data acquisition delay of 0.38 ms was deemed unimportant compared to maximum event frequency at 50 Hz (i.e. the maximum rotor speed).

7.1.5 Measuring the stator position

The stator lateral position can be measured at its round shoulder (see Figure 7.7) which houses the 2301 bearing. However, this would lack the information about the angle of the stator in plane. Therefore, three lasers pointing at the stator edges are used in the study to track all three degrees of freedom of the stator in plane: two lateral displacements and one rotation angle.

Figure 7.8 shows a random orientation of the stator and the sensors when their laser beams are pointing at the stator edge with an offset from the centre, as well as with an angle. The stator position is governed by the following equations:

$$y_m = \frac{y_s}{\cos\beta} - \frac{R\tan\frac{\alpha_s}{2} + x_s - x_{sh} + y_s\tan\beta_{sh}}{\cos\beta_{sh}\cot\alpha_s + \sin\beta_{sh}} \tag{7.20}$$

$$x_A = \frac{x_s}{\cos\beta_A} + \frac{-R\tan\frac{\alpha_s}{2} + y_s + y_A - x\tan\beta_A}{\cos\beta_A\cot\alpha_s + \sin\beta_A} \tag{7.21}$$

$$x_B = \frac{x_s}{\cos\beta_B} - \frac{-R\tan\frac{\alpha_s}{2} - y_s + y_B + x\tan\beta_B}{\cos\beta_B\cot\alpha_s + \sin\beta_B} \tag{7.22}$$

where, y_m, x_A, and x_B are the MTI, OW, and OG measured displacements, respectively (Figure 7.8).

With the angles of OW and OG sensors assumed equal, i.e. $\beta_A = \beta_B = \beta_{AB}$, Eq.

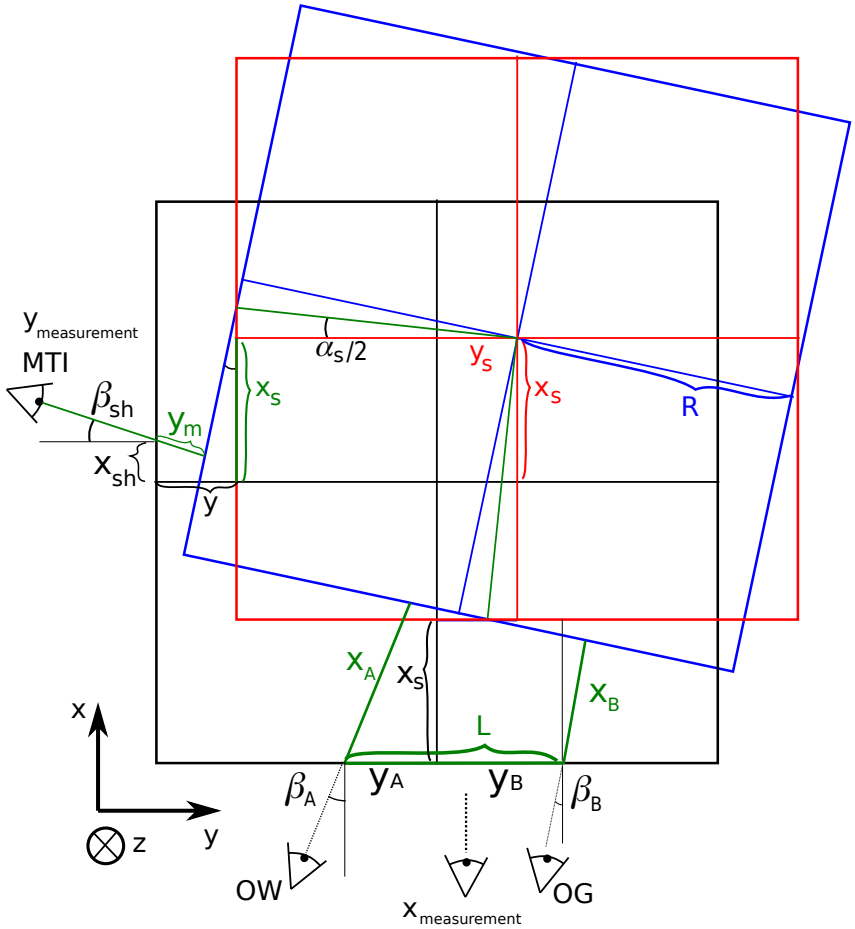


Figure 7.8: Three laser sensors are used to track the stator's motion in plane (lateral displacements and the rotation angle). The stator (black), has x_s and y_s translations (red), and a rotation by angle α_s (blue). Each laser beam hits the stator (black) at an angle and an offset as indicated.

Table 7.3: Offset values of the laser sensor setup.

Feature	**Value**
Stator edge size $2R$ = 100.13 mm	
MTI beam offset	$x_s = -0.3$ mm
OG offset	$y_A = 29.5$ mm
OW offset	$y_B = 29.5$ mm
MTI beam angle	$\beta_{sh} = -1.5$ deg
Omron beam angle	$\beta_{AB} = -0.5$ deg

(7.20) can be used to find the stator positions (x_s,y_s) linearly and α_s independently,

$$y_m = x_s\left(-\frac{1}{\gamma}\right) + y_s\left(\frac{1}{\cos\beta_{sh}} - \frac{\tan\beta_{sh}}{\gamma}\right) + \frac{x_{sh}}{\gamma} - \frac{R\tan\alpha_s/2}{\gamma} \tag{7.23a}$$

$$x_m = y_s\left(\frac{1}{\gamma_{AB}}\right) + x_s\left(\frac{1}{\cos\beta_{AB}} - \frac{\tan\beta_{AB}}{\gamma_{AB}}\right) + \frac{y_A - y_B}{2\gamma_{AB}} - \frac{R\tan\alpha_s/2}{\gamma_{AB}} \tag{7.23b}$$

$$\tan\alpha_s = \frac{\cos\beta_{AB}}{\frac{y_A+y_B}{x_A-x_B} - \sin\beta_{AB}} \tag{7.23c}$$

where x_A, x_B and y_m are the laser readings with $x_m = (x_A + x_B)/2$, and

$$\gamma = \cos\beta_{sh}\cot\alpha_s + \sin\beta_{sh} \tag{7.24}$$

$$\gamma_{AB} = \cos\beta_{AB}\cot\alpha_s + \sin\beta_{AB}. \tag{7.25}$$

The numerical values used are given in Table 7.3. These values are measured by locating the centre of the laser point on the stator by a ruler, and visually comparing the laser beam angle to a protractor, hence the accuracy and repeatability is low. However, the stator lateral shift and angle measurements were both qualitatively and quantitatively reliable in the range of motion it undergoes.

7.2 A 4-dof mathematical model for the gyroscopic cubic system

7.2.1 Definition of EOM

The disk lateral displacement and the disk angles are selected as the degrees of freedom of the system, neglecting the axial degree of freedom and the shaft mass as the axial natural frequency is much higher than the lateral natural frequency (see Eqs. (7.16) and (7.18)). Ref. [64] also neglected the axial force, though including the torsional vibrations; [70] investigated the effects of periodic axial load with combination resonance responses. The link between stator and the disk is assumed to be rigid since the 30 mm disk-stator

distance in the 4-dof EOM decreases to only 10 mm open shaft material.

$$T_{tra} = \frac{1}{2}m_d\left(x_d'^2 + y_d'^2\right) + \frac{1}{2}m_u\left(x_u'^2 + y_u'^2\right) + \frac{1}{2}m_s\left(x_s'^2 + y_s'^2\right) \tag{7.26}$$

$$T_{rot} = \frac{1}{2}J_d\left(\theta'^2 + \psi'^2\right) + \frac{1}{2}J_p\left(\Omega^2 - 2\,\omega\psi'\sin\theta + \psi'^2\sin^2\theta\right) \tag{7.27}$$

$$T_{tot} = T_{tra} + T_{rot} \tag{7.28}$$

$$V_{tot} = \frac{1}{2}\mathbf{w}^T\mathbf{K}\mathbf{w} + \frac{1}{2}k_{rb}r_s^2 + \frac{1}{4}k_{3b}r_s^4 \tag{7.29}$$

$$L = T_{tot} - V_{tot} \tag{7.30}$$

$$\delta W_{nc}^{active} = -\dot{x}_s c_{rb}\delta x_s - \dot{y}_s c_{rb}\delta y_s \tag{7.31}$$

where δW_{nc}^{active} is the nonconservative active force's virtual work. Ch. 3 gives the calculation of the rotational kinetic energy of the disk. The generalised coordinates are,

$$\mathbf{w} = \{x_d,\ y_d,\ \theta_d,\ \psi_d\}^T, \tag{7.32}$$

stator displacements are,

$$x_s = x_d + \psi_d b \tag{7.33}$$

$$y_s = y_d - \theta_d b \tag{7.34}$$

$$r_s^2 = x_s^2 + y_s^2 = x_d^2 + y_d^2 + \left(\theta_d^2 + \psi_d^2\right)b + 2x_d\psi_d b - 2y_d\theta_d b, \tag{7.35}$$

unbalance displacements are,

$$x_u = x_d + e\cos\phi \tag{7.36}$$

$$y_u = y_d + e\sin\phi \tag{7.37}$$

$$\dot{x}_u = \dot{x}_d - e\Omega\sin\phi \tag{7.38}$$

$$\dot{y}_u = \dot{y}_d + e\Omega\cos\phi, \tag{7.39}$$

the shaft stiffness matrix is,

$$K = \begin{bmatrix} k_{uu} & 0 & 0 & k_{u\psi} \\ 0 & k_{vv} & k_{v\theta} & 0 \\ 0 & k_{v\theta} & k_{\theta\theta} & 0 \\ k_{u\psi} & 0 & 0 & k_{\psi\psi} \end{bmatrix} = \frac{2EI}{a}\begin{bmatrix} 6/a^2 & 0 & 0 & -3/a \\ 0 & 6/a^2 & 3/a & 0 \\ 0 & 3/a & 2 & 0 \\ -3/a & 0 & 0 & 2 \end{bmatrix}, \tag{7.40}$$

where the stiffness coefficients for beam systems of clamped-free boundary condition (as in the case of overhung rotor here), can be utilised from [7], or extracted using the application of strength of materials (e.g. [173]).

Hamilton's principle can be applied:

$$\int_{t_1}^{t_2} \left(\delta L + \delta W_{nc}^{active} \right) \mathrm{d}t = 0 \tag{7.41}$$

or the 2nd type Lagrange's equations:

$$\frac{\mathrm{d}}{\mathrm{d}t}\left(\frac{\partial L}{\partial q_k'} \right) - \frac{\partial L}{\partial q_k} = Q_k \ , \quad Q_k = \frac{\partial \delta W_{nc}^{active}}{\partial q_k} \tag{7.42}$$

The resulting EOM is,

$$\mathbf{M}\ddot{\mathbf{x}} + \mathbf{G}\dot{\mathbf{x}} + \mathbf{C}\dot{\mathbf{x}} + \mathbf{K}_r\mathbf{x} + \mathbf{K}\mathbf{x} + \mathbf{N}\mathbf{x} = \mathbf{b} \tag{7.43a}$$

$$\mathbf{M} = \begin{bmatrix} m_d + m_u & 0 & 0 & 0 \\ 0 & m_d + m_u & 0 & 0 \\ 0 & 0 & J_d & 0 \\ 0 & 0 & 0 & J_d \end{bmatrix} + m_s\mathbf{P} \ , \quad \mathbf{G} = \begin{bmatrix} 0 & 0 & 0 & 0 \\ 0 & 0 & 0 & 0 \\ 0 & 0 & 0 & J_p\Omega \\ 0 & 0 & -J_p\Omega & 0 \end{bmatrix}$$

$$\mathbf{K} = \begin{bmatrix} k_{uu} & 0 & 0 & k_{u\psi} \\ 0 & k_{vv} & k_{v\theta} & 0 \\ 0 & k_{v\theta} & k_{\theta\theta} & 0 \\ k_{u\psi} & 0 & 0 & k_{\psi\psi} \end{bmatrix} = \frac{2EI}{a} \begin{bmatrix} 6/a^2 & 0 & 0 & -3/a \\ 0 & 6/a^2 & 3/a & 0 \\ 0 & 3/a & 2 & 0 \\ -3/a & 0 & 0 & 2 \end{bmatrix}$$

$$\mathbf{C} = c_{rb}\mathbf{P} \ , \quad \mathbf{K}_r = k_{rb}\mathbf{P} \ , \quad \mathbf{N} = k_{3b}r_s^2\mathbf{P}$$

$$\mathbf{b} = m_u e\Omega^2 \begin{Bmatrix} \cos\phi \\ \sin\psi \\ 0 \\ 0 \end{Bmatrix} \ , \quad \mathbf{x} = \begin{Bmatrix} x_d \\ y_d \\ \theta_d \\ \psi_d \end{Bmatrix} \ , \quad \mathbf{P} = \begin{bmatrix} 1 & 0 & 0 & b \\ 0 & 1 & -b & 0 \\ 0 & -b & b^2 & 0 \\ b & 0 & 0 & b^2 \end{bmatrix} \tag{7.43b}$$

7.3 Initial Campbell plots and initial simulation results

7.3.1 Initial Campbell plots

The linear, conservative 1st order form of Eq. (7.43) is derived as follows:

$$\mathbf{A}\mathbf{z}_r = s\mathbf{z}_r \ , \quad \mathbf{z} = \{\mathbf{w}^T, \mathbf{w}'^T\}^T = \mathbf{z}_r e^{s_r t} \tag{7.44}$$

$$\mathbf{A} = \begin{bmatrix} \mathbf{0} & -\mathbf{I} \\ \mathbf{M}^{-1}\mathbf{K} & \mathbf{M}^{-1}\mathbf{G} \end{bmatrix} \tag{7.45}$$

where $\mathbf{0}$ and $\mathbf{I}$ are the 4×4 zero and identity matrices, respectively. $\mathbf{z}_r$ and s_r are the r^{th} eigenvector and eigenvalue, respectively. The eigensolution of Eq. (7.43) is plotted at different rotor speeds to give the Campbell plot in Figure 7.9. The natural frequencies

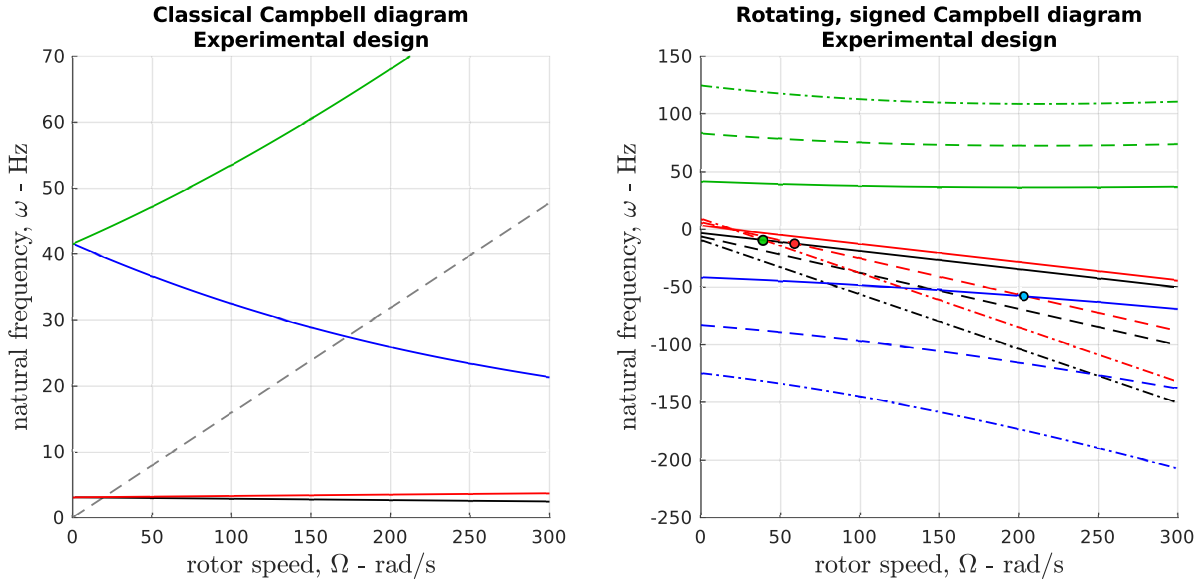


Figure 7.9: Experimental design Campbell plot from the eigensolution of Eq. (7.43). Left: Classical Campbell diagram. Right: Rotating frame, signed Campbell diagram [4]. Solid, dashed, and dash-dotted lines are one, two, and three times the natural frequencies of the same colour.

when the rotor is not rotating are 3.09 Hz (19.41 rad/s) and 41.54 Hz (261.00 rad/s). The 1X engine order intersects,

- The 1^{st} BW mode at 19.1 rad/s rotor speed
- The 1^{st} FW mode at 19.7 rad/s rotor speed
- The 2^{nd} BW mode at 172.6 rad/s rotor speed

Some IRs in the rotating frame are expected (right hand side of Figure 7.9),

- for $2\,\omega_{f1}^{rot} = \omega_{b1}^{rot}$ at 58.98 rad/s (red point in Figure 7.9), shortly denoted as $2^1{:}1^1$.
- for $3\,\omega_{f1}^{rot} = \omega_{b1}^{rot}$ at 39.32 rad/s (green point in Figure 7.9), shortly denoted as $3^1{:}1^1$.
- for $2\,\omega_{f1}^{rot} = \omega_{b2}^{rot}$ at 205.17 rad/s (blue point in Figure 7.9), shortly denoted as $2^1{:}1^2$.

7.3.2 Initial simulations

The time simulations of Eq. (7.43) were performed using Matlab [156] using `ode45` built in $4(5)^{\text{th}}$ order embedded Runge-Kutta integrator function. A relative tolerance of 10^{-7} and simulation time of 1000 s were used for transients to decay. The results are plotted in Figure 7.10 where in addition to an unbounded synchronous solution, the branches of $2^1{:}1^1$ and $2^1{:}1^2$ IR modes appear. All of these are shown in the Figure 7.11.

The modal damping of the second pair of modes decrease to extremely low levels at high speeds which caused an increased computational burden with the very long transient die-out times (see more details in Appendix C.1). High amplitude synchronous whirl solutions (as in Ω = 197 rad/s in Figure C.1) also appear which might arise because the

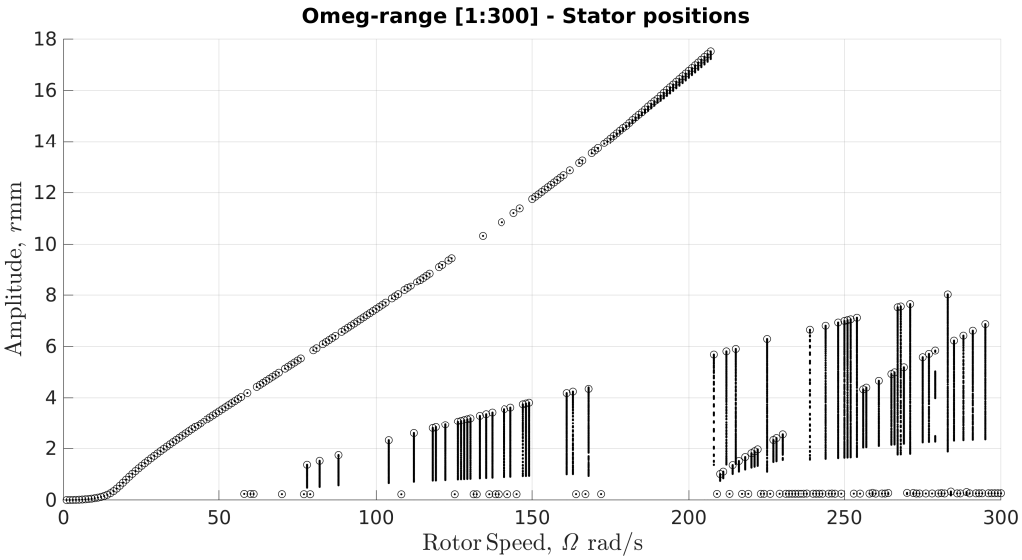


Figure 7.10: BD of the initial simulations of Eq. (7.43) with the design values, shown in stator positions. Stroboscopic Poincaré sections of at least 300 points are plotted as dots. Maximum amplitudes of the orbits are indicated with circles.

effective damping ratio becomes low at the high amplitudes where the cubic stiffness force becomes very high compared to the damping force.

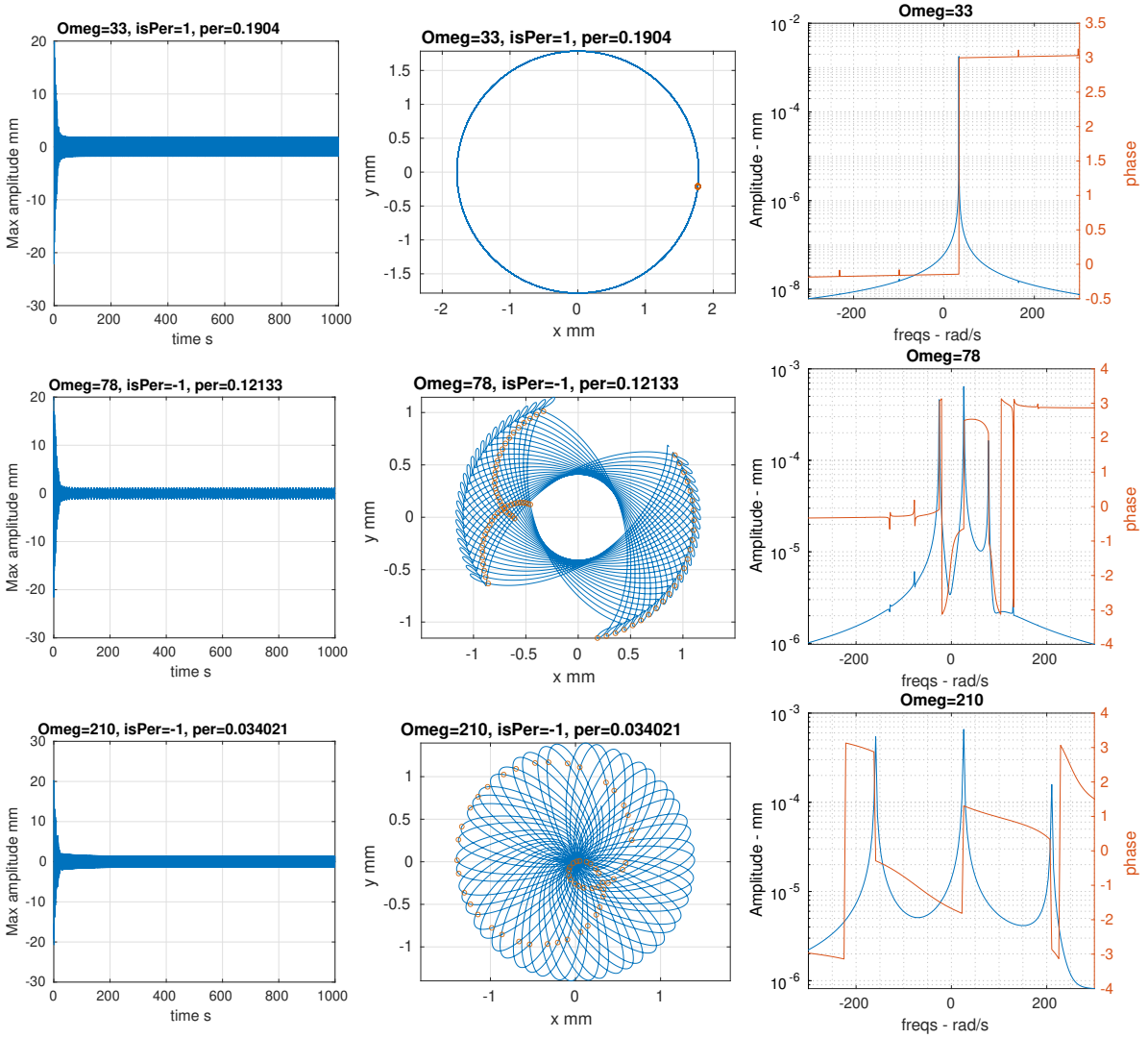


Figure 7.11: Simulation with experimental design values. Selected orbits that are expected in the experiment: synchronous (top), 2^1:1^1 (middle), and 2^1:1^2 (bottom).

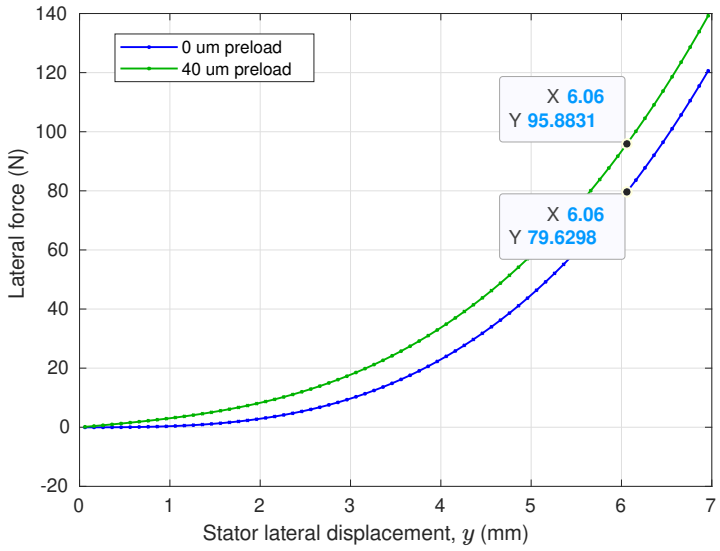


Figure 7.12: Force-displacement curve at the stator with the design values, without preload (blue) and with 40 μm preload (green).

7.4 Experimental procedures and calibration

Considerations and calibration

The test rig's global assembly drawing is given in Figure 7.1 and its photo is given in Figure 7.13. The manufactured test rig was designed based on the values in Eq. (7.15) and (7.16). The assembly drawing is given in Appendix C (Figure C.7).

The shaft had some initial bow when assembled, about 0.5 mm in diameter at the stator (see Section 7.4.1), due to a combination of factors involving the use of larger tolerances than designed during the manufacture.

Tapping tests on the stopped rotor were performed to measure the natural frequencies (see Section 7.4.2). Then, tightness of the rotor-stator assembly was assessed by daily tapping tests because of the the effect of the temperature variation (see Section 7.4.3): The rig frame, and the stiffness rods are made from aluminium, while the shaft is made from silver steel. If the expansion coefficient of steel is taken as $13 \cdot 10^{-6}$ °C^{-1} and that of aluminium as $26 \cdot 10^{-6}$ °C^{-1}, with the shaft of 300 mm length, an increase of temperature by 10 °C causes a preload of $(300 \text{ mm})\left((26-13)\cdot 10^{-6}\right)(10^{\circ}\text{C}) \approx 40\mu\text{m}$. The effect of this preload is illustrated in Figure 7.12 using the design values of the 2-dof system. Therefore, the temperature change of the lab affects the tightness of the rotor, hence the impact on the cubic stiffness and the perceived shaft bow. The force-displacement curve was measured and a cubic polynomial was fitted in Section 7.4.4) for high and low tightness of the rotor.

Tapping tests on the running rotor were done to get the experimental natural frequency maps (Campbell diagram) in Section 7.4.5 and compared to the rig's natural frequencies in Section 7.4.6.

Procedures

The rotor speed was controlled with its built in controller with only the speed control voltage input from the DAQ system. The Omron sensors and the MTI sensor measure positions in x- and y-direction, respectively (see Figure 7.1 for the coordinate frame). The data acquisition was not done in equal rotor speed intervals. Instead, when a particular feature of the response is near, the rotor speed intervals were shortened, and vice versa. The motor used has a tacho voltage output that issues 36 spikes of 5V in one revolution. This analog signal's main tone was interpreted using LabView [175] to infer the rotor speed reliably.

The main resonance experiences the jump phenomenon due to stiffening from the cubic stiffness. Therefore, as the slow runup was performed in a stepped sine fashion, after jump-down on the main resonance, the jump-up point was sought by decreasing the speed control voltage. Excitation of the responses other than the synchronous solutions were tried through a lateral impact at the stator. Once the response was obtained, the speed control voltage was incremented to continue on the branch according to the stepped sine test method.

As protective measures, four polycarbonate protective sheets were inserted into the frame around the disk and cut-outs were opened for lasers to pass through. Besides, a kill switch was incorporated for cutting the motor power in case of an emergency.

7.4.1 Measuring the shaft bow

Due to various factors such as not following the design tolerances, the shaft bow is present. The bearing fitting tolerances were not met. The bearing hub fit was uneven. The shaft sleeve had a concentricity issue, which is a difficult part of the design with a long narrow bore.

To obtain a meaningful measurement of the shaft bow, the rotor is first run at very low speed (0.41 Vdc speed control voltage, 2.3 rad/s or 0.36 rps[1] rotor speed), which gives the inner circle in Figure 7.14. Then it is run at a higher speed (3.0 Vdc motor control voltage, 170 rad/s or 27.1 rps rotor speed), which gives the outer circle in Figure 7.14.

The centre difference between these circles appears 0.06 mm, although this is subject to change even between each successive runs due to the clearance found in around the stator bearings. Therefore, this slight misalignment was neglected. The shaft bow has an x-span of 0.49 mm and y-span of 0.50 mm. The shaft bow is slightly elliptical which is thought to come from the slight anisotropy in the bearing plate and bearing hub where angular contact ball bearings are housed.

There is also another important implication of the shaft bow which happened in the way mentioned: the part of the shaft beam that is above the bearing housing up to the

[1] rps: revolutions per second

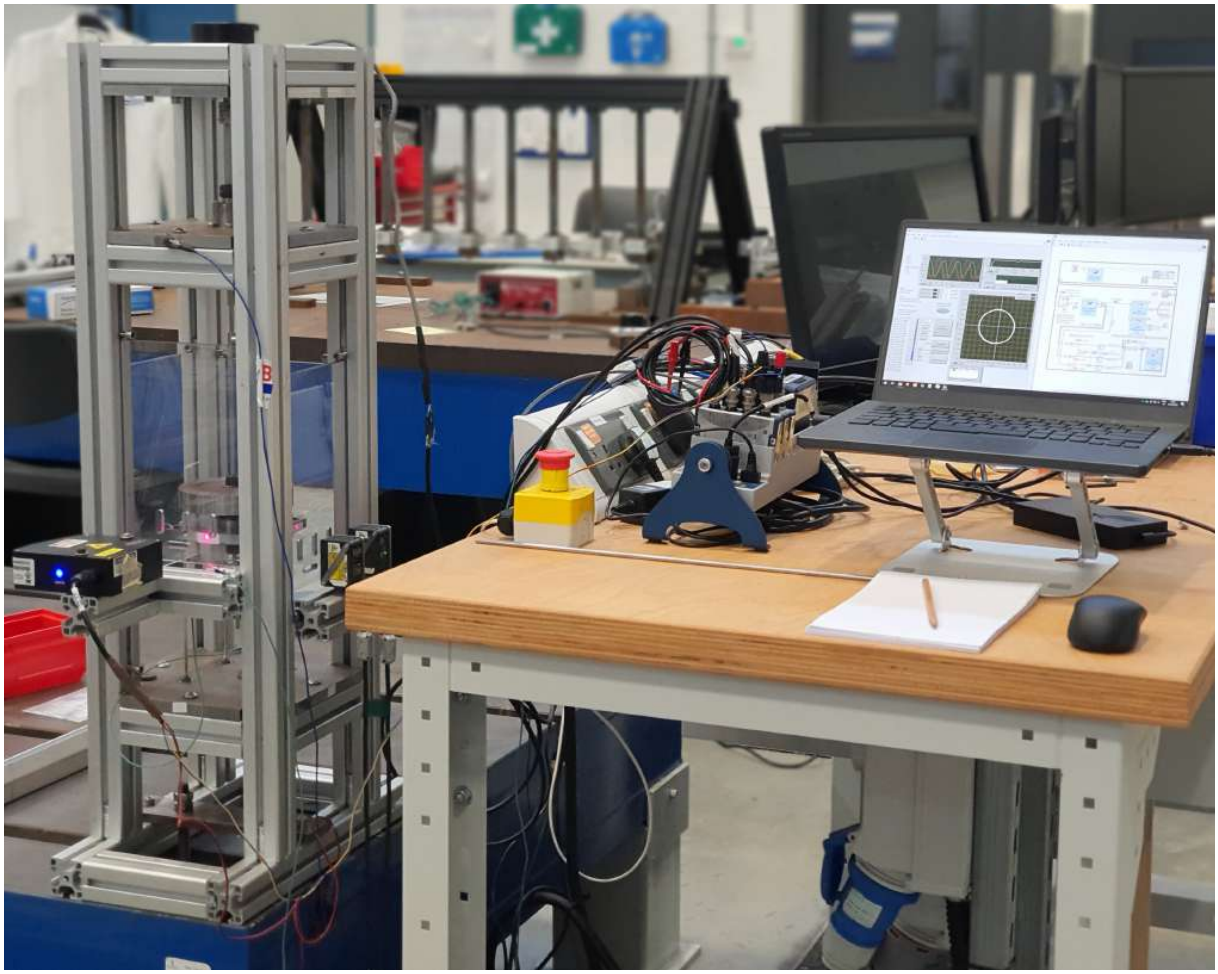


Figure 7.13: Photograph of the experimental test rig and data acquisition system.

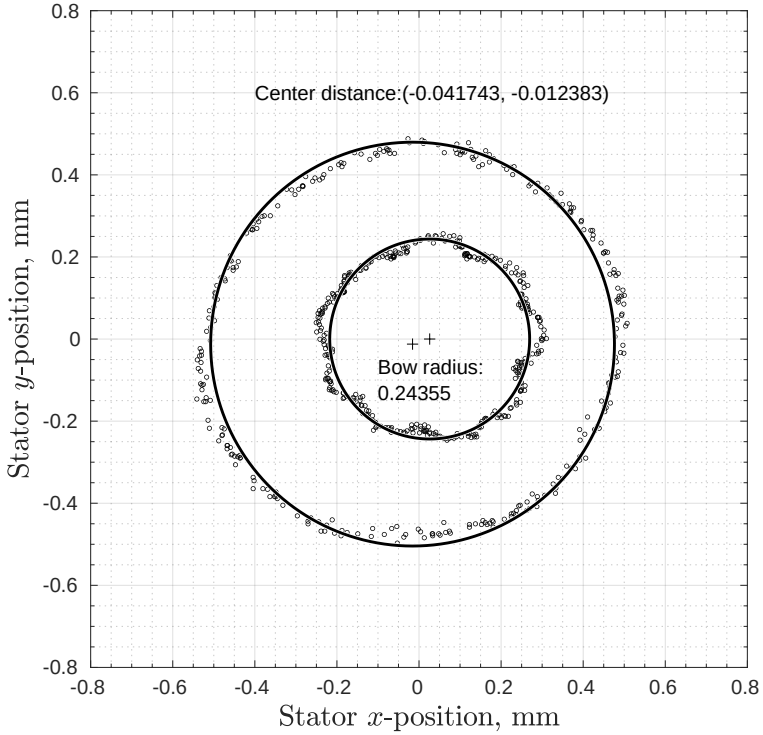


Figure 7.14: Shaft bend measurement – low (inner circle) and high speed (outer circle) runs' stator position samplings. Circles are compared.

motor is also bent. This causes a rotating bias force on the shaft. Despite the use of a DBD triple angular contact bearing arrangement, the bearing housing and the way the shaft is held in it is not rigid. This brings up the question of a nonlinear rotating force due to the interaction of the shaft bow, the motor and the angular contact bearings, which is not attempted to be measured.

7.4.2 Tapping test on the stopped rotor

Impact hammer tests were performed on the rotor and frequency response functions (FRF) are plotted as receptance H_1 and H_2 estimators. For the 1^{th} mode (swinging of the disk), the accelerometer was placed at one side of the disk while the impact was applied on the other side. For the 2^{th} mode (rotation of the disk), the accelerometer was kept at the same place as before, but the impact was applied at the shaft. The acquired data resulted from 10 samplings of 10 sec duration each, at 25.6 kHz. Figure 7.15 shows that the 1^{st} mode of the rotor appears at 3.1 Hz (19.48 rad/s) with a modal damping ratio of 0.073. Figure 7.16 shows that the 2^{nd} mode of the rotor appears at 36.9 Hz (231.84 rad/s) with a modal damping ratio of 0.017. Note that the rods, at the time of these measurements, were slack. Therefore, the results in Figure 7.15 and 7.16 reflect the natural frequencies of the rotor when there is strictly no extra tightness from the stiffness rods. However,

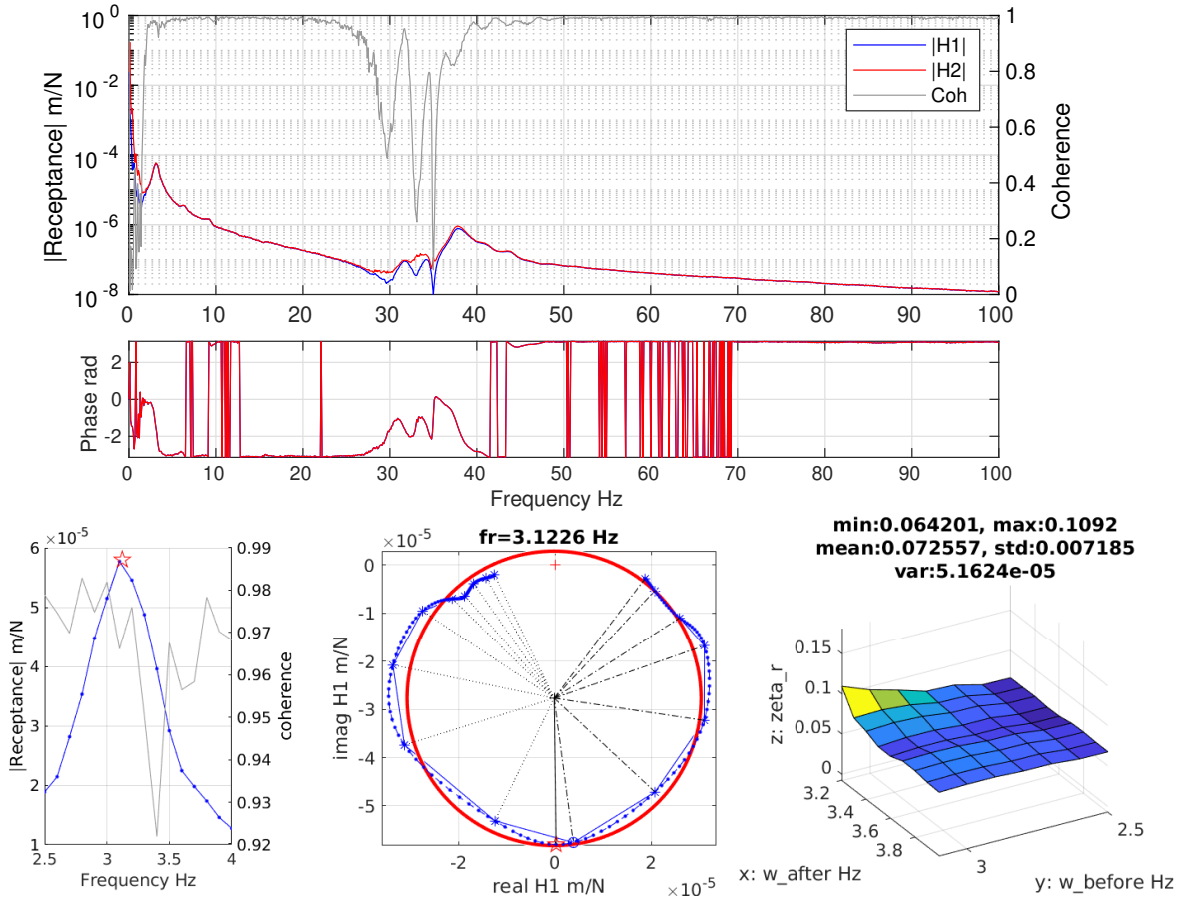


Figure 7.15: Receptance FRF estimators H_1 and H_2, the coherence and the circle-fit modal analysis for the rotor's 1^{st} vibrational mode when not rotating.

this must have added more damping than normally present.

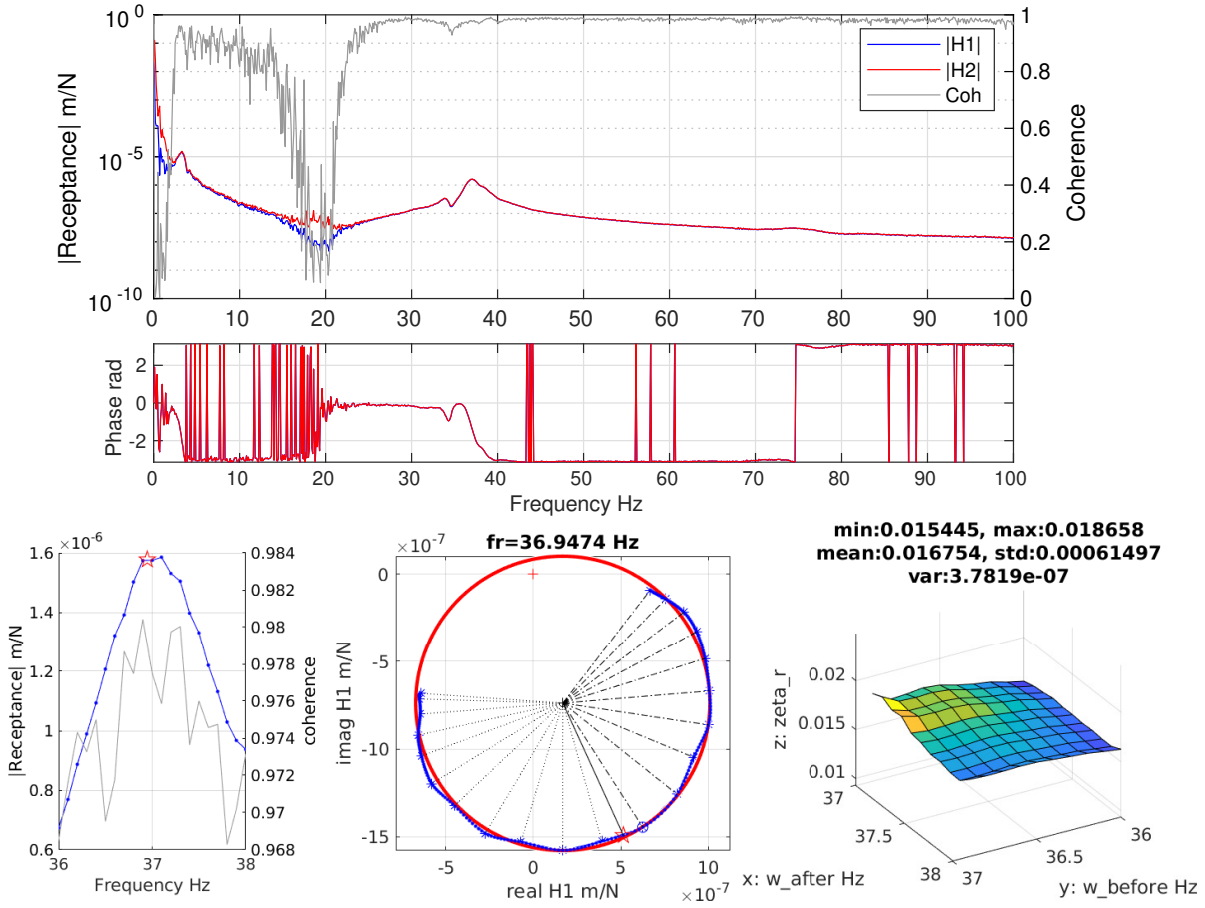


Figure 7.16: Receptance FRF estimators H_1 and H_2, the coherence and the circle-fit modal analysis for the rotor's 2$^{\text{nd}}$ vibrational mode when not rotating.

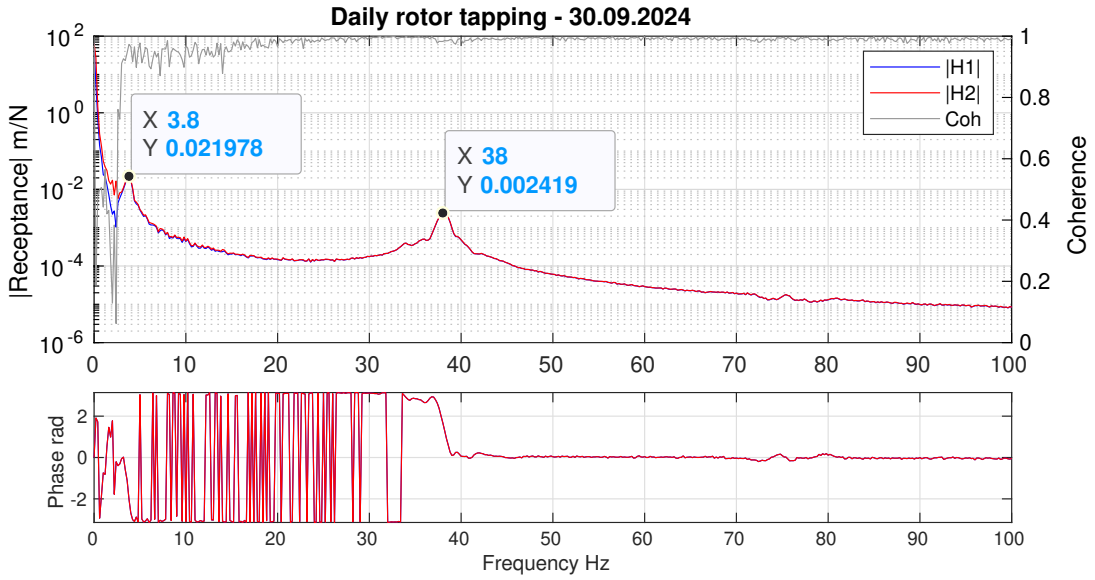


Figure 7.17: Daily tapping receptance FRF estimators H_1 and H_2 and the coherence for the rotor: 16:31 30.09.2024 (Run-4)

7.4.3 Tapping test on the stopped rotor daily

Two of the tapping test results from successive days without any changes on the rig are given in Figures 7.17 and 7.18, which reflect the range of natural frequencies of the rotor and would yield similar force-displacement curves to those in Figures 7.21a and 7.21b. The data resulted from 5 samplings of 5 sec duration each at 10 kHz sampling rate: 'Run4' showed peaks at 3.8 Hz, 38.0 Hz while 'Run5' showed peaks at 3.0 Hz, 37.6 Hz.

7.4.4 Obtaining the force-displacement curve

The photograph of the force-displacement measurement kit made up of extrusion segments can be found in Figure 7.19. The handle in the middle moves along the rail and pushes against two compression springs, each of $k = 4378$ N/m. The springs push the stator laterally. The MTI sensor tracks the position of the handle, denoted x_{MTI}, while Omron sensors (OG and OW) track the position of the stator by their average, $x_s = (x_{OG} + x_{OW})/2$. The force exerted on the stator is, therefore, $f = 2k\,(x_{MTI} - x_s)$. To prevent the effect of the shaft bow on the stiffness calculation, the bow was positioned perpendicular to the force-displacement kit axis at the time of the measurements.

The nonlinear force in the system is very sensitive to the amount of tightness of the stiffness rods. Their tightness is achieved with M3 nylocks and/or M3 locknuts, as illustrated in Figure 7.20. The bottom 135 bearings of the rods are sandwiched tightly between two M3 Nylocks. The upper 135 bearing of the rods are either sandwiched tightly between two M3 nylocks, or tightened only from the upper side with the help of one nylock and one locknut. The latter method was found more reliably applicable. The tightness

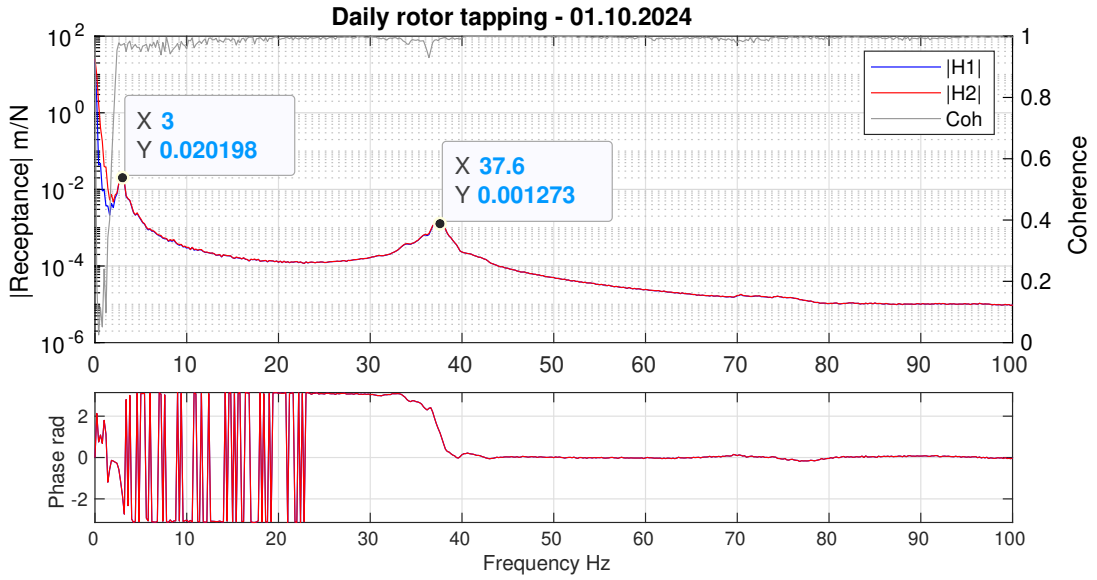


Figure 7.18: Daily tapping receptance FRF estimators H_1 and H_2 and the coherence for the rotor: 15:36 01.10.2024 (the day of formal runs that results in the BD (Run-5) presented in the next section.)

on all of the rods were managed in an iterative way, while at the same time keeping the stator level. Two different cases are presented: a higher tightness on the stator (Figure 7.21a), and an unnoticeably lower tightness on the stator (Figure 7.21b).

Note that the zeroing of the force-displacement data is difficult due to the small gaps in spring connections and bearings. However, the cubic term in the full cubic regression is not affected by any shift of the data in the x-y plane of the plot. Additionally, the cubic term in the cubic regression without the quadratic term is not affected by vertical shift. Therefore, the cubic regression must be reliable even with a slight data shift present in the measurement data.

In the higher level of tightness case (Figure 7.21a), the full cubic polynomial fit gives 0.155745 N/mm^3 (red), whereas the cubic fit without quadratic term gives 0.204435 N/mm^3. In the low tightness case (Figure 7.21b), the full cubic polynomial fit gives 0.163054 N/mm^3, whereas the cubic fit without quadratic term yields 0.157061 N/mm^3.

It is important to note that the visual judgement of the regression is important since the the force-displacement data is not evenly distributed and lumped data can cause bias in regression terms. Both in Figure 7.21a and 7.21b, the cubic regression without quadratic term represents the force-displacement data well; therefore, quadratic term is not used. Also, the linear stiffness that appear here (0.926619 N/mm) is not used in the 4-dof simulations later. Firstly, the linear stiffness in the system mainly comes from the cantilever motion of the shaft, which cannot simply be represented by a single lateral force at the stator. Secondly, the axial force was not modelled in the system for simplicity, hence the complication from its affect is already ignored in the mathematical model.

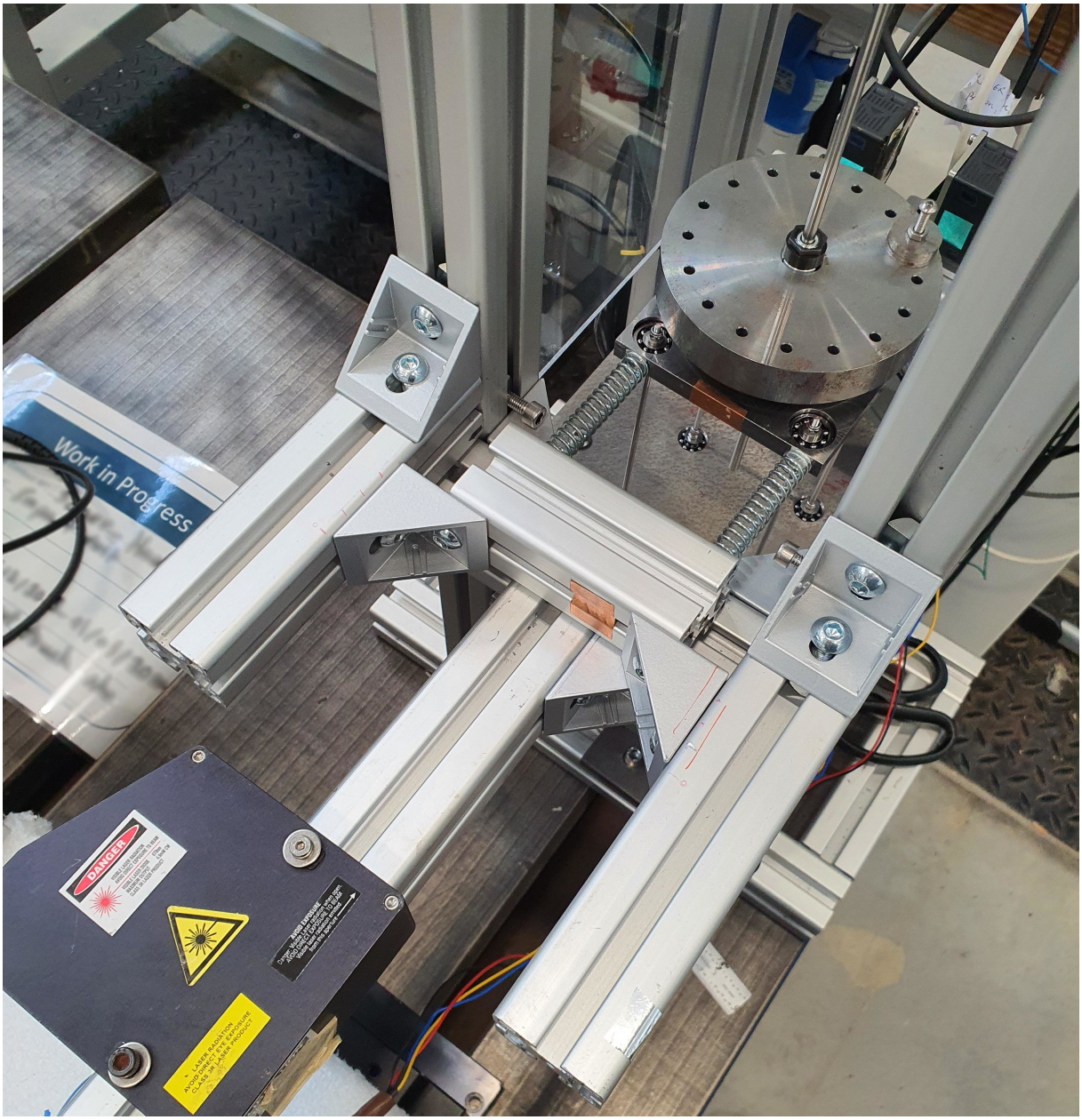


Figure 7.19: The force-displacement curve measurement kit installed on the rig.

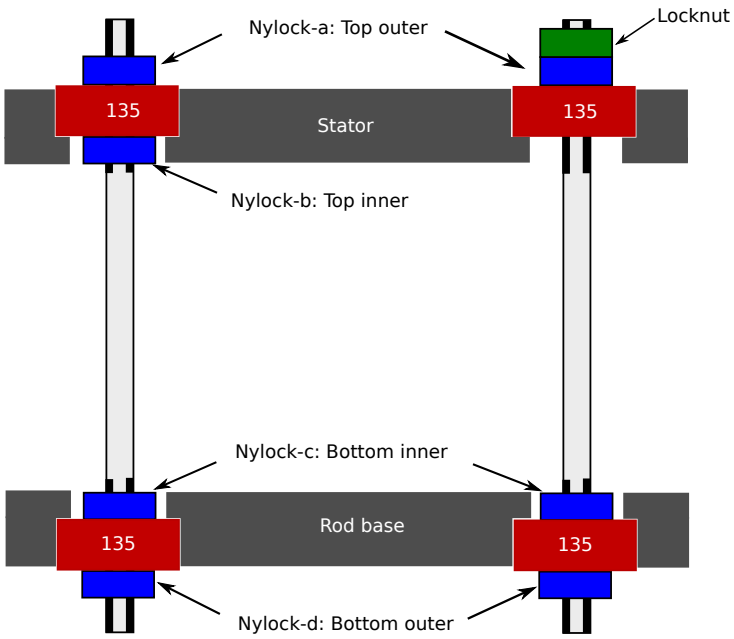
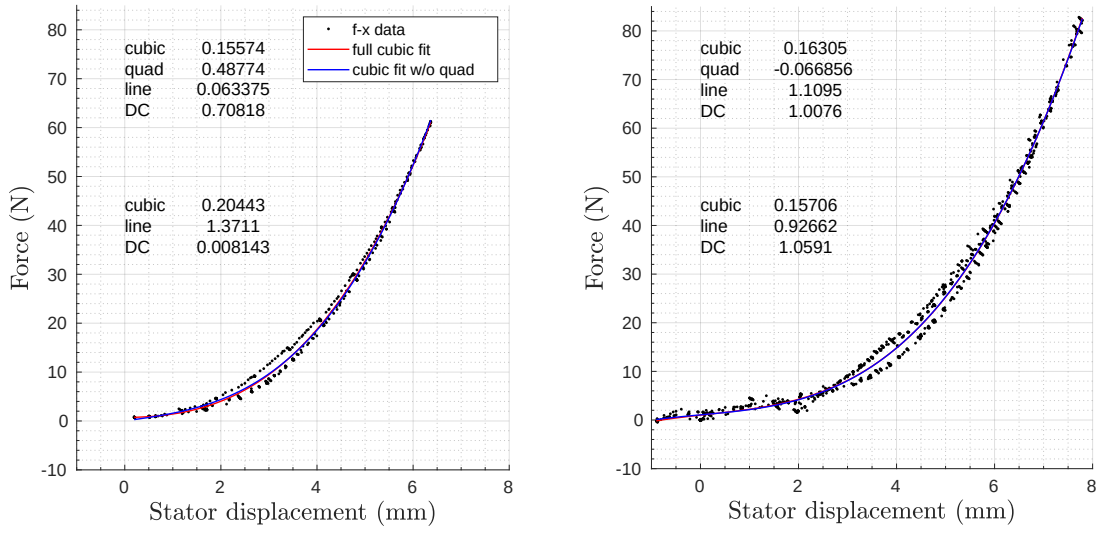


Figure 7.20: Schematic drawing explaining the tightening of the stiffness rods. '135' refers to the catalogue names of these self-aligning ball bearings.



(a) Data for higher level of tightness

(b) Data for low level of tightness

Figure 7.21: Force-displacement data from different measurements. Legend applies to both figures.

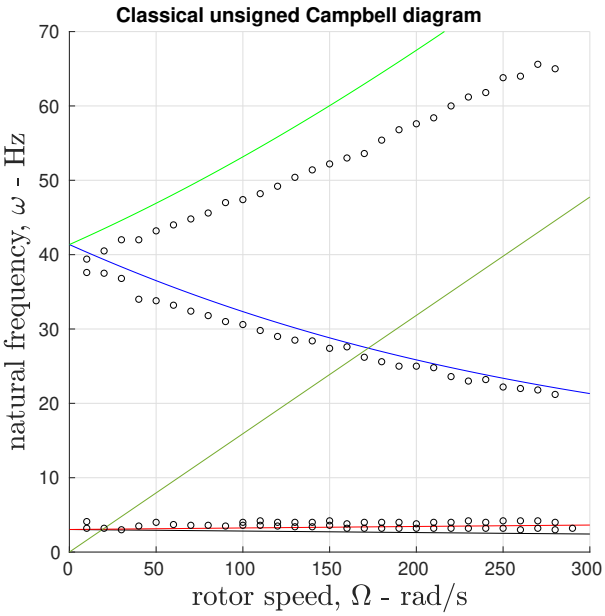


Figure 7.22: Experimental Campbell plot. Circles from the experimental tapping and lines from the design Campbell plot in Figure 7.9.

7.4.5 Tapping test on the rotor when running

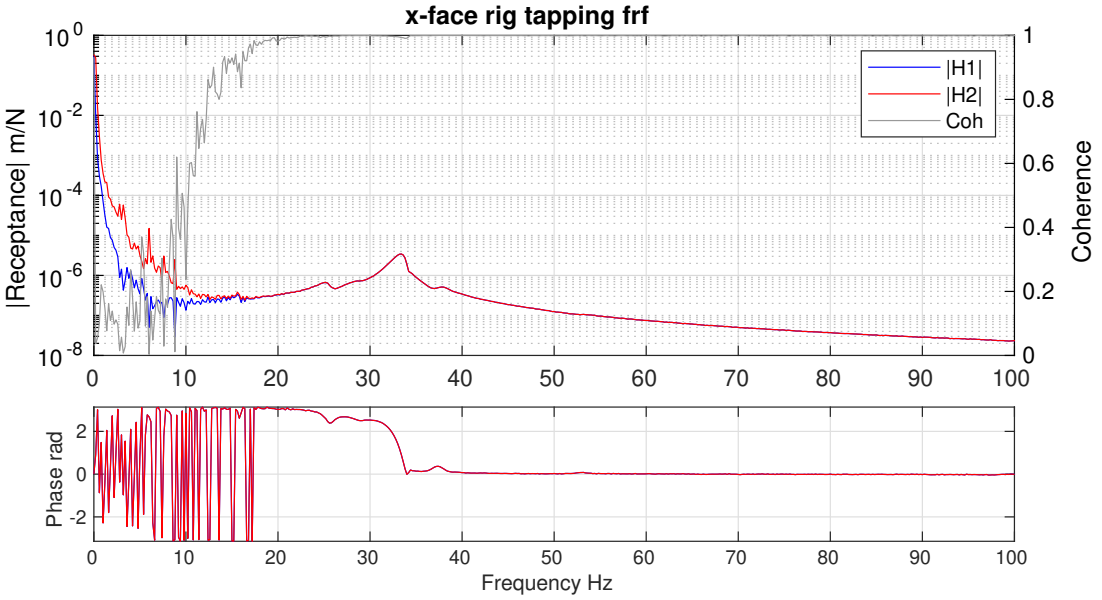
The Campbell plot was obtained on the experiment directly when the rotor was running for a range of speeds. The impact location was the side of the stator on x-face and the accelerometer was fixed to the opposite side of the stator. The data was produced from 5 samplings of 5 sec duration each, at 25.6 kHz sampling rate. The results are given in Figure 7.22.

Even though the experimental impact test has a relatively consistent evolution with the rotor speed, it is slightly different than Campbell plot of the design, which is overlaid. As in the case of the stopped rotor, the stiffness rods were left slack so that the underlying linear system is the dominant source of the results in Figure 7.22.

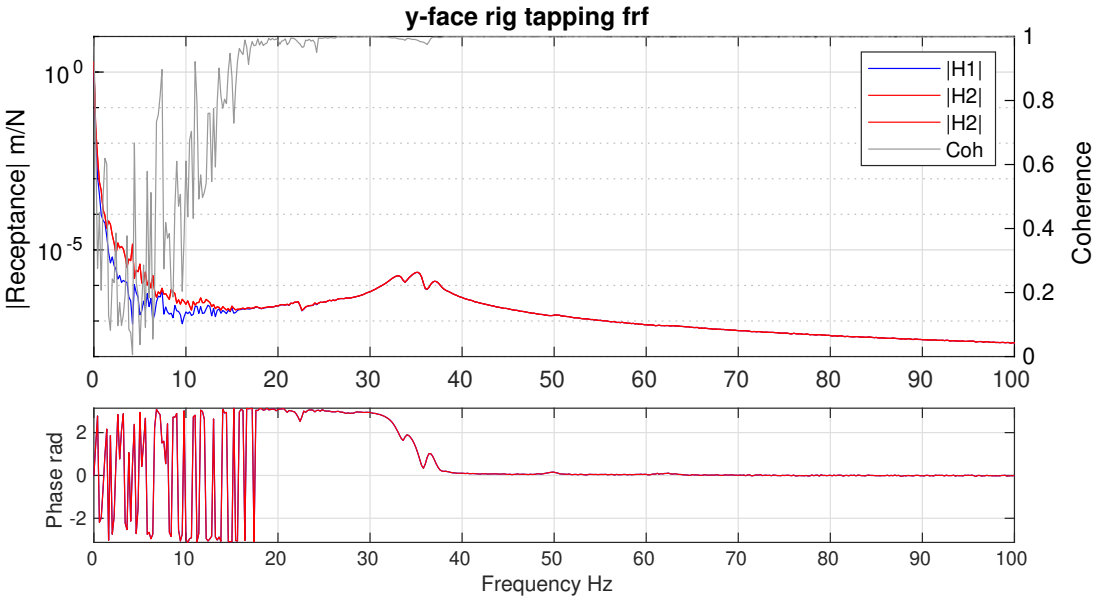
7.4.6 Tapping test on the rig

The test rig assembly 3D drawing is shown in Figure 7.1. For either face of the rig, the impact hammer input is applied at the middle of motor plate, and the accelerometer output is measured at the middle of the bearing plate. Only one such transfer FRF is obtained. Using a sampling rate of 10 kHz, 5 sets of 5 sec impact response data were averaged in auto- and cross-spectrums to get the receptance H_1 and H_2 FRF estimators and the coherence.

Both tapping results in Figure 7.23 show frequency peaks between 30 and 40 Hz (or 195 and 249 rad/s), which might cause interaction with the rotor. The Campbell plot in Figure 7.22 shows that the interaction can happen between the 2^{nd} BW mode of the



(a) Rig tapping test on x-face



(b) Rig tapping test on y-face

Figure 7.23: Impact hammer test on the rig. Five sets of five sec impact response acceleration data were averaged in auto- and cross-spectrums to get the receptance H_1 and H_2 FRF estimators and the coherence.

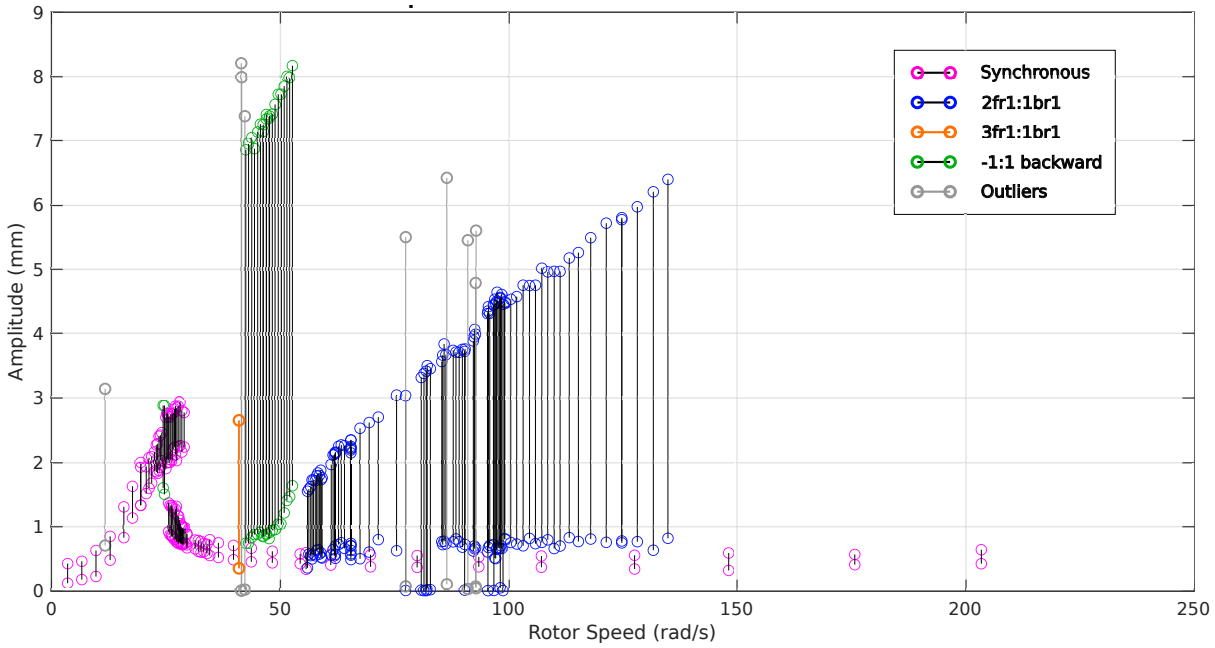


Figure 7.24: Experimental BD showing the amplitudes of stator lateral motion with drive speed. Maximum and minimum amplitudes of each family is given the same colour.

rotor and the rig natural frequencies in the range between the rotor speed of 0-130 rad/s, although this was not found to cause a significant effect in the actual response of the system.

7.5 Experiment results

The experimental data acquisition method is given in Section 7.4. The repeatability of the experimental response was low on the same rig when assembled at different times due to the difficulty in tightening stiffness rods to the same tightness, and fixing the stator and the disk at the same positions along the shaft, which is a recognised issue in industrial maintenance [176]. The repeatability of the response was medium from day to day due to the temperature changes which affected the tightness. However, the repeatability was high during each measurement run and for each of these cases the designed rig robustly generated the sought nonlinear phenomena. Figures 7.24 and 7.25 show the BDs obtained from one of the experimental runs that completed the BD in a few hours. All experimental and simulation BDs and trajectory plots are given for the stator positions. There are a few different responses which reflect the nonlinear nature of the test rig which are explained in the following.

7.5.1 Bifurcation diagram measurements

2^1**:**1^1 **internal resonance** From the Campbell diagram (Figure 7.9), the expectation for the IR $2\,\omega_{f1}^{rot} = \omega_{b1}^{rot}$ is after 59.3 rad/s. However, in actual experiments, the branch

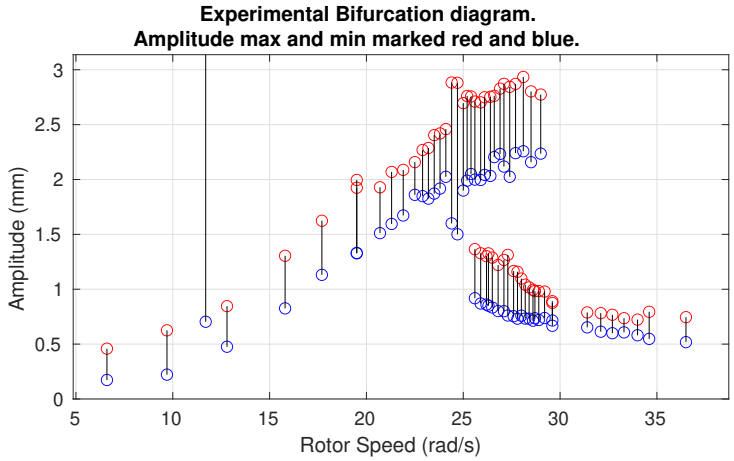


Figure 7.25: Zoom at the main resonance of the BD.

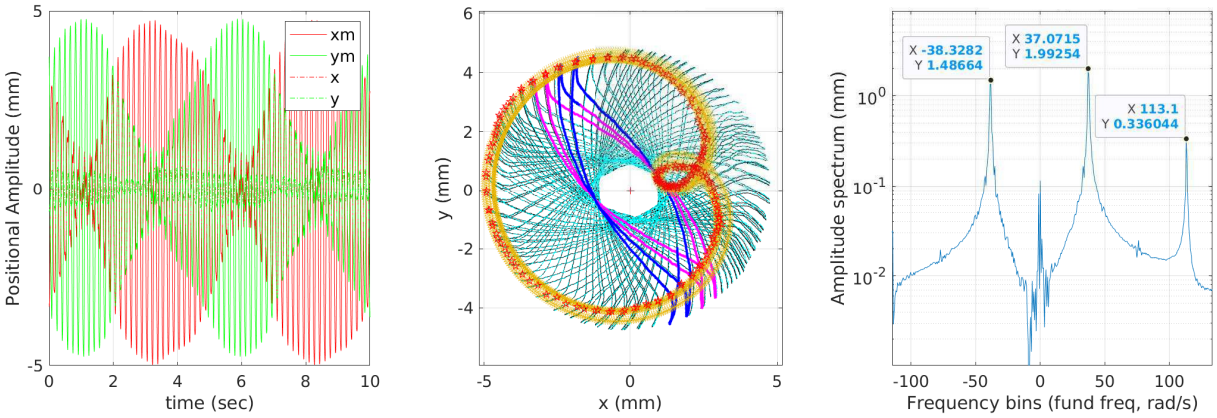


Figure 7.26: IR of type $2\,\omega_{f1}^{rot} = \omega_{b1}^{rot}$ at $\Omega = 113.3$ rad/s from the experimental BD in Figure 7.24.

appears as low as 56 rad/s. Because in the Campbell plot the resonance is located at the intersection of two lines making a shallow angle, the location of the resonance on the Campbell plot is sensitive to slight changes in the Campbell plot. A sample, well established 2^1:1^1 response is given in Figure 7.26. In the middle figure the legend is as follows:

- black line: measurements (x_m, y_m) (Eq. (7.23)),
- cyan line: deciphered stator trajectory in (x, y) stationary frame (Eq. (7.23)),
- pink line: first 1500 data points,
- blue line: second 1500 data points,
- red stars: Poincaré section for the duration of the measurements,
- yellow trajectory: rotating frame view of cyan line,

which also applies to other figures (Figure 7.26-7.31).

The stator was impacted at one of its edges to excite the mode. It was very difficult for this mode to hold consistently below 97 rad/s. At a certain orientation of the pre-

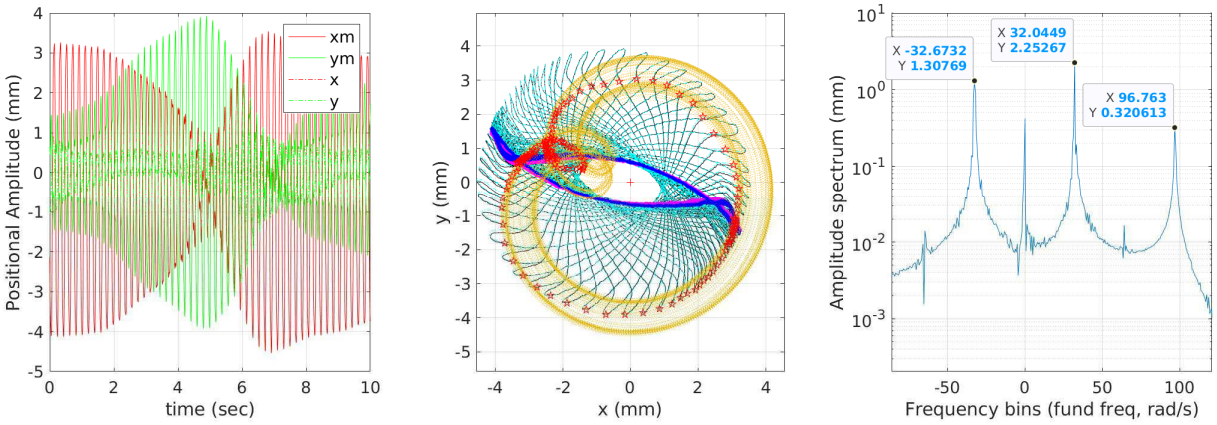


Figure 7.27: A sample 2^1:1^1 orbit at Ω = 97.0 rad/s that shows the preferred orientation.

cession, the stator started to vibrate torsionally. Immediately after the stator started to vibrate, the 2^1:1^1 mode was lost. Figure 7.27 shows that there was a noticeable precession orientation of the trajectory. However, below 65.1 rad/s, the mode started to hold well again, while the preferred orientation became less pronounced. Sometimes, it was completely *parked* in only one orientation, as in Figure 7.28, and the frequency content shows that the orbit is periodic in both stationary and rotating frames of reference. The stroboscopic Poincaré section in Figure 7.28 shows three dots, indicating the one-to-three ratio between the drive speed and the other main frequency components in the stationary frame: $3\,|\omega_f^{sta}| = 3\,|\omega_b^{sta}| = \Omega$ (see the right of Figure 7.28). This shows that this parked 2:1 response in the stationary frame is a period-3 motion, not a quasiperiodic motion unlike other 2:1 responses on the same branch. This happens while the rotating frame frequencies still show a 2:1 ratio between the FW and BW frequency components: $2\,\omega_f^{rot} = \omega_b^{rot}$. The stiffness rods might have marginally different lengths and the bearings holding the rods have slightly different damping characteristics. Additionally, their tightening to the same tightness was a practically difficult task. This might have caused the preferred orientation of the rotor when in that mode and also in the 3^1:1^1 IR mode (Figure 7.29).

The experimental setting with overhung rotor and cubic smooth nonlinearity has not been encountered in the experimental literature. However, Ishida et al. [20] confirmed in an analytical HBM and experimental study on a slender shaft that symmetric nonlinearity such as cubic nonlinearity can generate $2\,\omega_f^{sta} - \omega_b^{sta} = \Omega$, which is the 2:1 IR observed here. This response was also seen in the extended Jeffcott rotor experiments [19] IRs of 1:(−1) type are investigated in [55] which was excited thanks to the symmetry breaking effect of gravity forces. Ref. [51] investigated stochastic FEM rotor-stator rub impact and stated that response variance is high in IR compared to main resonance.

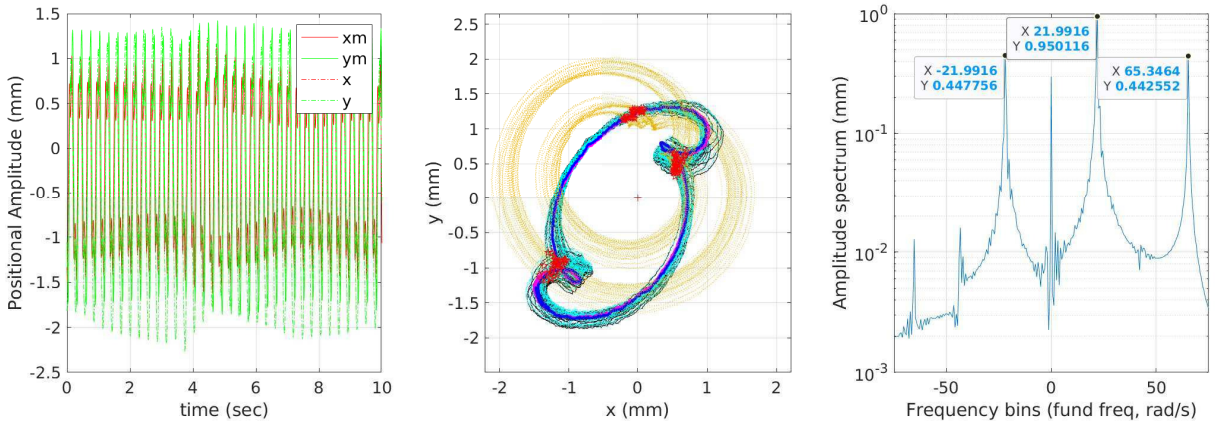


Figure 7.28: A sample $2^1{:}1^1$ orbit at Ω = 65.5 rad/s that shows that the trajectory is not precessing, but rather *parked*, and the orbit is periodic in both stationary and rotating frames of reference.

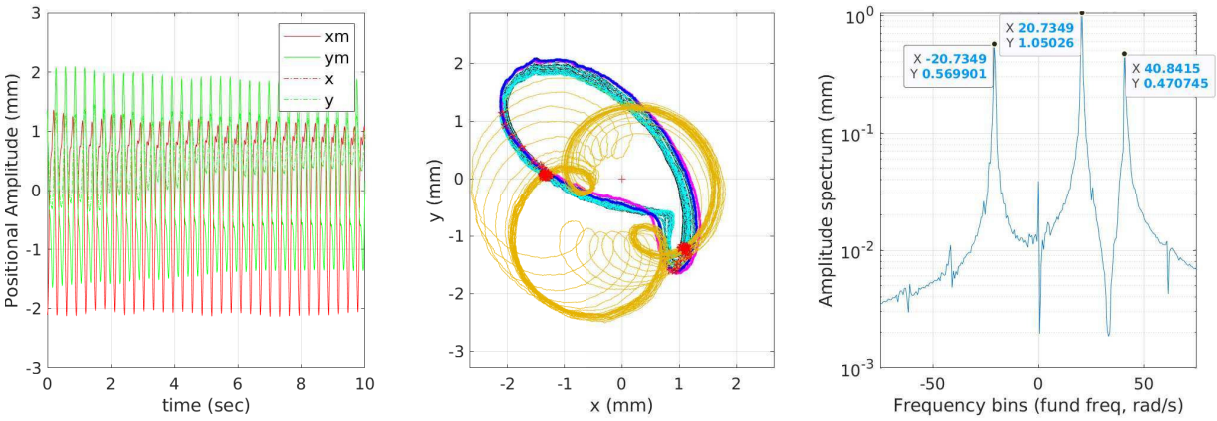


Figure 7.29: IR of type $3\,\omega_{f1}^{rot} = \omega_{b1}^{rot}$ ($3^1{:}1^1$) at Ω = 41.0 rad/s which appears periodic in both the rotating and the stationary frame.

$3^1{:}1^1$ internal resonance There is only one IR response with $3\,\omega_{f1}^{rot} = \omega_{b1}^{rot}$ frequency relation observed during the experiments which exhibit a parked orientation (see Figure 7.29). It appears as a period-2 motion, i.e., with two localised dots in the stroboscopic Poincaré section, due to the commensurate frequency ratios in the stationary frame: $2\,|\omega_f^{sta}| = 2\,|\omega_b^{sta}| = \Omega$ (see in the right of Figure 7.29). Note that this happens when the rotating frame frequency ratio for the $3^1{:}1^1$ response still holds: $3\,\omega_f^{rot} = \omega_b^{rot}$. Hence, the response is periodic in both frames. The difficulty of obtaining 3:1 IR responses was established in Ch. 3 compared to 2:1 mode which is impacted less by damping compared to 3:1. Ref. [25] numerically observed $3^2{:}1^2$.

$2^1{:}1^2$ internal resonance The IR response with $2\,\omega_{f1}^{rot} = \omega_{b1}^{rot}$ frequency relation was sought between 200-300 rad/s rotor speed but was not encountered in the experiments. This is attributed to the small basin of attraction of this response, as evident from the small number of converged responses in the simulation results in Figure 7.35a. Interest-

ingly, although numerically, $2_b^1{:}1_b^2$ and $2_b^2{:}1_f^2$ IR responses were observed by Wang et al. [25] where subscripts show the whirl of the interaction mode: "b" for BW and "f" for FW. Note that these subscripts are omitted in this thesis as the observed IR responses are of type $n_f{:}m_b$ in the rotating frame indicating the modal frequency relation $n\,\omega_f^{rot} = m\,\omega_b^{rot}$.

−1:1 backward resonance The experimental BD data shows a -1:1 backward precessing solution family that stems around the main resonance (see Figure 7.30). This resonance is not evident from the Campbell diagram 7.34 because this is not an internal resonance. For this response, the overall motion is FW (with higher FW frequency component) but the precession of the shape of the orbit is BW (as evident from the pink-to-blue trajectory transition).

The axial loads increased damping in the bearings holding the stator, which must have excited the friction-related backward motion. This mode is periodic in the rotating-frame with teardrop-shaped orbits [34, 63, 32]. A similar response was also seen in rotor-stator contact in [133]. The tear-drop orbits can be seen in the rotating frame trajectory (yellow trajectory in Figure 7.30). Because there in no impact here, the tear-drops are simply rounded as in [63]. This resonance is distinct from 2:1 and 3:1 in that here one of the two main frequencies is the drive speed Ω and, while in 2:1 and 3:1, there are three main frequencies and in the rotating frame the drive speed can be eliminated out of the resonance relation between the FW and BW frequencies.

Synchronous response Due to the stiffening effect of the cubic stiffness, the response shows jump phenomena (Figure 7.25). The jump down and jump up happens at 29.0 rad/s and 25.6 rad/s. The initial simulations do not show a bounded main resonance, whereas the experimental BD shows a defined synchronous resonance peak.

Some of the synchronous responses from Figure 7.25 are shown in Figure 7.31. The deviation of the stator position (—) from the measured (—) data is visible in the supercritical low amplitude orbit after jump down at 32.1 rad/s and at high speed at 203.5 rad/s. This is attributed to torsion on the stator by a low level of friction in 2305 bearing. The synchronous responses do not appear as perfect circles which might stem from anisotropy of the stator supports. At high speed, the response looks very noisy due to the bearing clearances and vibrations of the rods.

Main resonance The initial simulations show that the main synchronous resonance peak is unbounded. Nonetheless, the experiment featured a bounded main resonance peak. In order to investigate whether the main resonance peak has a hard drop-down limit due to modal interactions in the main backbone, a comparison between low and higher unbalance (Run-7) was studied. The test setup was disassembled before this was done for more accurate mass measurements. The reassembly created a slightly different

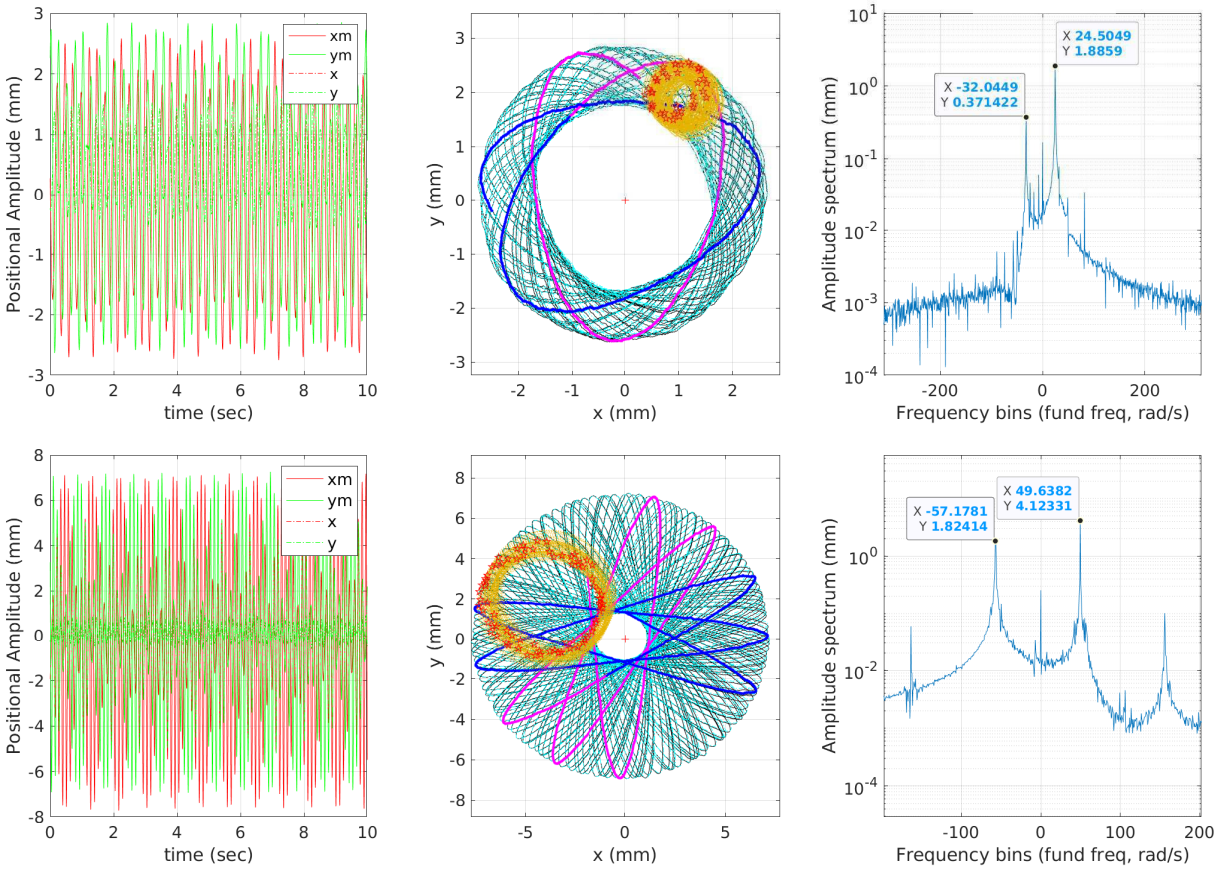


Figure 7.30: Two samples of quasiperiodic -1:1 BW resonance which also appears periodic in the rotating frame at Ω = 24.7 rad/s and at Ω = 49.6 rad/s from top to bottom (see the BD at 7.24).

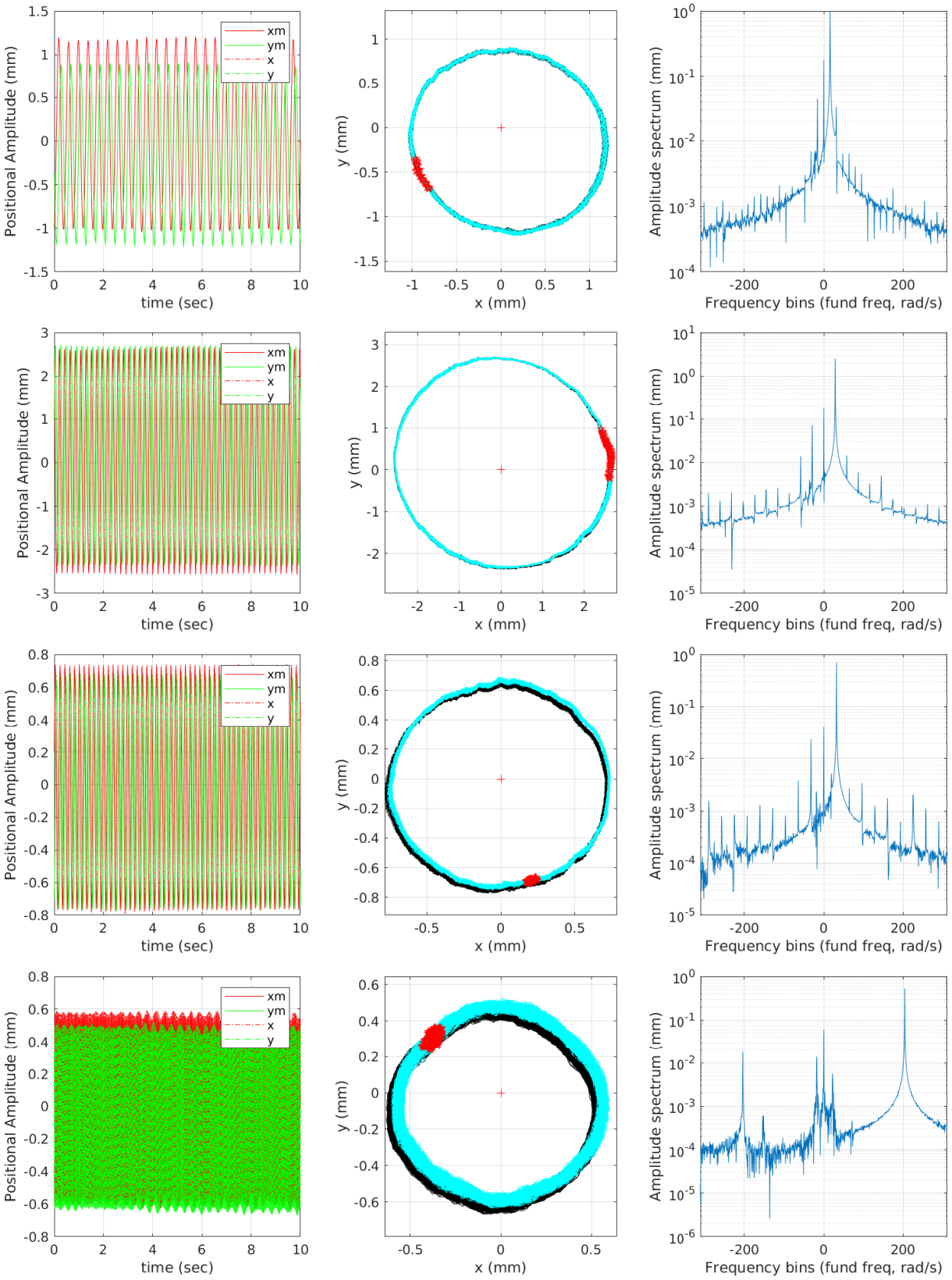


Figure 7.31: Selected orbits at Ω = 15.8, 29.0, 32.1 and 203.5 rad/s from top to bottom, from the BD given in Figure 7.24 and 7.25.

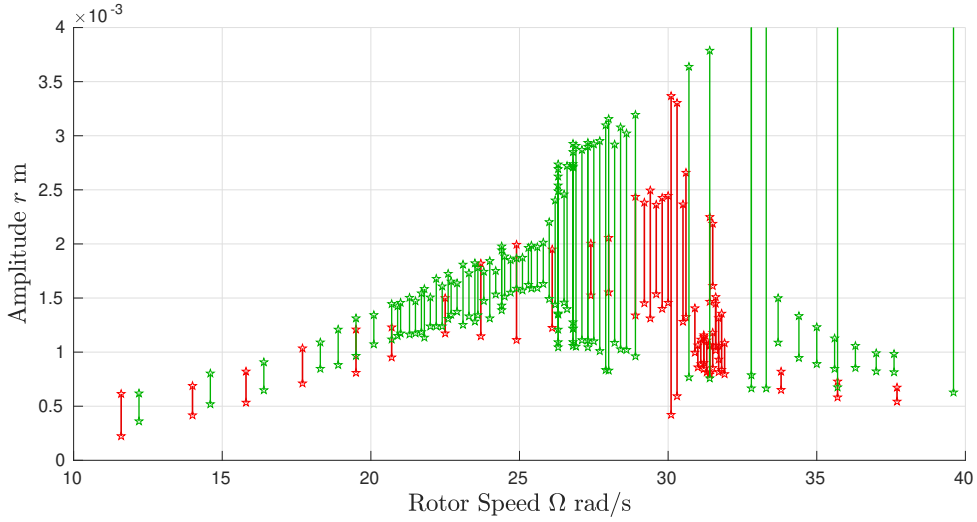


Figure 7.32: Comparison between the region of the BD around the main resonance with different unbalance masses. The red coloured data belong to the run with an unbalance mass of 19.46 g (Note that this is different than Figure 7.25). The green coloured data belong to the run with an unbalance mass of 28.87 g.

system. The results are shown in Figure 7.32. Higher unbalance causes higher response amplitudes, as expected. However, in the case of higher unbalance, the main resonance peak is obliterated by the the backward resonance which attracts all nearby trajectories.

7.5.2 Campbell diagram with manufactured and assembled experimental rig data

The manufactured rig has slightly different masses, dimensions and positions compared to the design which did not include the connecting elements and not knowing the exact physical properties of the materials used in the manufacture. This seems to have created the difference between the Campbell diagrams of the design and the experiments (Figure 7.22). Therefore, the initial Campbell diagram and the initial simulations need to be updated. A new "disk system" is defined whose mass centre is referred to as "the new mass centre" (see Figure 7.33). In the lists below, the quotation marks are used to indicate that a few parts lumped together, and the *italic* text refers to the designed part names.

The dimensions re-measured form the manufactured and assembled rig

1 *The rod* length (from "Nylock-c" to "Nylock-a & lockM3 couple", see Figure 7.20): L_2 = 145.30 mm

2 *The shaft* length (bearing plate bottom surface to *the disk* centre+"new mass centre"): a = 265 + 3.91 = 268.91 ± 0.5 mm

3 *Disk-stator* mass centre distance: b = 34.42 mm

4 Distance between *the disk's* bottom surface to *the stator* upper surface: 19.50 mm

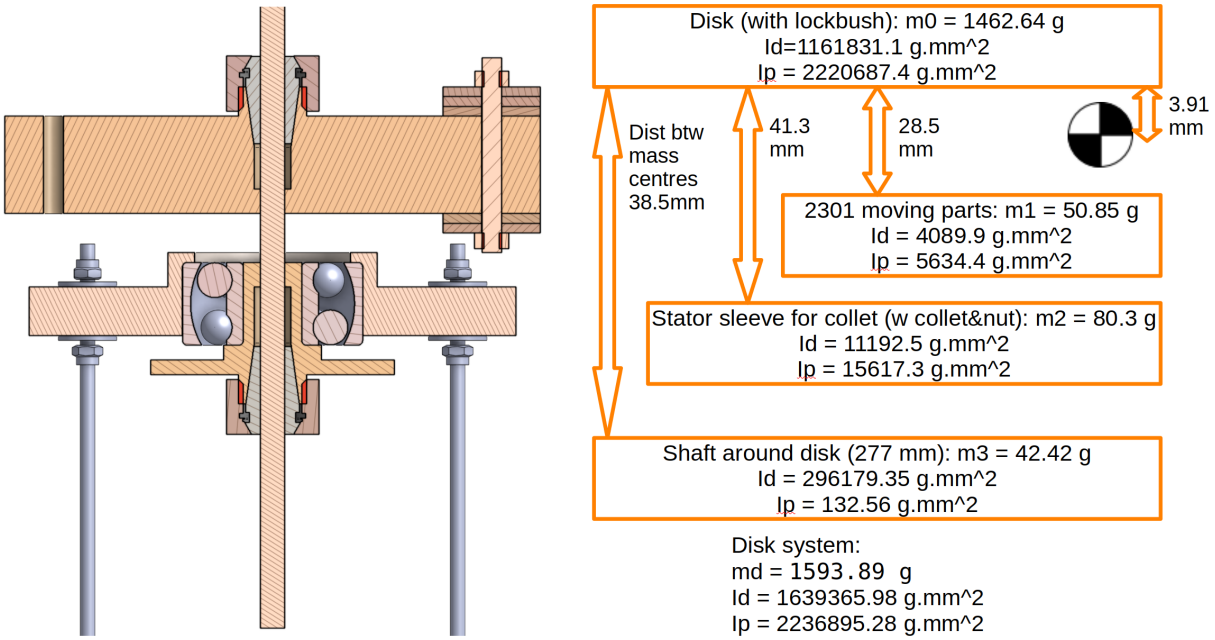


Figure 7.33: The new disk system that interprets the rotating parts as a single rigid system: the disk, stator sleeve, bearing moving parts and the connecting elements (collet and lock-bush), as well as "the shaft length around the disk" (80 mm before and 177 mm after the disk, total 277 mm shaft length).

5 Distance between "*the stator sleeve for collet* with *its collet-nut*" mass centre to "*the disk* with *its accompanying lock-bush*" mass centre: approx. 41.3 mm

6 Distance btw "*2301 bearing* balls and the inner race" mass centre to "*the disk* with *its accompanying lock bush*" mass centre: 28.5 mm

7 Length of shaft after *the disk* starts: 177 mm

8 Length of shaft before *the disk* that is included in "the disk system": 80 mm

9 Distance btw "the shaft length around *the disk*" mass centre and "*the disk* with *its accompanying lock-bush*" mass centre: 38.5 mm

10 *The stator's* distance from *the bearing plate* bottom surface: 299.42 mm.

11 *The stator's* thickness: 9.83 mm

12 *The stator's* one edge length: 100.13 mm

13 *The shaft's* lateral bow diameter at the stator: 0.5 mm

The mass related properties of the manufactured and assembled experiment rig The total unbalance mass used in the experiments is a combination of the following: 1 X M4 stud, 2 X M4 nut, 3 X *the unbalance disk*): $m_u = 19.46 \cdot 10^{-3}$ kg. Other values are tabulated in Tables 7.4-7.7.

With the values in the Tables 7.4, 7.5, 7.6 and 7.7, the mathematical model is updated. The matching nondimensional values for keeping $\gamma = 0.25$ are as follow: $c = \sqrt{\gamma k_{rb}/k_{3b}} = 0.001214$ m, $u = (m_u/m_e)\alpha(\varepsilon_b/c) = 0.3198707$ kg m. Therefore, with the values here, the aimed nondimensional cubic stiffness measure $\gamma = 0.25$ and the nondimensional unbalance

Table 7.4: "Equivalent disk mass" if considered with *the stator sleeve for collet* and *the accompanying collet-nut*): m_d = 1593.89 · 10^{-3} kg. The entries within parentheses are not summed.

The disk	1440.57 g
The disk accompanying lock-bush	22.17 g
The stator sleeve for collet with *its collet-nut* and *2301 bearing's* inner race and balls	131.15 g
(The calculated mass of *the stator sleeve for collet*)	(63.47 g)
(*The stator's accompanying collet-nut*)	(16.83 g)
(*2301 bearing*)	(50.85 (inner race + balls) + 38.144 (outer race) = 89 g from NSK catalogue.)
"Equivalent disk mass"	Total = 1593.89 · 10^{-}3 kg.

Table 7.5: "Equivalent stator mass": m_s = 750.43·10^{-3} kg. The entries within parentheses are not summed.

The stator	626.94 g
M3x4	1.26 g
M3 Nylock x 8	3.36 g
The rod spacer x 4	9.05 g
The stiffness (rod) sleeve x 4	4.30 g
135 bearing x 4	36 g (9 g each from NSK cat.)
(*The rod/3*) x 4	4.37 g
"The shaft length mass after disk starts" until the end	(81.47g/532mm) 177mm = 27 g
2301 bearing outer race	38.14 g
"Equivalent stator mass"	Total = 750.43 · 10^{-3} kg.

Table 7.6: "Equivalent disk diametral MOI at "the new mass centre": $J_d = 1639365.98 \cdot 10^{-9}$ kg m^2. "The new mass centre" is of the system: *the disk* + "*the stator sleeve for collet* and *the accompanying collet-nut*" + "*2301 bearing's* inner race and balls" + "the shaft length around *the disk*" and it is 3.91 mm down the disk mass centre. The entries within parentheses are not summed.

"*The disk* and *the accompanying lock-bush*"s diametral MOI at "the new mass centre" (and at their own mass center)	$1161831.10 \cdot 10^{-9} + 1440.57 \cdot 3.91^2 \cdot 10^{-9}$ $= 1183854.68 \cdot 10^{-9}$kg m^2 $(1161831.10 \cdot 10^{-9}$ kg m$^2)$
"*The stator sleeve for collet* and *the accompanying collet-nut*"s diametral MOI at "the new mass centre" (and at their mass centre)	$11192.51 \cdot 10^{-9} + 80.3 \cdot (41.3 - 3.91)^2 \cdot 10^{-9}$ $= 123452.88 \cdot 10^{-9}$ $(11192.51 \cdot 10^{-9})$ kg m^2
("*The stator sleeve for collet* and *the accompanying collet-nut*"s mass centre is at the middle of the flange of *the stator sleeve for collet*.)	
"*2305 bearing* inner balls and race"s diametral MOI at "the new mass centre" (and at its mass centre)	$4089.88 \cdot 10^{-9} + 50.85 * (28.5 - 3.91)^2 * 10^{-9}$ $= 34837.25 \cdot 10^{-9}$ $(4089.88 \cdot 10^{-9})$kg m^2
"The shaft length around disk (177 mm below the bottom surface of the disk and 100 mm above)"s diametral MOI at "the new mass centre"	$(81.47/532(177 + 100))(1/12 * (177 + 100)^2$ $+(78.5 - 100/2 - 3.91)^2) \cdot 10^{-9}$ $= 296883.75 \cdot 10^{-9}$ kg m^2
"Equivalent disk diametral MOI" at the new mass centre"	Total: $J_d = 1639365.98 \cdot 10^{-9}$ kg m^2

Table 7.7: "Equivalent disk polar moment of inertia": $J_p = 2236895.28 \cdot 10^{-9}$ kg m^2. The entries within parentheses are not summed.

"*The disk* with the accompanying lock-bush" (and *the disk's* own alone)	$2220687.44 \cdot 10^{-9}$ $(2219925.18 \cdot 10^{-9})$ kg m^2
"*The stator sleeve for collet* and *the accompanying collet-nut*"	$15617.30 \cdot 10^{-9}$ kg m^2
"*2301 bearing* inner balls and race"	$d_b = 7.144$mm, $d_i = 16.624$mm, $\beta = 0$, $FTF = .5(1 - \frac{d_b}{d_i} \cos\beta) = 0.2851$: $5634.43 \cdot 10^{-9} 0.2851^2 = 457.98 \cdot 10^{-9}$ kg m^2
"The shaft length around disk until the end"	$1/8((81.47/532)(177 + 100))5^2 \cdot 10^{-9}$ $= 132.56 \cdot 10^{-9}$ kg m^2
"Equivalent disk polar MOI"	Total: $J_p = 2236895.28 \cdot 10^{-9}$ kg m^2

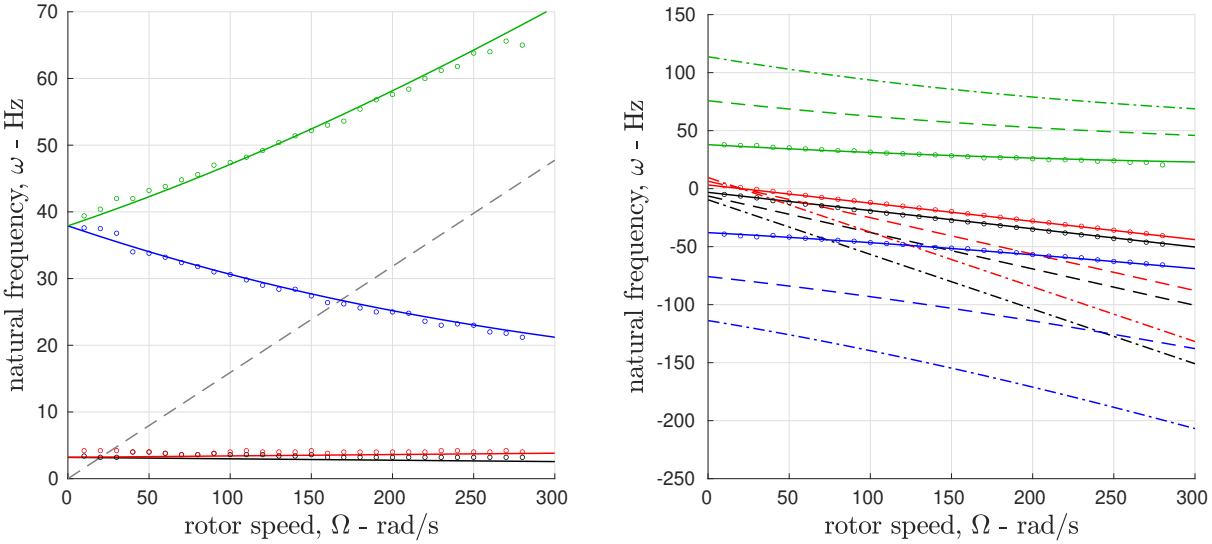


Figure 7.34: Classical (left), rotating-frame (right) signed Campbell diagram with the updated experimental values.

Table 7.8: Expected resonances from the Campbell diagram in Figure 7.34.

Resonance	**Expected rotor speed**
$2^1{:}1^1$	Ω = 61.0 rad/s
$3^1{:}1^1$	Ω = 40.7 rad/s
$3^1{:}2^1$	Ω = 101.7 rad/s
$2^1{:}1^2$	Ω = 206.0 rad/s
$3^1{:}1^2$	Ω = 124.2 rad/s

measure of u = 0.3177 are both met. With these new values, the new Campbell plot in Figure 7.34 matches that of the experimental one in Figure 7.22. In Figure 7.34, the resonance points might be expected as tabulated in Table 7.8.

7.5.3 Numerical simulations and comparison with the experiment

The updated EOM

Shaft bow was included in the simulations (see Eq. (7.46)) (see e.g. [7]). Misalignment was not included which did not cause any noticeable effect in the BD of the unbalance

response.

$$\mathbf{M}\ddot{\mathbf{w}} + \mathbf{G}(\Omega)\dot{\mathbf{w}} + \mathbf{C}\dot{\mathbf{w}} + \mathbf{K}_r\mathbf{w} + \mathbf{K}\mathbf{w} + \mathbf{N}(\mathbf{w})\mathbf{w} = \mathbf{b}$$

$$\mathbf{M} = \begin{bmatrix} m_d + m_u & 0 & 0 & 0 \\ 0 & m_d + m_u & 0 & 0 \\ 0 & 0 & J_d & 0 \\ 0 & 0 & 0 & J_d \end{bmatrix} + m_s\mathbf{P}\ , \quad \mathbf{G} = \begin{bmatrix} 0 & 0 & 0 & 0 \\ 0 & 0 & 0 & 0 \\ 0 & 0 & 0 & J_p\Omega \\ 0 & 0 & -J_p\Omega & 0 \end{bmatrix}$$

$$\mathbf{K} = \begin{bmatrix} k_{uu} & 0 & 0 & k_{u\psi} \\ 0 & k_{vv} & k_{v\theta} & 0 \\ 0 & k_{v\theta} & k_{\theta\theta} & 0 \\ k_{u\psi} & 0 & 0 & k_{\psi\psi} \end{bmatrix} = \frac{2EI}{a}\begin{bmatrix} 6/a^2 & 0 & 0 & -3/a \\ 0 & 6/a^2 & 3/a & 0 \\ 0 & 3/a & 2 & 0 \\ -3/a & 0 & 0 & 2 \end{bmatrix}$$

$$\mathbf{C} = c_{rb}\mathbf{P}\ , \quad \mathbf{K}_r = k_{rb}\mathbf{P}\ , \quad \mathbf{N} = k_{3b}r_s^2\mathbf{P}\ , \quad \mathbf{b}_g = \{g_x\ g_y\ 0\ 0\}^T$$

$$\mathbf{b}_u = \Omega^2\begin{Bmatrix} m_u\varepsilon_b\cos(\Omega t + \delta_u) \\ m_u\varepsilon_b\sin(\Omega t + \delta_u) \\ -(J_d - J_p)\beta_u\sin(\Omega t + \gamma_u) \\ (J_d - J_p)\beta_u\cos(\Omega t + \gamma_u) \end{Bmatrix}\ , \ \mathbf{b}_b = (\mathbf{K} + \mathbf{K}_r)\begin{Bmatrix} \varepsilon_b\cos(\Omega t + \delta_b) \\ \varepsilon_b\sin(\Omega t + \delta_b) \\ -\beta_b\sin(\Omega t + \gamma_b) \\ \beta_b\cos(\Omega t + \gamma_b) \end{Bmatrix}$$

$$\mathbf{w} = \begin{Bmatrix} x_d \\ y_d \\ \theta_d \\ \psi_d \end{Bmatrix}\ , \quad \mathbf{P} = \begin{bmatrix} 1 & 0 & 0 & b \\ 0 & 1 & -b & 0 \\ 0 & -b & b^2 & 0 \\ b & 0 & 0 & b^2 \end{bmatrix}\ , \quad \mathbf{b} = \mathbf{b}_u + \mathbf{b}_b + \mathbf{b}_g \tag{7.46a}$$

where the following values are used:

$$E_1 = 230\ \text{GPa} \qquad I_1 = 30.69\ \text{mm}^4 \qquad a = 269.25\ \text{mm} \tag{7.47a}$$

$$\varepsilon_b = 45\ \text{mm} \qquad \beta_u = 0 \qquad \delta_u = \gamma_u = 0 \tag{7.47b}$$

$$\varepsilon_b = 0.5(a/L_1) = 0.45\ \text{mm} \qquad \beta_b = \varepsilon_b/L_1 = 86.0\ \text{m deg} \qquad \delta_b = \gamma_b = 0 \tag{7.47c}$$

$$m_d = 1593.89\ \text{g} \qquad m_u = 19.46\text{g} \qquad m_s = 750.43\ \text{g} \tag{7.47d}$$

$$J_d = 1639.366\ \text{kg mm}^2 \qquad J_p = 2236.895\ \text{kg mm}^2 \qquad g_x = g_y = 0 \tag{7.47e}$$

$$k_{rb} = 926.62\ \text{kN/m} \qquad c_{rb} = 0.738\ \text{kN/(m/s)} \qquad k_{3b} = 157061\ \text{kN/m}^3 \tag{7.47f}$$

In the experiments, the orientation of the shaft bow was aligned with the unbalance mass, and the shaft was assumed to be straight but only bent at the cantilever end. Also, although the linear stiffness that act laterally at the stator is given as k_{rb}, this is not used. Therefore, effectively $\mathbf{K}_r = 0$ is used as the linear shaft stiffness in the EOM. This is because the shaft stiffness $\mathbf{K}$ already includes both angular and lateral displacement stiffnesses together, which cannot be represented by a simple lateral stiffness definition via k_{rb}. The effect of misalignment was neglected as it was within the margin of error and the vertical rotor allowed to ignore the gravity effect; therefore, $g_x = g_y = 0$. Gravity effect

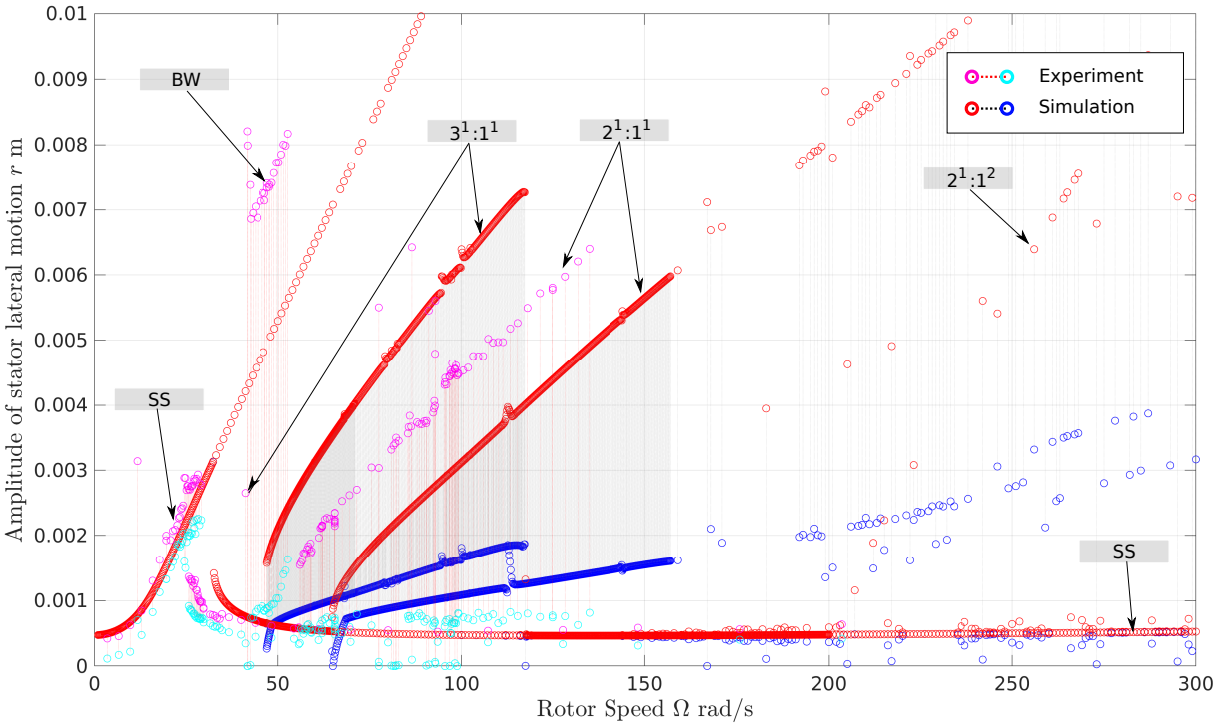
is generally neglected in vertical rotors [50, 20, 19] whereas Wang et al. [25] included the gravity effects despite the rotor being vertical.

Simulation Results

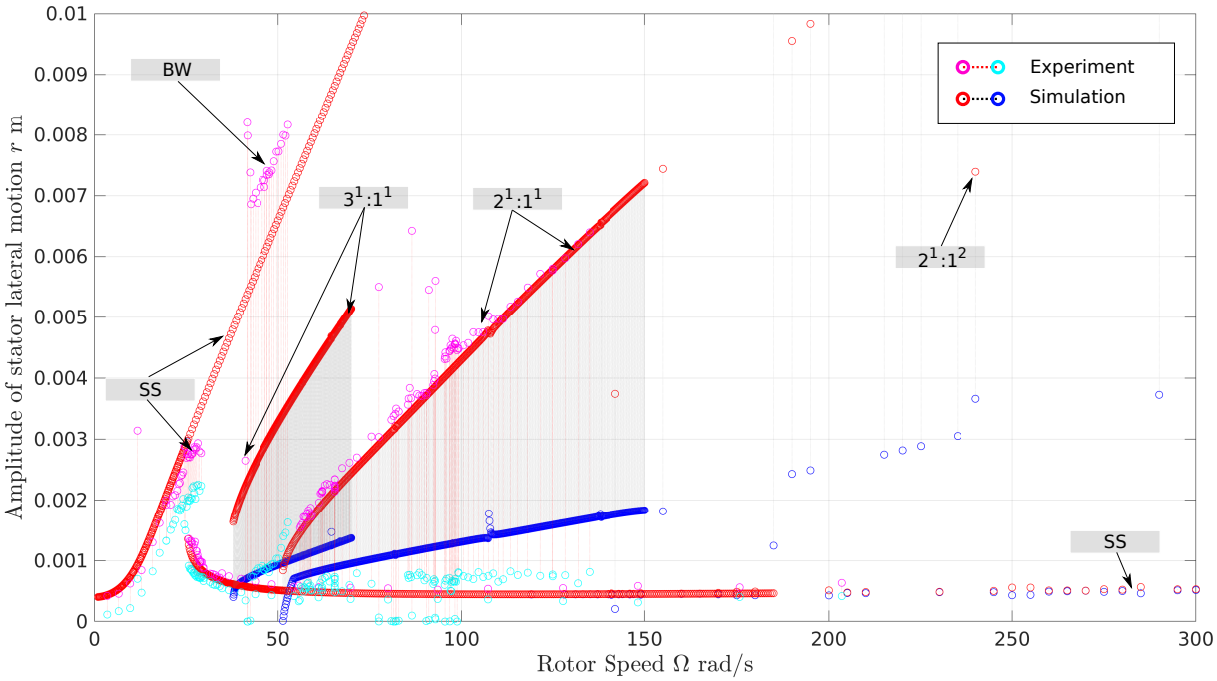
The BD obtained from the simulations are given in Figure 7.35a which was supported with partial sine-sweep tests (up or down) on the synchronous response and on the IR responses of 2^1:1^1 and 3^1:1^1. The figure also included the experimentally obtained BD from Figure 7.24.

The values used in the simulations are from Table 7.1, Section 7.4.4 and Section 7.5.2 and from Eq. 7.47. However, the damping had to be decreased compared to the design. Firstly, the modal damping values from Figures 7.15 and 7.16 are used to define the damping matrix. However, this resulted in the 2^1:1^1 response to be lost below Ω = 102 rad/s. Then, the damping matrix with c_{rb} damping coefficient value from the Section 7.1.2 is used. However, this was also found quite restrictive as to rotor speed region for the IR 2^1:1^1. A value of $0.7c_{rb}$ was used in Figure 7.35a. This tweaking of the damping in the system can be legitimized based on the fact that the modal damping values were calculated when the rotor was still, meaning that the bearing balls contacting races and the cage might have caused increased friction which are less effective for the lateral motion in the running rotor. This effect was felt by hand significantly. Most of the damping must come from the connections the stator makes; therefore, a damping force acting at the stator is logical. As a side-effect of the decrease in damping, the BD shows many response patterns that were not possible in the experiments. Also, some features are different in the experiments, compared to the simulations, which are explained below. The difficulty of damping quantification in rotating systems has been acknowledged and addressed in the literature [177, 178].

The two BDs are broadly similar in shape, with the exception that for the experimental BD there is an additional region of backward whirl response not modelled numerically, and the SS response is bounded (see Figure 7.32). These differences are attributed to the increased damping in the bearings with axial load. Additionally, in the IR 2^1:1^1 and 3^1:1^1 that appear in the simulations, the Campbell diagram values seen in Figure 7.34 are followed well. However, the BD features of the experiments appear systematically lower in the rotor speed range. Although the experimental Campbell diagram from tapping tests is very similar to that of the theoretical Campbell diagram from the experimental rig values (Figure 7.34), it is worth noticing the shallow angle between the intersecting lines in Figure 7.34. This means that these lines' points of intersection, which govern onset drive speeds of IR, will be highly sensitive to small changes in the modal frequencies or even in the gyroscopic effect on the frequency that might have been altered by the axial pull of the stator. Therefore, any effect on the Campbell diagram can shift the position of the IR branches in the Ω axis significantly. This might also be related to the fact that the



(a) Experimental BD from Figure 7.24 merged with the simulation with the new experimental rig values from Section 7.5.2.



(b) Experimental BD from Figure 7.24 merged with the simulation with the experimental rig values from Section 7.5.2 except the following modifications: E_1 = 270 GPa, k_{3b} := 0.7 k_{3b} = 109942700 N/m^2, and with the addition of the 7900 bearing's movement compensation as the extra shaft length D = 65 mm. (See Figure C.6 for the linked Campbell plot.)

Figure 7.35: Experimental and simulations BDs.

7900 angular contact ball bearings cannot provide a perfectly rigid support, increasing the shaft length and decreasing the stiffness value. Combining the above, the location of the 2:1 branch in the rotor-speed axis is very close: the experimental branch appeared at 56 rpm, while the theoretical one at 65 rpm, at their lowest tips which is where the Campbell diagram values predict. This discussion above also explains why the IRs in the experimental and theoretical BDs must not be compared in amplitude, but in the x-axis of the BD. Therefore, the aim of the experiment being the regeneration of the theoretical IR phenomena was fulfilled by the experiments implemented as shown in this chapter. However, slightly different test rig parameters can give a much closer match as illustrated in Figure 7.35b, indicating the sensitivity of the BD to the test rig parameters which in this case was not manufactured to be a high fidelity representation of the mathematical 4-dof model.

There are other factors such as the temperature of the test environment that affected the force-displacement measurements by around 20% (see Figures 7.21a and 7.21b and the force difference thereof). However, this would rather influence the inclination of the experimental $2^1{:}1^1$ branch instead of directly affecting its position along the BD. Since the presented experimental run had a very low level of tightness, the value chosen for the cubic stiffness in the experiments was 0.15706 N/m^3 which was derived from the force displacement curve in Figure 7.21b. This value appears to be legitimate because the inclination of the resulting experimental 2:1 branch is matched well by that of the theoretical simulations throughout the branches covering their respective ranges of amplitude of motion for the parameters chosen.

During the experiments, the IR of the 1st FW mode (swinging of the disk) with the 2nd BW mode (angling of the disk), named $2^1{:}1^2$ was not observed. The basin of attraction of this mode was small. When the rotor was rotating with high speeds (e.g. 250 rad/s), it was keeping its angle thanks to high angular momentum despite the external impacts. It was readily achieved in the simulations, though only when the viscous damping constant was decreased to lower values such as $0.7\,c_{rb}$.

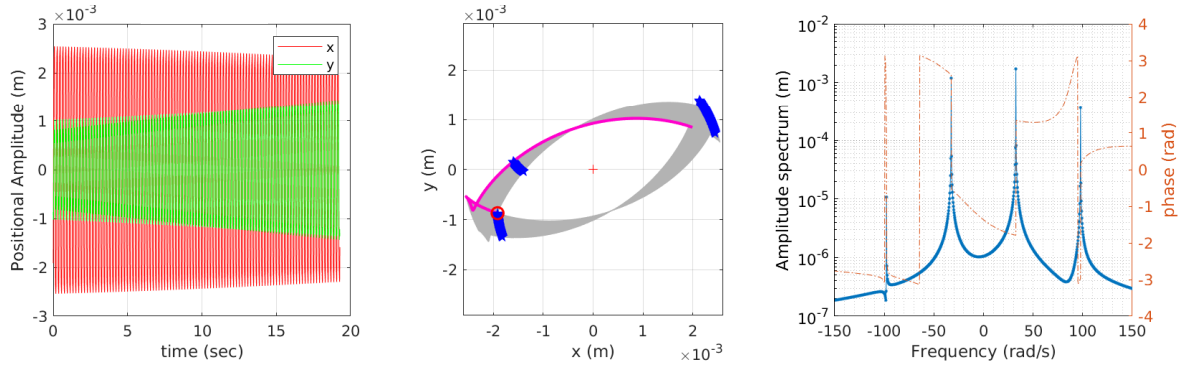
Interestingly, both IR branches of $2^1{:}1^1$ and $3^1{:}1^1$ exhibit a stationary frame periodic solution, which is named here as *stagnation* and does not appear in the literature to the knowledge of the author. Above that rotor speed the precession of the trajectory appears BW whirling and below FW whirling, i.e., filling the configuration space in these directions. This is illustrated in Figure 7.36 and Figure 7.37. At first glance, these are similar to the parked orbits of the same resonance from the experiments (Figure 7.28 for $2^1{:}1^1$, Figure 7.29 for $3^1{:}1^1$). As a result, the same discussion on their appearance as period-3 for $2^1{:}1^1$ and period-2 for $3^1{:}1^1$ IR is relevant from Section 7.5.1. However, while stagnation is a reflection of the physical phenomena and happens at a particular rotor speed for a given IR branch in both experiments and the time simulations, the parked orbits are the result of the imperfect experimental conditions and happened at various

speeds.

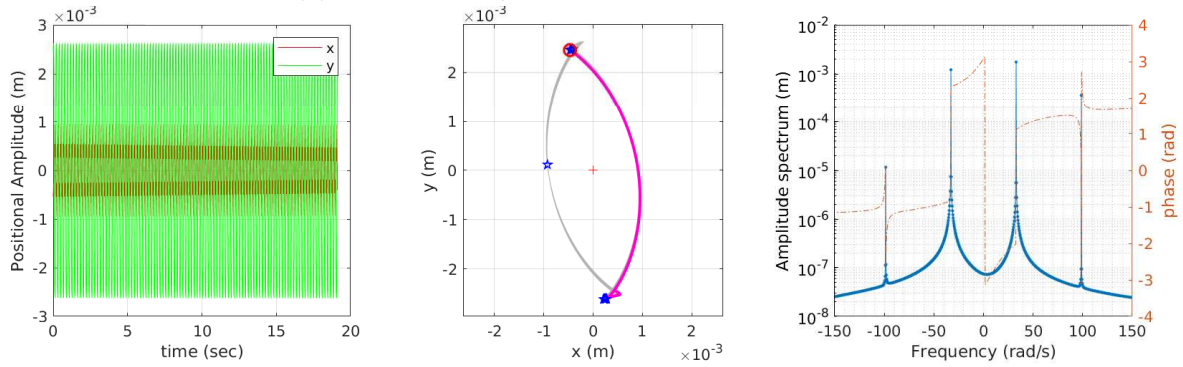
The only achieved 3^1:1^1 response in the experiment was a parked trajectory, i.e. appeared without any precession. There is not a complete 3^1:1^1 branch data from the experiments. The complete branch data for 3^1:1^1 resonance was already difficult even with lower damping values used in the simulations: only one solution was found which was sine-swept slowly (0.1 rad/s at a time) up and down the rotor speed. In that case, it is not obvious whether the only 3^1:1^1 response found experimentally was truly found stagnant, as in the simulations (Figure 7.37) or whether it is only parked in that orientation due to other unknown effects such as support anisotropy.

Figure 7.38 shows results from the experimental BD, though this time with pink and blue markings indicating the precession direction: from pink towards blue. Figure 7.38a shows a low speed orbit that is precessing in the FW direction, as expected from the above discussion on the simulation results. However, the parked 2^1:1^1 experimental orbit in Figure 7.38b did not happen at the stagnation where the transition from FW to BW precession happens. Therefore parking phenomena is separate to stagnation.

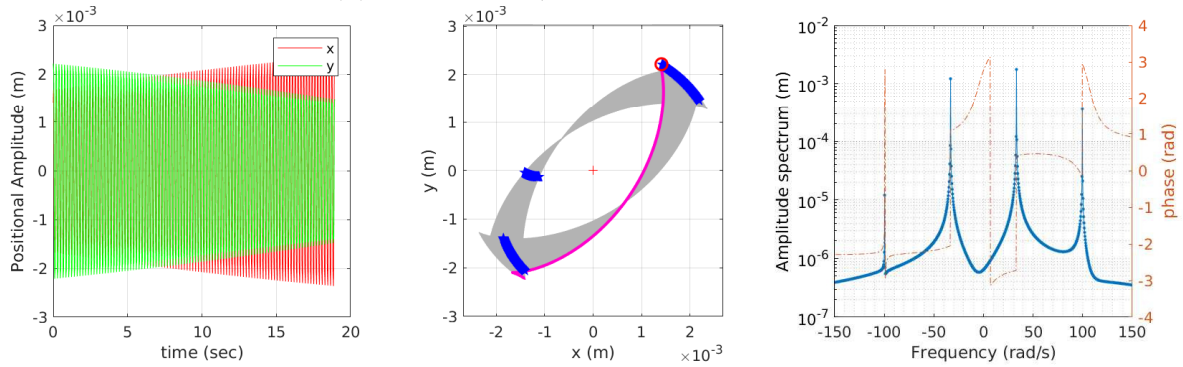
The FW precession of the experimental 2^1:1^1 was present up to 69.5 rad/s (Figure 7.38) which changed to BW in 71.5 rad/s (Figure 7.38d). However, until around 100 rad/s, the orbits were not easily sustained: once the stator started vibrating, the IR was lost, which was linked to the possible effect of slightly unequal force profiles from the stiffness rods in the experiment. This means that during low speeds of FW or BW precession, the stator vibrations are excited which interferes with and disengages the 2^1:1^1 IR. This effect was more pronounced for the BW precessing (i.e. above stagnation) orbits.



(a) Ω = 97.8 rad/s, FW precessing trajectory.

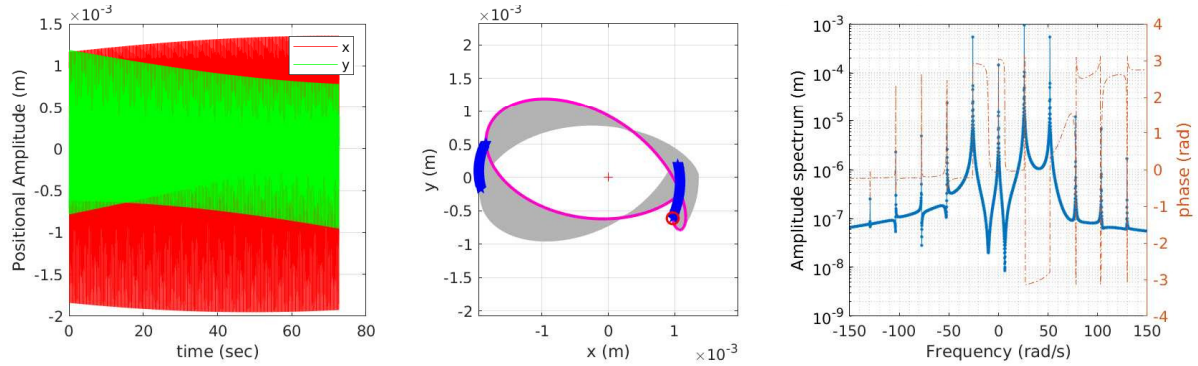


(b) Ω = 98.6 rad/s, stagnant trajectory.

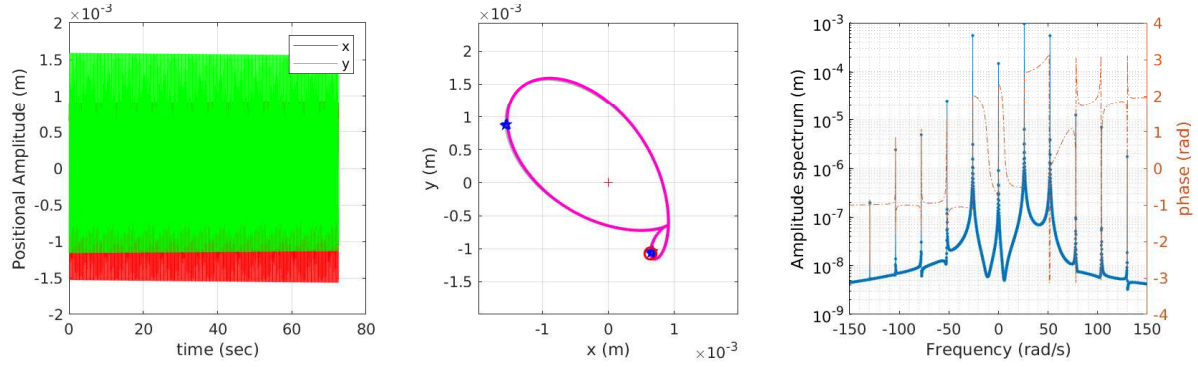


(c) Ω = 99.6 rad/s, BW precessing trajectory.

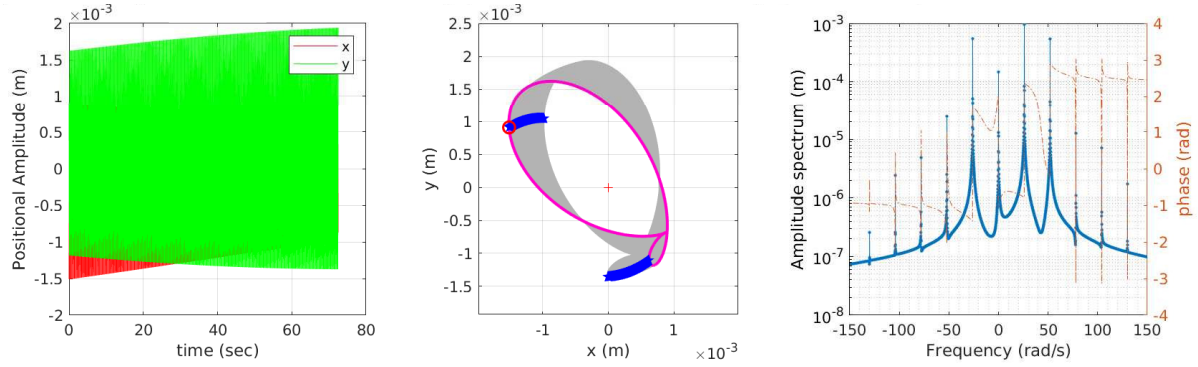
Figure 7.36: The stagnant (period-3) orbit on the quasiperiodic 2^1:1^1 branch. In the middle column: The pink orbit shows one quasiperiod (i.e. one repeating, precessing pattern). Blue pentagrams show the stroboscopic Poincaré section. Gray line is the trajectory of the stator that covers the time of 200 pink orbits.



(a) Ω = 51.8 rad/s, FW precessing trajectory.

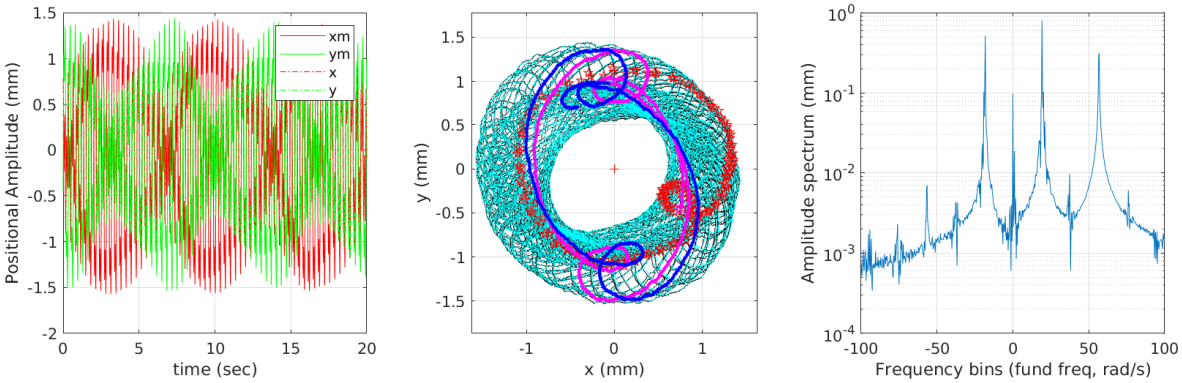


(b) Ω = 51.9 rad/s, stagnant trajectory.

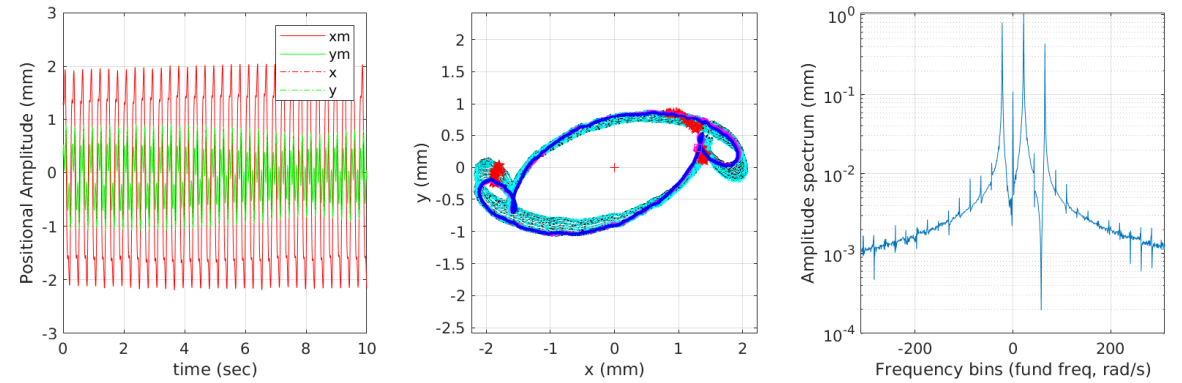


(c) Ω = 52.0 rad/s, BW precessing trajectory.

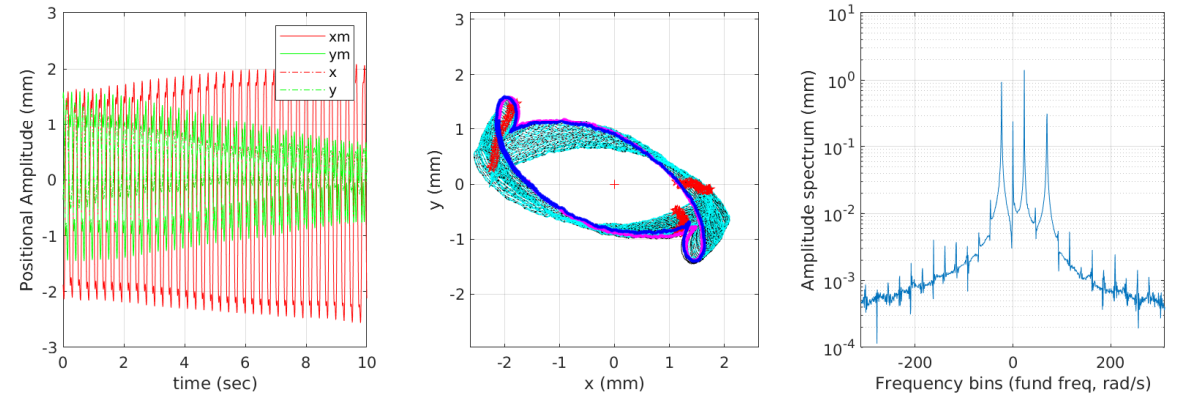
Figure 7.37: The stagnant (period-2) orbit on the quasiperiodic 3^1:1^1 branch. In the middle column: The pink orbit shows the first quasiperiod (i.e. one repeating, precessing pattern). Blue pentagrams show the stroboscopic Poincaré section. Gray line is the trajectory of the stator that covers the time of 200 pink orbits.



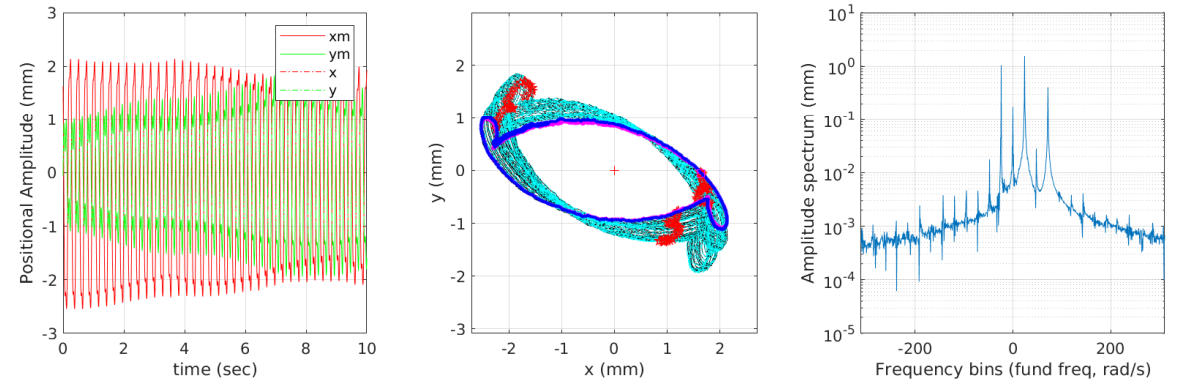
(a) Low speed orbit that is precessing FW (56.7 rad/s).



(b) The parked orbit that is not precessing (65.5 rad/s).



(c) The last forwards precessing orbit in the run-up direction (69.5 rad/s).



(d) The start of BW precessing orbit in the run-up direction (71.5 rad/s).

Figure 7.38: The parked orbit on 2^1:1^1 of the experiments (see Figure 7.24). The first and second 1500 data points are marked pink and blue, respectively.

7.6 Conclusion

Chs. 3 and 4 showed that the cubic nonlinearity is able to generate some of the nonlinear responses that are excited due to a compliant or rigid contact nonlinearity. In order to test these findings experimentally, a test rig was built that can generate cubic force as nonlinearity. A cantilever overhung rotor was designed that is comparable in terms of nondimensional design values to those used in Ch. 3 and 4.

A stator that is connected to the shaft and linked to the ground with pinned-pinned boundary condition were designed. Note that this design is easily adaptable to a stator design that features a contact nonlinearity rather than a soft nonlinearity.

A 4-dof equations of motion was developed where the degrees of freedom are the stationary frame lateral displacements, (x, y) of the disk and the two angles of the disk about x and y axes, namely, (θ, ψ).

The following conclusions can be drawn in this study:

On the test rig

1. Cubic stiffness effect can be achieved with bend-stretch coupling, despite the use of a cantilever boundary condition. Even though the cubic polynomial curve fits in both experimental force-displacement curve and the theoretical force-displacement curves show some degree of quadratic terms, the omission of the quadratic term did not cause a large difference on the fit curve, nor on the cubic stiffness inferred.
2. One of the features of the experimental design that caused complications was the use of four stiffness rods for the stator in pinned-pinned boundary condition. Although they are tightened systematically on the stator, it was difficult to keep the stator level, resulting in uneven force carried by the rods.
3. The part named stator sleeve that adapts the shaft to the 7900 angular contact ball bearings, had a long, 5 mm bore, which was difficult to manufacture. This was the main reason for the shaft bend which was included in the updated simulations.
4. Because the tolerances were not fully met in the manufacture of the rig, excessively larger bearing fitting tolerances were adapted which resulted in slight gaps and changing support centres during the runs.
5. Modal damping obtained from the non-rotating rotor turns out to be very high in the simulations due to the bearings' friction. Instead, a viscous damping coefficient that acts laterally at the stator was used effectively.

On the observed phenomenon

1. In the experiment's numerical simulations, $2^1{:}1^1$, $3^1{:}1^1$, and $2^1{:}1^2$ IRs in the rotating frame can be predicted by the extended Campbell plots. This confirms the results presented in the preceding chapter (Ch. 3 and 4).

2. The 2:1 IR response, as well as 3:1, show sensitivity to the Campbell plot frequency line's evolution due to the low angles they make when intersecting:
3. In the experiments, it was observed that the rotor speeds where the nonlinear resonances were seen in the BD were consistently lower compared to the simulations. The imperfect cantilever end might have caused this effect, because when compensated, the BDs can be made overlap.
4. The main resonance was found to be bounded, contrary to the simulations where the main resonance is unbounded. The reason behind this might be the fact that the axial force on the eight 135 self-aligning ball bearings markedly increases the damping in them. It is expected that the synchronous response is impacted the most as the almost pure circular whirl makes the response experience the high damping for longer. However, the $2^1{:}1^1$ ($2\,\omega_{f1}^{rot} = \omega_{b1}^{rot}$) resonances that include an oscillation between high and low amplitude (hence high and low damping) in their trajectories look unbounded, as the simulations predict. For the sake of the structural safety of the rig, amplitudes beyond 9 mm were not excited.
5. The simulations showed the $2^1{:}1^2$ IR ($2\,\omega_{f1}^{rot} = \omega_{b2}^{rot}$) response with a small basin of attraction. They are obtained relatively easily when the damping in the simulations is decreased. However, in the experiments it was not achieved: the level of external excitation, i.e., the high angle given to the disk, was not possible even with a strong hit on the shaft and stator in opposite directions. The high level of angular momentum locked the response in the synchronous response.
6. Although the simulations did not generate backward (teardrop) resonance, the experiments clearly show it. In the high unbalance case, this resonance masked the main resonance completely during the experiments. The imperfections in the support anisotropy and the bearing hub fit might have caused the elliptical orbits, which all contributed to backward whirl components around the main resonance. This, combined with the high bearing friction induced with amplitude, is responsible for the sustaining of this backward resonance that is periodic in the rotating frame.
7. In the run-up direction, for the IRs $2^1{:}1^1$ and $3^1{:}1^1$, the precession of the trajectory switched from forwards to backwards. This effect was seen in the experiments on the $2^1{:}1^1$ IR. At the transition, the orbits become *stagnant*, i.e. without any precession. Therefore, they are periodic both in the stationary frame and the rotating frame.
8. Some experimental orbits stayed *parked* in one orientation. This is in contrast to the stagnation at the switch of precession direction. The reason was associated with the interaction of the rotor with the slight anisotropy of the stator support. This must have caused a "preferred" orientation.
9. The effect of "preferred" orientation is also visible in the sustained and fully precessing, higher-speed $2^1{:}1^1$ orbits: the trajectory spends more time when in that preferred orientation while it passes through the rest of the space rapidly.

10. As in the brute force time simulations, it was very difficult to obtain the $3^1{:}1^1$ response, in the experiment. Only one such response that is *parked* in orientation was obtained. Though, it is not clear whether this is due to the stagnation of the precession along the branch or due to the predicted reason of the anisotropy in the stator supports.

Chapter 8

Conclusion

The diversity of the nonlinear rotordynamic system's response is rich. Therefore, a checklist for response classification was proposed. This thesis has mainly focused on understanding the quasiperiodic internal resonances (IRs) exhibited by nonlinear rotor-stator interactions by means of numerical and experimental analyses. In order to theoretically investigate these resonances, a nondimensional 2-dof gyroscopic model with cubic stiffness was used which represented the softer extreme of the rotor-stator interactions. Numerical continuation and time simulation were used and assessed. The cubic formulation was then switched to tanh-contact that approximates the discontinuous contact with a continuous function. The use of the tanh function was then discussed. The theoretical study investigated the effects of damping and excitation of the system which are the most variable parameters.

A new quasiperiodic continuation method was devised to show that the available continuation methods can be generalised to include not only periodic motion. If the solution is quasiperiodic in the stationary frame, but periodic in the rotating frame, this method can be used to continue forced and damped IR responses of nonautonomous systems. The stability calculation by Floquet theory was adapted. Then, nonlinear normal modes (NNMs) of the underlying linear system were derived in order to investigate the coupling of the FW and BW modes. To do that, an idea of NNM correlation was proposed.

The following conclusions are drawn from the theoretical studies in this thesis:

1. A 2-dof gyroscopic system is able to generate quasiperiodic IR response even with softer nonlinearities such as cubic stiffness nonlinearity. The nonlinear response is not limited to a contact amplitude and can be achieved at very low amplitudes with low damping, thereby making it susceptible to be excited even by little transient energy.

2. Homotopy from a simple nonlinearity to a complex one is plausible and enables the drawing of the bifurcation diagram without prior simulation knowledge. However, this is possible for the responses that are manifested by both nonlinearities. Therefore, the

richness of the bifurcation diagram of the new nonlinearity might not be discovered by a homotopy from a different nonlinearity.

3. The hyperbolic tangent function represented contact very well both in time simulations and numerical continuation using adaptive mesh updates of AUTO. However, the tanh-steepness has to be adjusted for accuracy and computational efficiency to avoid fictitious effects in the bifurcation diagram.

4. Higher damping eliminates the IR responses either by means of shrinking the region they are observed, or for the unbounded responses, driving their region to higher amplitudes, thereby making their excitation more difficult.

5. Very low damping makes the asynchronous IR response amplitude reach the synchronous response amplitude, seemingly combining the branches of the two solutions in a bifurcation diagram. However, the two responses never combine through a bifurcation but rather stay isolated from each other.

6. Lower damping and forcing shifts the IR response closer to the Campbell diagram value, until the proximity around the unforced, undamped case. In the conservative case, this IR response is degenerate and can happen in a range of rotor speeds and vibration amplitudes without a defined backbone.

7. In the contact case, higher unbalance force can warp the IR solution families in such a way that the same response can be present in different amplitude ranges.

8. Quasiperiodic continuation based on a shooting-continuation method was demonstrated to be effective in the unification of some of these diverse response patterns. The method is currently limited to quasiperiodic trajectories that can be represented as a periodic orbit.

9. The coupling between the FW and BW NNMs to form an IR response can be predicted by their frequency content: if the frequency content of the two modes have matching harmonics, then they can lock together. Off-centring effects, such as gravity sag or OOB forcing, are ways of making the frequency content rich with harmonics, and making their coupling more likely.

In the experiments, the test rig design values were obtained from the dimensionalisation of the nondimensional 2-dof EOM used in the theoretical study. An overhung disk was designed with a stator attached to the end of the shaft. Cubic stiffness effect was achieved with bend-stretch coupling, despite the use of a cantilever boundary condition. However, the calibration of four rods to the same level of tightness required diligent effort. In the experiments, the versatility of the rig was achieved by designing the stator and cubic stiffness device separately. The disk position and the unbalance excitation were made

variable, as well. The rig was oriented vertically but support dynamics did not interfere with the rotor responses. The experimental bifurcation diagrams were compared to those from a 4-dof model for validation. The experimental bifurcation diagram features were consistently lower in the rotor speed range which might be a result of imperfect cantilever boundary conditions. The experimental study yielded the following conclusions:

1. The intersection of the lines in the Campbell diagram makes a shallow angle. Therefore, the predicted rotor speed for onset of IR responses can shift significantly with slight changes in the test rig parameters.

2. The experimental main resonance was bounded contrary to the simulations. This is linked to the higher damping that occurs with higher amplitudes resulting from the increased friction of the self-aligning ball bearings under high axial loads.

3. The IR response termed $2^1 : 1^2$ ($2\omega_{f1}^{rot} = \omega_{b2}^{rot}$) which includes the first FW mode (displacement) and the second BW mode (rotation), was not achieved in the experiments due to small basin of attraction. Additionally, high angular momentum of the disk was difficult to overcome at those higher rotor speeds.

4. In the run-up direction the IR precession switches from FW to BW, which happened both in the simulations and the experiments. At the transition, the orbits are called *stagnated* as they stop precessing.

5. The experimental IR responses showed a preferred orientation where the response parked indeterminately longer, which is linked to the support anisotropy.

6. The experiments and the simulations each showed only one $3^1 : 1^1$ IR response, but this was sine-swept in the simulations for a more complete branch. This must be due to the effect of damping firstly eliminating the 3:1 among the IR responses, as shown in this thesis in the theoretical studies.

Rotating machinery is a vast field which ranges from drilling machines to turbomachinery and could be as simple as a fan or as complex as a high-speed jet engine. Each application possesses different needs for the test rig implementation. However, instead of being representative of a purpose-built industrial machine, the produced test rig is designed for the reproduction and study of the particular nonlinear responses, namely, the internal resonances, observed in rotating machinery. Nonetheless, gyroscopics, boundary conditions, stiffness, aerodynamics, etc. are factors to consider when one needs to adapt the test rig to one of these industrial, real-life cases.

8.1 Future work

Several future work ideas are presented below:

1. Investigation of industrial systems necessitates higher-dof models which rapidly increases the matrix sizes, hence the computational burden. Therefore, the feasibility of generalisation of the numerical continuation formulated by time discretisation to higher-dof rotor-stator systems should be evaluated, especially in comparison to the numerical continuation formulations that utilise HBM to obtain the algebraic equation. The comparison would reflect the powers of each method when the state-of-the-art implementations of these methods are used, e.g., with mesh updates for the orthogonal collocation method and harmonic selection for the HBM.
2. Due to the close resemblance of the intermittent response patterns in this thesis to those in previous stiffness discontinuity studies, the effect of the time spent during contact on the response patterns is a point of interest.
3. Although previous theoretical research and some experimental research has revealed various aspects of contact friction (such as regarding full rubbing, route to chaos etc.), the effect of friction in a smooth geometric nonlinearity such as the cubic nonlinearity employed in the thesis has not been investigated.
4. The formation of the internal resonance modes through the NNMs has not been answered thoroughly, although the present thesis uncovers the relation of such nonlinear resonances with the underlying NNMs' frequency content.
5. A more generic quasiperiodic continuation method needs to be developed for the continuation of more general quasiperiodic responses, such as those that involve many different frequencies, or such as the combination resonance $\omega_f^{sta} - \omega_b^{sta} = \Omega$ observed under the effect of misalignment and OOB-forcing which is not necessarily periodic in any reference frame.
6. Control-based continuation and NNMs has recently found experimental application in stationary structures; however, rotating structures, particularly involving gyroscopic couples, has not been apparent in the related research.

Appendix A

AUTO files

The proper use of the software AUTO [84] requires to utilise the AUTO files correctly. For the problem investigated in Ch. 3, the following descriptions are made.

A.1 Constants file

The constants file that is used in AUTO setup is where the user mainly specifies,

- type of solution (IPS=1 for stationary, IPS=2 for periodic),
- the continuation parameters (ICP list e.g. rotational speed, damping),
- tolerances of convergence conditions (EPSL, EPSU, EPSS),
- minimum, maximum and starting step sizes (DSMIN, DSMAX, DS)
- number of Newton-Chord iterations (ITNW, NWTN) to be performed before re-attempt of solution,
- mesh discretisation (NTST) for accuracy control
- user requested data points (UZR)
- stopping conditions for continuation (STOP, UZSTOP, NMX) or parameter lower and upper limits (RL0, RL1).

It is suggested [84] that the mesh interval count should be as low as possible for convergence. A tolerance of convergence (EPSL, EPSU) of 10^{-6} to 10^{-7} is recommended, and a special solution (such as branch points) an accuracy (EPSS) of 10^{2} to 10^{3} times the tolerance of convergence is advised. These limits were kept in all continuation runs of this study. The constants-file content that is used to start the synchronous AUTO runs is given below:

```
unames={1: "u", 2: "v",3:" u\_dot" , 4:"v\_dot"}
parnames={1:"gamma",2:"Omeg",3:"mH",4:"JpH",5:"epsH", 6:"zeta",
          9:"Amplitude"}
NDIM= 4, IPS = 1, ICP = [3,9], IPLT= 9, IRS = 0, ILP = 1,
ISW = 1, ISP = 2, UZSTOP = {3:0.9}
```

Table A.1: AUTO initial conditions for rotating frame EOM

ζ	10^{-2}	$8{\cdot}10^{-3}$	$5{\cdot}10^{-3}$	10^{-3}	10^{-4}	10^{-5}
u	-0.3801	-0.3801	-0.3800	-0.3779	-0.3812	-0.3800
v	-0.0013	-0.0010	-0.0005	0.0014	-0.0023	0.0000
u'	0.0000	0.0000	0.0008	0.0119	-0.0174	0.0004
v'	0.0000	-0.0000	-0.0009	-0.0167	0.0081	-0.0011
t_{end}	$3{\cdot}10^3$	$3{\cdot}10^3$	$3{\cdot}10^3$	10^4	10^5	10^6

```
NTST= 200, DS  = 0.005, DSMIN= 1e-4, DSMAX= 0.05,
IADS= 1, EPSL= 1e-06, EPSU = 1e-06, EPSS =1e-4,
NMX = 10000, ITMX= 8, ITNW= 7, NWTN= 5
NCOL= 4, IAD = 3
NBC = 0, NINT= 0
NPR = 1000, IID = 3
MXBF= 5, JAC = 0, NPAR= 36, THU = {}, THL = {}
```

Particularly, ICP, NTST, NMX, EPSL, EPSU, EPSS, DS, DSMIN, DSMAX, UZSTOP, RL0, RL1 were checked specifically for each run, with some level of experimentation for better accuracy and convergence [84].

A.2 Auto data file generation

Synchronous solution initial conditions are given in Table A.1. Table A.1 also shows the simulation duration in nondimensional time t_{end} for both synchronous and asynchronous responses. After a simulation completed, the converged orbit's data of time versus all four states were stored in a tab-separated .dat file [84] to be used as starting data in AUTO.

Appendix B

Required derivatives for the quasiperiodic shooting-continuation method

During the shooting-continuation process, in order to calculate the solution by Newton method, linearisation of the nonlinear algebraic equations are needed which give rise to the following partial derivatives to be calculated (Ch. 5).

B.1 Partial derivative of the periodicity condition with respect to the period

This can be calculated as follows:

$$\begin{aligned}\frac{\partial \mathbf{H}(T,\mathbf{z}_0,\Omega,\phi_\Omega)}{\partial T} &= \frac{\partial(\mathbf{R}(\Omega,T)\mathbf{z}(T,\mathbf{z}_0,\Omega,\phi_\Omega))}{\partial T} - \frac{\partial \mathbf{z}_0}{\partial T} = \left.\frac{\partial(\mathbf{R}(\Omega,T)\mathbf{z}(t,\mathbf{z}_0,\Omega))}{\partial t}\right|_{t=T} \\ &= \left[\frac{\partial \mathbf{R}(t,\Omega)}{\partial t}\mathbf{z}(t,\mathbf{z}_0,\Omega,\phi_\Omega) + \mathbf{R}(t,\Omega)\frac{\partial \mathbf{z}(t,\mathbf{z}_0,\Omega,\phi_\Omega)}{\partial t}\right]_{t=T} \\ &= \mathbf{R}_{se,t}(T,\Omega)\mathbf{z}(T,\mathbf{z}_0,\Omega,\phi_\Omega) + \mathbf{R}\mathbf{g}(\mathbf{z}(T,\mathbf{z}_0,\Omega,\phi_\Omega),\Omega,\phi_\Omega)\end{aligned} \tag{B.1}$$

Note, $\mathbf{z}_0$, T, Ω and ϕ_Ω are independent. Here,

$$\mathbf{R}_t = \Omega\begin{bmatrix} -\sin\theta_{se} & \cos\theta_{se} & 0 & 0 \\ -\cos\theta_{se} & -\sin\theta_{se} & 0 & 0 \\ 0 & 0 & -\sin\theta_{se} & \cos\theta_{se} \\ 0 & 0 & cos\theta_{se} & -\sin\theta_{se} \end{bmatrix}, \quad \theta_{se} = \Omega T \tag{B.2}$$

B.2 Partial derivative of the periodicity condition with respect to the initial condition

This can be found as follows:

$$\begin{aligned}\frac{\partial \mathbf{H}(T,\mathbf{z}_0,\Omega,\phi_\Omega)}{\partial \mathbf{z}_0} &= \frac{\partial \mathbf{R}(\Omega,T)\mathbf{z}(T,\mathbf{z}_0,\Omega,\phi_\Omega)}{\partial \mathbf{z}_0} - \frac{\partial \mathbf{z}_0}{\partial \mathbf{z}_0} \\ &= \mathbf{R}(\Omega,T)\frac{\partial \mathbf{z}(t,\mathbf{z}_0,\Omega,\phi_\Omega)}{\partial z_0}\bigg|_{t=T} - \mathbf{I}\end{aligned} \tag{B.3}$$

where $\partial \mathbf{z}(t,\mathbf{z}_0,\Omega,\phi_\Omega)/\partial \mathbf{z}_0$ can be derived to integrate:

$$\begin{aligned}\frac{\mathrm{d}}{\mathrm{d}t}\left(\frac{\partial \mathbf{z}(t,\mathbf{z}_0,\Omega,\phi_\Omega)}{\partial \mathbf{z}_0}\right) &= \frac{\mathrm{d}\boldsymbol{\alpha}(t,\mathbf{z}_0,\Omega,\phi_\Omega)}{\mathrm{d}t} = \frac{\partial \boldsymbol{\alpha}}{\partial t}\frac{\mathrm{d}t}{\mathrm{d}t} + \frac{\partial \boldsymbol{\alpha}}{\partial \mathbf{z}_0}\frac{\mathrm{d}\mathbf{z}_0}{\mathrm{d}t} + \frac{\partial \boldsymbol{\alpha}}{\partial \Omega}\frac{\mathrm{d}\Omega}{\mathrm{d}t} + \frac{\partial \boldsymbol{\alpha}}{\partial \phi_\Omega}\frac{\mathrm{d}\phi_\Omega}{\mathrm{d}t} \\ &= \frac{\partial \boldsymbol{\alpha}}{\partial t} = \frac{\partial^2 \mathbf{z}}{\partial t \partial \mathbf{z}_0} = \frac{\partial^2 \mathbf{z}}{\partial \mathbf{z}_0 \partial t} \\ &= \frac{\partial}{\partial \mathbf{z}_0}\left(\frac{\mathrm{d}\mathbf{z}}{\mathrm{d}t} - \frac{\partial \mathbf{z}}{\partial \mathbf{z}_0}\frac{\mathrm{d}\mathbf{z}_0}{\mathrm{d}t} - \frac{\partial \mathbf{z}}{\partial \Omega}\frac{\mathrm{d}\Omega}{\mathrm{d}t} - \frac{\partial \mathbf{z}}{\partial \phi_\Omega}\frac{\mathrm{d}\phi_\Omega}{\mathrm{d}t}\right) = \frac{\partial}{\partial \mathbf{z}_0}\frac{\mathrm{d}\mathbf{z}}{\mathrm{d}t} \\ &= \frac{\partial \mathbf{g}(t,\mathbf{z}(t,\mathbf{z}_0,\Omega,\phi_\Omega),\Omega,\phi_\Omega)}{\partial \mathbf{z}_0} \\ &= \frac{\partial \mathbf{g}}{\partial t}\frac{\partial t}{\partial \mathbf{z}_0} + \frac{\partial \mathbf{g}}{\partial \mathbf{z}}\frac{\partial \mathbf{z}}{\partial \mathbf{z}_0} + \frac{\partial \mathbf{g}}{\partial \Omega}\frac{\partial \Omega}{\partial \mathbf{z}_0} + \frac{\partial \mathbf{g}}{\partial \phi_\Omega}\frac{\partial \phi_\Omega}{\partial \mathbf{z}_0} = \mathbf{g}_\mathbf{z}\frac{\partial \mathbf{z}}{\partial \mathbf{z}_0}\end{aligned} \tag{B.4}$$

$$\frac{\mathrm{d}}{\mathrm{d}t}\left(\frac{\partial(\mathbf{R}(t,\Omega)\mathbf{z}(t,\mathbf{z}_0,\Omega,\phi_\Omega))}{\partial \mathbf{z}_0}\right) = \mathbf{R}(t,\Omega)\frac{\mathrm{d}\boldsymbol{\alpha}(t,\mathbf{z}_0,\Omega,\phi_\Omega)}{\mathrm{d}t} = \mathbf{R}(t,\Omega)\mathbf{g}_\mathbf{z}\frac{\partial \mathbf{z}}{\partial \mathbf{z}_0} \tag{B.5}$$

where the independence of t, $\mathbf{z}_0$, Ω and ϕ_Ω is used to switch between the partial and full derivatives. This gives the following ODE,

$$\dot{\boldsymbol{\alpha}}(t) = \mathbf{g}_\mathbf{z}(t,\mathbf{z}_0,\Omega,\phi_\Omega)\boldsymbol{\alpha}(t) \tag{B.6a}$$

$$\boldsymbol{\alpha}(t) = \frac{\partial \mathbf{z}(t,\mathbf{z}_0,\lambda)}{\partial \mathbf{z}_0} \tag{B.6b}$$

$$\boldsymbol{\alpha}(t=0) = \frac{\partial \mathbf{z}_0}{\partial \mathbf{z}_0} = I_{2n\times 2n} \tag{B.6c}$$

where $\dot{(\cdot)}$ denotes time derivation. The matrix $\boldsymbol{\alpha}(t)$ is the *evolution matrix* and its value $\boldsymbol{\alpha}(T) = \partial \mathbf{z}(T,\mathbf{z}_0,\lambda,\phi_\Omega)/\partial \mathbf{z}_0$ at $t = T$ is used in Eq. (5.11). Note, each column of the matrix $\boldsymbol{\alpha}(T)$ comes from the integration from the corresponding column of the initial condition $\boldsymbol{\alpha}(0) = I_{2n\times 2n}$ integrated in time from $t = 0$ to $t = T$. At $t = T$, it relates to the Monodromy matrix (see Section 5.2.3).

B.3 Partial derivative of the periodicity condition with respect to the rotor spin speed

This can be calculated as follows:

$$\begin{aligned}\frac{\partial \mathbf{H}(T,\mathbf{z}_0,\Omega,\phi_\Omega)}{\partial\Omega} &= \frac{\partial(\mathbf{R}(\Omega,T)\mathbf{z}(T,\mathbf{z}_0,\Omega,\phi_\Omega))}{\partial\Omega} - \frac{\partial \mathbf{z}_0}{\partial\Omega}\\ &= \left[\mathbf{R}_{se,\Omega}(\Omega,T)\mathbf{z}(T,\mathbf{z}_0,\Omega,\phi_\Omega) + \mathbf{R}(\Omega,T)\frac{\partial \mathbf{z}(t,\mathbf{z}_0,\Omega,\phi_\Omega)}{\partial\Omega}\right]_{t=T}\\ &= \mathbf{R}_{se,\Omega}(T,\Omega)\mathbf{z}(T,\mathbf{z}_0,\Omega,\phi_\Omega) + \mathbf{R}(\Omega,T)\left.\frac{\partial \mathbf{z}(t,\mathbf{z}_0,\Omega,\phi_\Omega)}{\partial\Omega}\right|_{t=T}\end{aligned} \tag{B.7}$$

where,

$$\mathbf{R}_{se,\Omega} = t\begin{bmatrix} -\sin\theta_{se} & \cos\theta_{se} & 0 & 0\\ -\cos\theta_{se} & -\sin\theta_{se} & 0 & 0\\ 0 & 0 & -\sin\theta_{se} & \cos\theta_{se}\\ 0 & 0 & -\cos\theta_{se} & -\sin\theta_{se}\end{bmatrix}, \quad \theta_{se} = \Omega T - 2\pi \tag{B.8}$$

Here, $\partial\mathbf{z}(t,\mathbf{z}_0,\Omega,\phi_\Omega)/\partial\Omega$ can be derived to integrate,

$$\begin{aligned}\frac{\mathrm{d}}{\mathrm{d}t}\left(\frac{\partial \mathbf{z}(t,\mathbf{z}_0,\Omega,\phi_\Omega)}{\partial\Omega}\right) &= \frac{\mathrm{d}\boldsymbol{\beta}(t,\mathbf{z}_0,\Omega,\phi_\Omega)}{\mathrm{d}t} = \frac{\partial\boldsymbol{\beta}}{\partial t}\frac{\mathrm{d}t}{\mathrm{d}t} + \frac{\partial\boldsymbol{\beta}}{\mathbf{z}_0}\frac{\mathrm{d}\mathbf{z}_0}{\mathrm{d}t} + \frac{\partial\boldsymbol{\beta}}{\Omega}\frac{\mathrm{d}\Omega}{\mathrm{d}t} + \frac{\partial\boldsymbol{\beta}}{\phi_\Omega}\frac{\mathrm{d}\phi_\Omega}{\mathrm{d}t}\\ &= \frac{\partial\boldsymbol{\beta}}{\partial t} = \frac{\partial^2\mathbf{z}}{\partial t\partial\Omega} = \frac{\partial}{\partial\Omega}\frac{\partial\mathbf{z}}{\partial t}\\ &= \frac{\partial}{\partial\Omega}\left(\frac{\mathrm{d}\mathbf{z}}{\mathrm{d}t} - \frac{\partial\mathbf{z}}{\partial\mathbf{z}_0}\frac{\mathrm{d}\mathbf{z}_0}{\mathrm{d}t} - \frac{\partial\mathbf{z}}{\partial\Omega}\frac{\mathrm{d}\Omega}{\mathrm{d}t} - \frac{\partial\mathbf{z}}{\partial\phi_\Omega}\frac{\mathrm{d}\phi_\Omega}{\mathrm{d}t}\right) = \frac{\partial}{\partial\Omega}\frac{\mathrm{d}\mathbf{z}}{\mathrm{d}t}\\ &= \frac{\partial\mathbf{g}(t,\mathbf{z}(t,\mathbf{z}_0,\Omega,\phi_\Omega),\Omega,\phi_\Omega)}{\partial\Omega}\\ &= \frac{\partial\mathbf{g}}{\partial t}\frac{\partial t}{\partial\Omega} + \frac{\partial\mathbf{g}}{\partial\mathbf{z}}\frac{\partial\mathbf{z}}{\partial\Omega} + \frac{\partial\mathbf{g}}{\partial\Omega}\frac{\partial\Omega}{\partial\Omega} + \frac{\partial\mathbf{g}}{\partial\phi_\Omega}\frac{\partial\phi_\Omega}{\partial\Omega}\\ &= \mathbf{g}_\mathbf{z}\frac{\partial\mathbf{z}}{\partial\Omega} + \mathbf{g}_\Omega\end{aligned} \tag{B.9}$$

where the independence of t ,$\mathbf{z}_0$, Ω and ϕ_Ω is used to switch between the partial and full derivatives. This gives,

$$\dot{\boldsymbol{\beta}}(t) = \mathbf{g}_\mathbf{z}(\mathbf{z}(t,\mathbf{z}_0,\Omega,\phi_\Omega),\Omega,\phi_\Omega)\boldsymbol{\beta}(t) + \mathbf{g}_\Omega(\mathbf{z}(t,\mathbf{z}_0,\Omega,\phi_\Omega),\Omega,\phi_\Omega) \tag{B.10a}$$

$$\boldsymbol{\beta}(t) = \frac{\partial\mathbf{z}(t,\mathbf{z}_0,\Omega,\phi_\Omega)}{\partial\Omega} \tag{B.10b}$$

$$\boldsymbol{\beta}(0) = \frac{\partial\mathbf{z}_0}{\partial\Omega} = \{0\}_{2n\times 1} \tag{B.10c}$$

to integrate from $t = 0$ to $t = T$ with the initial condition, which is the same as given by [72]. The vector $\boldsymbol{\beta}(T) = \partial\mathbf{z}(T,\mathbf{z}_0.\Omega,\phi_\Omega)/\partial\Omega$ at time $t = T$ is used in Eq. (5.11).

B.4 Partial derivative of the periodicity condition with respect to out-of-balance angle

The oob angle refers to the angle the unbalance mass is oriented at when $t = 0$.

$$\begin{aligned}\frac{\partial \mathbf{H}}{\partial \phi_\Omega} &= \frac{\partial \mathbf{R}(\Omega, T)\mathbf{z}(T, \mathbf{z}_0, \Omega, \phi_\Omega)}{\partial \phi_\Omega} - \frac{\partial \mathbf{z}_0}{\partial \phi_\Omega} \\ &= \mathbf{R}(\Omega, T)\left.\frac{\partial \mathbf{z}(t, \mathbf{z}_0, \Omega, \phi_\Omega)}{\partial \phi_\Omega}\right|_{t=T}\end{aligned} \tag{B.11}$$

where, $\partial \mathbf{z}(t, \mathbf{z}_0, \Omega, \phi_\Omega)/\partial \phi_\Omega$ can be derived to integrate:

$$\begin{aligned}\frac{\mathrm{d}}{\mathrm{d}t}\left(\frac{\partial \mathbf{z}(t, \mathbf{z}_0, \Omega, \phi_\Omega)}{\partial \phi_\Omega}\right) &= \frac{\mathrm{d}\boldsymbol{\eta}(t, \mathbf{z}_0, \Omega, \phi_\Omega)}{\mathrm{d}t} = \frac{\partial \boldsymbol{\eta}}{\partial t}\frac{\mathrm{d}t}{\mathrm{d}t} + \frac{\partial \boldsymbol{\eta}}{\partial \mathbf{z}_0}\frac{\mathrm{d}\mathbf{z}_0}{\mathrm{d}t} + \frac{\partial \boldsymbol{\eta}}{\partial \Omega}\frac{\mathrm{d}\Omega}{\mathrm{d}t} + \frac{\partial \boldsymbol{\eta}}{\partial \phi_\Omega}\frac{\mathrm{d}\phi_\Omega}{\mathrm{d}t} \\ &= \frac{\partial \boldsymbol{\eta}}{\partial t} = \frac{\partial^2 \mathbf{z}}{\partial t \partial \phi_\Omega} = \frac{\partial}{\partial \phi_\Omega}\frac{\partial \mathbf{z}}{\partial t} \\ &= \frac{\partial}{\partial \Omega}\left(\frac{\mathrm{d}\mathbf{z}}{\mathrm{d}t} - \frac{\partial \mathbf{z}}{\partial \mathbf{z}_0}\frac{\mathrm{d}\mathbf{z}_0}{\mathrm{d}t} - \frac{\partial \mathbf{z}}{\partial \Omega}\frac{\mathrm{d}\Omega}{\mathrm{d}t} - \frac{\partial \mathbf{z}}{\partial \phi_\Omega}\frac{\mathrm{d}\phi_\Omega}{\mathrm{d}t}\right) = \frac{\partial}{\partial \phi_\Omega}\frac{\mathrm{d}\mathbf{z}}{\mathrm{d}t} \\ &= \frac{\partial \mathbf{g}(t, \mathbf{z}(t, \mathbf{z}_0, \Omega, \phi_\Omega), \Omega, \phi_\Omega)}{\partial \phi_\Omega} \\ &= \frac{\partial \mathbf{g}}{\partial t}\frac{\partial t}{\partial \phi_\Omega} + \frac{\partial \mathbf{g}}{\partial \mathbf{z}}\frac{\partial \mathbf{z}}{\partial \phi_\Omega} + \frac{\partial \mathbf{g}}{\partial \Omega}\frac{\partial \Omega}{\partial \phi_\Omega} + \frac{\partial \mathbf{g}}{\partial \phi_\Omega}\frac{\partial \phi_\Omega}{\partial \phi_\Omega} \\ &= \mathbf{g}_\mathbf{z}\frac{\partial \mathbf{z}}{\partial \phi_\Omega} + \mathbf{g}_{\phi_\Omega}\end{aligned} \tag{B.12}$$

where the independence of $\mathbf{z}_0$, Ω and ϕ_Ω is used to switch between the partial and full derivatives. This gives,

$$\dot{\boldsymbol{\eta}}(t) = \mathbf{g}_\mathbf{z}(\mathbf{z}(t, \mathbf{z}_0, \Omega, \phi_\Omega), \Omega, \phi_\Omega)\boldsymbol{\eta}(t) + \mathbf{g}_{\phi_\Omega}(\mathbf{z}(t, \mathbf{z}_0, \Omega, \phi_\Omega), \Omega, \phi_\Omega) \tag{B.13a}$$

$$\boldsymbol{\eta}(t) = \frac{\partial \mathbf{z}(t, \mathbf{z}_0, \Omega, \phi_\Omega)}{\partial \phi_\Omega} \tag{B.13b}$$

$$\boldsymbol{\eta}(0) = \frac{\partial \mathbf{z}_0}{\partial \phi_\Omega} = \{0\}_{2n\times 1} \tag{B.13c}$$

to integrate from $t = 0$ to $t = T$ with the initial condition B.13c.

Appendix C

Experiment's Appendices

Below, the appendices referred to by Ch. 7 are presented which includes extra content for the rig's design and calibration, as well as the assembly drawing.

C.1 Transient 2nd BW mode not decaying in initial simulations

The modal damping of the second pair of modes decrease to extremely low levels in high speeds. For example, the eigenvalues, damping ratios and natural frequencies of the system in Eq. (7.44) for Ω = 259 rad/s are (following the expansion of an eigenvalue as: $s_r = -\zeta_r\omega_r \pm j\omega_r\sqrt{1-\zeta_r^2}$) are given in Table C.1. The natural frequency of the second BW mode, 144.57 rad/s, appears in the corresponding DFT in Figure C.1. The corresponding damping ratio is 0.000022, which is very low compared to the non-rotating rotor design value that comes out as ζ = 0.002 (see Table C.1).

C.2 Selection of bearings

NSK rolling bearing catalogue [174], SKF rolling bearing catalogue [179], and INA plain bearing catalogue [180] and SKF plain bearing catalogue [181] were utilised to select ball bearings.

C.2.1 The stator's self-aligning ball bearing

Based on the calculation in Section 7.1.2, the self-aligning ball bearing of the stator is expected to experience the following maximum force,

$$\begin{aligned} &N_z = 1800 \text{ N (axially)} \\ &N_y = m_s r_s^{max} \Omega_{max}^2 = 0.82803 \cdot 0.007 \cdot 194.121^2 = 218.4 \text{ N (laterally)}. \end{aligned} \tag{C.1}$$

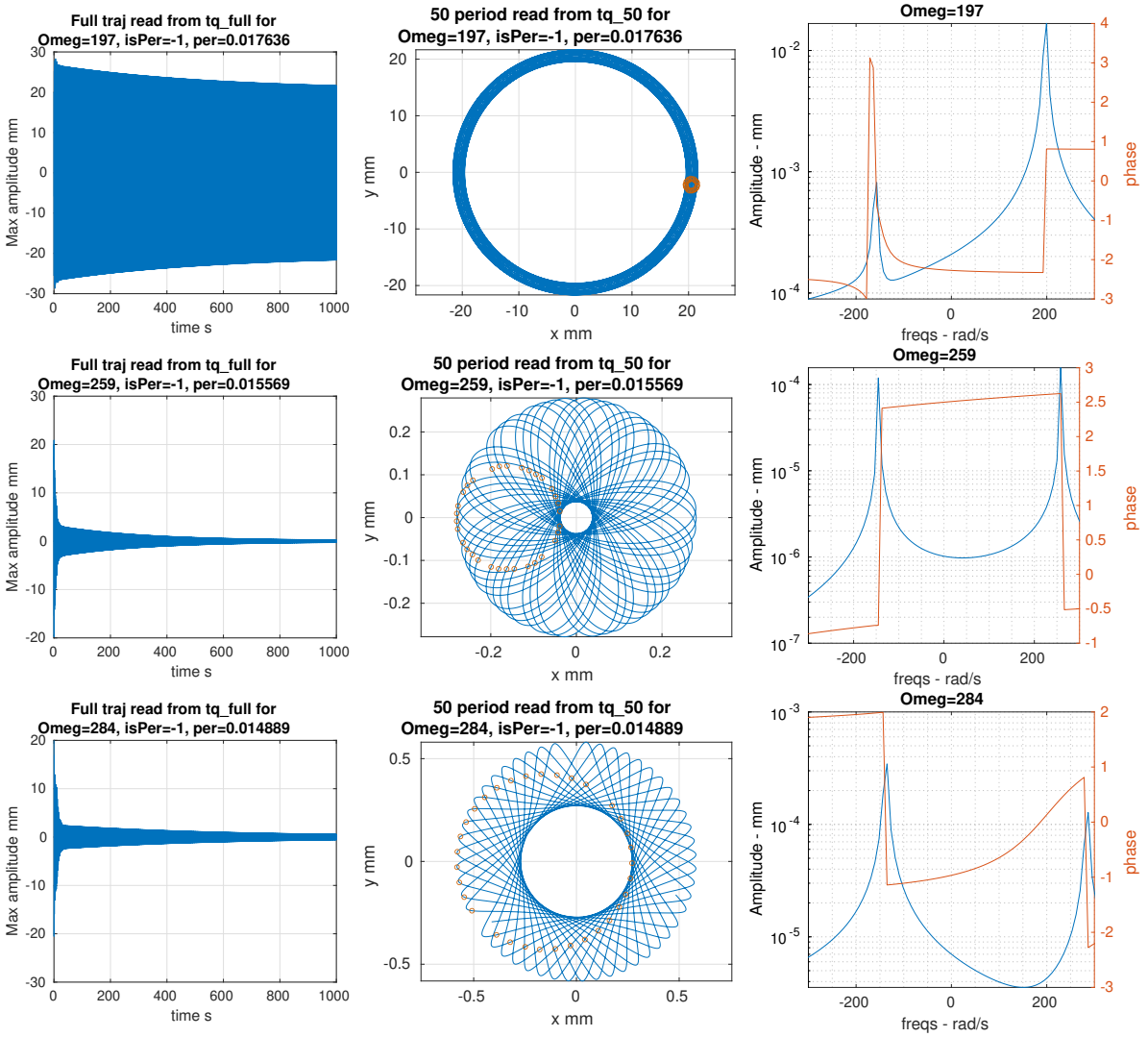


Figure C.1: Simulation with experimental design values. Selected orbits with 2^{nd} BW mode not decayed even after 1000 second of simulation: synchronous (top), $2^1 : 1^1$ (middle), and $2^1 : 1^2$ (bottom). Selected orbits . The eigenvalue data for $\Omega = 259$ rad/s is given in Eq. (C.1).

Table C.1: The eigenvalues, damping ratios and natural angular frequencies of Eq. (7.44) when Ω = 259.

Ω = 259 (rad/s)		
λ (rad/s)	ζ	ω (rad/s)
-0.115468 + 487.916031i	0.000237	487.916044
-0.115468 - 487.916031i	0.000237	487.916044
-0.003245 + 144.569597i	0.000022	144.569597
-0.003245 - 144.569597i	0.000022	144.569597
-0.217075 + 22.779210i	0.009529	22.780244
-0.217075 - 22.779210i	0.009529	22.780244
-0.155547 + 15.963714i	0.009743	15.964471
-0.155547 - 15.963714i	0.009743	15.964471

Ω = 0 (rad/s)		
λ (rad/s)	ζ	ω (rad/s)
-0.0523414 + 261.122962i	0.000200	261.122967
-0.0523414 - 261.122962i	0.000200	261.122967
-0.0523414 + 261.122962i	0.000200	261.122967
-0.0523414 - 261.122962i	0.000200	261.122967
-0.1933263 + 19.3954945i	0.009967	19.396458
-0.1933263 - 19.3954945i	0.009967	19.396458
-0.1933263 + 19.3954945i	0.009967	19.396458
-0.1933263 - 19.3954945i	0.009967	19.396458

The selection criteria from the NSK rolling bearing catalogue [174] is given in Table C.2. Here,

`C0`	Basic static load rating
`C`	Basic dynamic load rating
`P0`	Static equivalent load
`P`	Dynamic equivalent load
`r`	Radial
`a`	Axial
`X`	Radial load factor
`Y`	Axial load factor
`e`	Equation selector of the catalogue depending of the load
`fn`	Speed factor
`fh`	Fatigue life factor
`n`	Rotational speed (rpm)
`_req`	Required in design
`_cat`	Catalogue value of the selected bearing

Table C.2: Selection of the stator's self aligning ball bearing from NSK catalogue.

2301 Self-aligning ball bearing selection for stator	
F_r	218.4184
F_a	1800
n	1000
X	0.65
Y_2	1.6
Y_0	1.1
$P_r = X\ F_r + Y_2\ F_a$	3021.9719
$P_{r0} = F_r + Y_0\ F_a$	2198.4184
$f_n = (0.03\ n)^{-(1/3)}$	0.32183
$f_h = (L_h/500)^{(1/3)}$	0.342
$C_r^{req} = (f_h/f_n)\ P_r$	3211.3244
$C_{r0}^{req} = (f_h/f_n)\ P_{r0}$	2336.1681
C_r^{cat}	12100
C_{r0}^{cat}	2730
Bearing selection under normal loads:	
$C_r^{req} < C_r^{cat}$: 3211.3244<12100	true
$C_{r0}^{req} < C_{r0}^{cat}$: 2336.1681<2730	true
Vibration Factor:	
$1.0\ P_{r0} < C_{r0}^{cat}$: 2198.4184<2730	true
$1.5\ P_{r0} < C_{r0}^{cat}$: 3297.6275<2730	false
Fatigue formula applicability	
$P_r < C_{r0}^{cat}$: 3021.9719<2730	false
$P_r < 0.5\ C_r^{cat}$: 3021.9719<6050	true
Fit:	
Hub fit, heavy load, general precise application	K6
Shaft fit, any loading with only axial loads	js6

This bearing (NSK 2301) was found adequate although the fatigue formula applicability is false (or low) and the vibration factor under vibration and shock is not satisfied. The reason is that the operation conditions will include mostly low frequency of vibration from the rotor's lateral motion instead of shocks from impacts. Also, the short run times of the test rig will be sufficient for data acquisition purposes and there is no need to run the rig for extended periods. In order to decrease the noise in the acquired signals, the bearing accuracy (manufacturing precision) class was selected as P4 (Class 4).

C.2.2 The rods' self-aligning ball bearing

Expected axial load of 1800 N is shared between the four stiffness rods giving 450 N to each or them. NSK rolling bearing catalogue was used to find a suitable bearing. (See Table C.3). Similar to the case of 2301 bearing for the stator, despite some of the bearing size checks are not met, this was found satisfactory, as the rods self-aligning ball bearings are not designed to rotate.

C.2.3 The shaft's angular contact ball bearings

More importance was given to the selection of the axial contact ball bearing to ensure a relatively high reliability at the bearings that hold the shaft. Again, NSK catalogue was utilised [174], see Table C.4. Three NSK 7900 A5 TNY P4 angular contact ball bearings were selected in Triplex DBD arrangement. For precision, the contact angle was chosen to be 25 deg (A5), with moulded polyamide cage (TNY) and Class 4 manufacture accuracy (P4). The bearing size checks all give a "`true`" in this case, as it is expected that the bearing hub run with high reliability and no need for replacement for later uses of the rig.

C.2.4 The rods' alternative spherical plain bearing

Instead of using self-aligning ball bearings, one can chose to use spherical plain bearing. INA bearing catalogue [180] can be referred to.

Spherical plain bearings run in much lower speeds but can assume higher loads. Here, rods will move rapidly but the total angle range is low and there is no rotation about their axis. It would be more suitable to use angular contact spherical plain bearings. However, their sizes are quite large; therefore, more suitable radial spherical plain bearings are looked up. However, because the use case here is mainly the axial load, the selection of radial spherical plain bearings makes the selection to be very difficult using the catalogue [180]. Nonetheless, options that are similar in size to 135 self-aligning ball bearings chosen above are,

1. GE8-PW: d_{in} = 8 mm, d_{out} = 19 mm, B = 12 mm, C_{r0} = 32100 N, C_r = 12900 N
2. GE8-FW: d_{in} = 8 mm, d_{out} = 19 mm, B = 11 mm, C_{r0} = 21600 N, C_r = 8640 N

Table C.3: Self-aligning ball bearing selection for the stiffness rods from NSK catalogue.

135 Self-aligning ball bearing selection for rods	
F_r	10
F_a	450
n	10
X	0.65
Y_2	2.9
Y_0	1.9
$P_r = X\,F_r + Y_2\,F_a$	1311.5
$P_{r0} = F_r + Y_0\,F_a$	865
$f_n = (0.03\,n)^{-(1/3)}$	1.4938
$f_h = (L_h/500)^{(1/3)}$	0.73681
$C_r^{req} = (f_h/f_n)\,P_r$	646.8874
$C_{r0}^{req} = (f_h/f_n)\,P_{r0}$	426.6547
C_r^{cat}	2530
C_{r0}^{cat}	475
Bearing selection under normal loads:	
$C_r^{req} < C_r^{cat}$: 646.8874<2530	true
$C_{r0}^{req} < C_{r0}^{cat}$: 426.6547<475	true
Vibration Factor:	
$1.0\,P_{r0} < C_{r0}^{cat}$: 865<475	false
$1.5\,P_{r0} < C_{r0}^{cat}$: 1297.5<475	false
Fatigue formula applicability	
$P_r < C_{r0}^{cat}$: 1311.5<475	false
$P_r < 0.5\,C_r^{cat}$: 1311.5<1265	false
Fit:	
Hub fit, accurate running with indeter. load dir.	js6
Shaft fit, any loading with only axial loads	js6

Table C.4: Angular-contact ball bearing selection for the bearings holding the shaft from NSK catalogue.

7900 Angular contact ball bearing selection for rods	
$F_r = (N_{y1s}^{max} + F_{rs}^{max})$ $+((N_{y1s}^{max} + F_{rs}^{max})\, L_1/a_0)/3$	392.3947
F_a	1800
n	1000
X	0.54
Y	1.16
X_0	1
Y_0	0.76
$P_r = X\, F_r + Y\, F_a$	2299.8931
$P_{r0} = X_0\, F_r + Y_0\, F_a$	1760.3947
$f_n = (0.03\, n)^{-(1/3)}$	0.32183
$f_h = (L_h/500)^{(1/3)}$	0.342
$C_r^{req} = (f_h/f_n)\, P_r$	2444.0012
$C_{r0}^{req} = (f_h/f_n)\, P_{r0}$	1870.6985
$C_r^{cat} = 2.16\, C_r^{cat_single}$	6220.8
$C_{r0}^{cat} = 3.0\, C_{r0}^{cat_single}$	4350
Bearing selection under normal loads:	
$C_r^{req} < C_r^{cat}$: 2444.0012<6220.8	true
$C_{r0}^{req} < C_{r0}^{cat}$: 1870.69854<4350	true
Vibration Factor:	
$1.0\, P_{r0} < C_{r0}^{cat}$: 1760.3947<4350	true
$1.5\, P_{r0} < C_{r0}^{cat}$: 2640.5921<4350	true
Fatigue formula applicability:	
$P_r < C_{r0}^{cat}$: 2299.8931<4350	true
$P_r < 0.5\, C_r^{cat}$: 2299.8931<3110.4	true
Fit:	
Hub fit, accuracy, high loads, axial loads	K5
Shaft fit, axial loads, accuracy, small size	js4

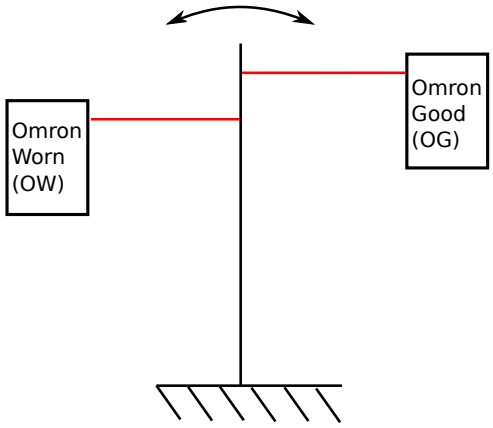


Figure C.2: Sensor delay study schematic drawing. Laser beams (red lines) are projected onto the vibrating cantilever beam.

3. GE10-UK: d_{in} = 10 mm, d_{out} = 19 mm, B = 9 mm, C_{r0} = 21600 N, C_r = 8640 N

The bearing INA GE10-UK is investigated as an example in Table C.5. Because of the complication mentioned above, to be on the safer side, bearing GE8-PW can be selected. GE8-PW can fit the same slot as that of the 135 self-aligning ball bearings. It has a smaller sphere diameter than GE10-UK, which will aid with the axial loads. It has a brass outer brace, which might further ease the stress concentration due to the high axial-to-radial load ratio. Lastly, GE8-PW has around 50% higher load ratings compared to GE10-UK.

C.3 Sensor delay study

There are three different laser displacement sensors that are used to track the position of the stator: MTI, OG and OW (as listed in the previous section.) The "sensor delay study" features a cantilever beam that is vibrating freely, and two of these sensors pointing their lasers laterally at the beam (see Figure C.2).

Analog voltage signals from the sensors are sampled using the data acquisition system and the displacement data are calculated whose DFT then are obtained. The phase of the main frequency peak of the free decay signals from the two sensors are compared and the difference is used to calculate the delay between the signals. Various sampling rates are used. Channels of the data acquisition module is swapped to see if the delay between the sensors were related to these channels. Laser beam points are changed to check whether there is torsional modes involved in the decay. For every different run of data acquisition, at least three free decay signals are acquired.

The results are summarised in Figure C.4 and C.5. Overall, Omron-MTI delay is 0.38 ms whose reciprocal is near 2650 Hz. This is 53 times the max motor speed of 3000 rpm or 50 Hz. Therefore, this much of delay is regarded as insignificant.

Table C.5: Selection of spherical plain bearing GE10-UK for rods.

Spherical plain bearing selection for stiffness rods	
Swivel angle	$\beta = 10$ deg
Tilt angle	$\alpha = 5$ deg
Swivel freq: 50 Hz, the closest value	0.5 Hz
Load freq: 50 Hz, the closest value	0.2 Hz
Operating temp	15-30 deg Celcius
Bearing data GE10-UK:	
C_r	8640 N
C_{0r}	21600 N
Sphere dia	d_k =16 mm
Sliding material	PTFE composite
Req rating life	20 hr
F_a	500 N (design)
F_r	20 N (design)
F_a/F_r	25 (desing)
F_a/F_r	0.3 (assumed p39)
F_r	1667 N (assumed)
X axial load factor	2.5 (p.39)
$P = X\ F_r$ combined load	4167.5 N
Specific bearing load	
$p = K\ P/C_r = 100\ 4167.5/8640$	48.23 N/mm^2
Combined swivel&tilt:	
$\beta_1 = \sqrt{\beta^2 + (\alpha_1 + \alpha_2)^2}$	14.14 deg
Swivel motion speed [swivel motion/min]	f=30 (assumed)
Sliding velocity in swivel motion:	
$v = d_k\pi/60e3\ (2\beta\ f/360)$	
$= 16\pi/60e3\ (2\beta\ 30/360)$	1.973-3m/s
Specific frictional energy	
$pv = 48.23\ 1.97e-3$	0.095 (within the range (p50))
Determining the rating life (p55):	
$L_h = K_L/(pv) f_p\ f_v\ f_{pv}\ f_\theta\ f_A\ F_{hz}$	
$= 1000/0.095\ 0.92\ 1\ 1\ 1\ 0.01$	96 hr
Reliability of the rating life (p29)	false
Recommended fit for this use	K7/j6

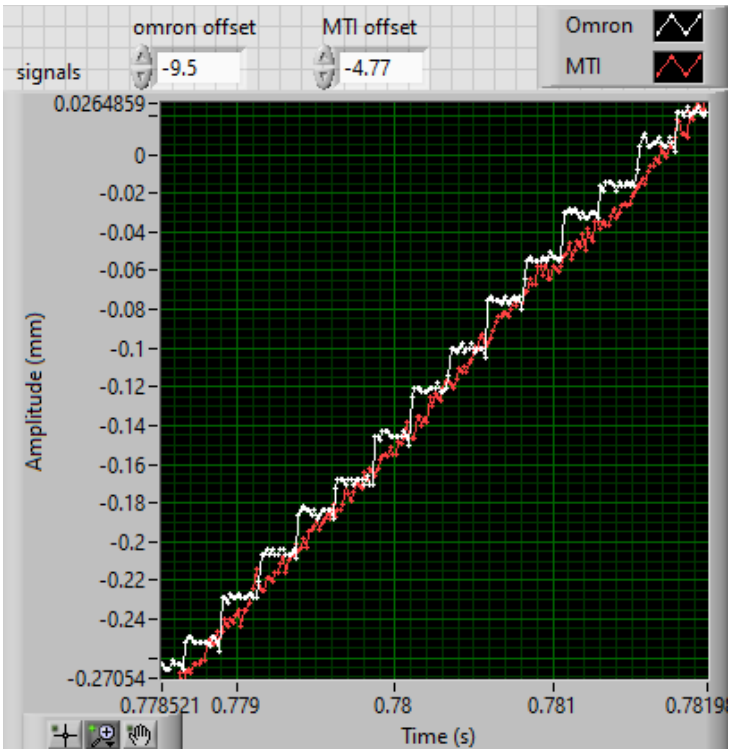


Figure C.3: 60 kHz sampling request from Labview gives away the stepped nature of the Omron signal.

Figure C.3 shows that there is a fundamental difference between the Omron sensors and the MTI sensor, which is the update of the output voltage. Omron sensor seems to update its output voltage around every 0.241 ms (about 4.15 kHz).

During the comparison between the sensors, OG vs OW,

C.4 Campbell plot with the modified test rig values

The modified values resulting in the bifurcation diagram in Figure 7.35b, yields the following Campbell plot: Note, that other modifications such as on the moment of inertia values and the masses are skipped, although it would make the resulting Campbell plot overlapping that of the experimental tapping test more closely. With the modified values, the experimental Campbell plot is less overlapping. However, the cantilever end being not rigid is a fact, as well as the sensitivity of the test rig to the environment (such as the laboratory temperatures). Therefore, as the moment of the data acquisition of the experiment, the Campbell plot must have been more like the one here.

C.5 The global assembly drawing of the test rig

The assembly drawing of the test rig is given in Figure C.7.

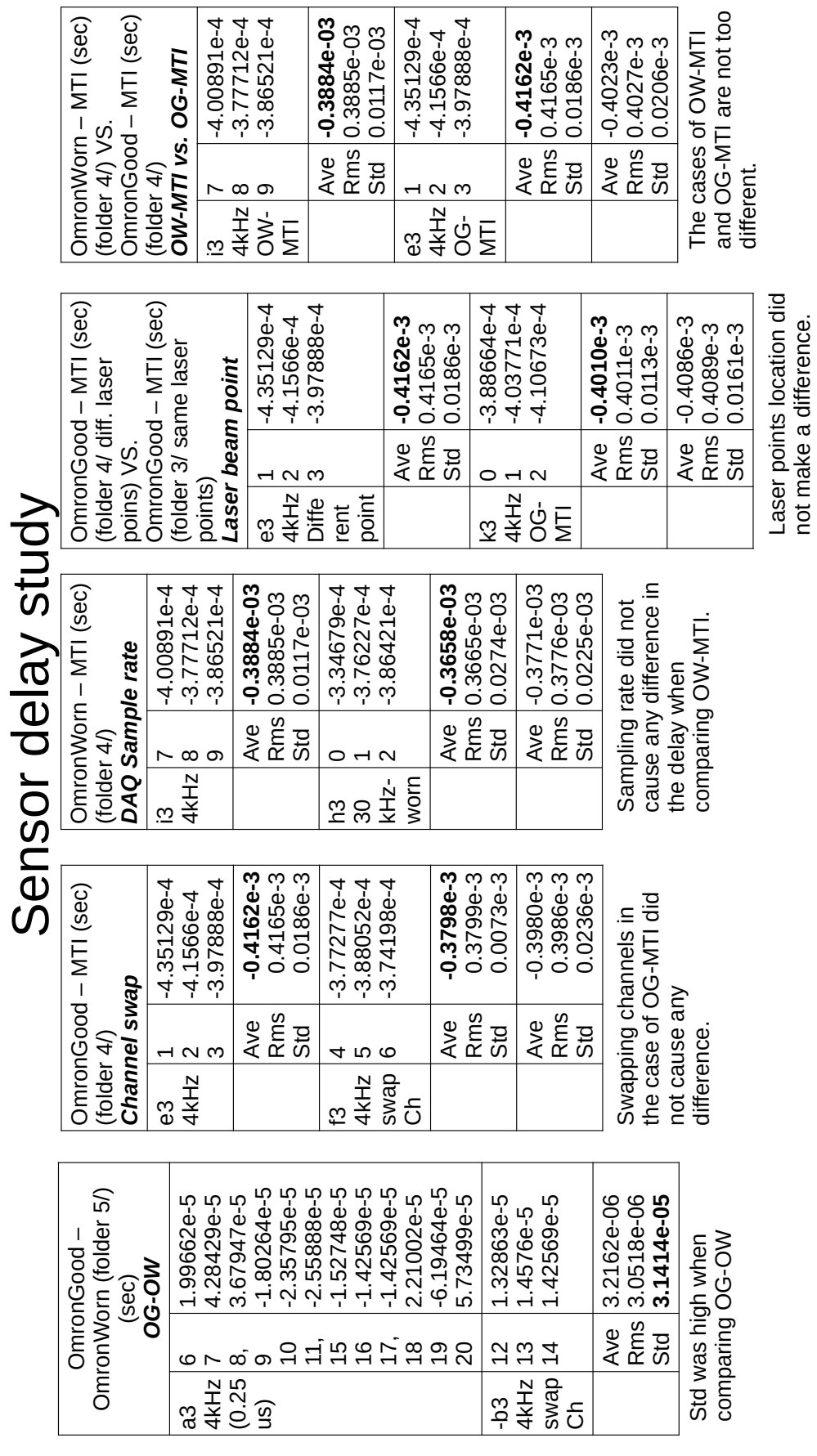


Figure C.4: The results of the sensor delay study: each measurement separately given.

Sensor delay study

OmronGood – OmronWorn (sec) ***OG-OW***		
a3 5/4kHz	6	1.99662e-5
	7	4.28429e-5
	8,	3.67947e-5
	9	-1.80264e-5
	10	-2.35795e-5
	11,	-2.55888e-5
	15	-1.52748e-5
	16	-1.42569e-5
	17,	-1.42569e-5
	18	2.21002e-5
	19	-6.19464e-5
	20	5.73499e-5
-b3 5/4kHz	12	1.32863e-5
	13	1.4576e-5
	14	1.42569e-5
d 5/1kHz	0	-9.48285e-6
C 5/60kHz	1	-4.08294e-5
	Ave	**-1.2170e-07**
	Rms	3.0416e-05
	Std	**3.1352e-05**

Overall, OG-OW delay is insignificant but still the standard deviation is present (31 us).

OmronGood – MTI (sec) ***OG-MTI***		
e3 4/4kHz	1	-4.35129e-4
	2	-4.1566e-4
	3	-3.97888e-4
f3 4/4kHz	4	-3.77277e-4
	5	-3.88052e-4
	6	-3.74198e-4
k3 3/4kHz	0	-3.88664e-4
	1	-4.03771e-4
	2	-4.10673e-4
g3 4/30kHz	0	-3.77277e-4
	1	-3.76803e-4
	2	-3.67539e-4
j 3/1kHz	0	-3.64936e-4
L 3/5kHz	0	-2.54335e-4
M 3/10kHz	0	-3.47033e-4
O 3/60kHz	0	-3.68015e-4
	Ave	**-3.7795e-04**
	Rms	3.7991e-04
	Std	**3.9726e-05**

OmronWorn – MTI (sec) ***OW-MTI***		
i3 4/4k Hz	7	-4.00891e-4
	8	-3.77712e-4
	9	-3.86521e-4
h3 4/30 kHz-worn	0	-3.34679e-4
	1	-3.76227e-4
	2	-3.86421e-4
	Ave	**-0.3771e-03**
	Rms	0.3776e-03
	Std	0.0225e-03

Overall, Omron-MTI delay is 0.38 ms (reciprocal is about 2650 Hz). (Compare to max rotor speed of 50 Hz)

Omron – MTI (sec) ***Omron-MTI***		
E3 4/4kHz	1	-4.35129e-4
	2	-4.15660e-4
	3	-3.97888e-4
F3 4/4kHz	4	-3.77277e-4
	5	-3.88052e-4
	6	-3.74198e-4
K3 3/4kHz	0	-3.88664e-4
	1	-4.03771e-4
	2	-4.10673e-4
G3 4/30kHz	0	-3.77277e-4
	1	-3.76803e-4
	2	-3.67539e-4
J 3/1kHz	0	-3.64936e-4
L 3/5kHz	0	-2.54335e-4
M 3/10kHz	0	-3.47033e-4
O 3/60kHz	0	-3.68015e-4
I3 4/4kHz	7	-4.00891e-4
	8	-3.77712e-4
	9	-3.86521e-4
H3 4/30 kHz-worn	0	-3.34679e-4
	1	-3.76227e-4
	2	-3.86421e-4
	Ave	**-3.7771e-04**
	Rms	3.7929e-04
	Std	3.5334e-05

Figure C.5: The results of the sensor delay study: overall results.

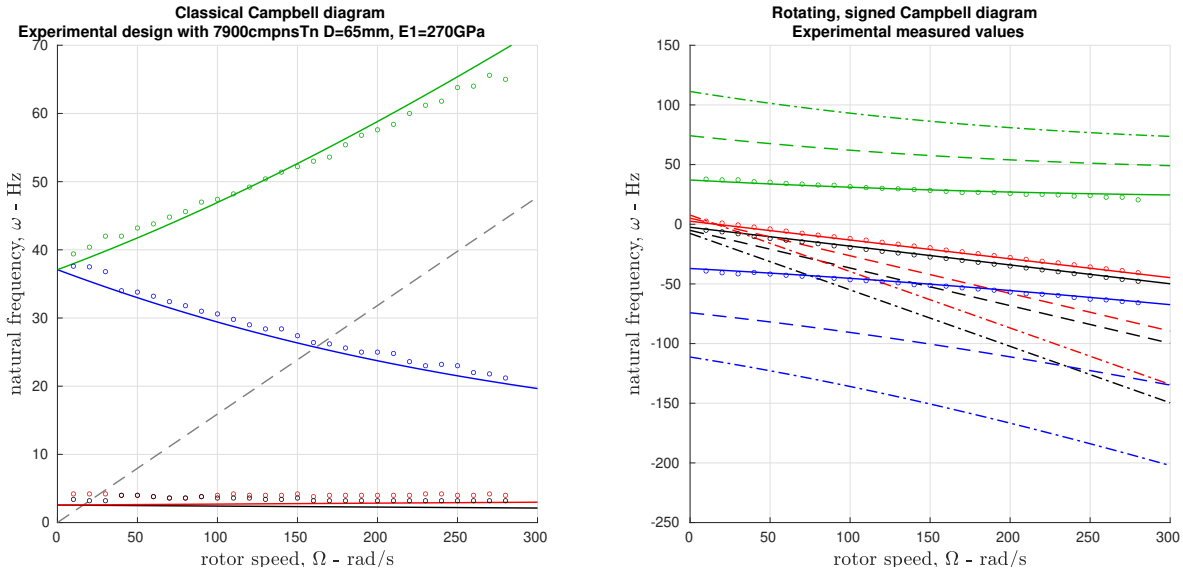


Figure C.6: Campbell diagram with the modified values: E_1 = 270 GPa, $k_{3b} := 0.7\,k_{3b}$ = 109942700 N/m^2, and with the addition of the 7900 bearing's movement compensation as the extra shaft length D = 65 mm. The internal resonance speed are: 48.8 rad/s for $2^1 : 1^1$, 32.5 rad/s for $3^1 : 1^1$, 81.3 rad/s for $3^1 : 2^1$, 188.3 rad/s for $2^1 : 1^2$. (See the accompanying bifurcation diagram in 7.35b)

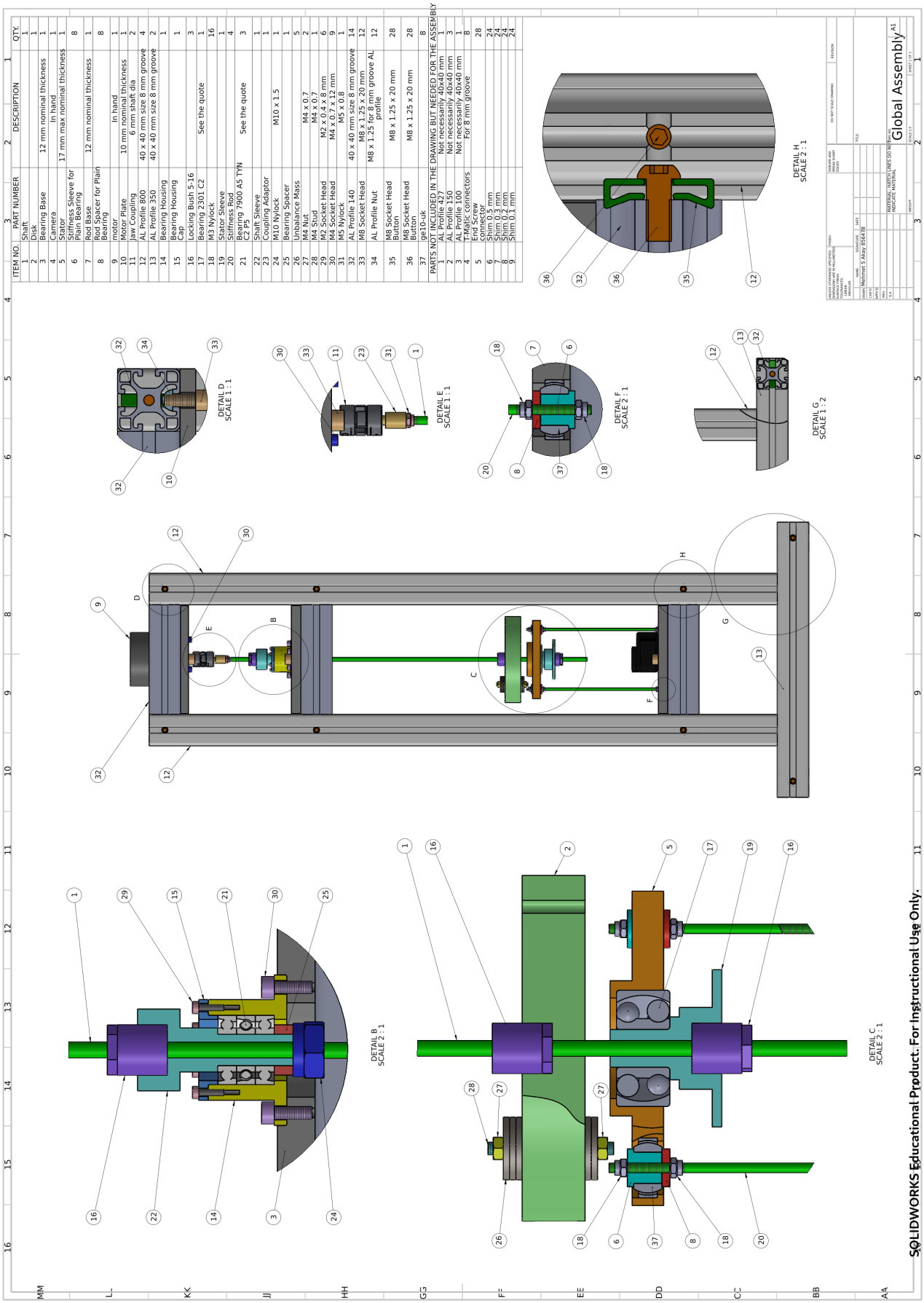


Figure C.7: Global assembly of the test rig.

Bibliography

[1] The Editors of Encyclopaedia Britannica, "Drilling Mud," *Encyclopedia Britannica*, June 2017.

[2] F. F. Ehrich and A. D. Baxter, "Jet Engine," *Encyclopedia Britannica*, Nov. 2024.

[3] A. Zilli, R. J. Williams, and D. J. Ewins, "Nonlinear Dynamics of a Simplified Model of an Overhung Rotor Subjected to Intermittent Annular Rubs," *Journal of Engineering for Gas Turbines and Power*, vol. 137, no. 6, 2015.

[4] A. D. Shaw, A. R. Champneys, and M. I. Friswell, "Asynchronous partial contact motion due to internal resonance in multiple degree-of-freedom rotordynamics," *Proceedings of the Royal Society A: Mathematical, Physical and Engineering Sciences*, vol. 472, p. 20160303, Aug. 2016.

[5] S. S. Rao, *Vibration of Continuous Systems*. Hoboken: John Wiley \& Sons, 2007.

[6] G. Jacquet-Richardet, M. Torkhani, P. Cartraud, F. Thouverez, T. Nouri Baranger, M. Herran, C. Gibert, S. Baguet, P. Almeida, and L. Peletan, "Rotor to stator contacts in turbomachines. Review and application," *Mechanical Systems and Signal Processing*, vol. 40, no. 2, pp. 401–420, 2013.

[7] M. I. Friswell, J. E. T. Penny, S. D. Garvey, and A. W. Lees, *Dynamics of Rotating Machines*. Cambridge University Press, 2010.

[8] G. Genta, *Dynamics of Rotating Systems*. New York: Springer, 2005.

[9] A. Muszynska, *Rotordynamics*. Boca Raton, FL: Taylor Francis Group, LLC, 2005.

[10] S. Ahmad, "Rotor casing contact phenomenon in rotor dynamics-literature survey," *J. Vib. Control*, vol. 16, no. 9, pp. 1369–1377, 2010.

[11] Y. Ishida and T. Yamamoto, *Linear and Nonlinear Rotordynamics: A Modern Treatment with Applications*. Wiley-VCH Verlag GmbH & Co. KGaA, 2012.

[12] G. Adiletta, A. R. Guido, and C. Rossi, "Chaotic motions of a rigid rotor in short journal bearings," *Nonlinear Dyn.*, vol. 10, no. 3, pp. 251–269, 1996.

[13] E. Chipato, A. D. Shaw, and M. I. Friswell, "Effect of gravity-induced asymmetry on the nonlinear vibration of an overhung rotor," *Communications in Nonlinear Science and Numerical Simulation*, vol. 62, pp. 78–89, 2018.

[14] P. Varney and I. Green, "Nonlinear phenomena, bifurcations, and routes to chaos in an asymmetrically supported rotor–stator contact system," *Journal of Sound and Vibration*, vol. 336, pp. 207–226, 2015.

[15] P. Pennacchi, N. Bachschmid, and E. Tanzi, "Light and short arc rubs in rotating machines: Experimental tests and modelling," *Mechanical Systems and Signal Processing*, vol. 23, no. 7, pp. 2205–2227, 2009.

[16] S. Wang, L. Hong, and J. Jiang, "Analytical prediction on stick-slip whirling oscillations induced by dry friction between a rotating imbalanced rotor and a flexibly supported stator," *Journal of Sound and Vibration*, vol. 511, p. 116333, Oct. 2021.

[17] Y. S. Choi, "Investigation on the whirling motion of full annular rotor rub," *Journal of Sound and Vibration*, vol. 258, no. 1, pp. 191–198, 2002.

[18] A. N. Nikiforov, "Simulating the Rolling of a Rotor Over a Stator with Dry Friction Whip and Whirl," *Journal of Friction and Wear*, vol. 46, pp. 61–68, Feb. 2025.

[19] Y. Ishida, M. Inagaki, R. Ejima, and A. Hayashi, "Nonlinear resonances and self-excited oscillations of a rotor caused by radial clearance and collision," *Nonlinear Dynamics*, vol. 57, no. 4, pp. 593–605, 2009.

[20] Y. Ishida, I. Nagasaka, T. Inoue, and S. Lee, "Forced oscillations of a vertical continuous rotor with geometric nonlinearity," *Nonlinear Dynamics*, vol. 11, pp. 107–120, Oct. 1996.

[21] F. Chu and W. Lu, "Experimental observation of nonlinear vibrations in a rub-impact rotor system," *Journal of Sound and Vibration*, vol. 283, no. 3-5, pp. 621–643, 2005.

[22] H. H. El-Mongy, T. A. El-Sayed, V. Vaziri, and M. Wiercigroch, "Nonlinear Dynamics of Whirling Rotor with Asymmetrically Supported Snubber Ring," *Machines*, vol. 12, p. 897, Dec. 2024.

[23] M. Torkhani, L. May, and P. Voinis, "Light, medium and heavy partial rubs during speed transients of rotating machines: Numerical simulation and experimental observation," *Mechanical Systems and Signal Processing*, vol. 29, pp. 45–66, 2012.

[24] A. Paiva, R. V. Moreira, A. Brandão, and M. A. Savi, "Nonlinear dynamics of a rotor–stator system with contacts," *Nonlinear Dynamics*, vol. 111, pp. 11753–11772, July 2023.

[25] H. Wang, X. Shen, T. Zhou, J. Sun, and G. Chen, "Effects of contact stiffness on the nonlinear motions induced by impacts on an overhung rotor system," *Communications in Nonlinear Science and Numerical Simulation*, vol. 138, p. 108216, Nov. 2024.

[26] A. Muszynska and P. Goldman, "Chaotic responses of unbalanced rotor/bearing/stator systems with looseness or rubs," *Chaos Solitons Fractals*, vol. 5, no. 9, pp. 1683–1704, 1995.

[27] X. Dai, Z. Jin, and X. Zhang, "Dynamic Behavior of the Full Rotorstop Rubbing: Numerical Simulation and Experimental Verification," *Journal of Sound and Vibration*, vol. 251, no. 5, pp. 807–822, 2002.

[28] D. E. Bently, J. J. Yu, P. Goldman, and A. Musynska, "Full annular rub in mechanical seals, Part I: Experimental results," *International Journal of Rotating Machinery*, vol. 8, no. 5, pp. 319–328, 2002.

[29] A. R. Bartha, *Dry Friction Backward Whirl of Rotors*. Doctoral Thesis, Swiss Federal Institute of Technology, 2000.

[30] A. D. Shaw, A. R. Champneys, and M. I. Friswell, "Normal form analysis of bouncing cycles in isotropic rotor stator contact problems," *International Journal of Mechanical Sciences*, vol. 155, pp. 83–97, 2019.

[31] E. Chipato, A. D. Shaw, and M. I. Friswell, "Frictional effects on the nonlinear dynamics of an overhung rotor," *Communications in Nonlinear Science and Numerical Simulation*, vol. 78, 2019.

[32] E. T. Chipato, A. D. Shaw, M. I. Friswell, and R. Sánchez Crespo, "Experimental Study of Rotor-Stator Contact Cycles," *Journal of Sound and Vibration*, vol. 502, 2021.

[33] P. S. Keogh and M. O. T. Cole, "Rotor vibration with auxiliary bearing contact in magnetic bearing systems part 1: Synchronous dynamics," *Proceedings of the Institution of Mechanical Engineers, Part C: Journal of Mechanical Engineering Science*, vol. 217, no. 4, pp. 377–392, 2003.

[34] M. O. T. Cole and P. S. Keogh, "Asynchronous periodic contact modes for rotor vibration within an annular clearance," *Proceedings of the Institution of Mechanical Engineers, Part C: Journal of Mechanical Engineering Science*, vol. 217, no. 10, pp. 1101–1115, 2003.

[35] P. Yu, Y. Ma, J. Hong, and G. Chen, "Application of complex nonlinear modes to determine dry whip motion in a rubbing rotor system," *Chinese Journal of Aeronautics*, vol. 34, no. 1, pp. 209–225, 2021.

[36] B. Saldivar, I. Boussaada, H. Mounier, S. Mondié, and S. Niculescu, "An overview on the modeling of oilwell drilling vibrations," in *IFAC Proceedings Volumes*, vol. 47, pp. 5169–5174, 2014.

[37] A. AlZibdeh, M. AlQaradawi, and B. Balachandran, "Effects of high frequency drive speed modulation on rotor with continuous stator contact," *International Journal of Mechanical Sciences*, vol. 131–132, pp. 559–571, 2017.

[38] D. R. Stroud, L. A. Lines, and D. J. Minett-Smith, "Analytical and Experimental Backward Whirl Simulations for Rotary Steerable Bottom Hole Assemblies," in *SPE/IADC Drilling Conference and Exhibition*, OnePetro, Mar. 2011.

[39] H. F. de Castro, K. L. Cavalca, and R. Nordmann, "Whirl and whip instabilities in rotor-bearing system considering a nonlinear force model," *Journal of Sound and Vibration*, vol. 317, no. 1-2, pp. 273–293, 2008.

[40] D. C. Johnson, "Synchronous Whirl of a Vertical Shaft Having Clearance in One Bearing," *Journal of Mechanical Engineering Science*, vol. 4, no. 1, pp. 85–93, 1962.

[41] F. F. Ehrich, "The Dynamic Stability of Rotor/Stator Radial Rubs in Rotating Machinery," *Journal of Engineering for Industry*, vol. 91, no. 4, pp. 1025–1028, 1969.

[42] F. F. Ehrich and J. J. O'Connor, "Stator whirl with rotors in bearing clearance," *Journal of Engineering for Industry*, pp. 381–389, 1967.

[43] H. F. Black, "Interaction of a Whirling Rotor with a Vibrating Stator across a Clearance Annulus," *Journal of Mechanical Engineering Science*, vol. 10, no. 1, pp. 1–12, 1968.

[44] F. F. Ehrich, "Observations of Nonlinear Phenomena in Rotordynamics," *Journal of System Design and Dynamics*, vol. 2, no. 3, pp. 641–651, 2008.

[45] K. Mora, A. R. Champneys, A. D. Shaw, and M. I. Friswell, "Explanation of the onset of bouncing cycles in isotropic rotor dynamics; a grazing bifurcation analysis," *Proceedings of the Royal Society A: Mathematical, Physical and Engineering Sciences*, vol. 476, p. 20190549, May 2020.

[46] E. V. Karpenko, M. Wiercigroch, E. E. Pavlovskaia, and M. P. Cartmell, "Piecewise approximate analytical solutions for a Jeffcott rotor with a snubber ring," *International Journal of Mechanical Sciences*, vol. 44, no. 3, pp. 475–488, 2002.

[47] E. E. Pavlovskaia, E. V. Karpenko, and M. Wiercigroch, "Non-linear dynamic interactions of a Jeffcott rotor with preloaded snubber ring," *Journal of Sound and Vibration*, vol. 276, no. 1-2, pp. 361–379, 2004.

[48] E. V. Karpenko, M. Wiercigroch, E. E. Pavlovskaia, and R. D. Neilson, "Experimental verification of Jeffcott rotor model with preloaded snubber ring," *Journal of Sound and Vibration*, vol. 298, no. 4-5, pp. 907–917, 2006.

[49] N. A. Saeed, E. M. Awwad, A. Maarouf, H. M. H. Farh, F. A. Alturki, and J. Awrejcewicz, "Rub-Impact Force Induces Periodic, Quasiperiodic, and Chaotic Motions of a Controlled Asymmetric Rotor System," *Shock and Vibration*, vol. 2021, no. 1, p. 1800022, 2021.

[50] D. Yoshimori, Y. Sugawara, and M. Takeda, "Bifurcation shifts in a rotor-stator contact system under frictional forces to higher rotational speeds caused by stator thickness," *Mechanical Engineering Journal*, vol. advpub, 2025.

[51] A. Kartheek and K. Vijayan, "Stochastic finite element analysis using polynomial chaos on a flexible rotor with contact nonlinearity," *Nonlinear Dynamics*, vol. 112, pp. 11299–11311, July 2024.

[52] G. A. F. Taher, E.-A. Rabeih, and H. H. El-Mongy, "Experimental and numerical study of lateral vibration of a rotor–stator rubbing system," *International Journal of Dynamics and Control*, vol. 12, pp. 3139–3154, Sept. 2024.

[53] Y. Briend, E. Chatelet, R. Dufour, M.-A. Andrianoely, F. Legrand, G. Fiore, and G. Pampolini, "Nonlinear dynamics of a rotor supported by hydrodynamic bearings and ball bearings with loose fit when passing through a critical speed," *Mechanical Systems and Signal Processing*, vol. 210, p. 111146, Mar. 2024.

[54] E. V. Karpenko, M. Wiercigroch, and M. P. Cartmell, "Regular and chaotic dynamics of a discontinuously nonlinear rotor system," *Chaos Solitons Fractals*, vol. 13, no. 6, pp. 1231–1242, 2002.

[55] I. Nagasaka, Y. Ishida, and J. Liu, "Forced Oscillations of a Continuous Asymmetrical Rotor With Geometric Nonlinearity (Major Critical Speed and Secondary Critical Speed)," *Journal of Vibration and Acoustics*, vol. 130, no. 3, 2008.

[56] S. Hosseini and S. Khadem, "Combination resonances in a rotating shaft," *Mechanism and Machine Theory*, vol. 44, no. 8, pp. 1535–1547, 2009.

[57] Y. Ishida, I. Nagasaka, T. Inoue, and S. W. Lee, "Forced Oscillations of a Continuous Rotor with Nonlinear Spring Characteristics (Vertical Shaft with Geometric

Nonlinearity)," *Transactions of the Japan Society of Mechanical Engineers Series C*, 1994.

[58] I. Nagasaka, J. Liu, Y. Ishida, and K. Katou, "Forced oscillations of a continuous rotor with strong geometric nonlinearity (separation of resonance point by effect of gravity and axial force)," *Nippon Kikai Gakkai Ronbunshu, C Hen/Transactions of the Japan Society of Mechanical Engineers, Part C*, 2002.

[59] C. Fu, Z. Zheng, W. Zhu, K. Lu, and Y. Yang, "Non-intrusive frequency response analysis of nonlinear systems with interval uncertainty: A comparative study," *Chaos, Solitons & Fractals*, vol. 165, p. 112815, Dec. 2022.

[60] D. Y. Yang, J. L. Huang, and W. D. Zhu, "Nonlinear dynamics of a misaligned and eccentric rotor system with three base motions," *Applied Mathematical Modelling*, vol. 148, p. 116240, Dec. 2025.

[61] R. Alcorta, B. Chouvion, and O. Montagnier, "Dynamics of a non-linear Jeffcott rotor in supercritical regime," *International Journal of Non-Linear Mechanics*, vol. 148, p. 104272, Jan. 2023.

[62] Z. Zheng, C. Fu, W. Zhu, J. Zhao, K. Zhang, and K. Lu, "A non-intrusive frequency normalisation approach for uncertain response analysis of nonlinear dynamic systems," *Mechanical Systems and Signal Processing*, vol. 188, p. 110005, Apr. 2023.

[63] E. T. Chipato, A. D. Shaw, and M. I. Friswell, "Nonlinear rotordynamics of a MDOF rotor–stator contact system subjected to frictional and gravitational effects," *Mechanical Systems and Signal Processing*, vol. 159, 2021.

[64] S. Lahriri, H. I. Weber, I. F. Santos, and H. Hartmann, "Rotor–stator contact dynamics using a non-ideal drive—Theoretical and experimental aspects," *Journal of Sound and Vibration*, vol. 331, no. 20, pp. 4518–4536, 2012.

[65] C. Wang, D. Zhang, Y. Ma, Z. Liang, and J. Hong, "Theoretical and experimental investigation on the sudden unbalance and rub-impact in rotor system caused by blade off," *Mechanical Systems and Signal Processing*, vol. 76–77, pp. 111–135, 2016.

[66] K. Prabith and I. R. Praveen Krishna, "Response and stability analysis of a two-spool aero-engine rotor system undergoing multi-disk rub-impact," *International Journal of Mechanical Sciences*, vol. 213, pp. 1–24, 2022.

[67] K. Prabith and I. R. Praveen Krishna, "A Time Variational Method for the Approximate Solution of Nonlinear Systems Undergoing Multiple-Frequency Excitations," *Journal of Computational and Nonlinear Dynamics*, vol. 15, Jan. 2020.

[68] A. N. Nikiforov, "Rotor-to-Stator Friction Simulation with Nonconstant Stiffness of the Contact Surfaces and Small Clearance between Them," *Journal of Friction and Wear*, vol. 44, pp. 178–188, June 2023.

[69] S. Hosseini and S. Khadem, "Free vibrations analysis of a rotating shaft with nonlinearities in curvature and inertia," *Mechanism and Machine Theory*, vol. 44, no. 1, pp. 272–288, 2009.

[70] M. S. Qaderi, S. A. A. Hosseini, and M. Zamanian, "Combination resonance of nonlinear rotating balanced shafts subjected to periodic axial load," *Journal of Solid Mechanics*, vol. 10, no. 2, pp. 249–262, 2018.

[71] R. Seydel, *From Equilibrium to Chaos: Practical Bifurcation and Stability Analysis*. New York: Elsevier, 1988.

[72] P. Sundararajan and S. T. Noah, "An algorithm for response and stability of large order non-linear systems - Application to rotor systems," *J. Sound Vib.*, vol. 214, no. 4, pp. 695–723, 1998.

[73] M. K. Al-Solihat and K. Behdinan, "Force transmissibility and frequency response of a flexible shaft–disk rotor supported by a nonlinear suspension system," *International Journal of Non-Linear Mechanics*, vol. 124, 2020.

[74] G. Von Groll and D. J. Ewins, "The Harmonic Balance Method with Arc-Length Continuation in Rotor/Stator Contact Problems," *Journal of Sound and Vibration*, vol. 241, no. 2, pp. 223–233, 2001.

[75] L. Peletan, S. Baguet, G. Jacquet-Richardet, and M. Torkhani, "Use and Limitations of the Harmonic Balance Method for Rub-Impact Phenomena in Rotor-Stator Dynamics," in *ASME Turbo Expo 2012: Turbine Technical Conference and Exposition*, pp. 647–655, American Society of Mechanical Engineers Digital Collection, July 2013.

[76] L. Peletan, S. Baguet, M. Torkhani, and G. Jacquet-Richardet, "Quasi-periodic harmonic balance method for rubbing self-induced vibrations in rotor–stator dynamics," *Nonlinear Dynamics*, vol. 78, no. 4, pp. 2501–2515, 2014.

[77] L. Peletan, S. Baguet, M. Torkhani, and G. Jacquet-Richardet, "A comparison of stability computational methods for periodic solution of nonlinear problems with application to rotordynamics," *Nonlinear Dynamics*, vol. 72, no. 3, pp. 671–682, 2013.

[78] L. Salles, B. Staples, N. Hoffmann, and C. Schwingshackl, "Continuation techniques for analysis of whole aeroengine dynamics with imperfect bifurcations and isolated solutions," *Nonlinear Dynamics*, vol. 86, no. 3, pp. 1897–1911, 2016.

[79] R. M. Rosenberg, "The Normal Modes of Nonlinear n-Degree-of-Freedom Systems," *Journal of Applied Mechanics*, vol. 29, no. 1, pp. 7–14, 1962.

[80] D. Laxalde and F. Thouverez, "Complex non-linear modal analysis for mechanical systems: Application to turbomachinery bladings with friction interfaces," *Journal of Sound and Vibration*, vol. 322, no. 4-5, pp. 1009–1025, 2009.

[81] F. Chu and W. Lu, "Stiffening effect of the rotor during the rotor-to-stator rub in a rotating machine," *Journal of Sound and Vibration*, vol. 308, no. 3-5, pp. 758–766, 2007.

[82] Z. C. Feng and X.-Z. Zhang, "Rubbing phenomena in rotor–stator contact," *Chaos, Solitons & Fractals*, vol. 14, pp. 257–267, Aug. 2002.

[83] A. B. Nordmark and P. T. Piiroinen, "Simulation and stability analysis of impacting systems with complete chattering," *Nonlinear Dynamics*, vol. 58, no. 1-2, pp. 85–106, 2009.

[84] E. J. Doedel and B. E. Oldeman, "AUTO-07P: Continuation and Bifurcation Software for Ordinary Differential Equations," 2019.

[85] G. H. M. van der Heijden, "Mode-locking in nonlinear rotordynamics," *Journal of nonlinear science*, vol. 5, no. 3, pp. 257–283, 1995.

[86] Y. Cao, H. Yao, Q. Li, P. Yang, and B. Wen, "Vibration mitigation and dynamics of a rotor-blade system with an attached nonlinear energy sink," *International Journal of Non-Linear Mechanics*, vol. 127, 2020.

[87] H. Yao, Y. Cao, Z. Ding, and B. Wen, "Using grounded nonlinear energy sinks to suppress lateral vibration in rotor systems," *Mechanical Systems and Signal Processing*, vol. 124, pp. 237–253, 2019.

[88] H. Zhang, K. Lu, W. Zhang, and C. Fu, "Investigation on dynamic behaviors of rotor system with looseness and nonlinear supporting," *Mechanical Systems and Signal Processing*, vol. 166, 2022.

[89] Y. Zhang, Liu Suixian, L. Xiang, and A. Hu, "Dynamic analysis of a multi-disk rod fastening rotor system with rub-impact based on multiple parameters," *Nonlinear Dynamics*, vol. 107, pp. 2133–2152, Feb. 2022.

[90] Y. Li, T. Long, W. Wu, C. Wen, and Z. Zhu, "Vibration characteristics of a bolted joint rotor-bearing system with rubbing and pedestal looseness coupled fault: Simulation and experiment," *Applied Mathematical Modelling*, vol. 132, pp. 402–427, Aug. 2024.

[91] Y. Li, Z. Zhu, C. Wen, K. Liu, Z. Luo, and T. Long, "Rub-impact dynamic analysis of a dual-rotor system with bolted joint structure: Theoretical and experimental investigations," *Mechanical Systems and Signal Processing*, vol. 209, p. 111144, Mar. 2024.

[92] Y. Zhang, H. Xu, Y. Zhao, Y. Lü, X. Yang, and L. Xiong, "The modeling and experiment study on temperature characteristics of the rub-impact of titanium alloy rotor-stator system," *International Journal of Non-Linear Mechanics*, vol. 171, p. 105036, Apr. 2025.

[93] C. Jacobs, F. Thouverez, M. Legrand, and P. Almeida, "Thermomechanical transient dynamics of radial rotor–stator contact," *Journal of Sound and Vibration*, vol. 617, p. 119207, Nov. 2025.

[94] H. Kou, Y. Shi, J. Du, Z. Zhu, F. Zhang, F. Liang, and L. Zeng, "Rub-impact dynamic analysis of a rotor with multiple wide-chord blades under the gyroscopic effect and geometric nonlinearity," *Mechanical Systems and Signal Processing*, vol. 168, 2022.

[95] W. Pan, L. Ling, H. Qu, and M. Wang, "Nonlinear response analysis of aero-engine rotor bearing rub-impact system caused by horizontal yawing maneuver load," *International Journal of Non-Linear Mechanics*, vol. 137, 2021.

[96] M. Legrand, C. Pierre, P. Cartraud, and J.-P. Lombard, "Two-dimensional modeling of an aircraft engine structural bladed disk-casing modal interaction," *Journal of Sound and Vibration*, vol. 319, no. 1-2, pp. 366–391, 2009.

[97] E. Delhez, F. Nyssen, J.-C. Golinval, and A. Batailly, "Reduced order modeling of blades with geometric nonlinearities and contact interactions," *Journal of Sound and Vibration*, vol. 500, p. 116037, May 2021.

[98] F. Nyssen, Y. Colaïtis, and A. Batailly, "Numerical investigation of a mistuned industrial bladed disk dynamics with structural contacts using time and frequency methods," *Journal of Sound and Vibration*, vol. 535, p. 117077, Sept. 2022.

[99] X. Song, Z. Chai, C. Wang, Q. Han, and X. Hao, "Vibration performance of rotating thin-walled cylindrical shell with tip-rubbing excitation between drum and stator vane segment of aero-engine," *Journal of Sound and Vibration*, vol. 525, p. 116759, May 2022.

[100] F. Thiery and P. Chandran, "On the operational similarities of bladed rotor vibrations with casing contacts," *International Journal of System Assurance Engineering and Management*, Aug. 2024.

[101] T. Zhou, Y. Jia, L. Zou, Z. Jiang, W. Wang, and M. Hu, "Vibration characteristics of blade-casing rubbing fault considering rotor–stator coupling," *Mechanical Systems and Signal Processing*, vol. 218, p. 111589, Sept. 2024.

[102] Y. Qv, Z. Chang, N. Wang, and T. Han, "Experimental and theoretical investigation on casing vibration for dual-rotor-support-casing system with rotor-casing rub," *Journal of Vibration and Control*, p. 10775463251325060, Mar. 2025.

[103] C. A. L. L. Fonseca, I. F. Santos, and H. I. Weber, "Experimental comparison of the nonlinear dynamic behavior of a rigid rotor interacting with two types of different radial backup bearings: Ball & pinned," *Tribology International*, vol. 119, pp. 250–261, 2018.

[104] C. A. Fonseca, I. F. Santos, and H. I. Weber, "Influence of unbalance levels on nonlinear dynamics of a rotor-backup rolling bearing system," *Journal of Sound and Vibration*, vol. 394, pp. 482–496, 2017.

[105] C. Jarroux, J. Mahfoud, R. Dufour, F. Legrand, B. Defoy, and T. Alban, "Investigations on the dynamic behaviour of an on-board rotor-AMB system with touchdown bearing contacts: Modelling and experimentation," *Mechanical Systems and Signal Processing*, vol. 159, p. 107787, Oct. 2021.

[106] H. Kou, C. Xu, J. Du, T. Zhang, Z. Zhu, and L. Zeng, "Multilocation-rub-impact behaviors of a magnetic-levitation bladed rotor with magnetic saturation nonlinearity," *Applied Mathematical Modelling*, vol. 138, p. 115827, Feb. 2025.

[107] V. M. Zaccardo and G. D. Buckner, "Active magnetic dampers for controlling lateral rotor vibration in high-speed rotating shafts," *Mechanical Systems and Signal Processing*, vol. 152, p. 107445, May 2021.

[108] B. X. Tchomeni and A. Alugongo, "Vibrations of Misaligned Rotor System with Hysteretic Friction Arising from Driveshaft–Stator Contact under Dispersed Viscous Fluid Influences," *Applied Sciences*, vol. 11, no. 17, p. 8089, 2021.

[109] D. F. Sozinando, B. X. Tchomeni, and A. A. Alugongo, "Experimental Study of Coupled Torsional and Lateral Vibration of Vertical Rotor-to-Stator Contact in an Inviscid Fluid," *Mathematical and Computational Applications*, vol. 28, p. 44, Apr. 2023.

[110] X.-M. Liu, J. Jiang, and L. Hong, "A numerical method to solve a fuzzy differential equation via differential inclusions," *Fuzzy Sets and Systems*, vol. 404, pp. 38–61, Feb. 2021.

[111] J. Cao, C. Ma, Z. Jiang, and S. Liu, "Nonlinear dynamic analysis of fractional order rub-impact rotor system," *Communications in Nonlinear Science and Numerical Simulation*, vol. 16, no. 3, pp. 1443–1463, 2011.

[112] Y. Yang, J. Tang, G. Chen, Y. Yang, and D. Cao, "Rub-Impact Investigation of a Single-Rotor System Considering Coating Effect and Coating Hardness," *Journal of Vibration Engineering & Technologies*, vol. 9, pp. 491–505, Apr. 2021.

[113] H. Cheng, G. Ma, X. Li, Y. Cui, and Z. Shang, "Nonlinear dynamic response and load distribution of coupled fault complex dual-disk rotor-bearing system," *Nonlinear Dynamics*, July 2025.

[114] A. H. Nayfeh and B. Balachandran, "Quasiperiodic solutions," in *Applied Nonlinear Dynamics: Analytical, Computational, and Experimental Methods*, ch. 4, pp. 231–275, John Wiley & Sons, Ltd, 1995.

[115] M. Lakshmanan and K. Murali, *Chaos in Nonlinear Oscillators Controlling and Synchronization*. World Scientific Series on Nonlinear Science. Series A, Monographs and Treatises; Vol. 13, Singapore: World Scientific Pub. Co, 1996.

[116] L. Renson, G. Kerschen, and B. Cochelin, "Numerical computation of nonlinear normal modes in mechanical engineering," *Journal of Sound and Vibration*, vol. 364, pp. 177–206, Mar. 2016.

[117] G. Kerschen, M. Peeters, J. C. Golinval, and A. F. Vakakis, "Nonlinear normal modes, Part I: A useful framework for the structural dynamicist," *Mechanical Systems and Signal Processing*, vol. 23, no. 1, pp. 170–194, 2009.

[118] M. Peeters, R. Viguié, G. Sérandour, G. Kerschen, and J. C. Golinval, "Nonlinear normal modes, Part II: Toward a practical computation using numerical continuation techniques," *Mechanical Systems and Signal Processing*, vol. 23, no. 1, pp. 195–216, 2009.

[119] A. H. Nayfeh, *Nonlinear Interactions: Analytical, Computational, and Experimental Methods*. New York: Wiley, 2000.

[120] S. Shaw and C. Pierre, "Normal modes for non-linear vibratory systems," *Journal of Sound and Vibration*, vol. 164, no. 1, pp. 85–124, 1993.

[121] E. Pesheck, C. Pierre, and S. W. Shaw, "A New Galerkin-Based Approach for Accurate Non-Linear Normal Modes through Invariant Manifolds," *Journal of Sound and Vibration*, vol. 249, no. 5, pp. 971–993, 2002.

[122] E. Pesheck, *Reduced Order Modeling of Nonlinear Structural Systems Using Nonlinar Normal Modes and Invariant Manifold*. PhD thesis, The University of Michigan, 2000.

[123] E. Pesheck, C. Pierre, and S. W. Shaw, "Modal reduction of a nonlinear rotating beam through nonlinear normal modes*," *Journal of Vibration and Acoustics*, vol. 124, pp. 229–236, Mar. 2002.

[124] D. Liu and J. Hong, "Failure analysis of backward whirl motion in an aero-engine rotor," *Engineering Failure Analysis*, vol. 128, 2021.

[125] J. Hong, P. Yu, D. Zhang, and Y. Ma, "Nonlinear dynamic analysis using the complex nonlinear modes for a rotor system with an additional constraint due to rub-impact," *Mechanical Systems and Signal Processing*, vol. 116, pp. 443–461, 2019.

[126] T. Wang and Q. Ding, "Modal balancing for ball bearing-rotor system using nonlinear normal modes," *Journal of Sound and Vibration*, vol. 547, p. 117507, 2023.

[127] Y. Ishida, "Review of Research on Nonlinear Rotordynamics in Japan," *Journal of System Design and Dynamics*, vol. 7, no. 2, pp. 151–169, 2013.

[128] M. F. A. Azeez and A. F. Vakakis, "Numerical and experimental analysis of a continuous overhung rotor undergoing vibro-impacts," *International Journal of Non-Linear Mechanics*, vol. 34, no. 3, pp. 415–435, 1999.

[129] F. Cong, J. Chen, G. Dong, and K. Huang, "Experimental validation of impact energy model for the rub–impact assessment in a rotor system," *Mechanical Systems and Signal Processing*, vol. 25, no. 7, pp. 2549–2558, 2011.

[130] H. Diangui, "Experiment on the characteristics of torsional vibration of rotor-to-stator rub in turbomachinery," *Tribology International*, vol. 33, pp. 75–79, Feb. 2000.

[131] L. Yang, X. Chen, S. Wang, and H. Zuo, "Rub-Impact Detection of Rotor Systems Using Time-Frequency Techniques," in *ASME 2016 International Mechanical Engineering Congress and Exposition*, American Society of Mechanical Engineers Digital Collection, Feb. 2017.

[132] H. Bing, B. Chen, L. Xiang, A. Hu, and K. Chen, "Dynamic simulation and experimental study of dual-rotor system induced by rub-impact fault with variable state and parameter," *Engineering Research Express*, vol. 7, p. 015353, Feb. 2025.

[133] U. Ehehalt, O. Alber, R. Markert, and G. Wegener, "Experimental observations on rotor-to-stator contact," *Journal of Sound and Vibration*, vol. 446, pp. 453–467, 2019.

[134] B. Nevada, "RK 4 Model Rotor Kit Datasheet - 141592," 2023.

[135] H. C. Piccoli and H. I. Weber, "Experimental Observation of Chaotic Motion in a Rotor with Rubbing," *Nonlinear Dynamics*, vol. 16, pp. 55–70, May 1998.

[136] K. Nam and S. Lee, "Diagnosis of rotating machines by utilizing a backpropagation neural net," in *And Automation Proceedings of the 1992 International Conference on Industrial Electronics, Control, Instrumentation*, pp. 1064–1067 vol.2, Nov. 1992.

[137] S. W. Shaw, "Chaotic dynamics of a slender beam rotating about its longitudinal axis," *Journal of Sound and Vibration*, vol. 124, pp. 329–343, June 1988.

[138] F. Chu and Z. Zhang, "Periodic, quasi-periodic and chaotic vibrations of a rub-impact rotor system supported on oil film bearings," *International Journal of Engineering Science*, vol. 35, pp. 963–973, Aug. 1997.

[139] F. F. Ehrich, "Some Observations of Chaotic Vibration Phenomena in High-Speed Rotordynamics," *Journal of Vibration and Acoustics*, vol. 113, pp. 50–57, Jan. 1991.

[140] Y. Ishida, I. Nagasaka, and S. Lee, "Forced oscillations of a continuous rotor with geometric nonlinearity (Subharmonic resonances of order 1/2 and internal resonance)," *Nippon Kikai Gakkai Ronbunshu, C Hen/Transactions of the Japan Society of Mechanical Engineers, Part C*, 1996.

[141] M. A. Fumagalli, "Modelling and measurement analysis of the contact interaction between a high speed rotor and its stator," 1997.

[142] G. X. Li and M. P. Païdoussis, "Impact phenomena of rotor-casing dynamical systems," *Nonlinear Dynamics*, vol. 5, no. 1, pp. 53–70, 1994.

[143] Z. Shang, J. Jiang, and L. Hong, "The global responses characteristics of a rotor/stator rubbing system with dry friction effects," *Journal of Sound and Vibration*, vol. 330, no. 10, pp. 2150–2160, 2011.

[144] N. Q. Hu and X. S. Wen, "Chaotic behaviour identification of a rub-impact rotor using short-term predictability of measured data," *Proceedings of the Institution of Mechanical Engineers, Part C: Journal of Mechanical Engineering Science*, vol. 216, pp. 675–681, June 2002.

[145] S. Chen, Y. Yang, Z. Peng, S. Wang, W. Zhang, and X. Chen, "Detection of rub-impact fault for rotor-stator systems: A novel method based on adaptive chirp mode decomposition," *Journal of Sound and Vibration*, vol. 440, pp. 83–99, Feb. 2019.

[146] S. Chen, X. Dong, Z. Peng, W. Zhang, and G. Meng, "Nonlinear Chirp Mode Decomposition: A Variational Method," *IEEE Transactions on Signal Processing*, vol. 65, pp. 6024–6037, Nov. 2017.

[147] Z. Peng, Y. He, Q. Lu, and F. Chu, "Feature Extraction of the Rub-Impact Rotor System by Means of Wavelet Analysis," *Journal of Sound and Vibration*, vol. 259, no. 4, pp. 1000–1010, 2003.

[148] Q. Wang and F. Chu, "Experimental Determination of the Rubbing Location by Means of Acoustic Emission and Wavelet Transform," *Journal of Sound and Vibration*, vol. 248, no. 1, pp. 91–103, 2001.

[149] J. Sieber and B. Krauskopf, "Control based bifurcation analysis for experiments," *Nonlinear Dynamics*, vol. 51, pp. 365–377, Feb. 2008.

[150] D. A. W. Barton, B. P. Mann, and S. G. Burrow, "Control-based continuation for investigating nonlinear experiments," *Journal of Vibration and Control*, vol. 18, no. 4, pp. 509–520, 2011.

[151] D. A. Barton and J. Sieber, "Systematic experimental exploration of bifurcations with noninvasive control," *Phys Rev E Stat Nonlin Soft Matter Phys*, vol. 87, p. 052916, May 2013.

[152] D. A. W. Barton, "Control-based continuation: Bifurcation and stability analysis for physical experiments," *Mechanical Systems and Signal Processing*, vol. 84, pp. 54–64, 2017.

[153] L. Renson, A. Gonzalez-Buelga, D. Barton, and S. Neild, "Robust identification of backbone curves using control-based continuation," *Journal of Sound and Vibration*, vol. 367, pp. 145–158, 2016.

[154] L. Renson, A. Shaw, D. Barton, and S. Neild, "Application of control-based continuation to a nonlinear structure with harmonically coupled modes," *Mechanical Systems and Signal Processing*, vol. 120, pp. 449–464, 2019.

[155] H. Xu, P. Wang, Y. Yang, H. Ma, Z. Luo, Q. Han, and B. Wen, "Effects of supporting stiffness of deep groove ball bearings with raceway misalignment on vibration behaviors of a gear-rotor system," *Mechanism and Machine Theory*, vol. 177, p. 105041, Nov. 2022.

[156] MathWorks, "Matlab." The MathWorks Inc., 2020.

[157] J. R. Dormand and P. J. Prince, "A family of embedded Runge-Kutta formula," *Journal of Computational and Applied Mathematics*, vol. 6, no. 1, pp. 19–26, 1980.

[158] S. Chapra and R. Canale, *Numerical Methods for Engineers.* McGraw-Hill Higher Education, 2010.

[159] T. Detroux, L. Renson, L. Masset, and G. Kerschen, "The harmonic balance method for bifurcation analysis of large-scale nonlinear mechanical systems," *Computer Methods in Applied Mechanics and Engineering*, vol. 296, pp. 18–38, 2015.

[160] E. Doedel, "Lecture Notes on Numerical analysis of Nonlinear Equations," 2010.

[161] T. F. Fairgrieve and A. D. Jepson, "O. K. Floquet Multipliers," *SIAM Journal on Numerical Analysis*, vol. 28, pp. 1446–1462, Oct. 1991.

[162] T. C. Kim, T. E. Rook, and R. Singh, "Effect of smoothening functions on the frequency response of an oscillator with clearance non-linearity," *Journal of Sound and Vibration*, vol. 263, pp. 665–678, June 2003.

[163] J. Nocedal and S. J. Wright, *Numerical Optimization.* Springer, 2nd ed., 2006.

[164] P. Varney and I. Green, "Rotordynamic Analysis of Rotor–Stator Rub Using Rough Surface Contact," *Journal of Vibration and Acoustics*, vol. 138, no. 2, 2016.

[165] F. Quinci, W. Litwin, M. Wodtke, and R. van den Nieuwendijk, "A comparative performance assessment of a hydrodynamic journal bearing lubricated with oil and magnetorheological fluid," *Tribology International*, vol. 162, 2021.

[166] C. Martinelli, A. Coraddu, and A. Cammarano, "Approximating piecewise nonlinearities in dynamic systems with sigmoid functions: Advantages and limitations," *Nonlinear Dynamics*, vol. 111, pp. 8545–8569, May 2023.

[167] P. Sundararajan and S. T. Noah, "Dynamics of forced nonlinear systems using shooting/are-length continuation method-application to rotor systems," *J. Vib. Acoust., Transactions of the ASME*, 1997.

[168] A. Mereles, D. S. Alves, and K. L. Cavalca, "On the continuation of quasi-periodic solutions of rotor systems with fluid-film bearings," *Nonlinear dynamics*, vol. 113, no. 9, pp. 9645–9665, 2025.

[169] S. Kheybari, M. T. Darvishi, F. Alizadeh, S. M. Boulaaras, and K. Hosseini, "A modified scheme to the multiple shooting method for BVPs," *Alexandria Engineering Journal*, vol. 118, pp. 649–663, Apr. 2025.

[170] E. J. Doedel and R. F. Heinemann, "Numerical computation of periodic solution branches and oscillatory dynamics of the stirred tank reactor with A - B - C reactions," *Chemical Engineering Science*, vol. 38, pp. 1493–1499, Jan. 1983.

[171] G. Teschl, *Ordinary Differential Equations and Dynamical Systems*. Providence: Amer Mathematical Society, 2024.

[172] A. Shaw, T. Hill, S. Neild, and M. Friswell, "Periodic responses of a structure with 3:1 internal resonance," *Mechanical Systems and Signal Processing*, vol. 81, pp. 19–34, Dec. 2016.

[173] W. Nash and M. Potter, *Schaum's Outline of Strength of Materials*. US: McGraw-Hill, 5th ed., 2010.

[174] NSK, *Rolling Bearing for Industrial Machinery*. No. Catalogue Number E1103, Japan: NSK, n.d.

[175] National Instruments, "Labview." National Instruments, 2017.

[176] E. Brusa, C. Delprete, L. Giorio, L. G. Di Maggio, and V. Zanella, "Design of an Innovative Test Rig for Industrial Bearing Monitoring with Self-Balancing Layout," *Machines*, vol. 10, p. 54, Jan. 2022.

[177] C. H. Cloud, E. H. Maslen, and L. E. Barrett, "Damping Ratio Estimation Techniques for Rotordynamic Stability Measurements," *Journal of Engineering for Gas Turbines and Power*, vol. 131, Oct. 2008.

[178] Q. Li, B. Weaver, F. Chu, and W. Wang, "A fast damping ratio identification method for rotating machinery based on the singular value of a directional power spectra density function matrix," *Journal of Sound and Vibration*, vol. 488, p. 115630, Dec. 2020.

[179] SKF, *Rolling Bearings*. No. PUB BU/P1 17000/1 EN, SKF, Oct. 2018.

[180] Schaeffler-Technologies, *INA Plain Bearings*. Schaeffler, Mar. 2016.

[181] SKF, *Spherical Plain Bearings and Rod Ends*. No. PUB BU/P1 06116/1 EN, SKF, Sept. 2011.